Probing the active site of anthranilate phosphoribosyltransferase from *Mycobacterium tuberculosis* to facilitate novel drug development

---

A thesis

submitted in partial fulfilment

of the requirements for the degree

of

Doctor of Philosophy in Chemistry

at the

University of Canterbury

by

Tammie Violet Marie Cookson

November 2013

Acknowledgements

I almost can't believe I've made it to this point. This PhD journey has been full of ups and downs for me, with many, 'Woohoo! I've got this done' moments, 'Man, this must be the millionth time I've done this' moments and the ultimately depressing, 'What am I even doing here?' moments. What I do believe is that I would not have come this far without the amazing support system I am lucky to have around me, and I would like to thank every one of you from the bottom of my heart.

My first and foremost mention must be to my primary supervisor, Professor Emily Parker, whose happy, upbeat and optimistic attitude about this science business is one of the main reasons I wanted to work with her in the first place. Mostly though, I would like to thank Emily for her constant patience, understanding and reassurances that no, I am not an imposter in the chemistry department.

I would also like to thank all past and present members of the fairly sizeable Parker group. I have made some wonderful friends here, and I want you all to know how awesome you are. To Dmitri Joseph – what started out as a decidedly rocky first year working together has transformed into a relationship I could not do without. Thank you for all your help in the lab, and for the many happy memories you have helped me create during my time here. To my office neighbour, Sarah Wilson-Coutts, you are absolutely one of the nicest, warmest, friendliest and most willing to help people that I have ever met. I shall miss our dance parties in the lab/hallway/office, and I hope you keep these up in my absence!! Frances Huisman – conversing with you about all things television, movies, award-show fashion and a huge range of other random stuff helped to keep me sane and smiling. Michael Hunter – a good friend with the uncanny ability to make you laugh as he insults you – thank you for taking the time to help me out with problems in my research. As the only one studying my enzyme within the Parker group, it meant a lot to have someone to nut things out with. To my other friends - Nicky Blackmore, David Tran, Wanting Jiao, Eric Lang, Richard Hutton and all the rest of you in the Parker Group – you are all people I am glad to have met.

I would also like to acknowledge and thank the lovely people I have worked and collaborated with at the University of Auckland – Dr Shaun Lott, Dr Esther Bulloch, Dr Genevieve Evans and Dr Alina Castell. Thank you for your continued help and friendship during the course of this project, and for taking me in as an earthquake refugee for a few weeks! A special thank you must go to Dr Genevieve Evans, who has spent many hours helping me in the lab and with crystallography techniques.

Many hours have been spent in the lab over the past few years, and I wish to particularly thank Dr Tim Allison for introducing me to the Parker lab and showing me how everything works, Dr Richard Hutton for his invaluable help with my variant proteins, Dr Marie Squire for running many, many, many samples through the Mass Spectrometer for me, and lastly Dr Meike Holzenkaempfer, Dr Matt Polson and Alistair Duff for general technical assistance. Thank you also to Dr Wanting Jiao and Dr Sebastian Reichau for helping me with crystallography, and to the various people who collected data on my behalf at the Australian Synchrotron.

The Maurice-Wilkins Centre has generously provided me with funding for this research, as well as for several excursions to and from Auckland, which was very gratefully received. I wish to especially acknowledge Rochelle Ramsay, a research manager within the centre, who always took the time to make us Christchurch lot feel welcome and to chat with us about our research. I was also provided with a travel scholarship by the New Zealand Federation of Graduate Women, which greatly assisted with my expenses for travel to the Pacifichem 2010 conference, held in Hawaii, USA.

My family has been my rock during this PhD saga, and I am so thankful for the unwavering support and encouragement they continue to give me every day. Thank you also for telling everyone that I am curing tuberculosis and making me sound awesome!

Abstract

Tuberculosis (TB) is a highly infectious disease that claims the lives of millions of people per year in numerous countries around the world. The bacterium responsible for this disease, *Mycobacterium tuberculosis* (*Mtu*), is becoming resistant to many of the current anti-TB drugs currenly available, making the discovery of novel anti-TB drugs crucial. The enzyme anthranilate phosphoribosyl transferase (AnPRT) from *Mtu* catalyses the Mg^{2+}-dependent reaction between α-5'-phosphoribosyl 1'-pyrophosphate (PRPP) and anthranilate to form *N*-(5'-phosphoribosyl)anthranilate (PRA), which is the second committed step of the tryptophan biosynthetic pathway in *Mtu*. The presence of AnPRT within *Mtu* has been shown to be absolutely necessary for the bacteria's virulence, making it a viable drug target.

Crystal structures of *apo* wild-type *Mtu*-AnPRT and wild-type *Mtu*-AnPRT with PRPP and Mg^{2+} bound have been solved prior to this study, and have elucidated the binding sites for these ligands as well as the conformational changes triggered upon ligand binding. Kinetic parameters for *Mtu*-AnPRT have also been previously obtained using a fluorimetric assay. Conversely, the anthranilate binding site/s within *Mtu*-AnPRT have not been well characterised, and the reaction mechanism is unknown. This thesis describes the functional and structural studies of the active site of *Mtu*-AnPRT, with the end goal of increasing *Mtu*-AnPRT knowledge to improve future drug design.

Chapter 2 of this thesis describes the physical and kinetic characterisation of wild-type *Mtu*-AnPRT, and the inhibition of this enzyme using a range of anthranilate-like compounds. A novel enzyme-coupled UV-based assay was developed to kinetically characterise *Mtu*-AnPRT, which yielded apparent K_M values for each substrate and a turnover number of 2 s^{-1}. The potencies of several inhibitors were characterised against *Mtu*-AnPRT, and demonstrated that a 'bi-anthranilate'-like compound was the strongest inhibitor. Crystal structures of *Mtu*-AnPRT with these inhibitor compounds bound identified several common inhibitor-binding residues, as well as a third potential binding site for anthranilate (previously only two anthranilate sites were predicted).

In Chapter 3, the substrate specificity of *Mtu*-AnPRT is explored using a range of fluoro-, methyl- and methoxy-substituted anthranilate analogues. These analogues were characterised as substrates of *Mtu*-AnPRT using a commercially available pyrophosphate assay. The methoxy-substituted compounds did not act as *Mtu*-AnPRT substrates, whereas all fluoro-substituted compounds were readily accepted. The methyl-substituted compounds were also accepted, but had considerably weaker binding affinities for the enzyme and lower turnover numbers. ^{1}H NMR spectroscopy

confirmed the turnover of these compounds by *Mtu*-AnPRT, and the formation of α and β PRA anomers that interconvert via an imine intermediate. Crystal structures of the fluoro- and methyl-substituted anthranilate analogues bound to *Mtu*-AnPRT provided further insight into the reaction mechanism of the enzyme, and highlighted the presence of several anthranilate binding sites.

The effects of mutating six key residues individually in the *Mtu*-AnPRT active site are outlined in Chapter 4, including physical, kinetic and structural characterisation. The variant proteins *Mtu*-G107P, *Mtu*-N183A, *Mtu*-P180A, *Mtu*-R193A, *Mtu*-R193L and *Mtu*-R194A were all successfully expressed and purified, and displayed similar physical attributes to the wild-type *Mtu*-AnPRT enzyme. Kinetic characterisation of the variants emphasised the importance of the conserved R193 residue for both substrate binding and catalysis, and the crucial role of G107 for enzyme function. Structures of these variants were obtained in the presence of various ligands, with *Mtu*-R194A and *Mtu*-R193A capturing anthranilate in three different binding sites between them.

Chapter 5 involves the kinetic and structural characterisation of *Mtu*-N138A, *Mtu*-P180A and *Mtu*-R194A in the presence of two inhibitors: an anthranilate-like inhibitor with two additional methyl groups on the C3 and C5 positions (ACS142), and a 'bi-anthranilate'-like inhibitor (ACS172). No significant differences were observed between the variant and wild-type enzymes for ACS172, however, several considerable changes in inhibitor potency and Mtu-AnPRT binding were observed for ACS142.

Finally, Chapter 6 discusses and interprets all aspects of the thesis and the applications of the research with respect to novel drug design.

Table of Contents

Chapter 2

Chapter 3

Chapter 4

Chapter 6

Chapter 7

List of Figures

Chapter 1

Chapter 2

Chapter 3

Chapter 4

Chapter 5

Chapter 6

List of Tables

Chapter 1

Chapter 2

Chapter 3

Chapter 4

Chapter 5

List of Abbreviations

Aba	*Acinetobacter baylyi*
Abs	absorbance
ACSRC	Auckland Cancer Society Research Centre
Amu	atomic mass unit
AnPRT	anthranilate phosphoribosyltransferase
Ant/Anth	anthranilate
apo	*apo*enzyme
AS	anthranilate synthase
ATP	adenosine triphosphate
Atu	*Agrobacterium tumefaciens*
Bme	*Brucella melitensis*
Bp	base pairs
Cac	*Clostridium acetobutylicum*
CD	circular dichroism
CDRP	1-(*o*-carboxyphenylamino)-1'-deoxyribulose-5'-phosphate
DAH7PS	3-deoxy-D-*arabino*-heptulosonate 7-phosphate synthase
DHQS	dehydroquinate synthase
DNA	deoxyribose nucleic acid
dNTP	dinucleotide triphosphate
DSF	differential scanning fluorimetry

E4P	erythrose 4-phosphate
EPSP	5-enolpyruvyl shikimate 3-phosphate
HIV	human immunodeficiency virus
IMAC	immobilised metal affinity column
InGPS	indole-3-glycerol phosphate synthase
ISZ	isoniazid
k_{cat}	turnover number
kDa	kilodalton
K_i	inhibition constant
K_M	Michaelis-Menten constant
LB	lysogeny broth
Maf	*Mycobacterium africanum*
Mbo	*Mycobacterium bovis*
Mca	*Mycobacterium canetti*
MDR	multi-drug resistant
MESG	2-amino-6-mercapto-7-methylpurine ribonucleoside
Mtu	*Mycobacterium tuberculosis*
MWCO	molecular weight cut-off
NAD	nicotinamide adenine dinucleotide
NMR	nuclear magnetic resonance
ORF	open reading frame
Pca	*Pectobacterium carotovorum*
PCR	polymerase chain reaction

PDB ID	Protein Data Bank identification code
PEP	phosphoenolpyruvate
P_i	inorganic phosphate
PNP	purine nucleoside phosphorylase
PP_i	inorganic pyrophosphate
PRA	*N*-(5'-phosphoribosyl)anthranilate
PRAI	phosphoribosyl anthranilate isomerase
ProFAR	N-((5'-phosphoribosyl)-formino)-5-aminoimidazol-4-carboxamideribonucleotide
PRPP	5'-phosphoribosyl 1'-pyrophosphate
PyNP	pyrimidine nucleoside phosphorylase
R5P	ribose-5-phosphate
RIF	rifampin
RMSD	root mean square deviation
Sau	*Staphylococcus aureus*
Sce	*Sacchromyces cerevisiae*
SDS-PAGE	sodium dodecyl sulphate – polyacylamide gel electrophoresis
SEC	size exclusion chromatography
SOC	super optimal broth with catabolite repression
Sso	*Sulfolobus solfataricus*
TAE	tris-acetate-ethylenediaminetetraacetic acid
TB	tuberculosis
TS	tryptophan synthase
TSP	trimethylsilyl propionate

Tth	*Thermus thermophilus*
UHF-TOF	ultra-high resolution time of flight
UV	ultra violet
Xca	*Xanthomonas campestris*
XDR	extensively drug resistant

Amino Acids

A	alanine
C	cysteine
D	aspartic acid
E	glutamic acid
F	phenylalanine
G	glycine
H	histidine
I	isoleucine
K	lysine
L	leucine
M	methionine
N	asparagine
P	proline
Q	glutamine
R	arginine
S	serine
T	threonine
V	valine
W	tryptophan
Y	tyrosine

Publications

- Castell, A.; Short, F. L.; Evans, G. L.; **Cookson, T. V. M.**; Bulloch, E. M. M.; Joseph, D. D. A.; Lee, C. E.; Parker, E. J.; Baker, E. N.; Lott, J. S.*,* The Substrate Capture Mechanism of *Mycobacterium tuberculosis* Anthranilate Phosphoribosyltransferase Provides a Mode for Inhibition. *Biochemistry* **2013,** 52 (10), 1776-1787

Chapter 1

Introduction

1.1 Tuberculosis

Tuberculosis (TB) is a highly infectious, pestilent disease that stretches back centuries into mankind's history,[1] and yet still we are unable to completely eradicate it. Infection is spread via inhalation of the TB bacteria into the lungs, where they are then engulfed by alveolar macrophages as part of the immune response.[2] Within these macrophages, the bacteria are able to survive and proliferate.[3] Lesions (or granulomas/tubercles) form within the lungs as the body attempts to eliminate these infected macrophages, within which caseous necrosis occurs.[4] The necrosis can erode the surrounding tissue, including blood vessels, leading to distribution of the bacteria throughout the body via the bloodstream.[5] Fatalities usually arise from internal bleeding, respiratory failure as granulomas spread throughout the lungs or suffocation due to excess phlegm/blood in the lungs.[6]

Before the rise of modern chemotherapy, treatments for TB tended to vary from extreme measures, such as surgical removal of infected lung tissue,[1] to less invasive remedies such as fresh air and bed rest in sanatoria.[1, 7] The discovery of the organism responsible for this disease, *Mycobacterium tuberculosis* (*M. tuberculosis, Mtu*), was made by Robert Koch in 1882, and his finding paved the way towards more effective chemotherapeutic treatment with antibiotics.[8]

As treatments of TB with first-line antibiotics such as isoniazid (ISZ), rifampin (RIF) and pyrazinamide as well as second-line antibiotics such as ethionamide, cycloserine and the quinolones were introduced, the incidences of mortality dramatically decreased from approximately 75% to 20% from the 1960s onward.[9] However, the emergence of Multi-Drug Resistant TB (MDR-TB) and Extensively Drug Resistant TB (XDR-TB) is seriously undermining the efforts made to control this disease.[10] MDR-TB is defined by resistance of *Mtu* to the two first-line drugs ISZ and RIF, and XDR-TB is defined by resistance to ISZ and RIF, as well as any fluoroquinoline and at least one of the three injectable second-line drugs, capreomycin, amikacin or kanamycin,[10] making treatment of patients with these resistant strains difficult. Additionally, patients who are co-infected with both HIV and TB suffer from the added complication of detrimental interactions between the drugs used for treating each of these diseases. For example, it has been observed that RIF activates the enzyme cytochrome P450, which causes some HIV protease inhibitors to be metabolised too quickly.[11]

In 2011, TB caused a total of 1.4 million deaths, with an estimated 8.7 million new cases of the disease reported.[12] With treatment options becoming more limited due to MDR-TB, XDR-TB and HIV, further understanding of the *Mtu* cell biology is necessary in order to locate novel drug targets and/or antibiotics.

1.2 *Mycobacterium tuberculosis*

The majority of TB infections are caused by the pathogen *Mtu*, however, other closely related organisms such as *Mycobacterium bovis* (*Mbo*), *Mycobacterium africanum* (*Maf*) and *Mycobacterium canetti* (*Mca*) can also cause the disease.[13] *Mbo* can infect both cattle and humans, though its prevalence in humans was drastically lowered once the pasteurisation of milk was introduced.[1] *Maf* and *Mca* are almost exclusively human pathogens, with both organisms found primarily in Sub-Saharan Africa.[14]

Mycobacteria are rod-shaped bacilli that are non-motile and do not form spores.[15] Their complex cell envelope is structurally distinct from those of other bacteria, with four main layers extending outwards from the plasma membrane. These layers are made up of peptidoglycan, arabinogalactan sugars and mycolic acids respectively, with a 'capsule layer' nearest to the surface (Figure 1.1).[9, 16] Upon exposure of *Mtu* to Gram stain, the bacteria resist decolourisation even in the presence of acidic alcohol, and are thus classified as 'acid-fast'.[17]

Upon phagocytosis of *Mtu* into an alveolar macrophage, the bacteria are faced with a hostile environment that is nitrosative, oxidative, acidic and nutrient-deficient.[18] In order to survive, *Mtu* must synthesise essential sugars and amino acids that cannot be ingested from its surroundings. There are many biosynthetic pathways within *Mtu* that are not present in mammalian organisms, which generate necessary cell wall components, amino acids and sugars.[19] These pathways provide an important focus for the synthesis of antibiotics, which will ideally target the bacteria while leaving the host unharmed.

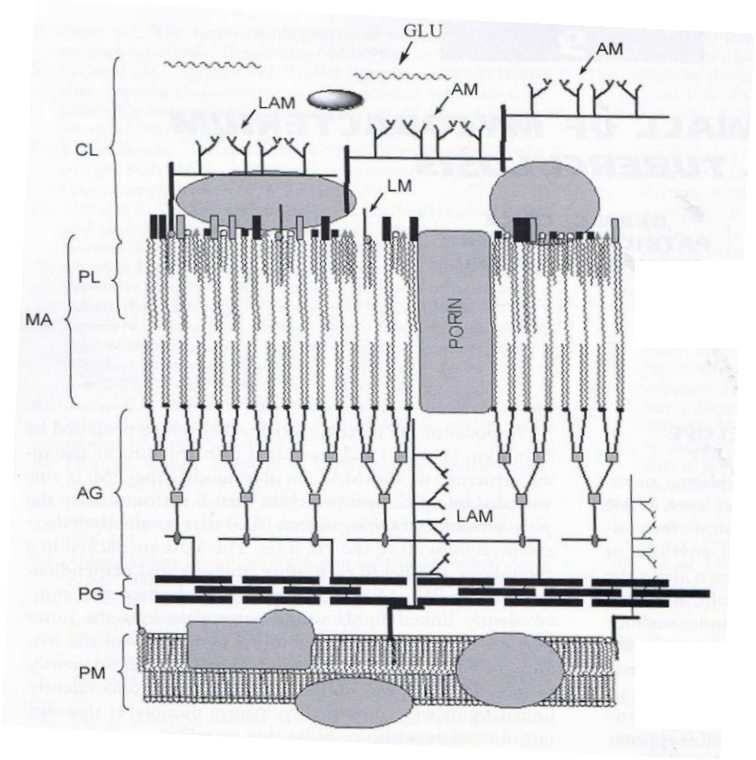

Figure 1.1 The cell wall of *Mycobacterium tuberculosis*. Figure extracted from Rom & Garay.[9] Abbreviations are as follows: PM – plasma membrane, PG – peptidoglycan, AG – arabinogalactan, MA – mycolic acids, PL – phospholipids, CL – capsule layer, AM – arabinomannan, LAM - lipoarabinomannan, GLU - glucan, LM – lipomannan.

1.3 Aromatic Amino Acid Biosynthesis

The amino acids tryptophan, phenylalanine and tyrosine share a similar aromatic structure, and as such *Mtu* and other bacteria utilise the same metabolic pathway to synthesise the precursors for these amino acids. This pathway, named the shikimate pathway, is present in bacteria, fungi, plants and parasites but is absent in mammals,[20] and has been a focal point for novel drug synthesis and herbicides.[21]

The shikimate pathway contains seven enzyme-catalysed reactions leading to the formation of chorismate, which acts as a branch-point for the formation of several important compounds including folic acid and vitamins E and K.[22] With respect to aromatic amino acid synthesis, the pathway splits in two directions after the synthesis of chorismate, where one branch leads to the formation of prephenate, the precursor for phenylalanine and tyrosine, and the other branch leads to anthranilate, from which tryptophan is made (Figure 1.2).

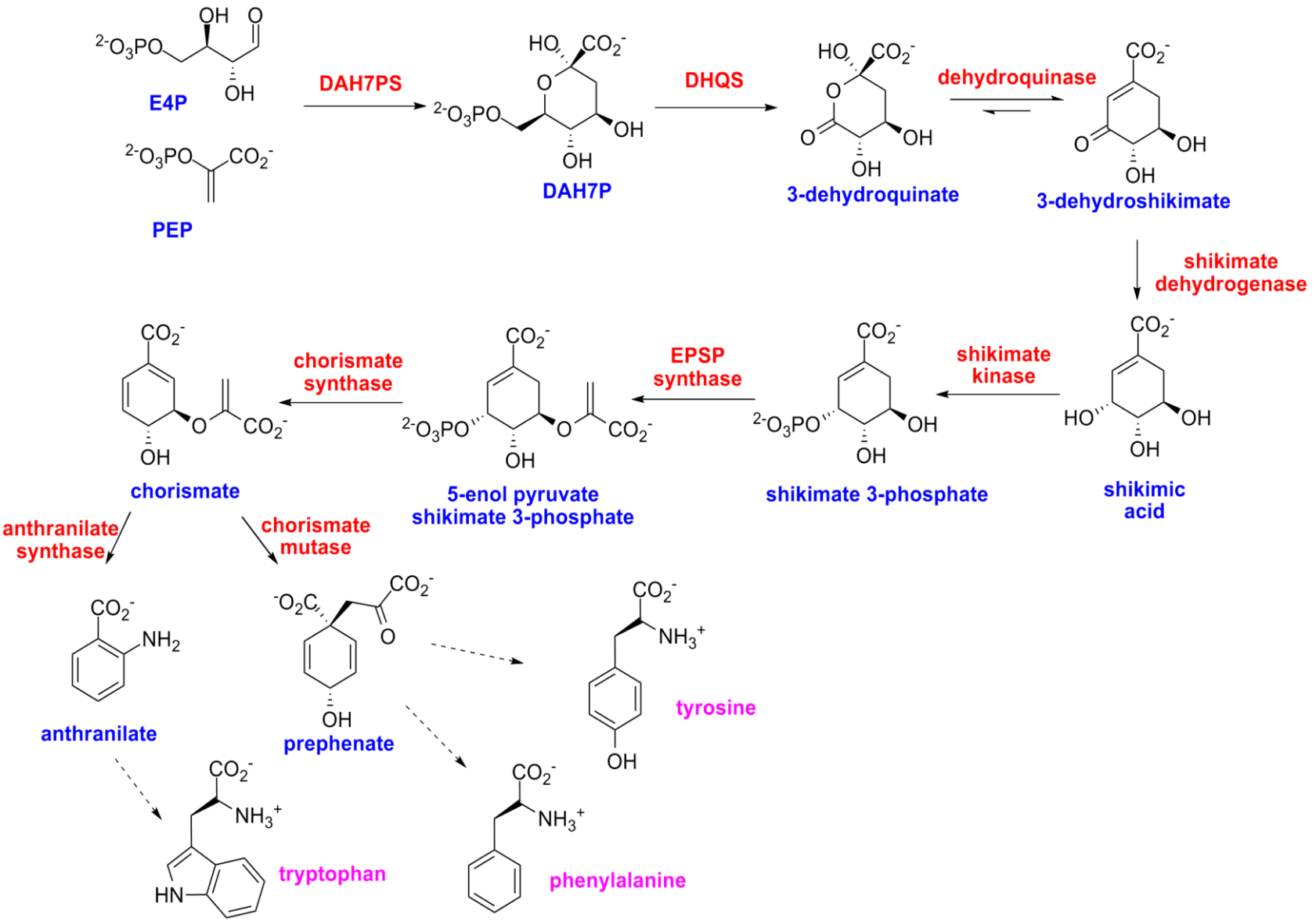

Figure 1.2 The seven enzyme-catalysed reactions of the shikimate pathway, which leads to the formation of chorismate and subsequent pathway branching to form the three aromatic amino acids.

1.4 Tryptophan Biosynthesis

The biosynthesis of the amino acid tryptophan from chorismate by *Mtu* is an example of a bacterial metabolic pathway that can be exploited as a potential drug target. Auxotrophic mutants of *Mtu* containing gene knockouts within the tryptophan pathway have been shown to be unable to replicate in cultured murine macrophages, while also showing an attenuation of virulence in mice.[23] These results indicate that tryptophan is not bio-available within the murine macrophage. The inability to infect mice was especially apparent in the TrpD knockout strain, which was found to be essentially avirulent in immune-deficient mice,[23] suggesting that removal of the TrpD gene leaves the bacteria with no alternate means to acquire tryptophan.

The tryptophan pathway is a series of six enzyme-catalysed reactions, which has been identified and characterised in several organisms.[24] The full reaction pathway is outlined in Figure 1.3. The pathway begins with the conversion of chorismate and glutamine into anthranilate by anthranilate synthase (AS), which also releases pyruvate and glutamate as byproducts. AS is a heterodimeric enzyme containing a synthase component and a glutamine amidotransferase component, coded for by the genes TrpE and TrpG respectively.[25] Anthranilate and 5'-phosphoribosyl 1'-pyrophosphate (PRPP) are then converted to *N*-(5'-phosphoribosyl)anthranilate (PRA) by anthranilate phosphoribosyl transferase (AnPRT) in a magnesium dependent reaction. PRA is then isomerised to 1-(*o*-carboxyphenylamino)-1'-deoxyribulose-5'-phosphate (CDRP). In some organisms, the isomerisation is performed by a dedicated PRA isomerase (PRAI), which is encoded for by TrpF. However, a homologue of TrpF has not been found anywhere in the *Mtu* genome, and the conversion of PRA to CDRP is thought to instead be catalysed by the ProFAR isomerase protein encoded by the gene HisA, which acts as part of the histidine biosynthesis pathway.[26]

The conversion of CDRP to indole-3-glycerol phosphate is carried out by indole-3-glycerol phosphate synthase (InGPS) (encoded by TrpC), with CO_2 and H_2O released in the process. The final two steps in this pathway are catalysed by tryptophan synthase (TS); a heterodimeric protein made up of an α subunit (encoded by TrpA) and a β subunit (encoded by TrpB). First, the α subunit catalyses the cleavage of glyceraldehyde-3-phosphate from the indole moiety, then the β subunit catalyses the reaction of the indole with L-serine to form L-tryptophan.

In some organisms, the genes encoding for proteins that catalyse consecutive reactions are fused into a single open reading frame (ORF). Examples of this phenomenon are found in *E. coli* where TrpD and TrpG are fused as well as TrpF and TrpC,[27] and in *Thermotoga maritima* where TrpD and TrpG are fused.[28]

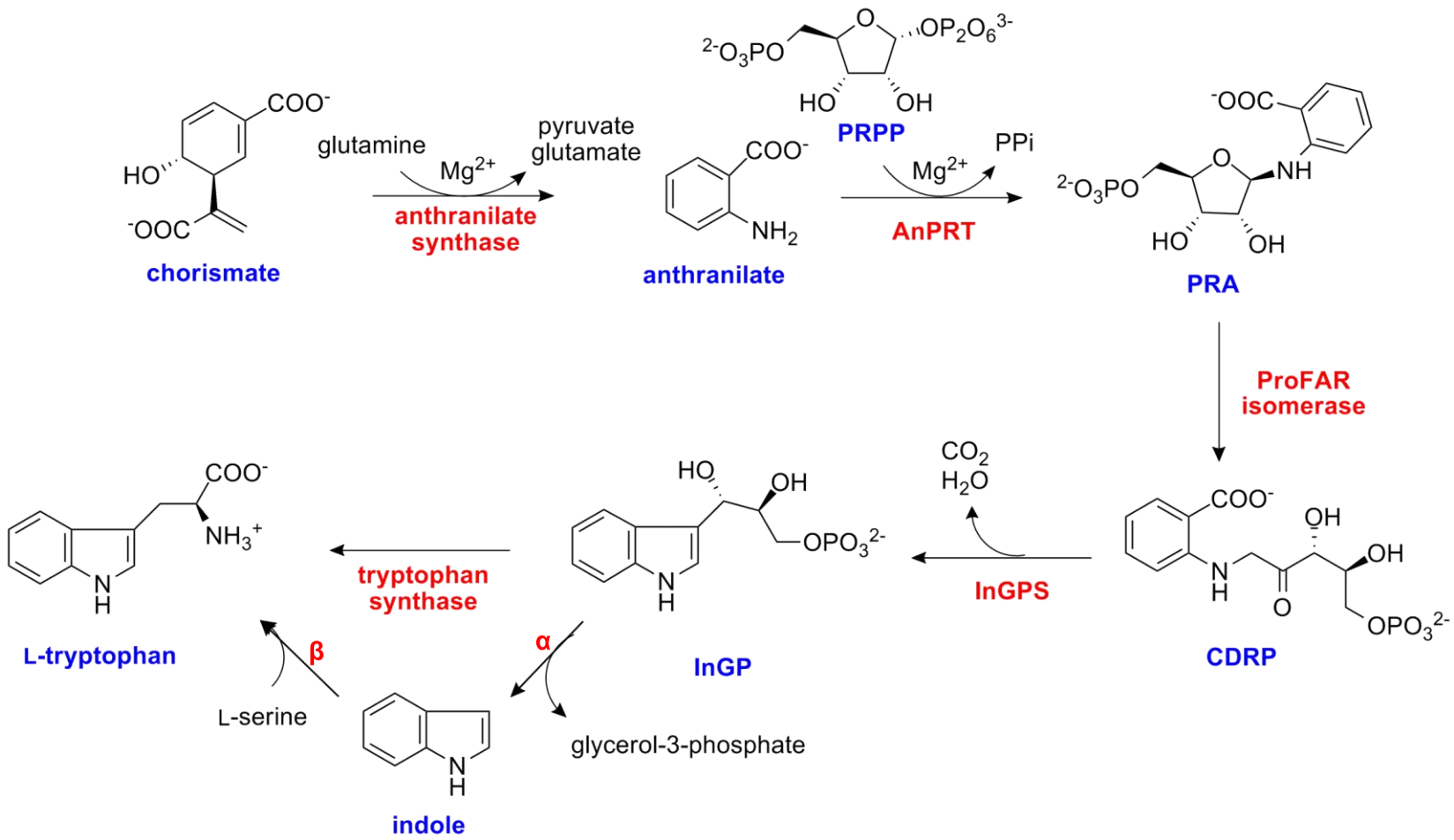

Figure 1.3 The enzyme-catalysed reactions of the tryptophan biosynthetic pathway in *Mtu*.

1.5 Phosphoribosyltransferases

All phosphoribosyltransferase (PRT) enzymes are characterised by their usage of PRPP, whereby the phosphoribosyl group of PRPP is transferred to a nitrogenous and generally aromatic base.[29] The glycosidic bond between the C1 carbon of the ribose ring and the oxygen of the pyrophosphate (PP_i) moiety of PRPP is cleaved in this process.[30] The reactions proceed with inversion of stereochemistry at the anomeric carbon, and require Mg^{2+} for catalysis.[31]

Mtu-AnPRT is encoded by the gene TrpD, which has previously been shown to be essential for the virulence of *Mtu* in mice.[23] This enzyme belongs to the phosphoribosyltranferase superfamily, which is divided into four sub-categories: type I, type II, type III and type IV.

The type I PRTs are a homologous group of enzymes that are part of the nucleotide synthesis and salvage pathways.[31c] They are defined by a common protein fold comprised of a central five-stranded β sheet surrounded by α helices, and also by a 13-residue sequence motif which corresponds to a PRPP binding loop.[32] Some type I PRTs are subject to allosteric regulation, such as glutamine PRPP amidotransferase which catalyses the first step of purine biosynthesis and is inhibited by the end-products of the pathway.[33] Many of these dimeric proteins require a conformational change to facilitate catalysis, which was first demonstrated in crystal structures of glutamine PRPP amidotransferase where the occlusion of the active site via the movement of a flexible loop could be observed.[34] Further examples of type I PRTs include orotate PRT (pyrimidine biosynthesis) (Figure 1.4A),[35] hypoxanthine-guanine PRT (purine biosynthesis)[36] and uracil PRT (uracil salvage).[37]

Some examples of type II PRTs include quinolinic acid PRT (NAD biosynthesis)[38] and nicotinic acid PRT (NAD salvage).[39] The type II PRTs do not display the protein fold and 13-residue sequence characteristic of type I PRTs, and instead exhibit an irregular seven-stranded α/β barrel and an N-terminal open-faced β-sandwich domain. The oligomeric structures of these proteins can vary, with some existing as hexamers (*Homo sapiens* quinolinic acid PRT),[40] domain-swapped dimers (*Salmonella typhimurium* quinolinic acid PRT)[38] or monomers (*Saccharomyces cerevisiae* (*Sce*) nicotinic acid PRT).[39] Structures of *Mtu* quinolinic acid PRTs (Figure 1.4B) showed little gross conformational change upon substrate binding, in contrast to what has been observed for type I PRTs.[31a]

AnPRTs are mostly considered to represent the type III category, with a few exceptions labelling them as type IV.[41] The type III AnPRT enzymes catalyse the reaction between anthranilate and PRPP to form PRA as part of the tryptophan biosynthesis pathway. Structures of AnPRTs from different

organisms such as *Sulfolobus solfataricus* (*Sso*),[42] *Pectobacterium carotovorum* (*Pca*)[43] and *Mtu*[41a, 44] (Figure 1.4C) have identified a novel protein fold distinct from the type I, type II and type IV enzymes. The AnPRT monomers are made up of a smaller N-terminal α helical domain and a larger C-terminal α/β domain, which are joined by a hinge region. This fold has a similar architecture to some pyrimidine nucleoside phosphorylases (PyNPs), which catalyse the near reverse reaction of AnPRTs to yield ribose-1-phosphate and a free nitrogenous base. AnPRTs and PyNPs also share a similar quaternary structure, consisting of a head-to-head homodimer, and it has been suggested that AnPRTs and thymidine NPs (a type of PyNP) have evolved from a common ancestor.[43, 45]

Type IV PRTs are solely represented by the adenosine triphosphate PRTs (ATP PRTs), which catalyse the formation of PR-ATP from PRPP and ATP as the first step of the histidine biosynthetic pathway. These enzymes are highly regulated by the end product of the pathway – histidine. There are two sub-families within these type IV enzymes, which are decidedly different in their quaternary structure. The first sub-family are the hexameric ATP PRTs, which contain six $HisG_L$ subunits composed of two domains that comprise an α/β bi-lobal catalytic domain, and a third domain for allosteric histidine binding (Figure 1.4D).[46] The second sub-family are hetero-octamer ATP PRTs, which are made up of four $HisG_S$ catalytic subunits and four regulatory HisZ subunits, with both subunits required for a functional complex (Figure 1.4E).[47]

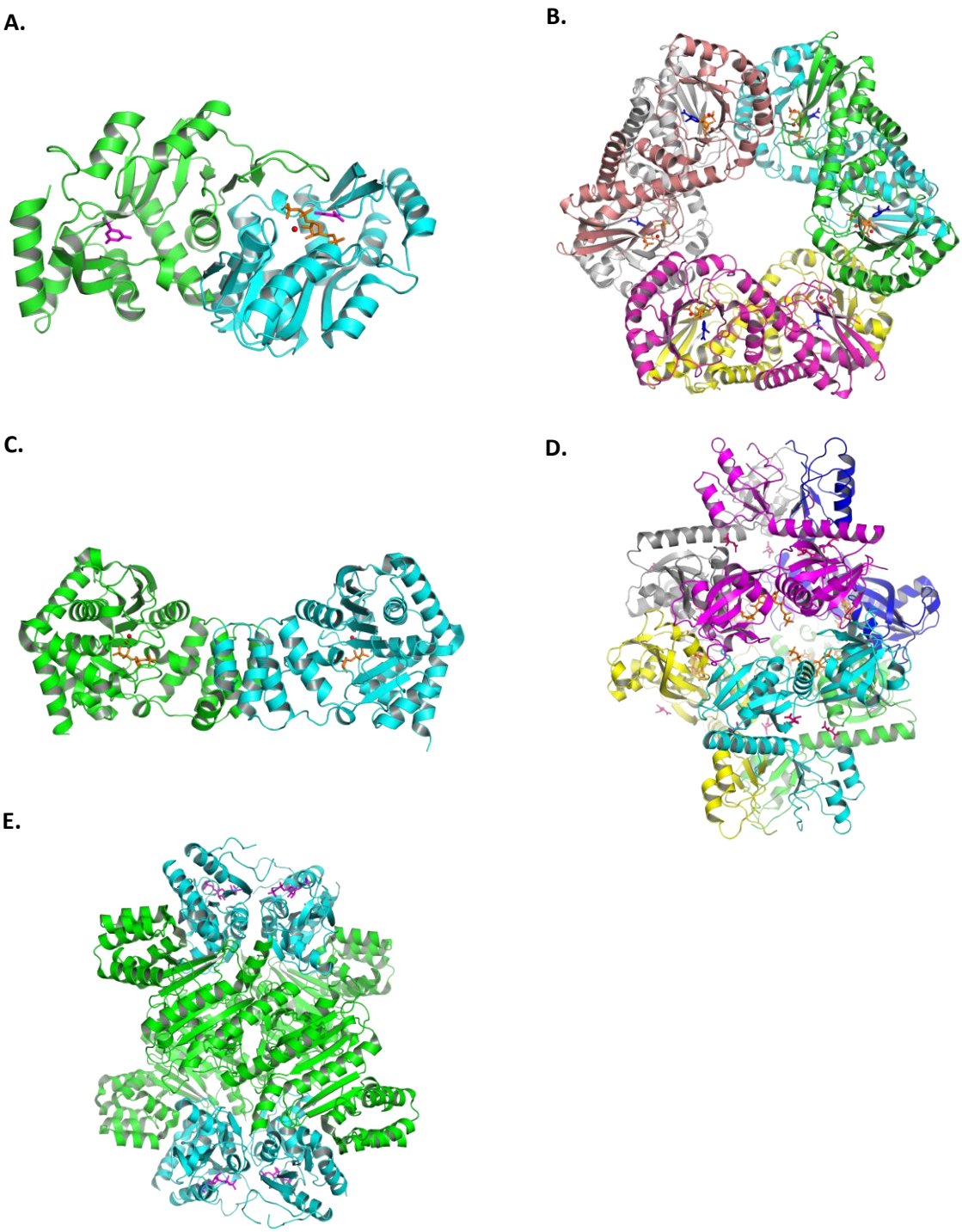

Figure 1.4 Representatives of the different types and sub-families of PRTs. Different protein chains are coloured separately unless specified. A) Type I *S. typhimurium* orotate PRT (PDB ID: 1LH0) with PRPP (orange), orotic acid (magenta) and Mg^{2+} (red spheres) bound. B) Type II *Mtu* quinolinic acid PRT (PDB ID: 1QPR) with 5'phosphoribosyl 1'-(β-methylene)-pyrophosphate (orange), phthalic acid (blue) and Mn^{2+} (red spheres) bound. C) Type III *Mtu* AnPRT (PDB ID: 1ZVW) with PRPP (orange) and Mg^{2+} (red spheres) bound). D) Type IV *Escherichia coli* ATP PRT hexamer (PDB ID: 1Q1K) with PR-ATP (orange) and tartaric acid (pink) bound. E) Type IV *Lactococcus lactis* ATP PRT hetero-octamer (PDB ID: 1Z7N) with PRPP (magenta) bound. The four $HisG_S$ subunits are coloured cyan, with the four HisZ subunits coloured green.

1.6 Anthranilate Phosphoribosyltransferases

The anthranilate phosphoribosyltransferases (AnPRTs) specifically catalyse the Mg^{2+} dependent reaction between anthranilate and PRPP to form PRA and PP_i (Figure 1.5), which constitutes the third committed step of the tryptophan biosynthetic pathway. This section will detail what is currently known about these enzymes, and draw comparisons of orthologues to *Mtu*-AnPRT where appropriate.

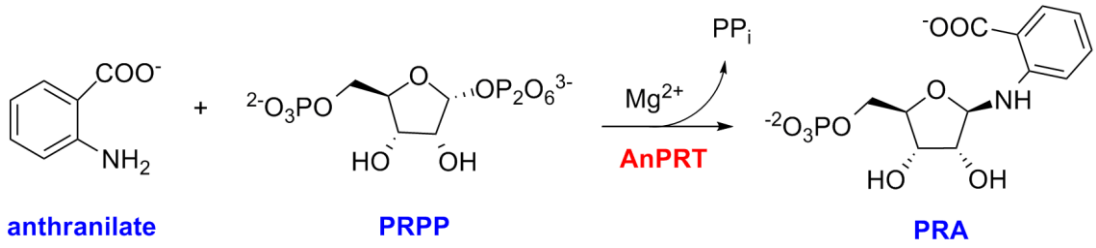

Figure 1.5 The reaction catalysed by AnPRT.

1.6.1 Sequence Alignment

A structure-based sequence alignment of AnPRT enzymes from *Mtu, Sso, Pca* and *Thermus thermophilus* (*Tth*) was performed and used to create a multiple sequence alignment from a diverse range of bacteria including *Clostridium acetobutylicum* (*Cac*), *Staphylococcus aureus* (*Sau*), *Brucella melitensis* (*Bme*) and *Agrobacterium tumefaciens* (*Atu*).[44] This sequence alignment is recreated in Figure 1.6. The alignment demonstrated the existence of several conserved sequence motifs, with some pertaining to the dimer interface and to the PRPP, Mg^{2+} and anthranilate binding sites.

Conserved residues with respect to ligand binding include an absolutely conserved GTGGD motif from residues 107-111 (numbered for the *Mtu* enzyme), which is located on the β1-α5 loop and is involved in PRPP binding. Two residues, D251 and E252, are absolutely conserved and pertain to Mg^{2+} binding. A ψψKHGN motif from residues 133-138 (where ψ stands for a hydrophobic amino acid) is located on the β2-α6 loop and is involved in both anthranilate and PRPP binding. A conserved R193 residue located on the α8 helix is also associated with anthranilate binding. There is also a conserved A179 residue which appears to be conserved for structural reasons. A conserved TψψNψψGPLxNP sequence from residues 200-211 is located on the α9 helix which makes up part of the hinge region between the two domains of the AnPRT monomer.

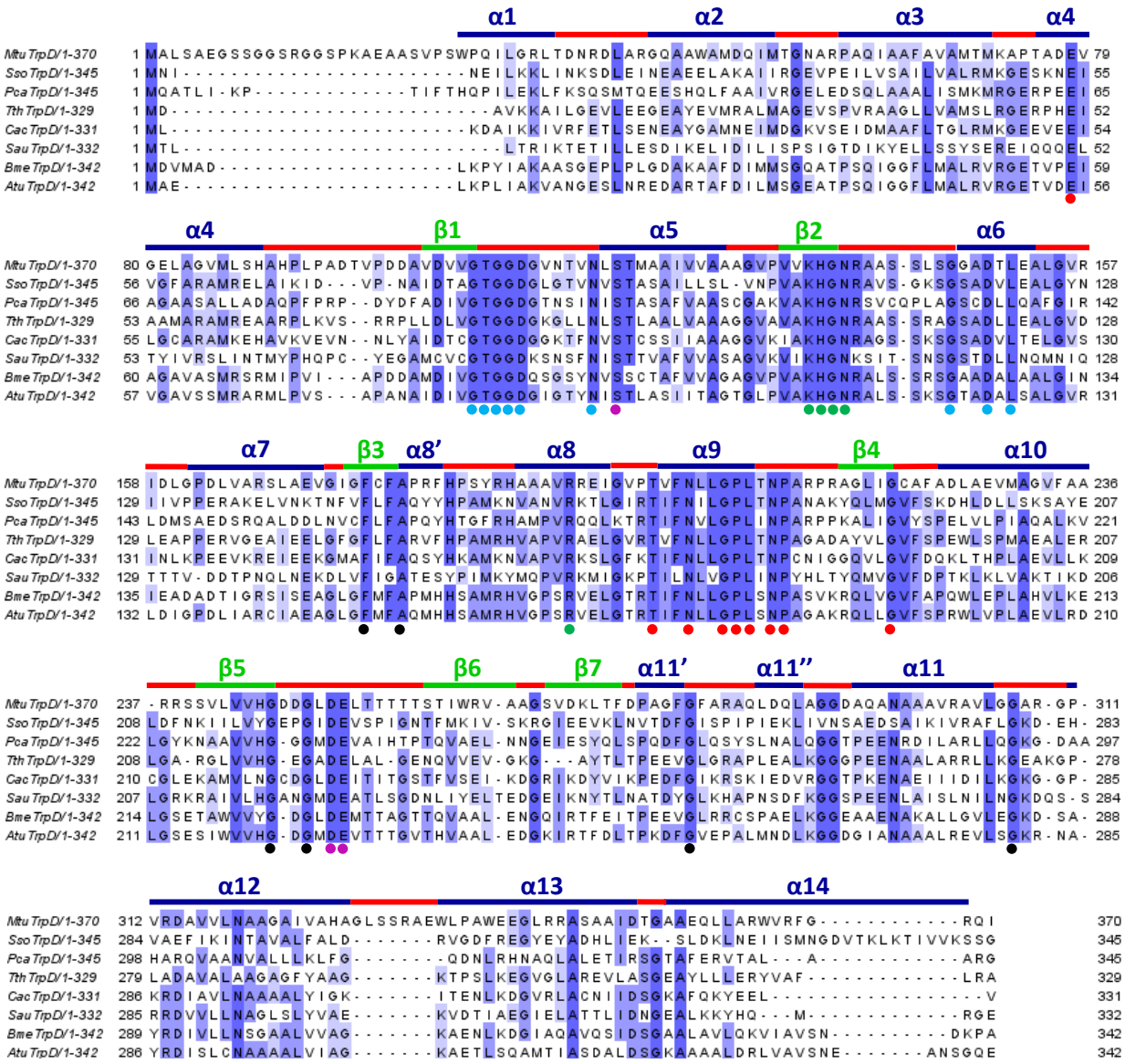

Figure 1.6 A sequence alignment of AnPRTs from *Mtu*, *Sso*, *Pca*, *Tth*, *Cac*, *Sau*, *Bme* and *Atu*, recreated from Lee *et al.*[44] using TCOFFEE: Advance.[48] The figure was created using Jalview.[49] Dots indicate residues involved with the hinge region (red), PRPP binding (blue), anthranilate binding (green) and Mg^{2+} binding (purple). Black dots indicate residues that appear to be conserved for structural reasons.[44] Blue solid lines indicate α helices, green solid lines indicate β strands and red solid lines indicate loop regions.

1.6.2 Crystal Structures

Structures of the enzymes from the organisms *Pca*,[43] *Sso*,[42, 50] *Tth* (PDB ID: 1V8G), *Acinetobacter baylyi* (*Aba*) (PDB ID: 4GTN), *Xanthomonas campestris* (*Xca*) (PDB ID: 4HKM) and *Mtu*[41a, 44, 51] have been obtained with various ligands bound. All structures are head-to-head homodimers, with the monomers interacting via the smaller N-terminal domain, which is composed of six α-helices. The N-

terminal domain is joined to the larger α/β domain via a hinge region. The α/β domain is folded around a central seven-stranded β-sheet, with a number of α-helices packed on either side of it (Figure 1.7).

The dimer interface of the AnPRTs has no salt bridge interactions, few hydrogen bonds and appears to be mostly hydrophobic, with some conservation of hydrophobic residues in this region.[44] The purpose of the dimeric structure of the AnPRTs is likely to maximise the stability of the enzyme, which was discovered when monomeric variants of *Sso*-AnPRT displayed similar kinetic activity to the wild-type dimer, but showed a decrease of 10 °C in their denaturation temperatures.[52]

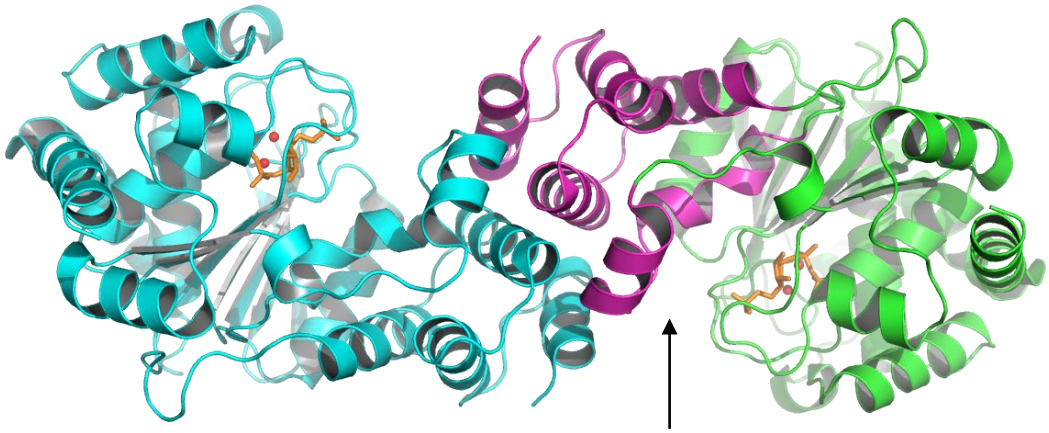

Figure 1.7 The *Mtu*-AnPRT dimer. *Mtu*-AnPRT with PRPP (orange) and Mg^{2+} (red spheres) bound (PDB ID: 1ZVW) showing chain A coloured in cyan, with chain B coloured by domain, with the smaller N-terminal helix bundle coloured magenta, and the larger C-terminal α/β domain coloured green. The hinge region is indicated by an arrow.

1.6.2.1 AnPRT *Apo*enzyme Structures

Structures of *apo* AnPRTs show a very similar protein fold, with the RMSD values of various *apo* structures as compared to *apo Mtu*-AnPRT outlined in Table 1.1. Some obvious differences include a C-terminal helix extension for *Sso*-AnPRT, an extended α12 – α13 loop and helix formation within the β2-α6 loop for *Mtu*-AnPRT, and an extended α11 – α12 loop for *Aba*-AnPRT (Figure 1.8). There is also a *Mtu*-AnPRT 25-residue N-terminal extension, which can be observed in the sequence alignment in Figure 1.6, however, this extension remains disordered in all known structures of *Mtu*-AnPRT.

AnPRT organism	PDB ID	RMSD value (Å) (monomer)*	RMSD value (Å) (dimer)
Sulfolobus solfataricus	1O17	1.794	4.331
Pectobacterium carotovorum	1KHD	1.764	5.481
Thermus thermophilus	1VG8	1.698	4.489
Acinetobacter baylyi	4GTN	1.989	3.983
Xanthomonas campestris	4HKM	1.419	4.600

Table 1.1 RMSD values of *apo* AnPRTs as compared to *apo Mtu*-AnPRT (PDB ID: 2BPQ) when superimposed using PyMOL software.[53] *Chain A from each organism is superimposed onto chain A from *Mtu*-AnPRT.

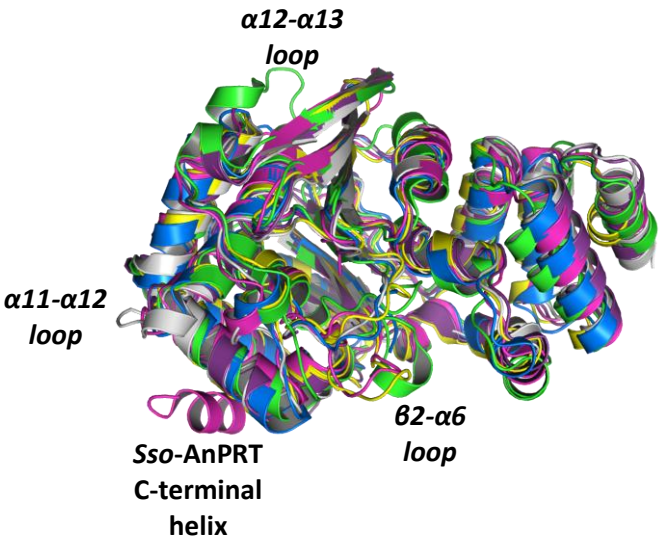

Figure 1.8 Superimposition of *apo* AnPRT structures. *Mtu*-AnPRT is shown in green, *Sso*-AnPRT is shown in magenta, *Pca*-AnPRT is shown in blue, *Tth*-AnPRT is shown in yellow, *Aba*-AnPRT is shown in grey and *Xca*-AnPRT is shown in purple.

1.6.2.2 AnPRT PRPP Binding

The active site of the AnPRTs is located in the cleft between the N-terminus α-helical domain and the larger α/β domain. Structures of *Pca*-AnPRT (PDB ID: 1KGZ), *Sso*-AnPRT (PDB ID: 1ZXY) and *Mtu*-

AnPRT (PDB ID: 1ZVW) have been solved with PRPP and Mg^{2+} bound in the active site, though the *Sso*-AnPRT structures place PRPP in a significantly different orientation compared to *Pca* and *Mtu*. Equivalent residue numbers between the different organisms mentioned are outlined in Table 1.2.

The *Pca* and *Mtu*-AnPRT structures place PRPP between the β1-α5 and β2-α6 loops, with the PP_i group buried the most deeply within the protein and the phosphate group facing out towards the solvent (Figure 1.9A and B). The PRPP molecule bound to chain A of the *Pca*-AnPRT structure makes hydrogen bond contacts to G94 via its phosphate group, and to G91, N101, S103, T104, S132 (numbered for *Pca* enzyme) and a Mn^{2+} (referred to as Mn1) ion via its PP_i group. The ribose ring does not make any hydrogen bonds with the protein, which is likely due to the disordered nature of the β2-α6 loop (Figure 1.9C). Chain B of *Pca*-AnPRTmakes slightly different contacts to the PRPP molecule, with contacts to G91, G94, S103 and T104 as before, but with extra hydrogen bonds to K119 via the PP_i group and S132 via the ribose ring. The PRPP molecules in each chain also make hydrogen bonds to several water molecules. Mn1 is octahedrally co-ordinated to two PP_i oxygen atoms, two water molecules and the side chains of S103 and E237, with a second Mn^{2+} ion (Mn2) octahedrally co-ordinated to four water molecules and the side chains of D236 and E237.

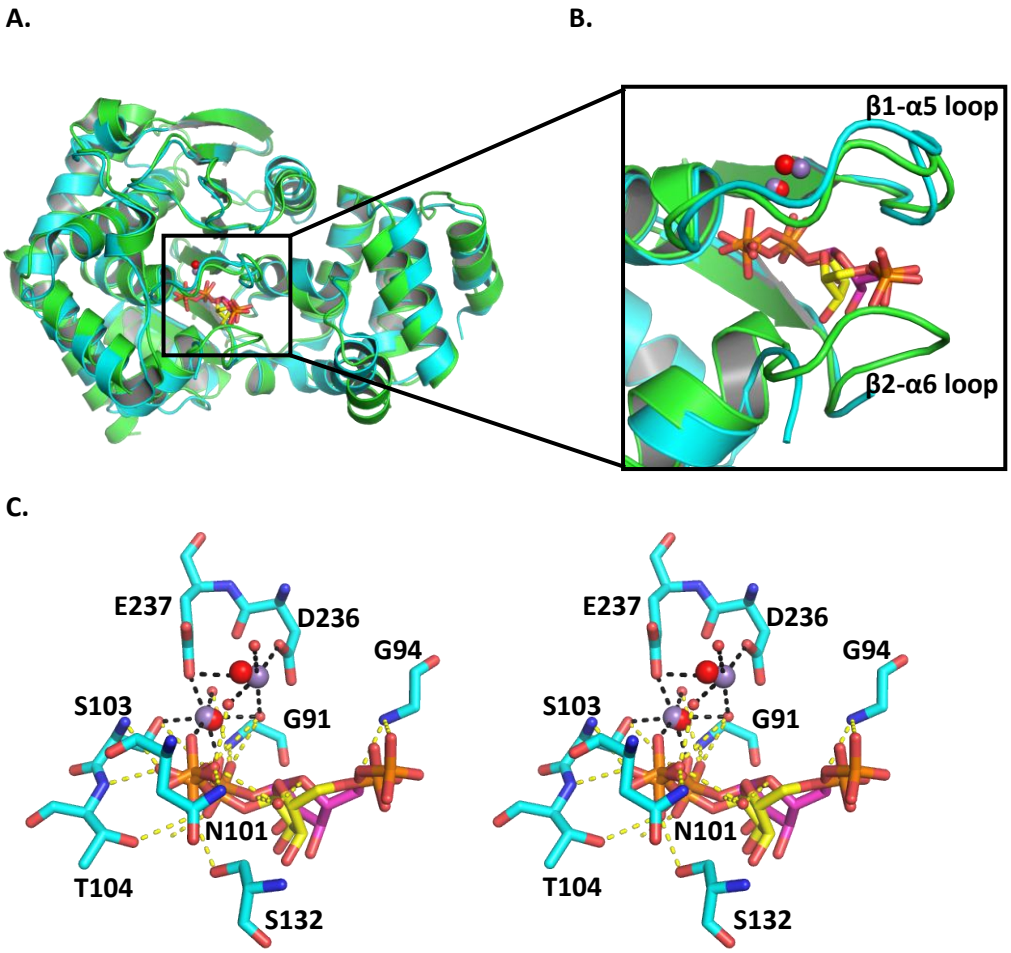

Figure 1.9 PRPP binding in *Pca*-AnPRT. A) An overlay of chain A of *Pca*-AnPRT (cyan) with PRPP (magenta) and Mn^{2+} (purple spheres) bound with chain A of *Mtu*-AnPRT (green) with PRPP (yellow) and Mg^{2+} (red spheres) bound. B) A closer view of the active site of *Pca*-AnPRT overlaid with *Mtu*-AnPRT. C) Stereo diagram of the *Pca*-AnPRT active site with PRPP (magenta) and Mn^{2+} (purple spheres) bound. The equivalent positions of the *Mtu*-AnPRT PRPP molecule (yellow) and Mg^{2+} ions (red spheres) are also shown. Yellow dashes indicate *Pca*-AnPRT polar contacts. Black dashes indicated Mn^{2+} contacts. Residues are numbered for the *Pca*-AnPRT enzyme.

PRPP/metal ion binding residues		
Mtu-AnPRT residues	Equivalent *Sso*-AnPRT residue	Equivalent *Pca*-AnPRT residue
V105	T77	I89
G107	G79	G91
G110	G82	G94
D111	D83	D95
T115	T87	S99
N117	N89	N101
S119	S91	S103
T120	T92	T104
K135	K106	K119
G147	S118	S132
D251	D223	D236
E252	E224	E237

Table 1.2 Equivalent PRPP/metal binding residues in *Mtu*-AnPRT, *Sso*-AnPRT and *Pca*-AnPRT.

The *Sso*-AnPRT structure (PDB ID: 1ZXY) has the PP_i group of the PRPP molecule in the same position as the *Mtu*-AnPRT and *Pca*-AnPRT structures. The PRPP molecule bound to chain A of *Sso*-AnPRT makes hydrogen bonds to G79, N89, S91, T92, K106 and a Mg^{2+} ion (Mg1) via the PP_i moiety. The ribose ring and phosphate group, however, extend out from the PP_i site in a completely different direction. The ribose ring makes hydrogen bonds to S91, D223, E224, a water molecule and Mg1, with the phosphate moiety hydrogen bonded to D83, T87 and a second Mg^{2+} ion (Mg2). Mg1 makes contacts to T77, S91, a water molecule, the two hydroxyls on the PRPP ribose ring and an oxygen from the PRPP PP_i group in a distorted octahedral co-ordination. Mg2 makes only three contacts to

D223, E224 and the PRPP phosphate group (Figure 1.9). Chains B, C and D of the *Sso*-AnPRT structure make similar hydrogen bond contacts to the PRPP and Mg^{2+} ligands.

An inspection of the electron density maps corresponding to 1ZXY, however, reveals that the binding mode of PRPP described is very unlikely. In the 1ZXY structure, the entire PRPP molecule and two Mg^{2+} ions are modelled into density which cannot feasibly accommodate them. Figure 1.10D depicts the $2F_o$-F_c map surrounding the PRPP and Mg^{2+} ligands in 1ZXY, and shows the sterically unfavourable positioning of the Mg^{2+} ions relative to the PRPP molecule. In Figure 1.10E, the $2F_o$-F_c map from the 1ZXY ligands is overlaid with the *Mtu*-AnPRT structure 1ZVW with PRPP and Mg^{2+} bound. An inspection of the density in this context illustrates that the electron density assigned to PRPP and Mg^{2+} in 1ZXY is likely to be incorrect, and in fact indicates the occupancy of a PP_i group and two Mg^{2+} ions only. Furthermore, in Figure 1.10E the phosphate moiety of PRPP from 1ZVW is positioned over electron density that accommodates a water molecule in the 1ZXY structure, which may suggest that incorrect ligand placement has introduced some model bias in the *SSo* 1ZXY structure.

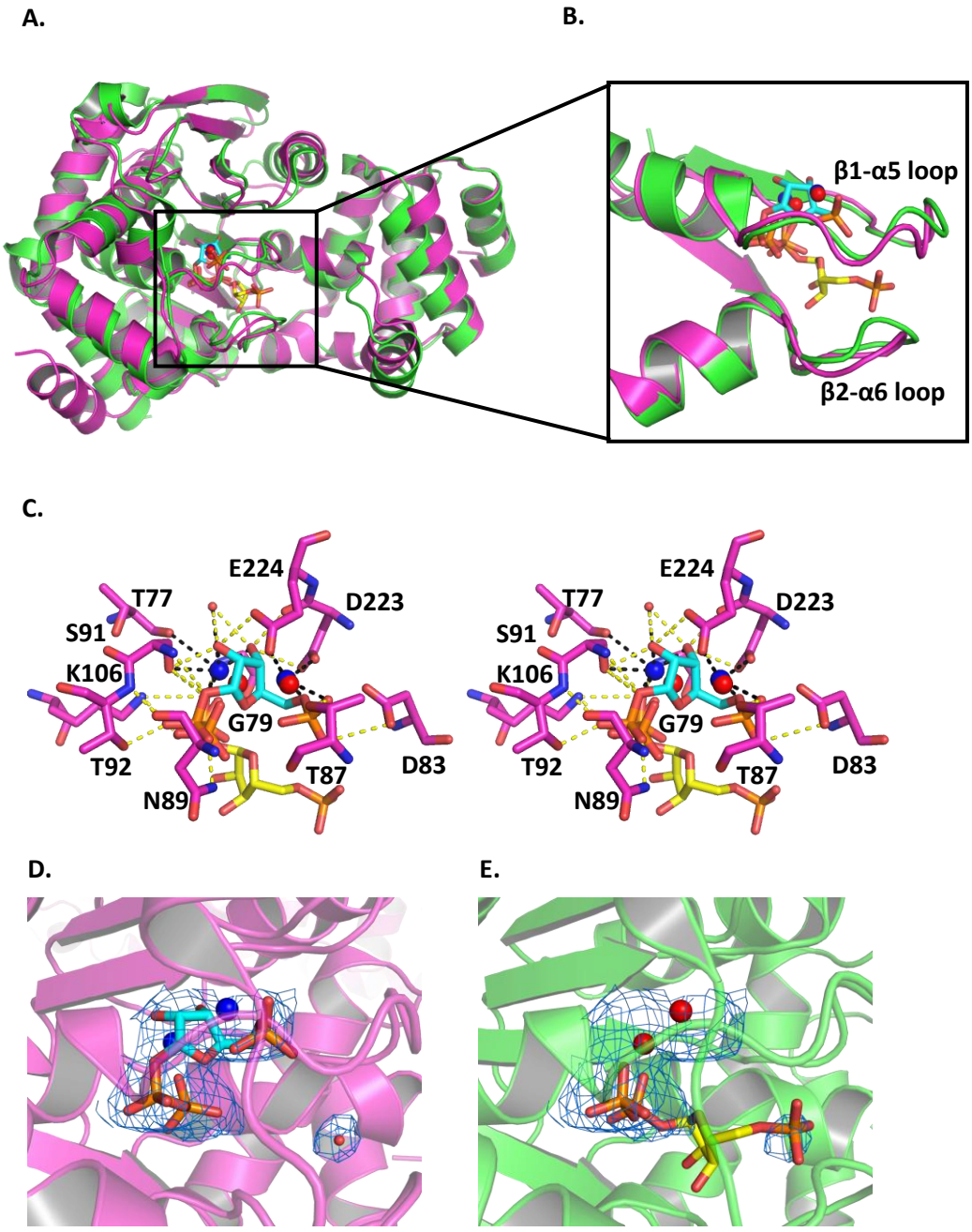

Figure 1.10 PRPP binding in *Sso*-AnPRT (PDB ID: 1ZXY). A) An overlay of chain A of *Sso*-AnPRT (magenta) with PRPP (cyan) and Mg^{2+} (blue spheres) bound with chain A of *Mtu*-AnPRT (green) with PRPP (yellow) and Mg^{2+} (red spheres) bound. B) A closer view of the active site of *Sso*-AnPRT overlaid with *Mtu*-AnPRT. C) Stereo diagram of the *Sso*-AnPRT active site with PRPP and Mg^{2+} bound. The equivalent positions of the *Mtu*-AnPRT PRPP molecule and Mg^{2+} ions are also shown. Yellow dashes indicate *Sso*-AnPRT polar contacts. Black dashes indicate Mg^{2+} contacts. Residues are numbered for the *Sso*-AnPRT enzyme. D) PRPP/Mg^{2+} binding in *Sso*-AnPRT, with the $2F_o$-F_c map for both ligands shown as blue mesh, contoured at 1.0 σ. E) $2F_o$-F_c map for *Sso*-AnPRT ligands overlaid with *Mtu*-AnPRT with PRPP/Mg^{2+} bound.

The *Sso*-AnPRT structure with PRPP, Mg^{2+} and anthranilate bound (PDB ID: 1ZYK) also shows PRPP in this dubious orientation. Figure 1.11A shows the $2F_o$-F_c map within the active site loops of 1ZYK, which is again suggestive of incorrect modelling of the PRPP substrate. When the map for the 1ZYK ligands is overlaid with the *Mtu*-AnPRT 1ZVW structure with PRPP and Mg^{2+} bound (Figure 1.11B), it can be seen that the density which houses PRPP in 1ZYK better accommodates the PP_i moiety of PRPP and the two Mg^{2+} ions only. Figures 1.11A and B also reveal that the phosphate of the 1ZVW PRPP molecule fits into suitable density that is not utilised by the PRPP from 1ZYK, which instead contains three water molecules. Instead the PRPP in 1ZYK is in a conformation that would be sterically unfavourable due to the proximity of the modelled Mg^{2+} ions (similar to the aforementioned 1ZYK structure).

The structure of a double mutant (D83G/F149S) of *Sso*-AnPRT with PRPP and Mn^{2+} bound (PDB ID: 3GBR) shows a further unique orientation (Figure 1.11C), with supporting electron density. The position of the PRPP molecule within the *Sso*-AnPRT D83G/F149S variant places the PP_i moiety in the same position observed for all other AnPRT structures, but with the ribose ring approximately perpendicular to the *Mtu*-AnPRT PRPP molecule from the 1ZVW structure. This mutant was generated via DNA shuffling,[50] a method similar to error-prone PCR,[54] with D83 located on the β1-α5 loop adjacent to the PRPP binding site, and F149 located on the β3-α8' loop. An overlay of chain A of the *Sso*-AnPRT D83G/F149S variant with chain A of the *Sso*-AnPRT 1ZXY structure gives an RMSD value of 0.461 Å.

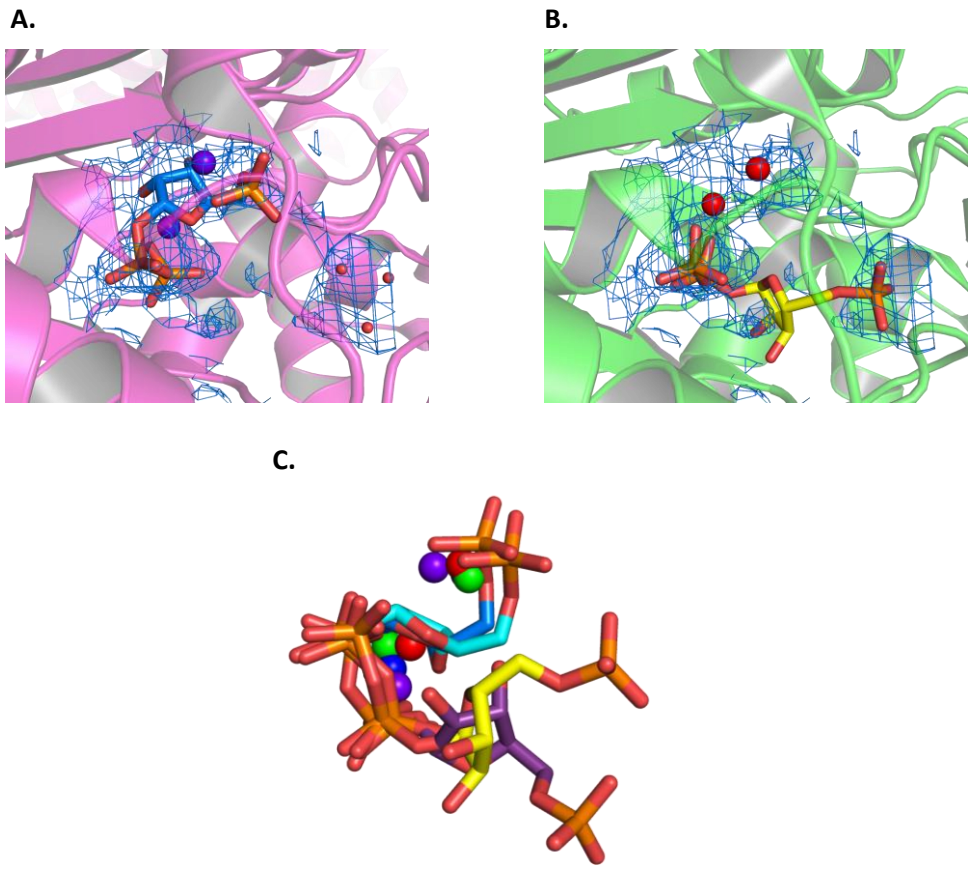

Figure 1.11 PRPP and metal ion binding in *Sso*-AnPRT and *Mtu*-AnPRT structures. A) *Sso*-AnPRT (magenta) (PDB ID: 1ZYK) with PRPP (blue) and Mg^{2+} (purple spheres) bound. The $2F_o$-F_c map for the *Sso*-AnPRT active site ligands is shown as blue mesh, contoured at 1.0 σ. B) The $2F_o$-F_c map for the *Sso*-AnPRT active site ligands is overlaid with *Mtu*-AnPRT (green) (PDB ID: 1ZVW) with PRPP (yellow) and Mg^{2+} (red spheres) bound. C) PRPP and Mg^{2+} ligands overlaid from different AnPRT structures. *Sso*-AnPRT (PDB ID: 1ZYK) PRPP is shown in blue, with Mg^{2+} as purple spheres. *Sso*-AnPRT (PDB ID: 1ZXY) PRPP is shown in cyan, with Mg^{2+} as blue spheres. *Sso*-AnPRT D83G/F149S (PDB ID: 3GBR) PRPP is shown in purple, with Mn^{2+} as green spheres. *Mtu*-AnPRT (PDB ID: 1ZVW) PRPP is shown in yellow, with Mg^{2+} as red spheres.

1.6.2.3 AnPRT Anthranilate Binding

The structures of *Sso*-AnPRT with PRPP, Mg^{2+} and anthranilate bound (PDB ID: 1ZYK) and with only anthranilate bound (PDB ID: 2GVQ) have also been solved.[42] The 1ZYK structure has four monomers present in the asymmetric unit associated as two dimers, with a total of four PRPP molecules (one per monomer), eight Mg^{2+} ions bound (two per monomer) and eight anthranilate molecules bound (two per monomer). Each PRPP and Mg^{2+} ligand is bound as described for the *Sso*-AnPRT 1ZXY structure (Section 1.5.2.2). The anthranilate molecules are bound in a channel that leads from the

solvent to the PRPP binding site (Figure 1.12D). The *Sso*-AnPRT 1ZYK structure has one anthranilate molecule positioned close to the PRPP molecule, making hydrogen bonds to G79 via its amino group, and to N109 via its carboxylate group. Other *Sso*-AnPRT residues such as A78, H107, G108, G177 and P178 are involved chiefly in hydrophobic interactions (Figure 1.12C). This anthranilate binding site will be referred to as the 'inner site' for the remainder of this study.

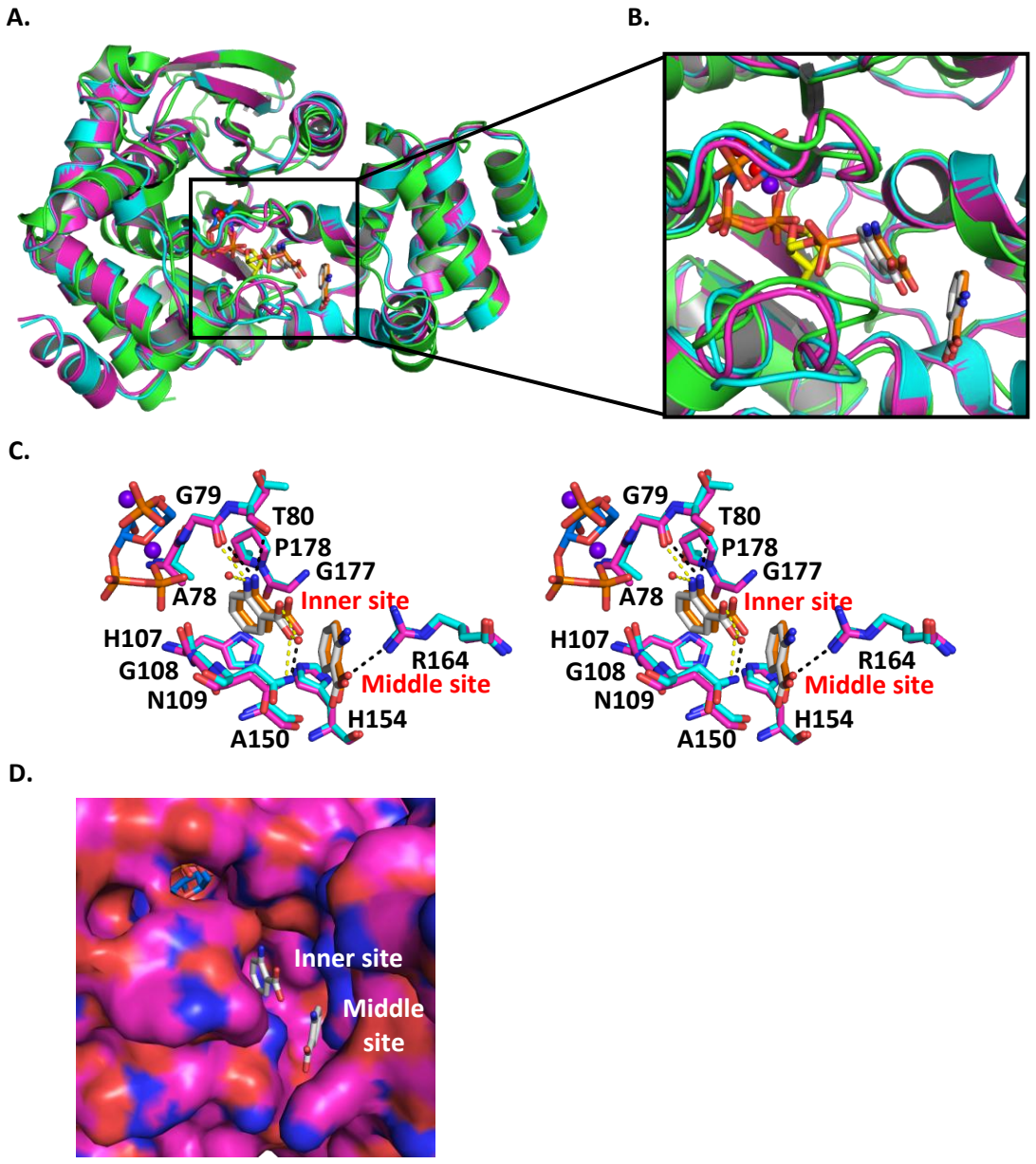

Figure 1.12 The active site of *Sso*-AnPRT. A) An overlay of chain A of *Sso*-AnPRT (magenta) with PRPP (blue), Mg^{2+} (purple spheres) and anthranilate (white) bound (PDB ID: 1ZYK) with chain B of *Sso*-AnPRT (cyan) with anthranilate (orange) bound (PDB ID: 2GVQ) and with chain A of *Mtu*-AnPRT (green) with PRPP (yellow) and Mg^{2+} (red spheres) bound (PDB ID: 1ZVW). B) A closer view of the active site of the *Sso*-AnPRTs overlaid with *Mtu*-AnPRT. C) Stereo diagram of the *Sso*-AnPRT (magenta) active site with PRPP (blue), Mg^{2+} (purple spheres) and anthranilate (white) bound overlaid with the active site of *Sso*-AnPRT (cyan) with anthranilate (orange) bound. The equivalent positions of the *Mtu*-AnPRT PRPP molecule (yellow) and Mg^{2+} ions (red spheres) are also shown. Yellow dashes indicate 1ZYK anthranilate polar contacts. Black dashes indicate 2GVQ anthranilate polar contacts. Residues are numbered for the *Sso*-AnPRT enzyme. D) Surface representation of the *Sso*-AnPRT 1ZYK structure with PRPP (blue), Mg^{2+} (not shown) and anthranilate (white) bound.

A second anthranilate molecule is positioned closer to the entrance of the anthranilate channel, and will be referred to as the 'middle site' for the remainder of this study. This middle site anthranilate makes contacts to N109 and R164 via its carboxylate group, with hydrophobic interactions to A150 and H154. All of the monomers within the asymmetric unit of the *Sso*-AnPRT 1ZYK structure demonstrate anthranilate bound both in the inner site and the middle site. Equivalent residue numbers between the different organisms mentioned are outlined in Table 1.3.

The *Sso*-AnPRT 2GVQ structure with only anthranilate bound also has two anthranilate molecules bound per monomer, with the exception of chain A which has only one anthranilate molecule bound in the middle site. For the monomers with two anthranilate molecules bound, there is one positioned in the inner site and one positioned in the middle site, as described for the *Sso*-AnPRT 1ZYK structure (Figure 1.11A, B and C). This structure also reveals that anthranilate can bind independently to *Sso*-AnPRT without prior PRPP binding, potentially pointing to a random sequential mechanism.

Anthranilate binding site residues	
Mtu-AnPRT residues	Equivalent *Sso*-AnPRT residues
V106	A78
G107	G79
T108	T80
H136	H107
G137	G108
N138	N109
A179	A150
H183	H154
R193	R164
G206	G177
P207	P178

Table 1.3 Equivalent anthranilate binding residues in *Sso*-AnPRT and *Mtu*-AnPRT.

1.6.2.4 Conformational Changes

A comparison of the different *apo* and ligand-bound structures of *Sso*-AnPRT showed little overall conformational change. An overlay of chain A of the *apo Sso*-AnPRT structure with either 2GVQ (anthranilate), 1ZYK (PRPP/Mg^{2+}/anthranilate) or 1ZXY (PRPP/Mg^{2+}) gave RMSD values of 0.224 Å, 0.292 Å and 0.283 Å respectively. A closer inspection of the active site showed an occlusion of the β2-α6 loop around the PRPP binding site upon the binding of PRPP/Mg^{2+}, which was not observed when anthranilate binding preceded PRPP/Mg^{2+} binding (Figure 1.13). This loop contains the conserved KHGN motif described in Section 1.5.1. *Mtu*-AnPRT also demonstrates this β2-α6 loop movement, and this will be discussed in Section 1.6. An overlay of the *Pca*-AnPRT *apo* structure with

the *Pca*-AnPRT PRPP/Mn^{2+} bound structure gives an RMSD value of 0.534 Å, however, both structures show the β2-α6 loop as disordered, unfortunately precluding a comparison of this region.

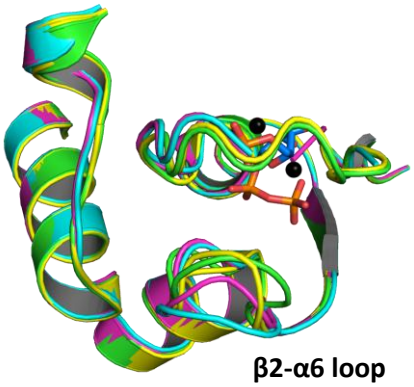

Figure 1.13 β2-α6 loop movement in *Sso*-AnPRT. *Sso*-AnPRT *apo* structure (PDB ID: 1O17) – magenta, *Sso*-AnPRT with PRPP and Mg^{2+} bound (PDB ID: 1ZXY) – green, *Sso*-AnPRT with anthranilate bound (PDB ID: 2GVQ) – cyan, *Sso*-AnPRT with PRPP, Mg^{2+} and anthranilate bound (PDB ID – 1ZYK) – yellow. The PRPP (blue) and Mg^{2+} ions (black spheres) from 1ZYK are also shown.

1.6.3 *Sso*-AnPRT Variant Kinetics

Several mutations have been performed on the *Sso*-AnPRT enzyme to probe the catalytic relevance of certain conserved residues involved with substrate binding, namely K106, H107, D223, E224, R164, H154 and P178.[42] It was concluded that residue R164 was crucial for anthranilate binding, as the variant *Sso*-R164A caused an increase in the anthranilate K_M value by a factor of 7000 (Section 1.6.2.3). However, the effect of the R164A mutation on the turnover number was not as marked, with a 7-fold decrease in the k_{cat} value.

A R164A/H154A double mutation had little additional effect on the *Sso*-AnPRT enzyme, with similar kinetic parameters as recorded for the *Sso*-R164A variant, though it is possible the R164A mutation has masked any H154A effects. The proximity of H154 to the anthranilate binding site coupled with its conservation within the AnPRT family suggests an important role for this residue, and it is unfortunate that Marino *et al.*[42] did not synthesise a *Sso*-H154A variant for comparison.

The variants *Sso*-K106Q, *Sso*-D223N and *Sso*-E224Q were synthesised to investigate whether differences in side-chain lengths and/or functionality in conserved residues proximal to the PRPP/Mg^{2+} binding site would have any effect on binding/catalysis. None of these mutations appeared to have any significant influence on substrate binding, with K_M values similar to those

observed for wild-type *Sso*-AnPRT. However, a 9-fold decrease in the k_{cat} value was recorded for the *Sso*-K106Q variant, and it was therefore suggested that K106 plays some role in catalysis. These mutants also showed no evidence of Mg^{2+} inhibition, as was observed in wild-type *Sso*-AnPRT.

The substitution of a histidine for an alanine at position 107 (H107A) had no significant effect on the *Sso*-AnPRT kinetic parameters, as with H154. A H107A/P178A double mutation caused a 300-fold increase in the anthranilate K_M value, but had little effect on the k_{cat} value, indicating that the presence of P178 appears necessary for binding, but not for catalysis. It is possible that H107 may also have played some role in reducing the binding affinity of anthranilate in the *Sso*-AnPRT H107A/P178A variant, however, the *Sso*-P178A variant was not synthesised for comparison. The active site co-ordination of nitrogenated bases via hydrogen bonding with the imidazole groups of histidines is a common structural theme among nucleotide/nucleoside-processing enzymes, including PRTs, nucleoside phosphorylases and nucleoside hydrolases.[31a, 38, 55] It is therefore surprising that the conserved H107 and H154 residues in *Sso*-AnPRT do not play a more central role in binding and/or catalysis. As AnPRTs have been suggested to have evolved from PyNPs, it is possible that the active site histidines in AnPRT are merely unnecessary evolutionary remnants.

1.7 *M. tuberculosis* Anthranilate Phosphoribosyltransferase

As has been stated in the previous section, structures of *Mtu*-AnPRT show that it exists as a head-to-head homodimer. The two monomers interact via the smaller N-terminal domain composed of four α-helices, and are joined to the larger α/β domain via a hinge region. The α/β domain is composed of a central seven-stranded β-sheet, consisting of six parallel and one anti-parallel β strands, with a number of α-helices packed on either side of it.

1.7.1 Crystal Structures

The *Mtu*-AnPRT *apo* structure (PDB ID: 2BPQ) and the structure of *Mtu*-AnPRT with PRPP and Mg^{2+} bound (PDB ID: 1ZVW) have previously been solved by Lee *et al*.[44] Both structures were obtained in the presence of the additive benzamidine, which was required for crystal formation.

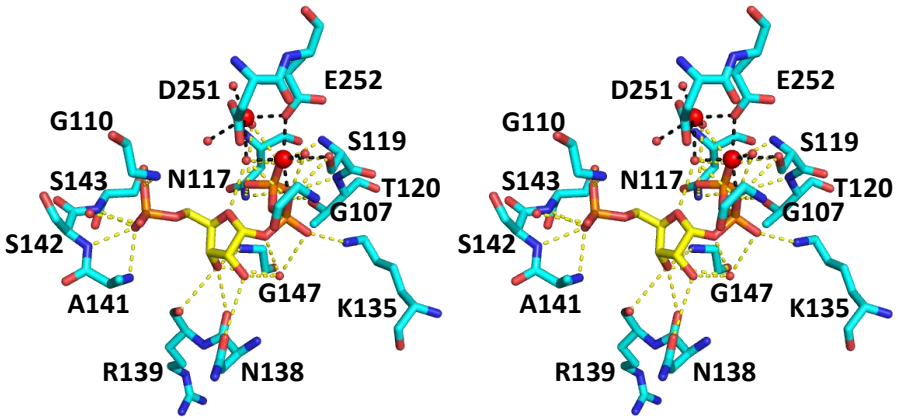

Figure 1.14 Stereo diagram of PRPP and Mg^{2+} bound to *Mtu*-AnPRT (PDB ID: 1ZVW). *Mtu*-AnPRT residues are shown in cyan, with PRPP in yellow and Mg^{2+} as red spheres.

The 1ZVW structure shows PRPP and Mg^{2+} bound to *Mtu*-AnPRT as shown in Figure 1.14, with the PP_i of PRPP forming contacts with the backbone nitrogens of residues G107, S119, T120, the side-chains of N117, S119 and K135, various water molecules and a Mg^{2+} ion (Mg1). The ribose ring of PRPP forms hydrogen bonds with N138 via the backbone and side-chain oxygens, with the phosphate group interacting with the backbone nitrogens of A141, S142, and G110 and the side-chain hydroxyl of S143. Both Mg^{2+} ions are octahedrally co-ordinated, with Mg1 forming contacts to the side-chain hydroxyls of S119 and E252, two water molecules and two PRPP PP_i oxygens. The second Mg^{2+} ion (Mg2) does not interact with the PRPP molecule, and forms contacts to the side-chain hydroxyls of D251 and E252, as well as four water molecules.

An overlay of chain A from both the *Mtu*-AnPRT *apo* and PRPP/Mg^{2+} bound structures gives an RMSD value of 0.200 Å, which is similar to the RMSD values of 0.224 – 0.292 Å recorded between overlaid *Sso*-AnPRT *apo* and ligand-bound structures. The position of the β2-α6 loop is significantly different between both *Mtu*-AnPRT structures, implying a high degree of flexibility. The β2-α6 loop in the *apo* structure shows some α helix formation, and projects into the PRPP binding site (Figure 1.15), while the PRPP/Mg^{2+} structure shows the β2-α6 loop has moved to enclose the PRPP molecule bound in the active site. This loop movement is also observed for *Sso*-AnPRT, and has been discussed in Section 1.5.2.4. Some differences between the *Mtu*-AnPRT structures can also be observed in the β1-α5 loop, which surrounds the Mg1/2 binding sites. This β1-α5 loop is extended slightly in the PRPP/Mg^{2+} structure due to uncoiling of the α5 helix N-terminus.

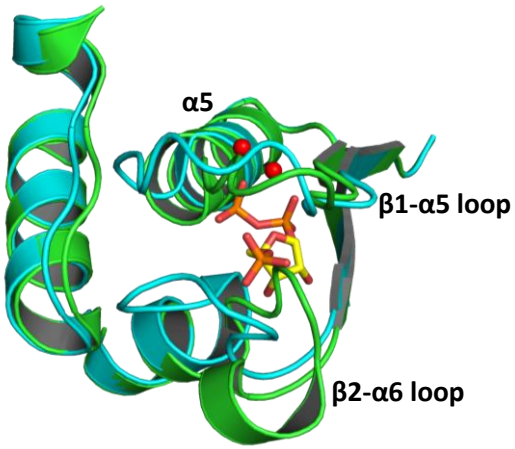

Figure 1.15 β2-α6 loop movement in *Mtu*-AnPRT. *Mtu*-AnPRT *apo* structure (PDB ID: 2BPQ) – green, *Mtu*-AnPRT with PRPP (yellow) and Mg^{2+} (red spheres) bound (PDB ID: 1ZVW) – cyan.

By superimposing the *Sso*-AnPRT structure with anthranilate bound with the *Mtu*-AnPRT structure with PRPP and Mg^{2+} bound, it is possible to predict the *Mtu*-AnPRT residues involved in anthranilate binding (Figure 1.16). Assuming that anthranilate binds to *Mtu*-AnPRT in equivalent positions to those observed for *Sso*-AnPRT, it is reasonable to suggest that residues G107, T108 and N138 are involved with anthranilate binding at the inner site. N138 could also form a hydrogen bond to an anthranilate molecule bound in the middle site, based on the hypothetical bond length of 3.5 Å between the side-chain nitrogen of residue N138 from *Mtu*-AnPRT and the carboxylate group of the middle site anthranilate molecule bound to *Sso*-AnPRT. As depicted in Figure 1.15, residue R193 from the overlaid *Mtu*-AnPRT structure is not suitably positioned to form a hydrogen bond to the anthranilate molecule bound in the middle site of the *Sso*-AnPRT structure. However, it is entirely

possible that residue R193 could be repositioned closer to the middle site through *Mtu*-AnPRT conformational changes.

It is likely that *Mtu*-AnPRT utilises the same anthranilate binding sites as *Sso*-AnPRT, given the similarities in their protein structures. It should also be noted that the binding mode of the PRPP molecule bound to the *Mtu*-AnPRT structure places the C1 carbon in an appropriate position for nucleophilic attack from an anthranilate molecule bound in the inner site (Figure 1.16).

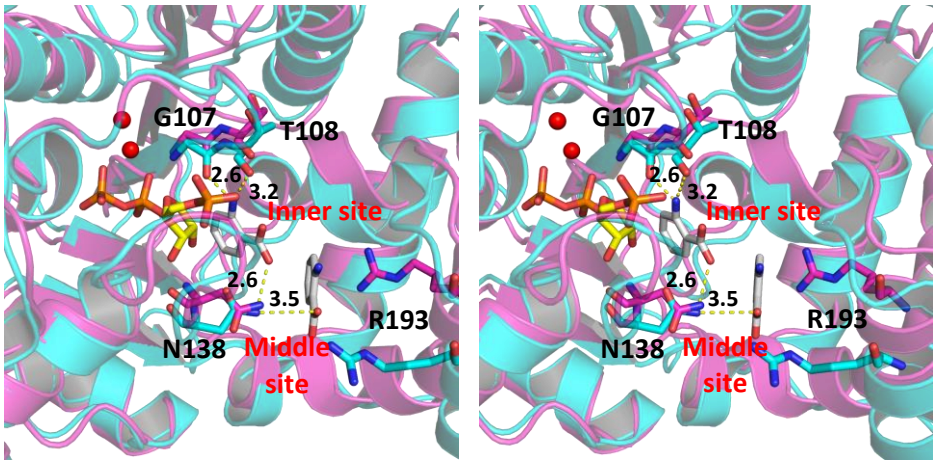

Figure 1.16 Stereo diagram of *Sso*-AnPRT and *Mtu*-AnPRT active sites. *Mtu*-AnPRT (cyan) with PRPP (yellow) and Mg^{2+} (red spheres) bound (PDB ID: 1ZVW) overlaid with *Sso*-AnPRT (magenta) with PRPP, Mg^{2+} (not shown) and anthranilate (white) bound (PDB ID: 1ZXY). Predicted hydrogen bonds between the *Sso*-AnPRT anthranilate molecules and the *Mtu*-AnPRT enzyme are displayed as yellow dashes, with bond distances (Å) shown. Residue labels pertain to the *Mtu*-AnPRT structure.

1.7.2 Kinetics

The activity of *Mtu*-AnPRT has previously been characterised by Dr Clare Lee using a fluorescence-based assay, with measurements taken using a 96-well plate spectrofluorimeter.[56] This assay incorporated two enzymes from the tryptophan biosynthetic pathway: *Mtu*-AnPRT, in order to convert anthranilate and PRPP into PRA, and *Eco*-PRAI:InGPS, which is a single protein in *E. coli* due to the TrpF and TrpC gene fusion,[27] in order to convert PRA into the stable InGP product (Figure 1.16). The presence of *Eco*-PRAI:InGPS was necessary to remove the build-up of the unstable *Mtu*-AnPRT reaction product PRA,[57] as the break-down of this compound into ribose-5-phosphate and anthranilate would alter the known concentrations of anthranilate in the wells. Removal of PRA also

avoided potential product-inhibition of *Mtu*-AnPRT.[56, 58] *Eco*-PRAI:InGPS was present in excess of *Mtu*-AnPRT in the wells, to ensure that the latter enzyme was rate-limiting.

The excitation and emission wavelengths were fixed at 313 nm and 390 nm respectively, and the disappearance of anthranilate was measured continuously for 1 hour. Reaction solutions were incubated at 25 °C, at a pH of 8.0. Using this method, the K_M values for anthranilate and PRPP were recorded as 3.3 ± 0.2 µM and 1.3 ± 0.2 µM respectively, with a turnover number (k_{cat}) of 1.1 ± 0.02 s^{-1}. A comparison of these values to those obtained in this study and in other orthologues is outlined in Section 2.5.1.

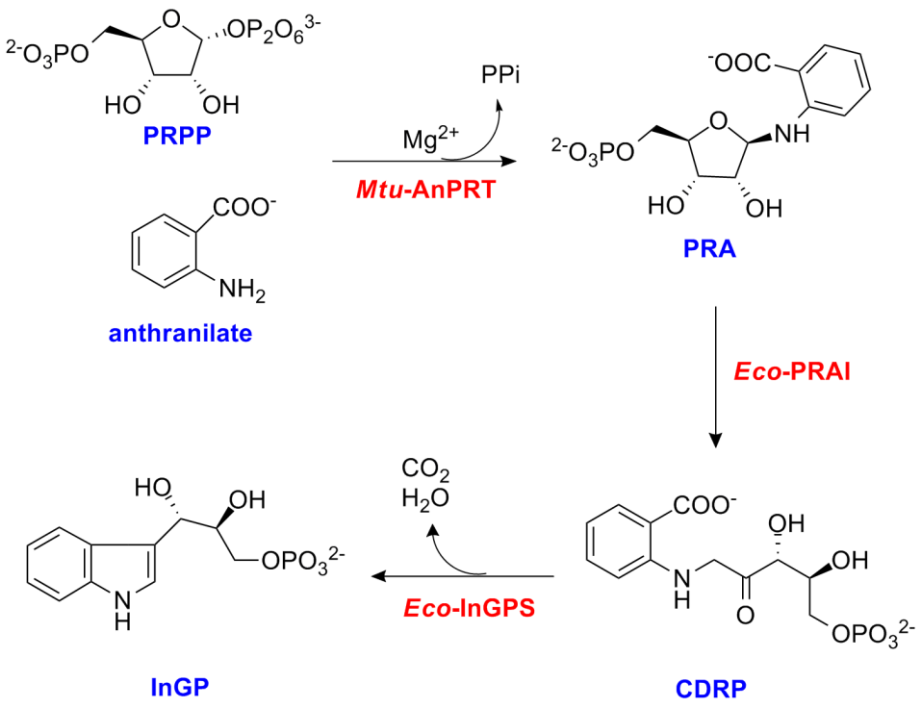

Figure 1.17 The enzymatic reactions utilised in the fluorescence assay used by Lee *et al*.[56]

1.8 Research Objectives

The overall aim of this project is to further understand how the *Mtu*-AnPRT active site facilitates the reaction between PRPP and anthranilate, in order to aid future tuberculosis drug development which will effectively target and inhibit this enzyme. The specific research objectives can be divided into four sections:

- Characterisation of the wild-type *Mtu*-AnPRT enzyme and subsequent development of a novel enzyme-coupled UV absorbance-based assay, with the aim of kinetically characterising previously identified potential inhibitor compounds.
- Investigation of the ability of *Mtu*-AnPRT to tolerate different anthranilate-like compounds as alternate substrates to anthranilate, including kinetic analysis and product characterisation.
- Synthesis and characterisation of variant *Mtu*-AnPRT enzymes with postulated key active site residues substituted, in order to determine their necessity for binding and/or catalysis.
- A comparison of the potency of previously identified inhibitor compounds against both wild-type and variant *Mtu*-AnPRT enzymes, with the aim of pinpointing any key inhibitor-protein interactions for future exploitation.

Previous characterisation of *Mtu*-AnPRT has been completed by Dr Clare Lee at the University of Auckland.[56] This research project follows on from her work, and is supervised jointly by Professor Emily Parker (University of Canterbury) and Dr Shaun Lott (University of Auckland).

Chapter 2

Characterisation and Inhibition of Wild-type *Mtu*-AnPRT

2.1 Overview

The first aim of this study was to purify and subsequently characterise wild type *Mtu*-AnPRT. It was also necessary to purify *Eco*-PRAI:InGPS, as it was required both for enzyme-coupled kinetic assays and mass spectrometry experiments. Physical characterisation of *Mtu*-AnPRT involved investigation into secondary structure, molecular mass and thermal stability of the protein.

Kinetic characterisation of *Mtu*-AnPRT was achieved via an enzyme-coupled assay developed in this study. Michaelis-Menten kinetic constants were obtained for the natural substrates PRPP and anthranilate, and the effects of anthranilate and Mg^{2+} at high concentrations were evaluated. A range of compounds that inhibited the enzyme were kinetically characterised.

The final part of this chapter describes structural studies of *Mtu*-AnPRT co-crystallised with several inhibitors, as carried out at the University of Auckland.

2.2 Introduction

Prior to this study, the crystal structures of *apo Mtu*-AnPRT (PDB ID: 2BPQ) and *Mtu*-AnPRT in the presence of PRPP and Mg^{2+} (PDB ID: 1ZVW) had been solved by Lee *et al.*[44] to resolutions of 1.9 Å and 2.3 Å respectively. These structures confirmed the classification of *Mtu*-AnPRT as a type III phosphoribosyltransferase,[41b] showing a similar structure to the previously described AnPRT structures from *S. solfataricus*[42] (PDB ID: 1GXB) and *P. carotovorum*[43] (PDB ID: 1KGZ).

A comparison of these two *Mtu*-AnPRT structures showed little differences (RMSD = 0.2 Å) apart from the β1-α5 and β2-α6 loops surrounding the PRPP binding site. Upon PRPP and Mg^{2+} binding, these loops rearrange to a position closer to the PRPP molecule (Figure 2.1), simultaneously providing some stability for the PRPP phosphate group via contacts to G110, A141, S142 and S143 and shielding the reactive PRPP from exposure to unproductive nucleophilic attack by water.

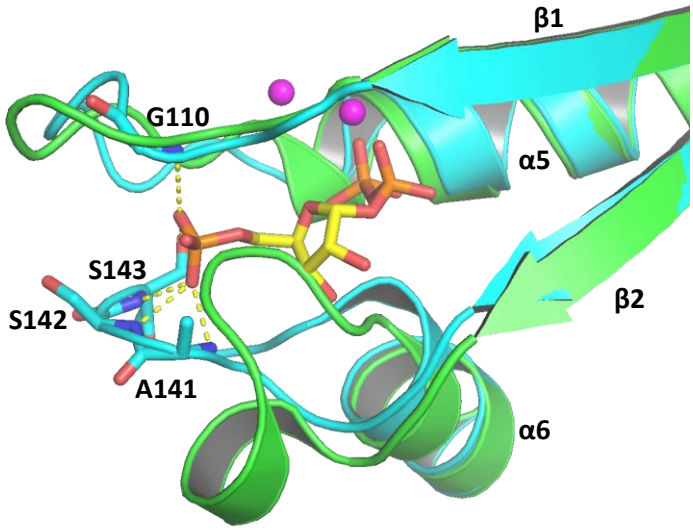

Figure 2.1 β1-α5 and β2-α6 loop movement in *Mtu*-AnPRT. *Apo Mtu*-AnPRT (green) overlaid with *Mtu*-AnPRT (cyan) with PRPP (yellow) and Mg^{2+} (magenta spheres) bound.

The structures of *Sso*-AnPRT co-crystallised with PRPP, Mg^{2+} and anthranilate (PDB ID: 1ZYK) and with anthranilate only (PDB ID: 2GVQ) had also been solved[42, 50] and both showed two anthranilate molecules present in the anthranilate channel (Figure 1.12).

2.3 Protein Isolation

2.3.1 Transformation

The *Mtu*-TrpD gene had previously been cloned into the expression vector pET-23a(+) (Novagen), with the *Eco*-TrpFC gene also previously cloned into the expression vector pProEX-HTb (Invitrogen™).[44] These plasmids were provided for use in this study courtesy of the University of Auckland.

Each plasmid was transformed as outlined in Section 7.1.7 into *E. coli* BL21 (DE3) cells and left to grow on LB/agar media containing ampicillin overnight. Successful colony growth was observed for cells containing each plasmid, and glycerol stocks of these colonies were made as outlined in Section 7.1.8.

Subsequent protein expression trials of *Mtu*-AnPRT and *Eco*-PRAI:InGPS in *E. coli* BL21 (DE3) cells showed a large portion of the proteins still present in the insoluble cell debris. Plasmids containing the *Mtu*-TrpD and *Eco*-TrpFC genes were thus transformed into *E. coli* BL21 (DE3) pBB528/pBB541 (chaperone 3 cells), which co-express chaperonins Gro-ES and Gro-EL to aid protein folding and solubility. This cell line produced a greater yield of soluble protein for both enzymes, as analysed by SDS-PAGE.

2.3.2 Protein Expression and Purification

Proteins were expressed and purified as detailed in Sections 7.1.11-17. Cell pellets from scaled up cell growths were lysed either by sonication or cell disruption, and the resulting lysate clarified by centrifugation to separate out the insoluble cell matter. The soluble protein was then filtered and applied to an immobilised metal-affinity column (IMAC) column for purification. Proteins were eluted from the column as a result of an increasing imidazole concentration gradient. The fractions of interest were then pooled and desalted to either remove or lower the concentration of imidazole present. The desalted protein was then concentrated, flash frozen and stored at -80 °C. Samples of each of these purification steps were analysed via SDS-PAGE, as can be seen in Figure 2.2 for *Mtu*-AnPRT and Figure 2.3 for *Eco*-PRAI:InGPS.

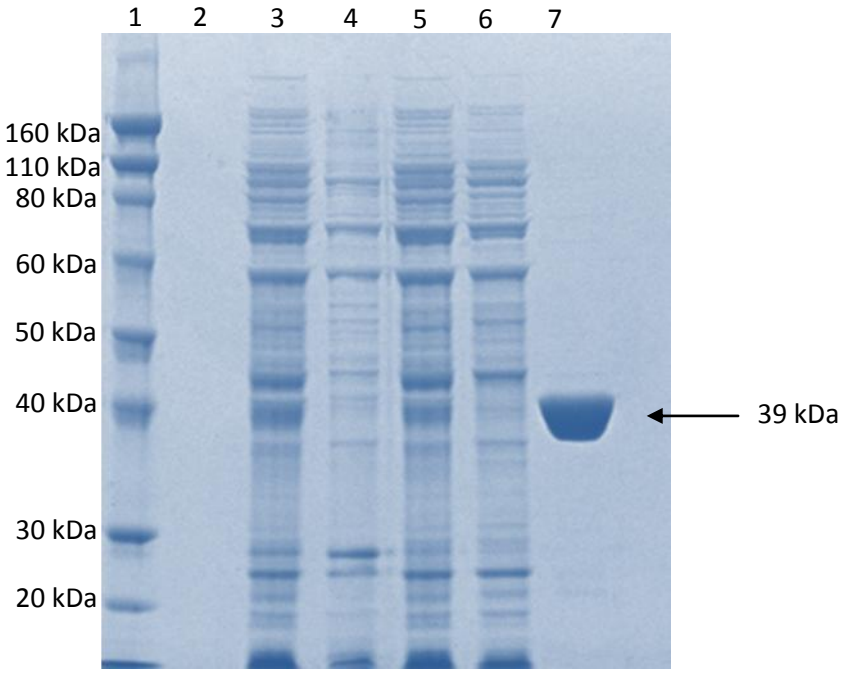

Figure 2.2 SDS-PAGE gel of the *Mtu*-AnPRT purification. Lane 1 contains the protein ladder, with molecular weights defined to the left. Lane 3 – proteins present after cell lysis. Lane 4 – insoluble proteins present in the cell debris. Lane 5 – soluble proteins present in the supernatant. Lane 6 – proteins present in the flowthrough liquid after purification via a HisTrap™ HP column. Lane 7 – purified *Mtu*-AnPRT at 39 kDa. Lane 2 is empty.

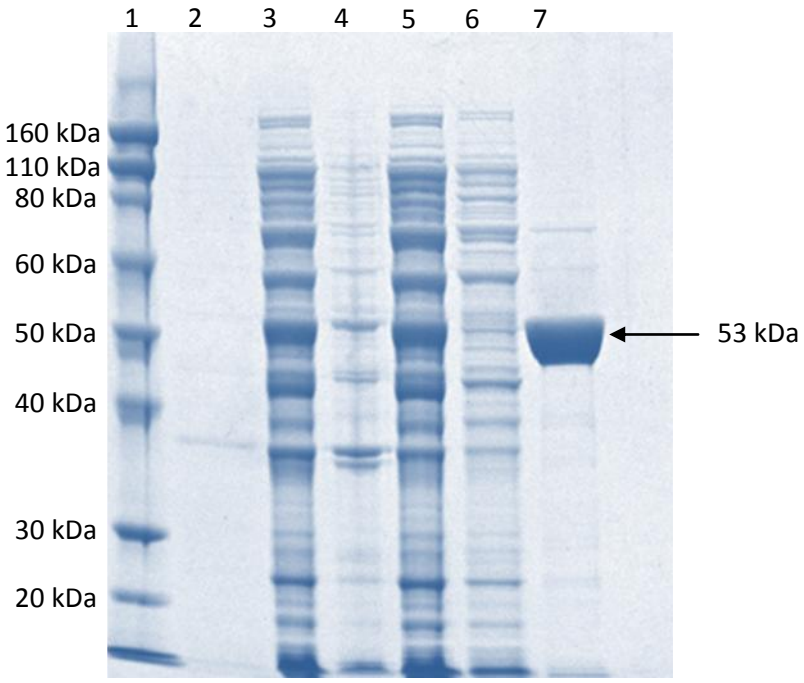

Figure 2.3 SDS-PAGE gel of the *Eco*-PRAI:InGPS purification. Lane 1 contains the protein ladder, with molecular weights defined to the left. Lane 3 – proteins present after cell lysis. Lane 4 – insoluble proteins present in the cell debris. Lane 5 – soluble proteins present in the supernatant. Lane 6 – proteins present in the flowthrough liquid after purification via a HisTrap™ HP column. Lane 7 – purified *Eco*-PRAI:InGPS at 53 kDa. Lane 2 is empty.

2.4 Physical Characterisation

2.4.1 Secondary Structure

Analysis of the secondary structure of both *Mtu*-AnPRT and *Eco*-PRAI:InGPS was carried out by circular dichroism (CD) to determine whether the proteins were folded correctly (Figure 2.4).

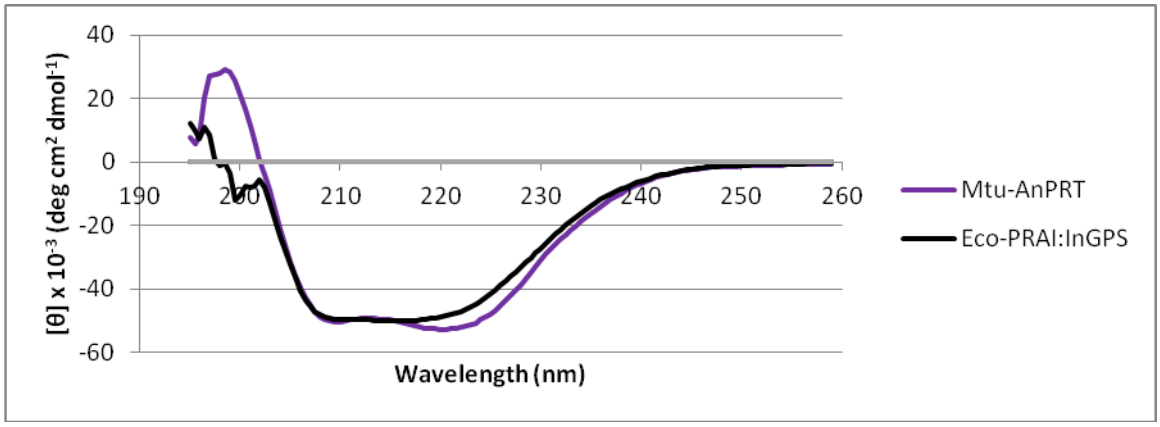

Figure 2.4 CD spectra of *Mtu*-AnPRT and *Eco*-PRAI:InGPS. Solutions contained 0.03 mg/mL enzyme made up to 3 mL with 20 mM sodium phosphate buffer (pH 8.0).

This data was analysed by the K2D3 secondary structure server,[59] which calculated that the ratio of α-helices to β-sheets in *Mtu*-AnPRT was 1.56, which does not match well with the expected value of 2.43 determined from the crystal structure. If the 4 smaller α-helices 6, 8', 11' and 11'' are ignored, a much more comparable value of 1.86 is obtained, though the discrepancy observed is more likely due to the inconstant nature of secondary structure determination.[60] The expected value of 1.13 for *Eco* PRAI:InGPS, as determined from the crystal structure,[61] matched the K2D3 calculated value of 1.13 exactly.

2.4.2 Molecular Mass

The molecular masses of *Mtu*-AnPRT and *Eco*-PRAI:InGPS were obtained via mass spectrometry. The predicted masses of these enzymes, including their His-tags, were 38804.9 Da and 52732.7 Da respectively, as calculated by their amino acid sequences on the ProtParam website.[62] The measured masses of *Mtu*-AnPRT and *Eco*-PRAI:InGPS were found to be 38672.2 Da and 52731.7 Da respectively, the latter of which correlates well to the expected value. The value obtained for *Mtu*-AnPRT is similar to the calculated value of 38673.7 Da, corresponding to the mass of the protein minus the start methionine. The eradication of this amino acid is fairly common in *E. coli* cells and is

likely caused by the presence of methionine aminopeptidase, which cleaves the start methionine when it precedes certain amino acids including alanine, such as with *Mtu*-AnPRT.[63]

2.4.3 Thermal Stability

Differential scanning fluorimetry (DSF) was used to determine the temperatures of denaturation for *Eco*-PRAI:InGPS and *Mtu*-AnPRT (Figure 2.5), and was carried out as described in Section 7.1.28.[64] This technique employs the use of a dye which fluoresces more strongly when it is bound to hydrophobic protein residues. As a protein denatures, the number of previously internalised hydrophobic residues available for binding by this dye increases. By steadily raising the temperature of a protein's environment and monitoring the fluorescence, the denaturation temperature can be measured as the point of greatest increase in fluorescence. *Mtu*-AnPRT was also measured in the presence of different combinations of its natural ligands at varying concentrations. Raw data from the DSF scans can be observed in Appendix 1.

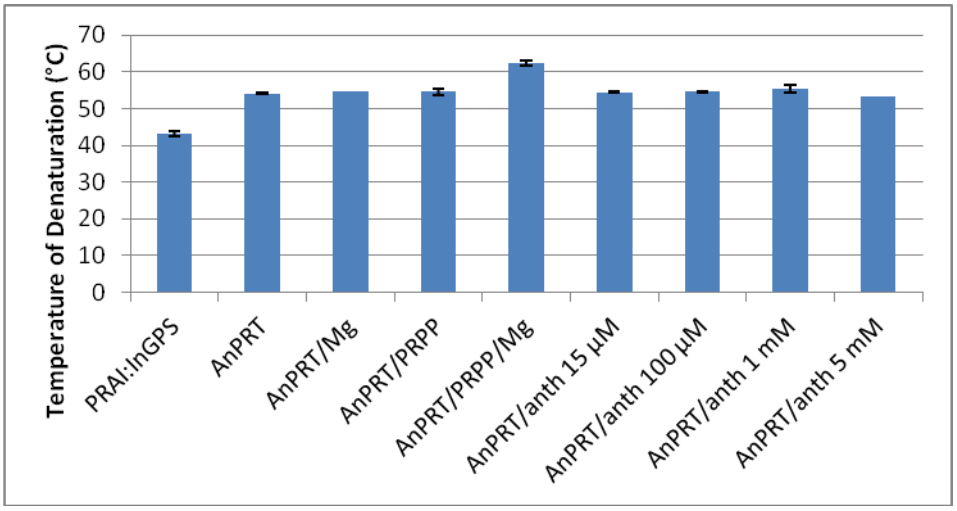

Figure 2.5 DSF denaturation temperatures for *Mtu*-AnPRT and *Eco*-PRAI:InGPS. When present, the final concentrations of ligands were 1 mM Mg^{2+}, 0.6 mM PRPP and either 15 µM, 100 µM, 1 mM or 5 mM anthranilate. Enzymes were analysed in Tris.HCl buffer (pH 8.0), at concentrations of 1 mg/mL.

The denaturation temperatures of *Mtu*-AnPRT and *Eco*-PRAI:InGPS were found to be 54.1 ± 0.3 °C and 43.1 ± 0.8 °C respectively. The presence of natural ligands with *Mtu*-AnPRT had no significant effect on the denaturation temperature, except for when both PRPP and Mg^{2+} were bound. This combination of ligands increased the denaturation temperature to 62.4 ± 0.7 °C, which could infer

that the stabilisation of the β1-α5/β2-α6 loops upon PRPP/Mg^{2+} binding (Figure 2.1) also elicits a global increase in stability.

Ligand(s) bound to *Mtu*-AnPRT	T_m (°C)
No ligand	54.1 ± 0.3
1 mM Mg^{2+}	54.7 ± 0.1
0.6 mM PRPP	54.6 ± 0.8
1 mM Mg^{2+} + 0.6 mM PRPP	62.4 ± 0.7
15 µM anthranilate	54.4 ± 0.2
100 µM anthranilate	54.5 ± 0.2
1 mM anthranilate	55.4 ± 1
5 mM anthranilate	53.3 ± 0.1

Table 2.1 *Mtu*-AnPRT denaturation temperatures (T_m) in the presence of natural ligands.

2.5 Kinetic Characterisation

An enzyme-coupled absorbance-based UV assay was developed in order to determine the kinetic parameters of *Mtu*-AnPRT. This assay was necessary as further experiments into potential inhibitors and alternate substrates of this enzyme cannot be analysed using the previously developed fluorescence assay (Section 1.6.2),[56] due to potential quenching of the fluorescent signal by anthranilate-like compounds.

The conversion of PRA into InGP, catalysed by PRAI-InGPS, can be monitored spectrophotometrically at 270 nm,[65] which was confirmed by a wavelength scan performed from 230-320 nm (Figure 2.6). The absorbance increase at 270 nm was not observed when *Eco*-PRAI:InGPS was absent from the assay. An assay was therefore developed where *Eco*-PRAI:InGPS was added in excess of *Mtu*-AnPRT to ensure the AnPRT-catalysed reaction is the rate-limiting step, and the reaction was monitored at 270 nm to detect the formation of the InGP product. The presence of excess *Eco*-PRAI:InGPS also prevents any PRA breakdown[57] as it is immediately removed from solution. Using known concentrations of anthranilate, the extinction coefficient for InGP production from anthranilate and PRPP was determined to be 7500 L mol^{-1} cm^{-1} at 270 nm. The assay was monitored at 25 °C in order to compare results with previous studies (Table 2.2).

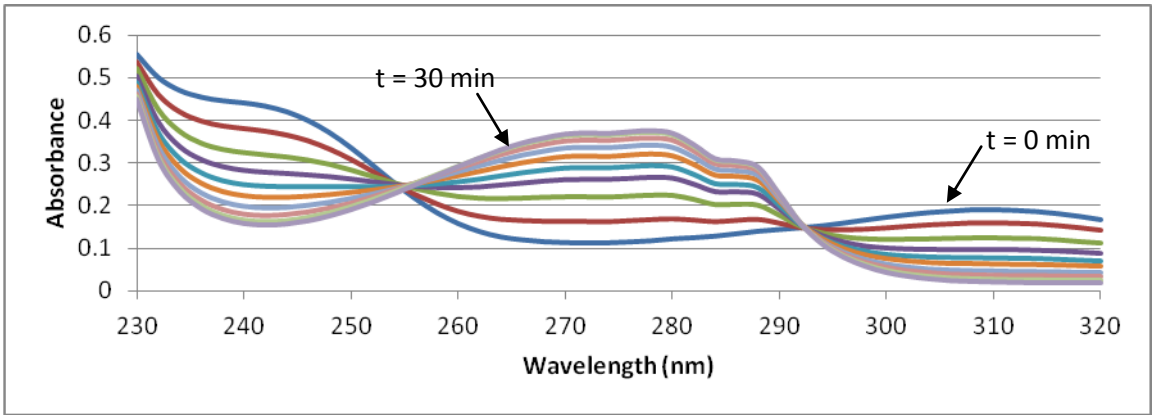

Figure 2.6 Wavelength scan of the *Mtu*-AnPRT reaction using the enzyme-coupled assay (t = time). The absorbance can be seen to increase in the 260-290 nm range, and decrease in the 230-255 nm and 295-320 nm ranges. Solutions contained 1 mM $MgCl_2$, 0.1 µM *Mtu*-AnPRT, 1.7 µM *Eco*-PRAI:InGPS, 0.6 mM PRPP and 100 µM anthranilate made up to 1 mL with buffer (50 mM Tris.HCl, 200 mM NaCl, pH 8.0). Reactions were scanned from 320-230 nm for 30 min with a cycle length time of 2.5 min. Solutions were thermally equilibrated for 5 min prior to initiation with anthranilate and allowed to go to completion.

2.5.1 Michaelis-Menten Kinetics

The turnover number (k_{cat}) and apparent K_M values were determined for *Mtu*-AnPRT (Figure 2.7) using the enzyme-coupled assay as outlined in Section 7.1.24/7.2.1. The apparent K_M value of 2.0 ± 0.2 µM for anthranilate is comparable to those obtained for enzymes isolated from other organisms (Table 2.2). The turnover number of 1.9 ± 0.1 s^{-1} also correlates well with other enzymes. The substrate PRPP has an apparent K_M value of 48 ± 2 µM, and falls within the range of 1.3 – 180 µM recorded for other enzymes. The discrepancies observed between the kinetic parameters of the AnPRT homologues listed in Table 2.2 can likely be attributed to differing experimental conditions. For example, fluorimetric assays were used to determine the kinetic parameters of *Sso*, *Sce* and previous *Mtu*-AnPRTs, with the latter utilising a fluorimetric plate-reader as opposed to cuvettes. An inspection of the experimental conditions also highlights variations in the buffer components, pH levels and incubation temperatures, all of which could potentially play some role in altering the kinetic parameters.[56, 58, 66]

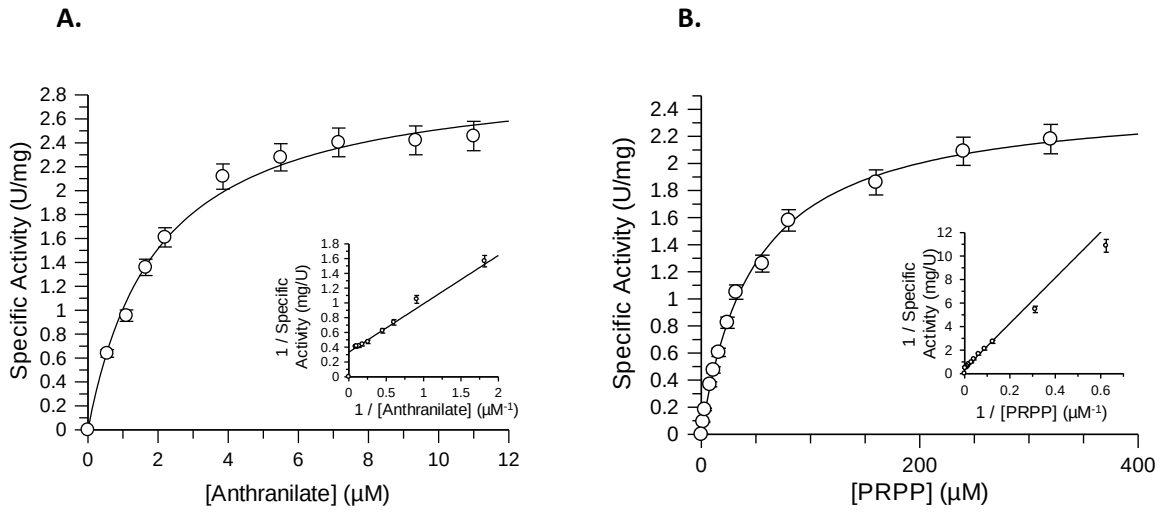

Figure 2.7 Plots of kinetic data for *Mtu*-AnPRT substrates. Insets: Lineweaver-Burk plots. A) The Michaelis-Menten plot for anthranilate, with PRPP held at a concentration of 0.6 mM. B) The Michaelis-Menten plot for PRPP, with anthranilate held at a concentration of 15 µM. All data was collected with reaction solutions at 25 °C, pH 8.0. Raw data was fitted to the Michaelis-Menten equation using Grafit 5 software.[67]

Organism	Temp (°C)	$K_{M(anth)}$ (μM)	$K_{M(PRPP)}$ (μM)	k_{cat} (s^{-1})	$k_{cat}/K_{M(anth)}$ ($\mu M^{-1}s^{-1}$)	$k_{cat}/K_{M(PRPP)}$ ($\mu M^{-1}s^{-1}$)
M. tuberculosis (this study)	25	2.0 ± 0.2	48 ± 2	1.9 ± 0.06	0.95 ± 0.13	0.04 ± 0.003
M. tuberculosis[56]	25	3.3 ± 0.2	1.3 ± 0.2	1.1 ± 0.02	0.3 ± 0.03	0.8 ± 0.1
S. solfataricus[52]	37	0.085	180	0.41 ± 0.04	4.8	2.3×10^{-3}
S. cerevisiae[66a]	25	1.6 ± 0.5	22.4 ± 2.6	2.9 ± 0.5	1.8 ± 0.9	0.13 ± 0.04
**E. coli*[66b]	25	0.28	50	4.4	15.7	0.088

Table 2.2 Kinetic data of AnPRT from different organisms. * indicates the enzyme is covalently linked to anthranilate synthase.

2.5.2 Anthranilate Inhibition

At higher concentrations of the substrate anthranilate, a significant drop in *Mtu*-AnPRT activity was observed. The substrate inhibition of *Mtu*-AnPRT by anthranilate was therefore examined (Figure 2.8), using the enzyme-coupled assay as described in Section 7.1.24/7.2.1, by increasing anthranilate concentrations from 0-100 μM. Results clearly demonstrate that the enzyme is subject to significant substrate inhibition, with a K_i value of 47 ± 7 μM. This observed inhibition is possibly a result of simultaneous occupancy of the anthranilate binding sites outlined in Section 1.6.2.3. Anthranilate inhibition has previously been reported for *Salmonella typhimurium* AnPRT only, which is covalently linked to the glutamine amidotransferase subunit of the previous tryptophan biosynthesis pathway enzyme anthranilate synthase due to the fusion of the TrpG and TrpD genes. However, this substrate inhibition was only observed in the presence of tryptophan.[68]

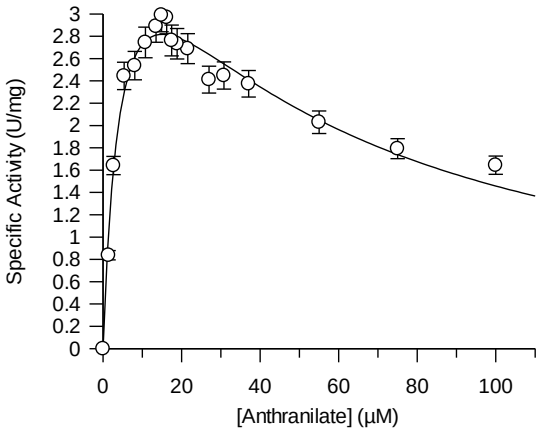

Figure 2.8 *Mtu*-AnPRT kinetic data for anthranilate inhibition, with PRPP held at a concentration of 0.6 mM. Solutions were monitored at 25 °C at pH 8.0, and raw data was fitted to the substrate inhibition equation using Grafit 5 software.[67]

2.5.3 Mg^{2+} Inhibition

The concentration of $MgCl_2$ used in the enzyme-coupled assay in this study is set at 1 mM based on previous work,[56] however, it has been observed during analysis of the *Sso*-AnPRT enzyme that there is a decrease in activity at concentrations of $MgCl_2$ greater than 0.1 mM.[42, 50] The inhibition of *Mtu*-AnPRT by $MgCl_2$ was therefore investigated, but contrary to the findings for *Sso*-AnPRT, no significant inhibition up to 10 mM $MgCl_2$ was observed (Figure 2.9).

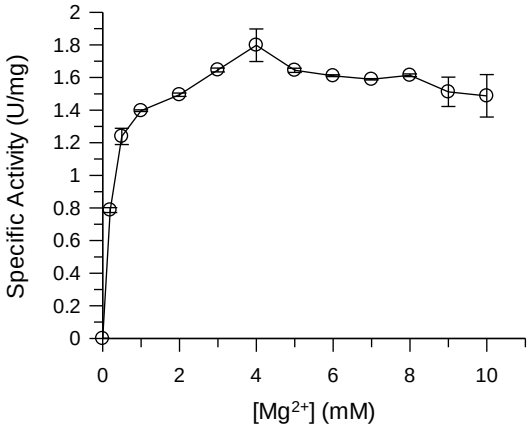

Figure 2.9 The effect of increasing concentrations of Mg^{2+} on *Mtu*-AnPRT activity. The concentrations of PRPP and anthranilate were held at 0.6 mM and 15 µM respectively, with solutions held at 25 °C, pH 8.0. Graph generated using Grafit 5 software.[67]

2.5.4 Mechanism

To determine the kinetic mechanism of *Mtu*-AnPRT, initial rate measurements were taken at varying concentrations of both substrates, as described in Section 7.1.24/7.2.1. This data was then fitted to the ternary mechanism equation (Figure 2.10), which clearly shows this enzyme has a sequential mechanism. In the crystal structures of *Mtu*-AnPRT,[44] it has been observed that residues from the flexible loops β1-α5 and β2-α6 that close over the bound PRPP molecule form contacts for anthranilate binding in the inner site. This observation, coupled with our findings of a sequential mechanism, could indicate that anthranilate can only bind in the inner site after PRPP has bound.

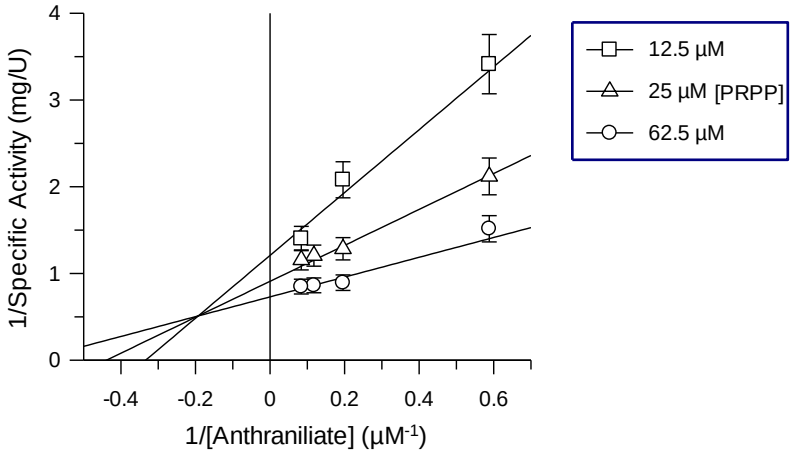

Figure 2.10 *Mtu*-AnPRT kinetic data as fitted to the ternary mechanism equation using Grafit 5 software[67] and presented as a double reciprocal plot. From this data the K_M values for anthranilate and PRPP were determined to be 0.9 ± 0.6 µM and 12 ± 4 µM respectively. Anthranilate concentrations were varied from 0 – 12 µM, with PRPP concentrations varied from 0 - 62.5 µM. Reaction solutions were monitored at 25 °C at pH 8.0.

2.6 Inhibition of *Mtu*-AnPRT

Previous work into potential inhibitors of *Mtu*-AnPRT involved the screening of 165 compounds from the Auckland Cancer Society Research Centre (ACSRC) using a fluorescence assay which monitored the consumption of anthranilate.[41a] These compounds were chosen based on their similarities to the natural substrate anthranilate, and were ranked based on the percentage decrease in *Mtu*-AnPRT activity observed in the presence of 0.3 mM PRPP, 100 µM inhibitor and 75 µM anthranilate. The top compounds from this screen all had aromatic rings with a carboxylate group, and most had functional groups present on C2. Some of these compounds acted as substrates for *Mtu*-AnPRT, and these will be discussed in Chapter 3.

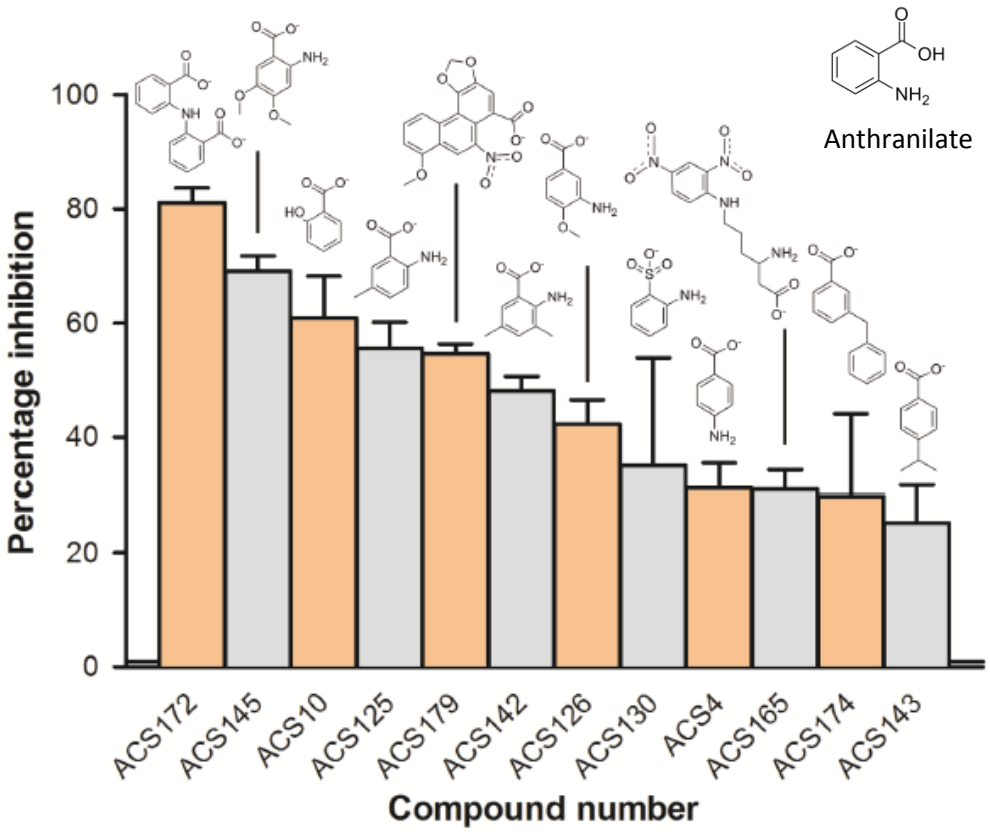

Figure 2.11 The top 12 hits from the fluorescence assay inhibitor screen. Figure extracted from Castell *et al.* Supplementary Material.[41a]

2.6.1 Inhibition Kinetics

Several compounds from Figure 2.11 were quantitatively examined using the UV enzyme-coupled assay developed in this study. The nine compounds chosen for further testing were ACS172, ACS145, ACS10, ACS179, ACS142, ACS126, ACS4, ACS165 and ACS174 (Table 2.3). Additional compounds tested were 3-aminobenzoic acid and ribose-5-phosphate (R5P). 3-Aminobenzoic acid was tested as it was readily available and to fully analyse the inhibitory effect caused by the position of the amino group on the anthranilate aromatic ring (C2 (anthranilate) and C4 (ACS4) were already under investigation). Ribose-5-phosphate (R5P) (Figure 2.13A) was tested as a potential PRPP-like inhibitor which, if successful at binding, could later be used in conjunction with anthranilate to elucidate different aspects of *Mtu*-AnPRT mechanics, by obtaining crystal structures with both compounds bound or dissociation constants.

Inhibitor compounds predicted to compete with anthranilate were tested using the enzyme coupled assay with anthranilate concentrations below 15 µM to avoid substrate inhibition. Results were fitted to each of four inhibition equations (competitive, pure non-competitive, uncompetitive and mixed inhibition) and the χ^2 values compared to determine which fit best described the data. Inhibition was observed for all compounds tested with the exception of ACS4 and 3-aminobenzoic acid. K_i values of anthranilate-like inhibitors ranged from 5.5 – 129 µM (Table 2.3, Figure 2.12), and all compounds demonstrated competitive inhibition, with the exception of ACS172 which showed pure non-competitive inhibition. The pure non-competitive inhibition displayed by ACS172 indicates that the binding affinity of this compound for the enzyme both with and without anthranilate bound is equal, allowing both ACS172 and anthranilate to be bound simultaneously. ACS172 had the lowest K_i value of 5.5 ± 0.3 µM and is bi-anthranilate-like in character, having no additional functional groups on the aromatic rings. The absence of extra groups likely allows this compound to bind to *Mtu*-AnPRT in a manner most similar to the natural substrate anthranilate, and has been observed to bind at different stages along the anthranilate channel (PDB ID: 3QQS, discussed in Section 2.7). These multiple binding modes support the pure-noncompetitive inhibition behaviour observed for ACS172, indicating that anthranilate and ACS172 could bind simultaneously.

Complementary structural information of ACS172, ACS142 (PDB ID: 3UU1), ACS174 (PDB ID: 3QS8), ACS145 (PDB ID: 3R88), ACS179 (PDB ID: 3R6C) and ACS10 (PDB ID: 3TWP) bound to *Mtu*-AnPRT (discussed further in Section 2.7) show the majority of inhibitors binding primarily at the entrance to the anthranilate channel. ACS172, ACS174 and ACS142 were the only inhibitors observed to bind in multiple sites within the channel, with all three having K_i values under 10 µM. This observation

indicates that stronger inhibition is obtained when multiple anthranilate sites are occupied by inhibitor compounds.

ACS number	Structure	K_i value (µM)	Type of inhibition
174	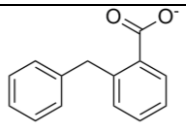	6.1 ± 0.5	Competitive
172	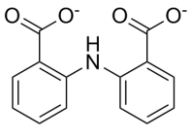	5.5 ± 0.3	Pure non-Competitive
142	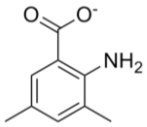	8.5 ± 0.7	Competitive
179	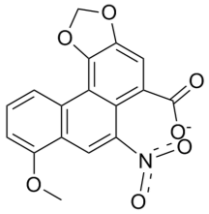	5.7 ± 0.5	Competitive
145	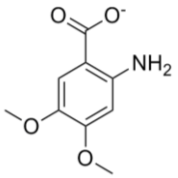	129 ± 14	Competitive
10	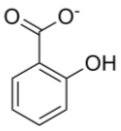	30 ± 3	Competitive
126	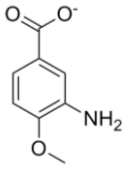	103 ± 10	Competitive
165	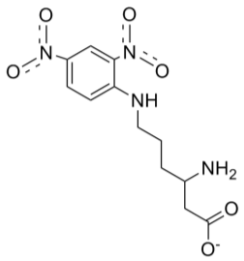	70 ± 8	Competitive

Table 2.3 Chemical structures, K_i values and types of inhibition displayed for anthranilate-like inhibitors tested against *Mtu*-AnPRT.

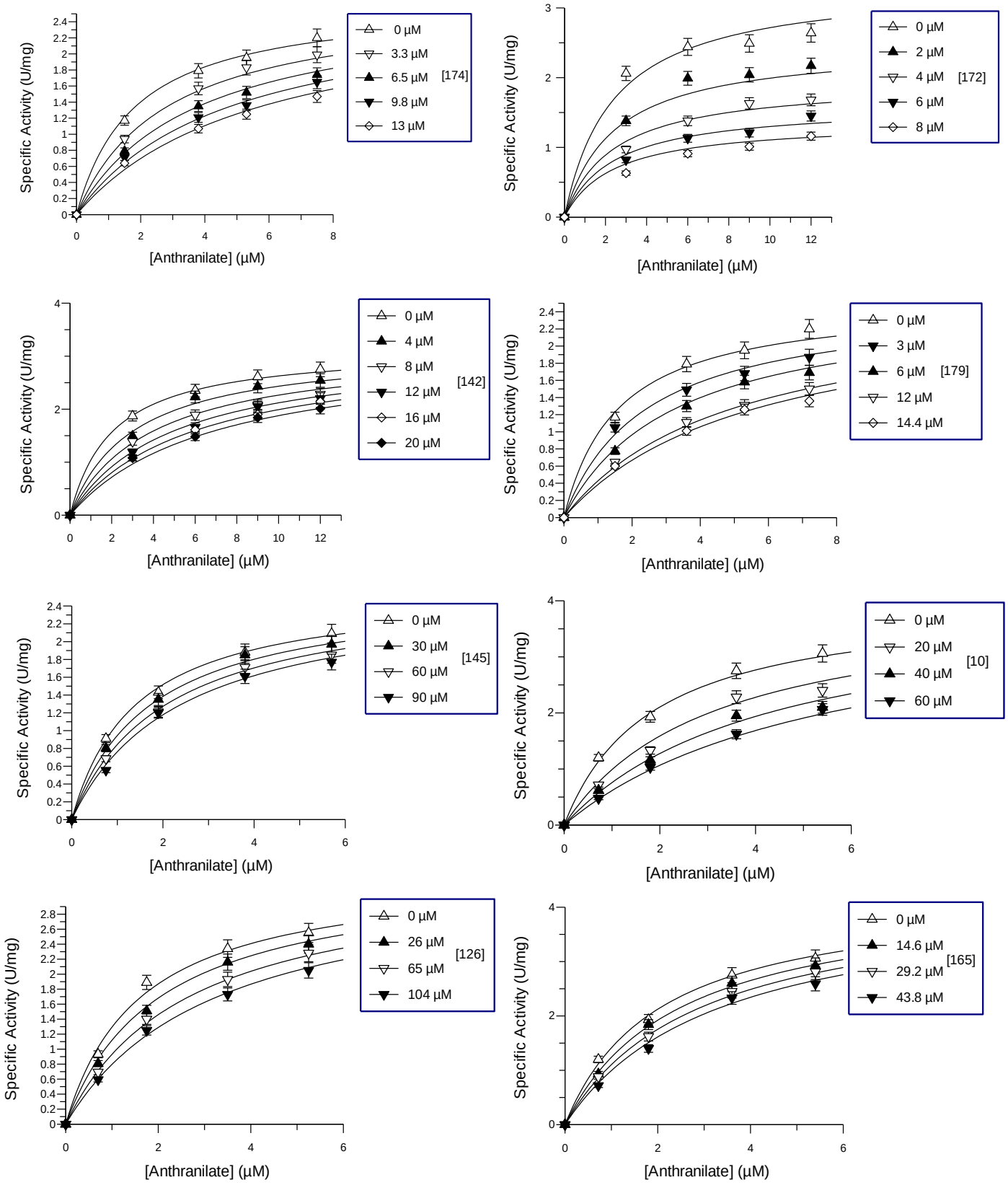

Figure 2.12 *Mtu*-AnPRT inhibition graphs for determination of inhibitor K_i values, as calculated by the graphing software Grafit 5.[67] Solutions contained PRPP held at a concentration of 0.6 mM, at a temperature of 25 °C, pH 8.0. ACS compound numbers and concentrations used are indicated in the blue boxes.

The compound R5P was tested as a PRPP-like inhibitor using the enzyme-coupled assay with anthranilate held at a concentration of 15 µM to avoid anthranilate inhibition. This compound demonstrated competitive inhibition but gave a high K_i value of 1 ± 0.1 mM. This is unsurprising as crystal structures of *Mtu*-AnPRT with PRPP and Mg^{2+} bound (PDB ID: 1ZVW) show that the PP_i group of PRPP, missing in R5P, is stabilised by numerous hydrogen bonds to *Mtu*-AnPRT, Mg^{2+} and several water molecules, implying a high degree of molecular recognition (Figure 2.13C).[44] It is possible that the inhibition of R5P would improve upon the addition of PP_i to the assay, though this was not tested.

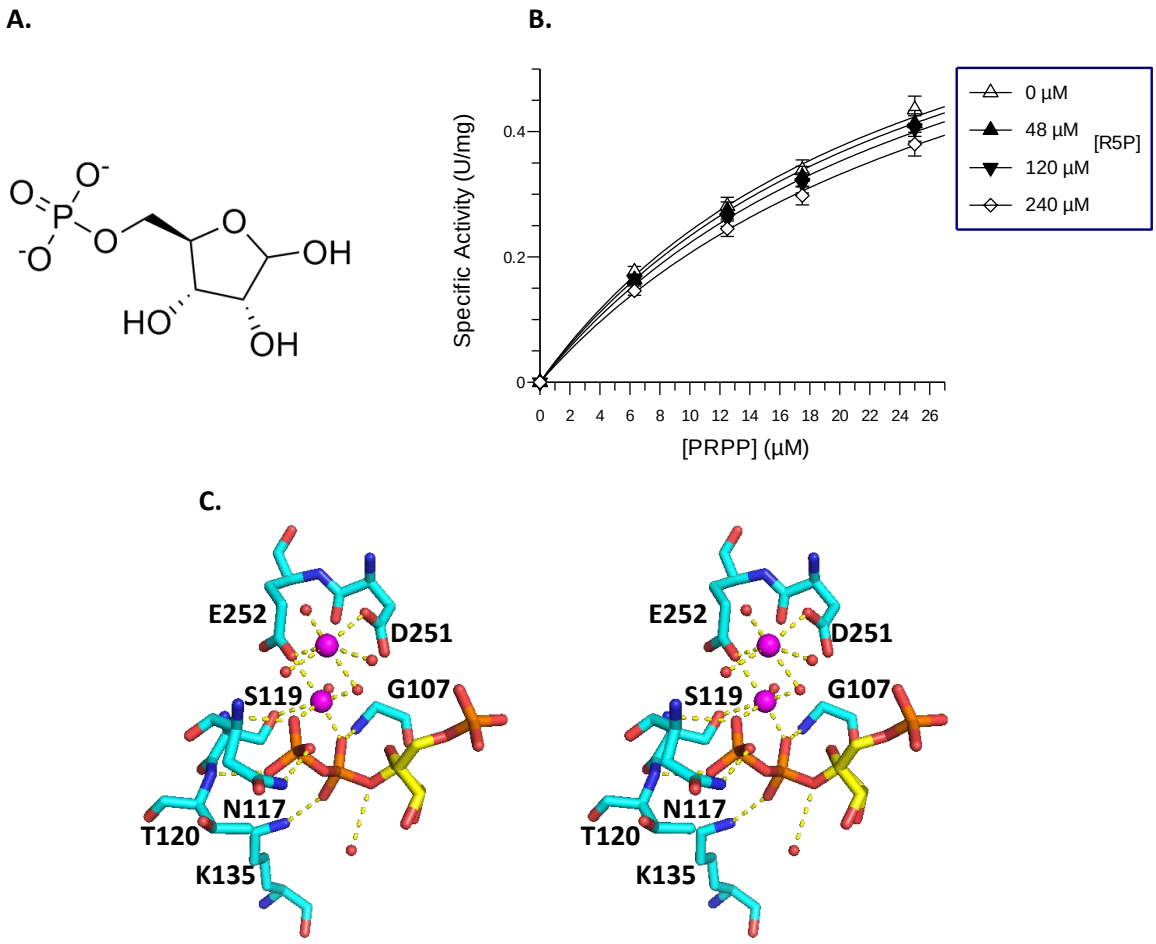

Figure 2.13 Inhibition of *Mtu*-AnPRT by R5P. A) The chemical structure of R5P. B) The *Mtu*-AnPRT Michaelis-Menten inhibition graph for determination of the K_i value of R5P. Anthranilate is held at a concentration of 15 µM, with reaction solutions monitored at 25 °C at pH 8.0. C) Wild-type *Mtu*-AnPRT (cyan) co-ordinated to PRPP (yellow) and Mg^{2+} (magenta spheres), with the PRPP PP_i group and Mg^{2+} polar contacts displayed as yellow dashes. Water molecules are shown as red spheres.

2.7 Crystal Structures of Anthranilate-Like Inhibitors Bound To *Mtu*-AnPRT

Crystal structures of ACS172 (PDB ID: 3QQS), ACS174 (PDB ID: 3QS8), ACS142 (PDB ID: 3UU1), ACS145 (PDB ID: 3R88), ACS179 (PDB ID: 3R6C) and ACS10 (PDB ID: 3TWP) bound to *Mtu*-AnPRT in the presence of PRPP and Mg^{2+} were obtained by Dr Alina Castell and Dr Genevieve Evans at the School of Biological Sciences, University of Auckland. These structures complement the information found via enzymology in this study and are discussed and interpreted in this section.

Mtu-AnPRT co-crystallised with ACS172, PRPP and Mg^{2+} showed the inhibitor bound to *Mtu*-AnPRT in three different binding modes (Figure 2.14). The first orientation, designated Mode 1, can be observed in chains A and B of the structure (PDB ID: 3QQS), where the innermost aromatic ring of ACS172 can be seen to overlap with the middle anthranilate binding site observed in *Sso*-AnPRT structures (Figure 2.14A).[42, 50] The carboxylate group on the innermost aromatic ring of ACS172 forms a salt bridge with R193 as well as a hydrogen bond to a water molecule, while the carboxylate group on the outermost ring forms hydrogen bonds to N138, R194 (both chains) and a water molecule (chain B only). This outermost ring is also oriented parallel to the P180 imidazole ring, suggestive of C-H$^{\cdots}\pi$ interactions.[69]

Chains C and D show ACS172 bound (occupancy = 0.6) in a position where the innermost aromatic ring of the inhibitor overlaps with the *Sso*-AnPRT inner binding site (Figure 2.14B), and is designated Mode 2. In this mode, the carboxylate group of the innermost aromatic ring of ACS172 makes hydrogen bonds to R193 and either one (chain C) or two (chain D) water molecules, while the carboxylate group on the outermost aromatic ring hydrogen bonds to N138 (both chains) and a water molecule (chain C only). Chains C and D also show a second ACS172 molecule bound, in a position designated Mode 3. In this mode the carboxylate group on the inner-most ring of ACS172 makes hydrogen bonds to R194 (both chains), N138 (chain C only) and a water molecule (both chains) and is oriented parallel to P180, however, the outer ring carboxylate group makes no contacts to the relevant protein chains. It is entirely possible that this binding mode arises due to crystal packing, though the innermost ring of ACS172 in this mode creates similar contacts to the outermost ring as it is bound in Mode 1.

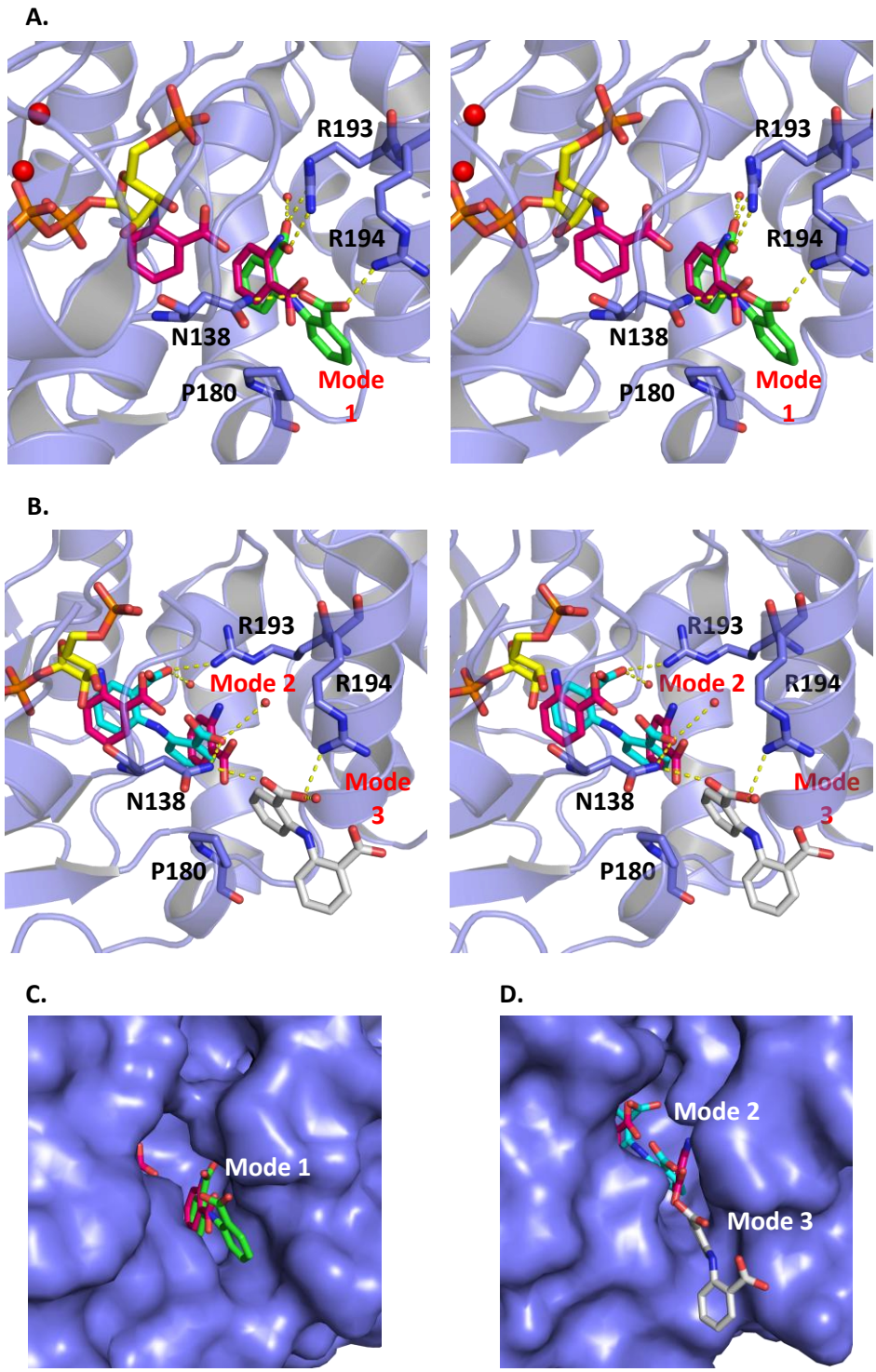

Figure 2.14 Wild-type *Mtu*-AnPRT with ACS172 bound. A) Stereo diagram of *Mtu*-AnPRT (purple) co-crystallised with ACS172, PRPP (yellow) and Mg^{2+} (red spheres) (PDB ID: 3QQS), with anthranilate (pink) overlaid from *Sso*-AnPRT (PDB ID: 1ZYK). Mode 1 of ACS172 (green) is shown, which overlaps with the middle site anthranilate molecule of *Sso*-AnPRT. B) Stereo diagram of Mode 2 of ACS172 (cyan) showing overlap with both inner site and middle site anthranilate molecules of *Sso*-AnPRT. Mode 3 of ACS172 (white) is also shown. C) Surface representation of *Mtu*-AnPRT showing Mode 1 of ACS172. D) Surface representation of *Mtu*-AnPRT showing Modes 2 and 3 of ACS172.

ACS174, PRPP and Mg^{2+} co-crystallised with *Mtu*-AnPRT shows ACS174 bound in two orientations. Interestingly, the orientation seen in all four chains shows ACS174 bound in a pose similar to Mode 2 for ACS172, where the outer aromatic ring of ACS174 overlaps with the middle anthranilate site observed in *Sso*-AnPRT. This is contrary to what is observed for the other inhibitors, the majority of which are bound near the entrance to the anthranilate channel. In this Mode 2 site, the carboxylate group of ACS174 makes hydrogen bonds with R193, Y186 and a water molecule. An additional ACS174 molecule is observed in chains A and D, where the carboxylate group is bound to R194 and two water molecules (Figure 2.15).

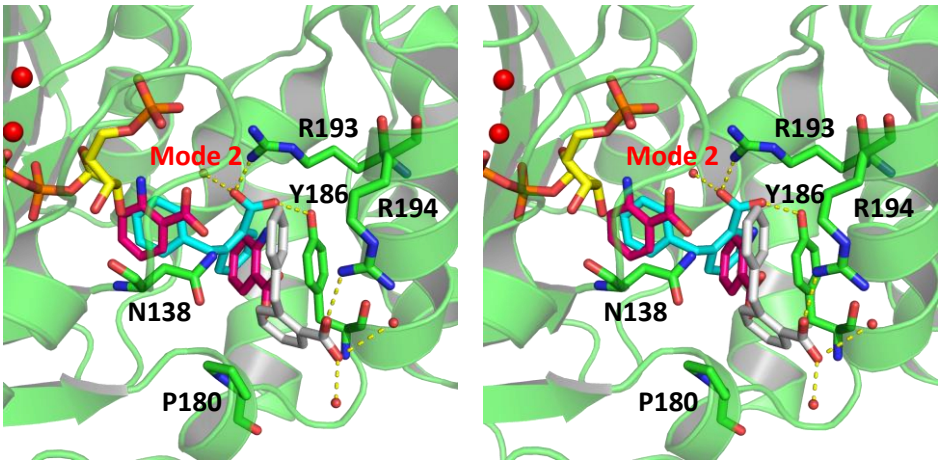

Figure 2.15 Stereo diagram of wild-type *Mtu*-AnPRT with ACS174 bound. *Mtu*-AnPRT (green) (PDB ID: 3QS8) co-crystallised with PRPP (yellow), Mg^{2+} (red spheres) and ACS174 (Mode 2 shown in cyan, and the other binding mode shown in white) with anthranilate (pink) overlaid from *Sso*-AnPRT (PDB ID: 1ZYK).

The *Mtu*-AnPRT structure co-crystallised with ACS142, PRPP and Mg^{2+} shows the inhibitor bound in two orientations. The orientation observed in all four chains shows ACS142 bound in the entrance to the anthranilate channel, making contacts via its carboxylate group to R194, N138, and one (chains A, C and D) or two (chain B) water molecules, and in chain B via its amino group to a water molecule. This binding site will be referred to as the 'outer site' for the remainder of this study. Chains B and C also show a second ACS142 (Figure 2.16) molecule bound in a site that overlaps with the inner anthranilate site observed for *Sso*-AnPRT. In this site ACS142 forms hydrogen bonds with R193 and two water molecules via its carboxylate group, and to two water molecules via its amino group.

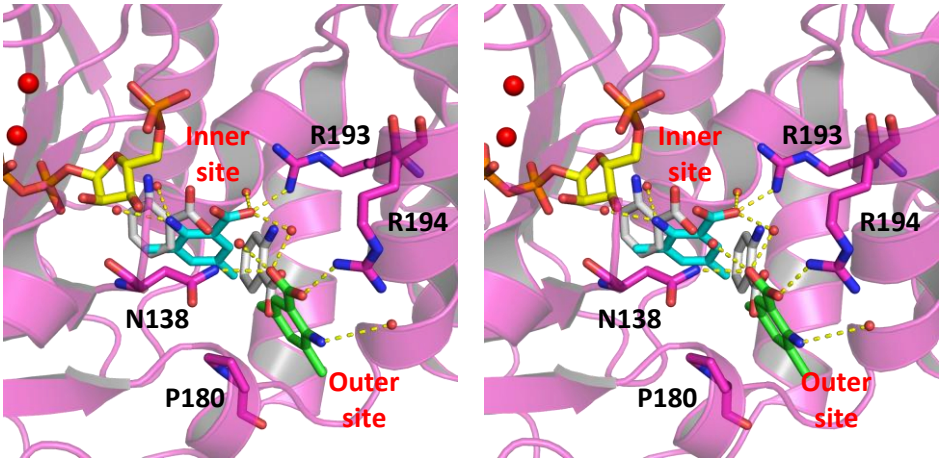

Figure 2.16 Stereo diagram of wild-type *Mtu*-AnPRT with ACS142 bound. *Mtu*-AnPRT (magenta) (PDB ID: 3UU1) co-crystallised with PRPP (yellow), Mg^{2+} (red spheres) and ACS142 (inner site shown in cyan, and the outer site shown in green) with anthranilate (white) overlaid from *Sso*-AnPRT (PDB ID: 1ZYK).

The remaining inhibitors ACS145, ACS179 and ACS10 bound solely in the entrance to the anthranilate channel, with their ring structures oriented parallel to P180. The binding modes of these inhibitors, and of ACS142, ACS172 and ACS174, bound in the anthranilate channel entrance can be compared in Figure 2.17.

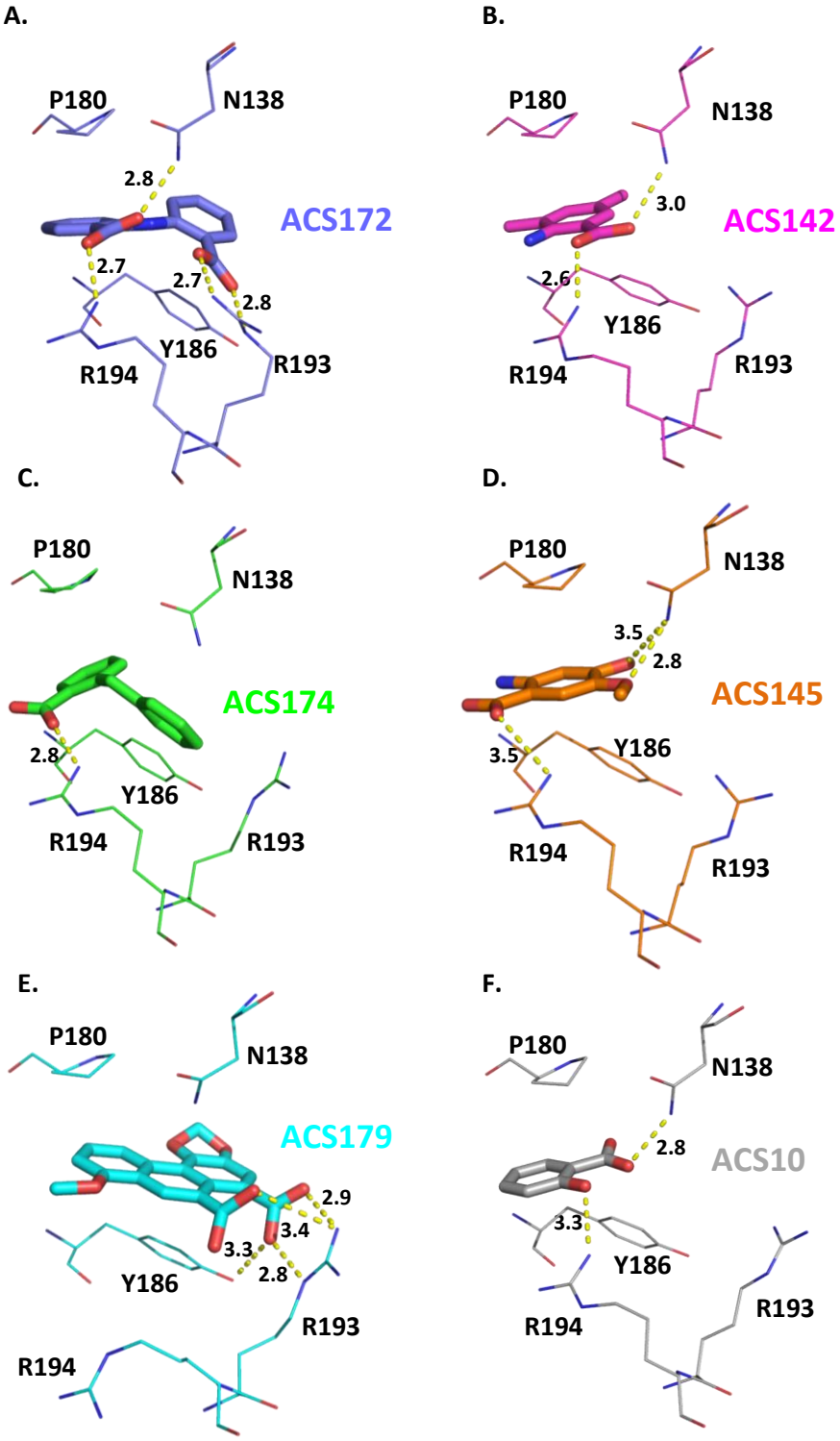

Figure 2.17 Inhibitors of *Mtu*-AnPRT as bound at the anthranilate channel entrance, with bond lengths indicated. A) Mode 1 of ACS172 (PDB ID: 3QQS, purple). B) ACS142 (PDB ID: 3UU1, magenta). C) ACS174 (PDB ID: 3QS8, green). D) ACS145 (PDB ID: 3R88, orange). E) ACS179 (PDB ID: 3R6C, cyan). F) ACS10 (PDB ID: 3TWP, grey).

During this crystallisation process, a new structure was also elucidated for *apo Mtu*-AnPRT (PDB ID: 3QR9) without the need for the additive benzamidine, previously required to obtain diffraction-quality crystals. This new *apo* structure illuminated differences in the positions of several helices compared to the previously solved *apo* structure, including the α8 and α9 helices and the β2-α6 loop, thought to be caused by rearrangement of these secondary structures to accommodate benzamidine (Figure 2.18).[41a] A comparison of the β2-α6 loop between the new *apo* structure and the *Mtu*-AnPRT structure with PRPP and Mg^{2+} bound still demonstrates the loop rearrangement discussed earlier in Section 2.2, however, the PRPP and Mg^{2+} bound structure also contains the benzamidine additive. Ideally, a better comparison would be between the new *apo* structure and a PRPP/Mg^{2+} bound structure without benzamidine present. Several attempts to obtain structures of the latter were undertaken during this study, however, none of the crystals sent for analysis were of diffraction quality (Figure 2.19).

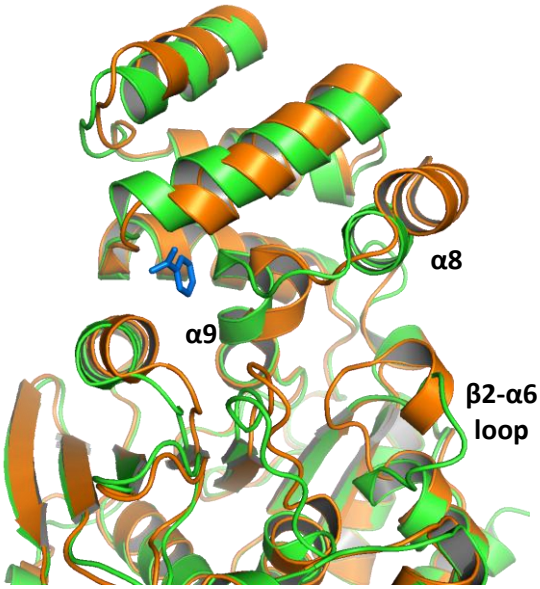

Figure 2.18 An overlay of the old and new *Mtu*-AnPRT *apo* structures. The old *apo Mtu*-AnPRT structure (PDB ID: 2BPQ) is shown in orange with benzamidine (blue) bound, with the new *apo Mtu*-AnPRT structure (PDB ID: 3QR9) shown in green.

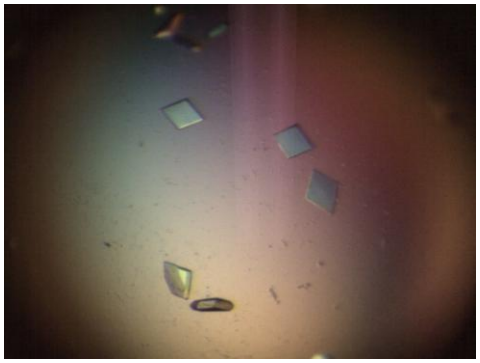

Figure 2.19 Crystals of wild-type *Mtu*-AnPRT co-crystallised with PRPP and Mg^{2+}, with the crystal solution containing 0.2 M imidazole malate (pH 7.0), 13% PEG-4000 (w/v).

2.8 Summary

Both *Mtu*-AnPRT and *Eco*-PRAI:InGPS plasmids were successfully transformed into BL21 (DE3) cell lines containing plasmids pBB528 and pBB541 for co-expression of the chaperonins Gro-ES and Gro-EL. These proteins were successfully purified, with masses of the expected size as determined via mass spectrometry. CD spectra were obtained indicating the proteins were properly folded, and DSF results showed melting temperatures of 54 ± 0.3 °C and 43 ± 0.8 °C for *Mtu*-AnPRT and *Eco*-PRAI:InGPS respectively. When PRPP and Mg^{2+} are included, the melting temperature of *Mtu*-AnPRT increased to 62 ± 0.7 °C.

Kinetic characterisation of *Mtu*-AnPRT was carried out using the UV enzyme-coupled assay developed in this study, with *Eco*-PRAI:InGPS as the coupling enzyme. The apparent K_M values for the natural substrates PRPP and anthranilate were 48 ± 2 μM and 2.0 ± 0.2 μM respectively, with a k_{cat} value of 1.9 ± 0.1 s^{-1}. Anthranilate inhibition was observed for *Mtu*-AnPRT, with a K_i value of 47 ± 7 μM, while Mg^{2+} inhibition, which has been observed for *Sso*-AnPRT, was not apparent. The kinetic profile of *Mtu*-AnPRT is consistent with that of a sequential mechanism, possibly indicating that PRPP binds first before anthranilate can bind in the catalytically relevant site.

A series of anthranilate-like inhibitors were tested against *Mtu*-AnPRT using the enzyme-coupled assay, with K_i values ranging from 5.5 – 129 μM. The most potent of these inhibitors was ACS172 with a pure non-competitive K_i value of 5.5 ± 0.3 μM, the only compound not to display competitive inhibition. R5P was the only compound to be tested as a possible PRPP-like inhibitor, but had a high K_i value of 1 ± 0.1 mM.

In conjunction with the inhibition enzymology studies, structures of *Mtu*-AnPRT co-crystallised with PRPP, Mg^{2+} and various anthranilate-like inhibitors were obtained by Dr Alina Castell and Dr Genevieve Evans. These structures showed the inhibitors bound in the anthranilate channel, with ACS172, ACS174 and ACS142 displaying multiple binding modes within the asymmetric unit. All inhibitors showed at least one binding mode at the entrance to the anthranilate channel; a position previously undefined by crystal structures or modelling as an anthranilate binding site. These structures point to the possibility of a third outer binding site for anthranilate within *Mtu*-AnPRT.

Chapter 3

Alternative Substrates of Wild-type *Mtu*-AnPRT

3.1 Overview

This chapter outlines the characterisation of *Mtu*-AnPRT-catalysed reactions utilising various alternate substrates to anthranilate. Initial kinetic characterisation was achieved via a commercially available PP_i assay to monitor *Mtu*-AnPRT turnover alone without relying on additional *Eco*-PRAI:InGPS turnover.

Physical characterisation of the PRA-substituted products arising from alternate substrate catalysis was achieved using techniques including NMR and mass spectrometry. The appearance of PRA anomers was observed, with interconversion via an imine intermediate. The ability of *Eco*-PRAI:InGPS to catalyse the PRA-substituted products was investigated using the enzyme-coupled assay developed in Chapter 2, and physical characterisation of any *Eco*-PRAI:InGPS reaction products were carried out using mass spectrometry.

The final part of this chapter describes structural studies of *Mtu*-AnPRT co-crystallised with several anthranilate-like substrates, as carried out by Dr Alina Castell at the University of Auckland.

3.2 Introduction

Mtu-AnPRT catalyses the displacement of PP_i of PRPP by anthranilate with inversion of stereochemistry at C1 of PRPP, creating β-PRA from α-PRPP. However, it is unknown whether this reaction proceeds via an S_N1 mechanism, whereby the PP_i moiety of PRPP is completely cleaved prior to nucleophilic attack of the anthranilate amine (creating a fully-formed oxocarbenium ion intermediate), or via an S_N2 mechanism where these two events occur in the same reaction step.

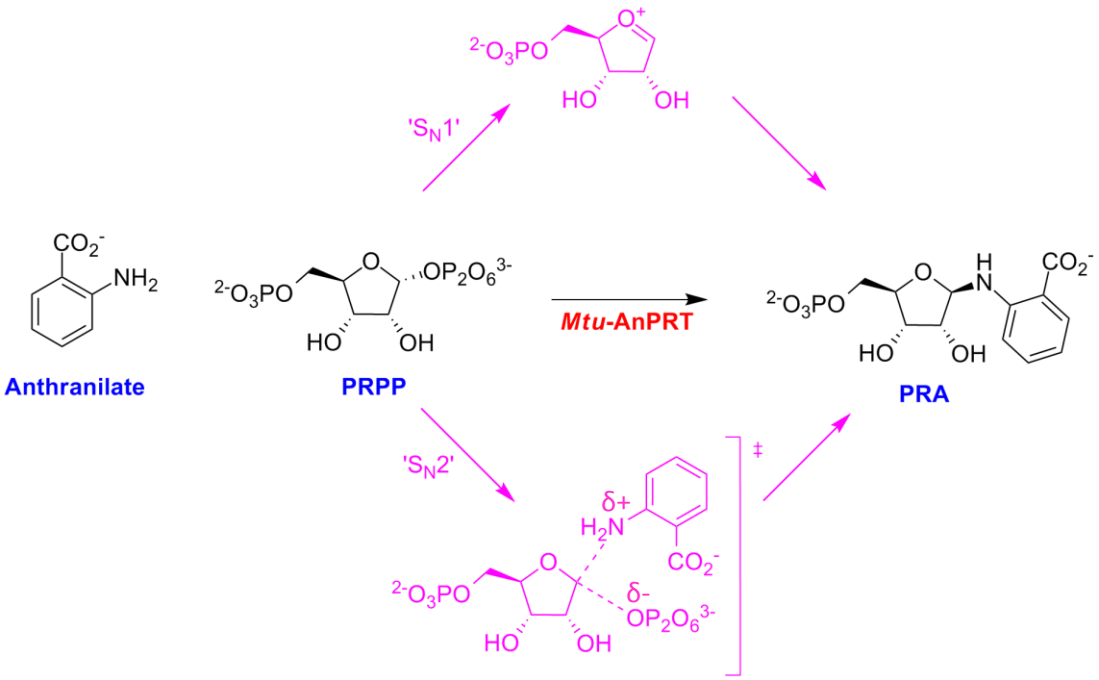

Figure 3.1 The reaction catalysed by *Mtu*-AnPRT, showing both possible mechanisms.

Kinetic isotope effect experiments with the type I orotate and hypoxanthine – guanine PRTs provided results which support an S_N1 mechanism, with evidence of a fully-formed carbocation transition state.[31b, 70] Structures of other type I PRT enzymes co-crystallised with substrates or transition state analogues demonstrate the C1 of PRPP in several different positions between the PP_i and nitrogenous base.[31b, 41b, 71] These results are indicative of a relatively mobile oxocarbenium ion characteristic of an S_N1 mechanism, as opposed to a stationary carbon held in place by an S_N2 mechanism. Kinetic isotope experiments have not been carried out on type II PRTs thus far, however, it has been suggested that the type II human nicotinamide PRT enzyme utilises an S_N2 transition state based on an inspection of the crystal structure with nicotinamide and PRPP bound.[72]

During the screening process of potential anthranilate-like inhibitors for *Mtu*-AnPRT (Section 2.6), several compounds were discovered that acted as alternate anthranilate substrates for this enzyme (e.g. ACS125 and ACS130). Based on this finding, a series of compounds were selected to investigate

the tolerance of *Mtu*-AnPRT to substitutions at various positions on the aromatic ring of anthranilate. These compounds included methyl-, methoxy- or fluoro- substitutions at positions C3-C6, substitution of the carboxylate group for a sulfonyl group, and repositioning of the amine group at C3 or C4. Investigation into the behaviour of these compounds with *Mtu*-AnPRT may elucidate key features of the kinetic mechanism of this enzyme that will further aid the development of potential inhibitors.

3.3 Kinetic Characterisation

As it was not known whether the PRA-like products produced by the reaction of the anthranilate analogues with PRPP would be turned over by *Eco*-PRAI:InGPS, the enzyme-coupled assay utilised in the previous chapter could not be used to monitor the formation of InGP. Instead, the commercially available EnzChek® Pyrophosphate Assay Kit (Invitrogen™) was used to monitor amount of inorganic pyrophosphate (PP_i) produced by the *Mtu*-AnPRT reaction.

Mtu-AnPRT produces PP_i in a 1:1 stoichiometric ratio with anthranilate. Using the EnzChek® Pyrophosphate Assay Kit (Invitrogen™), inorganic pyrophosphatase then converts the PP_i produced by the *Mtu*-AnPRT reaction into inorganic phosphate (P_i) with a 1:2 stoichiometry. The P_i is then reacted with the substrate 2-amino-6-mercapto-7-methylpurine ribonucleoside (MESG) by purine nucleoside phosphorylase (PNP) in a 1:1 ratio to form ribose-1-phosphate and 2-amino-6-mercapto-7-methylpurine, the latter of which can be monitored spectrophotometrically at 360 nm. Excess *Eco*-PRAI:InGPS was also included in this assay in an attempt to stem the breakdown of any PRA-substituted products. The reactions involved in this assay are summarised in Figure 3.2.

Inorganic pyrophosphatase and PNP were added in excess to ensure that the *Mtu*-AnPRT catalysed reaction was the rate-limiting step. The extinction coefficient for 2-amino-6-mercapto-7-methylpurine production from anthranilate and PRPP was determined to be 26200 L $mol^{-1}cm^{-1}$ using known concentrations of anthranilate under the assay conditions outlined in Section 7.1.26/7.3.1.

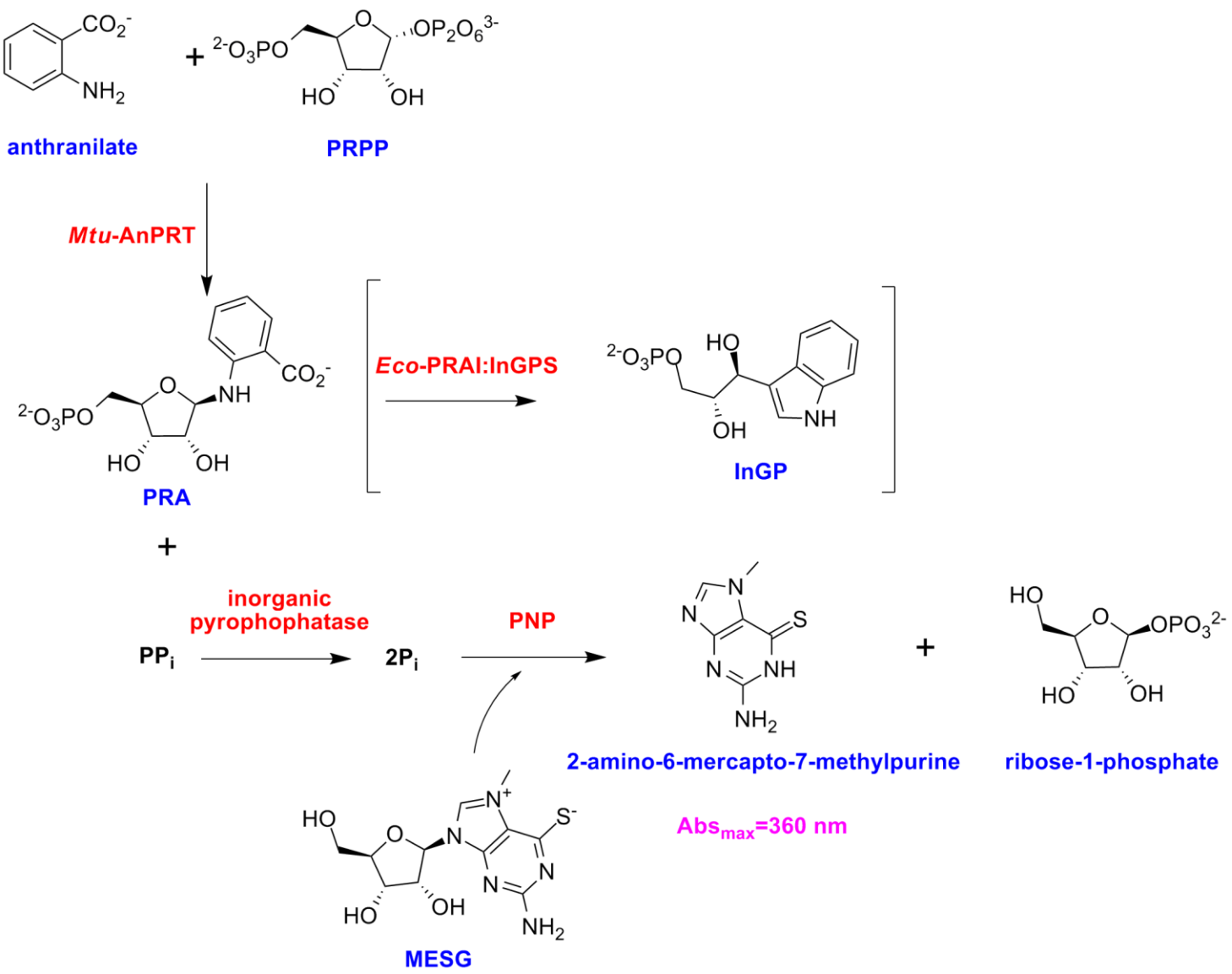

Figure 3.2 The reaction pathways involved in the pyrophosphate assay

3.3.1 Michaelis-Menten Kinetics

The apparent K_M value of 1.7 ± 0.1 μM for anthranilate using the PP_i assay is comparable to the value of 2.0 ± 0.2 μM obtained using the enzyme-coupled assay. The *Mtu*-AnPRT turnover numbers 1.9 ± 0.1 s^{-1} and 2.0 ± 0.1 s^{-1}, obtained using the enzyme-coupled assay and PP_i assay respectively, are identical within experimental error. The similarity of the kinetic parameters obtained between these two assays indicates that the PP_i assay is a valid alternative to investigate anthranilate analogue turnover.

The *Mtu*-AnPRT apparent K_M and k_{cat} values were found for all anthranilate analogues (Table 3.1, Figure 3.3) with the exceptions of ACS142, ACS145, ACS10, ACS4 and 3-aminobenzoic acid. The compounds which are not classified as substrates did not induce detectable *Mtu*-AnPRT activity greater than 0.001 s^{-1}, in the presence of ≤ 200 mM analogue. The apparent K_M values for the fluoro-substituted analogues ranged from 1.4 – 31 μM and are highly dependent on the site of substitution, with fluoro-substitution on C4 and C6 having little effect on binding, whereas fluoro-substitution on C3 and C5 showed an 18- and 6- fold increase in K_M, respectively. None of the fluoro-substituted analogues had a significant effect on the k_{cat} of *Mtu*-AnPRT, showing similar results to the natural substrate anthranilate.

Methyl-substitution around the aromatic ring of anthranilate had a substantially detrimental effect on both the K_M and k_{cat} values. The apparent K_M values for these analogues ranged from 290 – 800 μM, showing an increase of at least 17-fold compared to anthranilate, while k_{cat} values showed a minimum 3-fold decrease. These results demonstrate a lower tolerance for methyl-substitutions compared to fluoro-substitutions around the anthranilate ring, likely due to increased steric bulk of the methyl group creating unfavourable steric interactions within the anthranilate channel of *Mtu*-AnPRT.

Orthanilate showed a 76-fold increase in K_M value, showing a binding affinity significantly worse than the fluoro-analogues, though still better than the methyl-analogues. However, orthanilate had the slowest turnover rate of all the analogues tested with a k_{cat} value of 0.1 ± 0.004 s^{-1}, and highlights the importance of the anthranilate carboxylate group for efficient catalysis.

Substrate	Structure	K_M value (μM)	k_{cat} value (s^{-1})	k_{cat}/K_M (s^{-1} μM^{-1})
Anthranilate	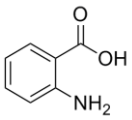	1.7 ± 0.1	2.0 ± 0.1	1.2 ± 0.1
3-fluoroanthranilate (3FA)	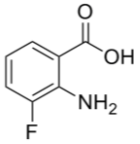	31 ± 3	1.4 ± 0.03	0.05 ± 0.006
4-fluoroanthranilate (4FA)	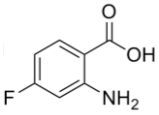	2.1 ± 0.2	1.2 ± 0.1	0.6 ± 0.1
5-fluoroanthranilate (5FA)	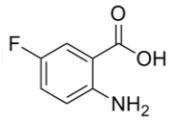	10 ± 1	1.3 ± 0.1	0.13 ± 0.01
6-fluoroanthranilate (6FA)	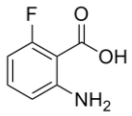	1.4 ± 0.1	1.3 ± 0.1	0.9 ± 0.1
3-methylanthranilate (3MA)	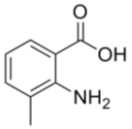	290 ± 20	0.63 ± 0.03	0.002 ± 0.0002
4-methylanthranilate (4MA)	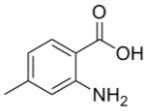	490 ± 130	0.15 ± 0.02	0.0003 ± 0.0001
5-methylanthranilate (5MA) (ACS125)	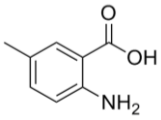	570 ± 120	0.62 ± 0.07	0.0011 ± 0.0004
6-methylanthranilate (6MA)	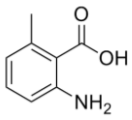	800 ±120	0.62 ± 0.07	0.0009 ± 0.0002
Orthanilate (ACS130)	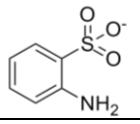	130 ± 11	0.1 ± 0.004	0.0008 ± 0.0001

Table 3.1 Chemical structures, K_M values, k_{cat} values and k_{cat}/K_M values for anthranilate analogues tested as substrates for *Mtu*-AnPRT.

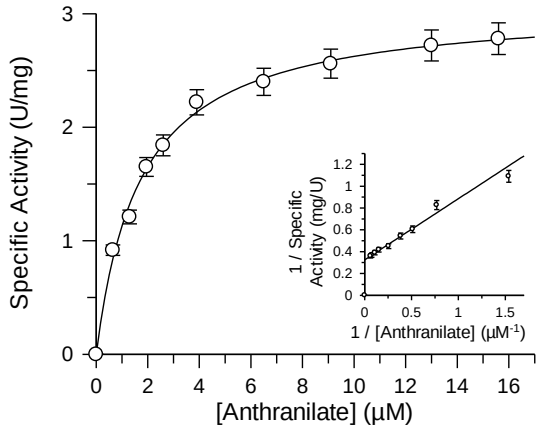
Specific Activity (U/mg)
[Anthranilate] (μM)
1 / Specific Activity (mg/U)
1 / [Anthranilate] (μM-1)

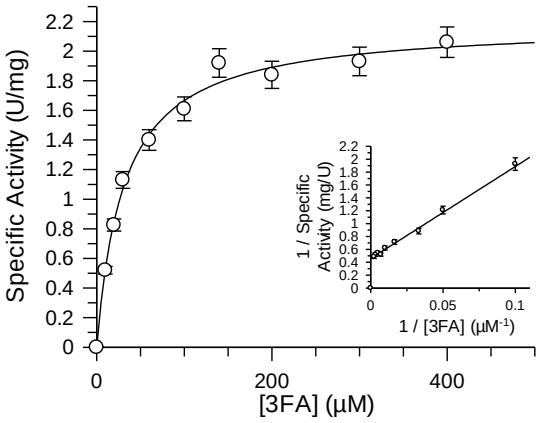
Specific Activity (U/mg)
[3FA] (μM)
1 / Specific Activity (mg/U)
1 / [3FA] (μM-1)

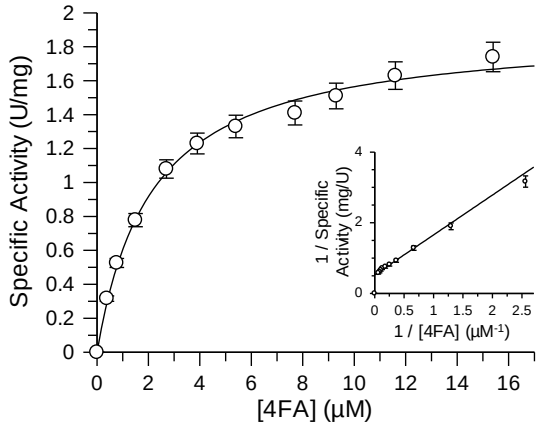
Specific Activity (U/mg)
[4FA] (μM)
1 / Specific Activity (mg/U)
1 / [4FA] (μM-1)

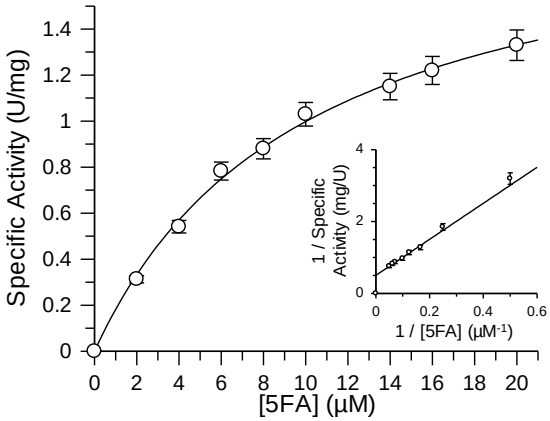
Specific Activity (U/mg)
[5FA] (μM)
1 / Specific Activity (mg/U)
1 / [5FA] (μM-1)

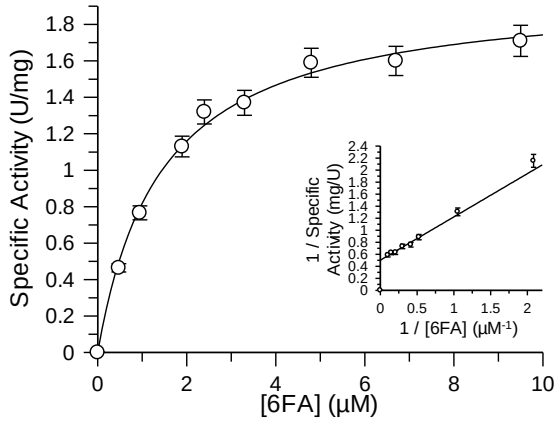
Specific Activity (U/mg)
[6FA] (μM)
1 / Specific Activity (mg/U)
1 / [6FA] (μM-1)

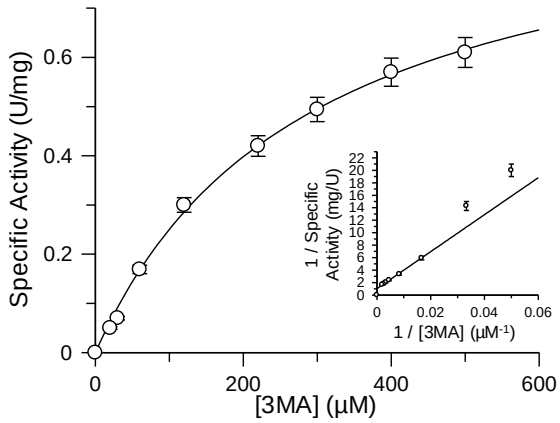
Specific Activity (U/mg)
[3MA] (μM)
1 / Specific Activity (mg/U)
1 / [3MA] (μM-1)

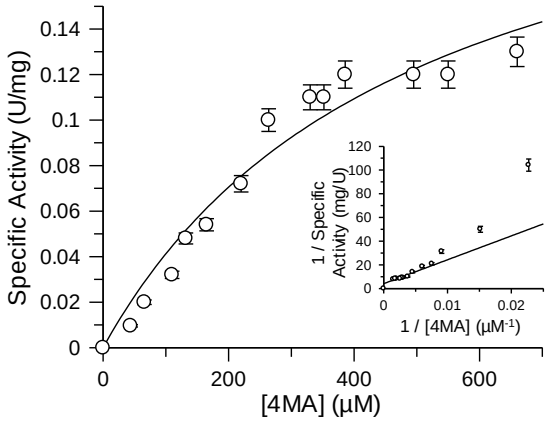
Specific Activity (U/mg)
[4MA] (μM)
1 / Specific Activity (mg/U)
1 / [4MA] (μM-1)

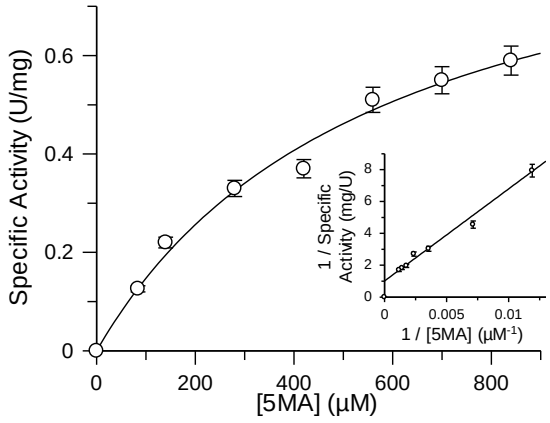
Specific Activity (U/mg)
[5MA] (μM)
1 / Specific Activity (mg/U)
1 / [5MA] (μM-1)

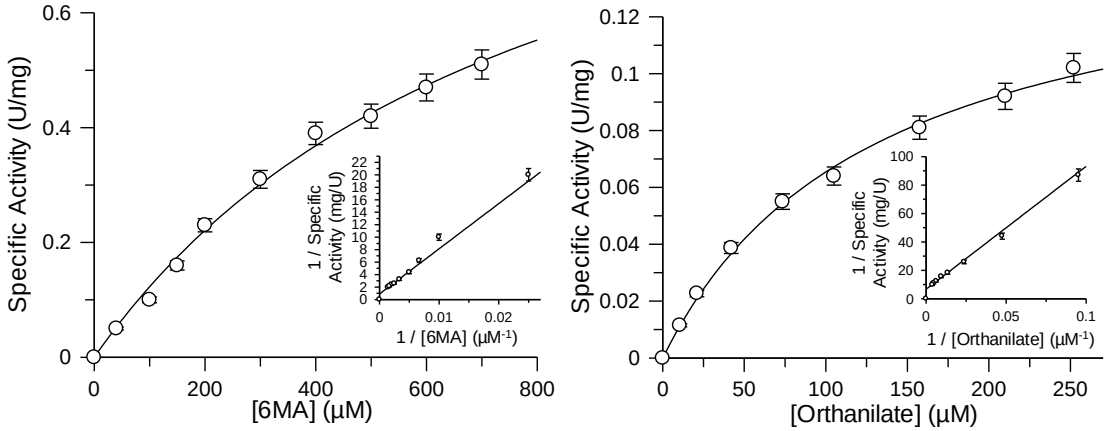

Figure 3.3 The Michaelis-Menten plots for determination of the anthranilate-analogue kinetic parameters. Insets: Lineweaver-Burk plots. Data was obtained using the EnzChek® Pyrophosphate Assay Kit (Invitrogen™) with PRPP held at a concentration of 120 μM. Reactions were initiated with the addition of anthranilate/analogue. All data points were fitted using the graphing software Grafit 5.[67]

3.3.2 Anthranilate-Analogue Inhibition

Due to the observation of anthranilate inhibition discussed in Section 2.5.2, the fluoro-substituted anthranilate analogues were further tested at higher concentrations to investigate whether this phenomenon still occurred. The fluoro-analogues were selected due to the similarity of their kinetic parameters to anthranilate.

Substrate inhibition of anthranilate and the fluoro-substituted analogues was examined using the PP_i assay as outlined in Section 7.1.26/7.3.1, with analogue concentration increased up to a 800 μM maximum (Table 3.2, Figure 3.4). Inhibition of the natural substrate anthranilate gave a similar K_i value of 45 ± 6 μM to that obtained using the enzyme-coupled assay (47 ± 7 μM). Substrate inhibition was observed for all fluoro-analogues tested, and again showed dependence on the site of fluoro-substitution, though with a different trend to that observed for the K_M values in Section 3.3.1. Fluoro-substitutions at the C3 and C4 positions showed the most significant influence on the K_i values, with a 24- and 8- fold increase respectively. Substitution at the C5 and C6 positions, however, had less of an effect, with these analogues displaying similar K_i values to anthranilate. Combined with the results in Section 3.3.1, it can be seen that 6FA possesses kinetic parameters that are most similar to those of anthranilate.

Substrate	Structure	K_i value (μM)
Anthranilate	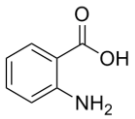	45 ± 6
3-fluoroanthranilate (3FA)	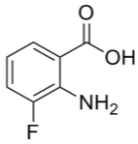	1090 ± 330
4-fluoroanthranilate (4FA)	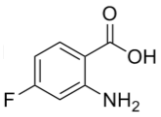	380 ± 100
5-fluoroanthranilate (5FA)	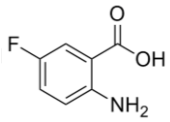	60 ± 11
6-fluoroanthranilate (6FA)	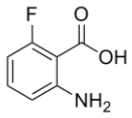	34 ± 5

Table 3.2 Chemical structures and K_i values for the fluoro-analogues as substrate inhibitors of *Mtu*-AnPRT.

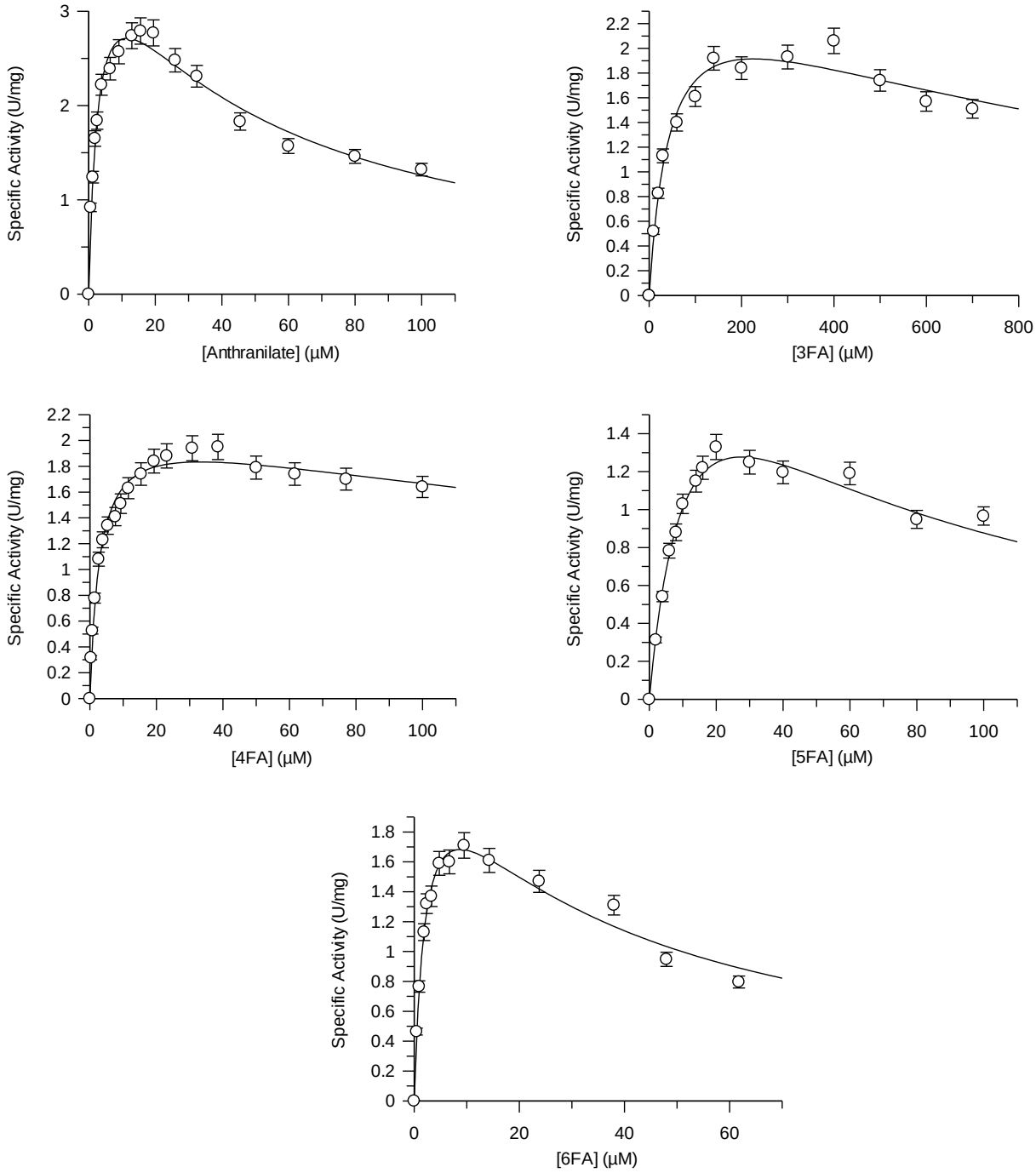

Figure 3.4 Substrate inhibition plots for fluoro-/anthranilate. Data was obtained using the EnzChek® Pyrophosphate Assay Kit (Invitrogen™) with PRPP held at a concentration of 120 µM. Reactions were initiated with the addition of fluoro-/anthranilate. All data points are fitted to the substrate inhibition equation using Grafit 5 software.[67]

3.4 Product Characterisation

3.4.1 NMR

As the PP_i assay described in Section 3.3 monitors PP_i production only, it was necessary to confirm the presence of substituted PRA products produced by the reactions between PRPP and the anthranilate analogues. Thus, ^{1}H NMR spectroscopy was carried out by Dr Esther Bulloch at the University of Auckland to follow the *Mtu*-AnPRT-catalysed reaction of each of these analogues with PRPP.

An excess of *Mtu*-AnPRT and both natural substrates were incubated and the ^{1}H spectra recorded at 100 – 300 s intervals, with results showing an obvious loss of both substrates coupled with the appearance of peaks corresponding to PRA (Figure 3.5). However, the emergence of two anomeric proton peaks (at 5.70 and 5.31 ppm) and two sets of aromatic proton peaks corresponding to PRA indicated that both α and β anomers of this product were present. Due to spectral peak overlap, the PRA aromatic protons and the ribose protons could not be uniquely assigned.

This ^{1}H NMR method was used to follow all the *Mtu*-AnPRT-catalysed reactions of PRPP with the fluoro- and methyl-substituted anthranilate analogues and orthanilate. Peaks corresponding to the analogues and PRPP were observed to disappear concurrently with the formation of PRA analogues, with the exception of 3MA (Appendix 2).[51] As with PRA, the PRA analogues all existed as a mixture of α and β anomers of which the anomeric protons could all be uniquely assigned, despite the significant overlap of peaks corresponding to other structural features. It is surprising that the PRA product resulting from PRPP and 3MA is not detected using this technique, as the k_{cat} value was observed to be similar to both 5MA and 6MA (Table 3.1). It is possible that this product has a relatively short half life, and thus is conducive to break-down before detection, or that substrate inhibition for this compound is triggered at lower concentrations.

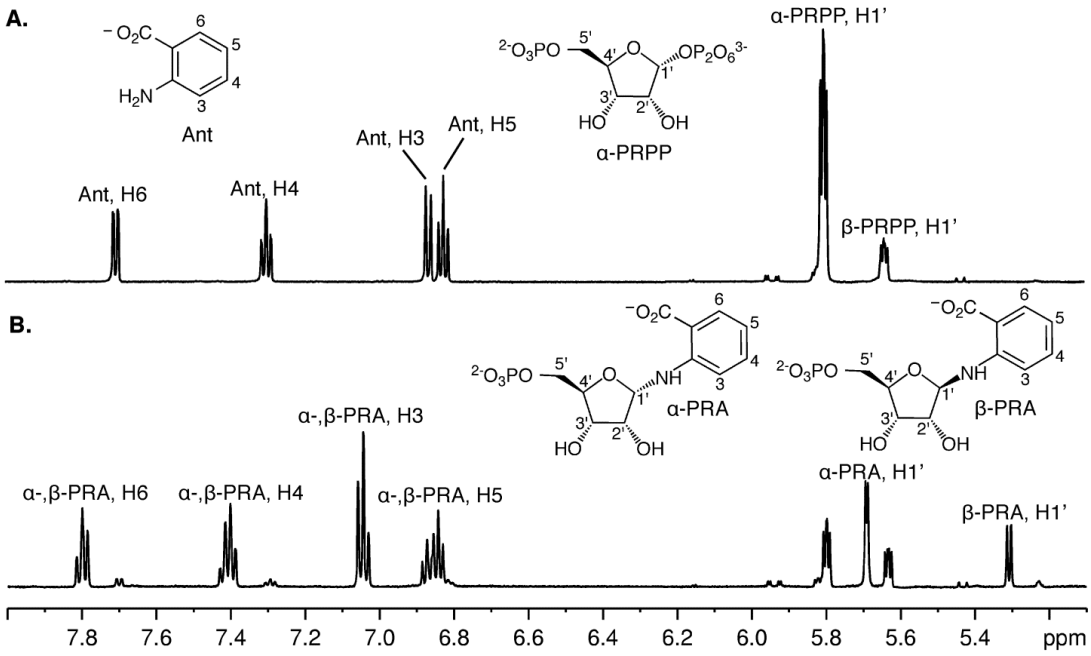

Figure 3.5 Monitoring the reaction catalysed by *Mtu*-AnPRT using ^{1}H NMR spectroscopy. A) Spectrum of assay solution containing α-PRPP (2.5 mM) and anthranilate (1 mM) at pH 8 before incubation with *Mtu*-AnPRT. Note that the commercially obtained α-PRPP also contains β-PRPP as an impurity, which is not a substrate for *Mtu*-AnPRT. B) Spectrum of assay solution following incubation with *Mtu*-AnPRT (0.8 μM) at 25 °C for 10 min. The substrates PRPP and anthranilate are consumed, and both α-PRA and β-PRA are present in approximately a 7:3 molar ratio. Chemical shifts are given relative to TSP (δ 0 ppm). Figure extracted from Cookson *et al*.[51]

3.4.2 Mechanism of Anomerisation

It is likely that the *Mtu*-AnPRT reaction proceeds with inversion of stereochemistry at the C1 position of the ribose ring of PRPP, as has been observed with other PRT enzymes.[31a, 73] Crystal structures of AnPRT orthologues support this prediction,[42, 44, 74] as anthranilate can only approach PRPP from the β position, thereby only forming β-PRA. α-PRA could therefore be formed post-reaction via the rapid anomerisation of β-PRA in solution, a phenomenon that has been identified in other PRA-like compounds such as phosphoribosyl amine.[75] Anomerisation is likely to occur via intramolecular rearrangement through an imine intermediate (Figure 3.6).

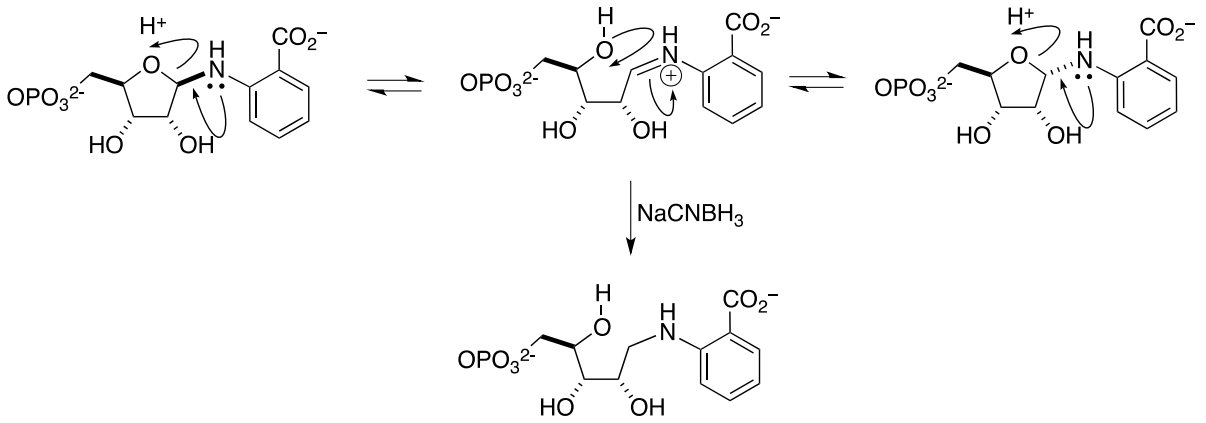

Figure 3.6 The anomerisation of the *Mtu*-AnPRT product PRA via an imine intermediate and its reduction to the open chain form.

To investigate this hypothesis*, Mtu*-AnPRT was incubated with PRPP and anthranilate with an excess of the reducing agent $NaCNBH_3$, as outlined in Section 7.3.2, with the intent of trapping the iminium ion intermediate in its amine open-chain form. $NaCNBH_3$ was chosen based on its ability as a mild reducing agent, widely used for converting imines to amines. After 5 mins reaction time, samples were collected and analysed via mass spectrometry. Evidence for the reduced amine open-chain product was observed with m/z peaks present at 352.0782 and 374.0603 amu corresponding to the masses of the expected product and its sodium salt. These values compare well with the calculated values of 352.0792 and 374.0611 amu for the reduced amine open-chain product and its sodium salt respectively.

3.5 *Eco*-PRAI:InGPS Turnover

As it had been confirmed that all the anthranilate analogues could be turned over by *Mtu*-AnPRT, with all observed to form the corresponding PRA-substituted product (excluding 3MA), the ability of the PRA-substituted products to be turned over by *Eco*-PRAI:InGPS was then investigated.

Initially these compounds were tested for *Eco*-PRAI:InGPS turnover using the enzyme-coupled assay, also used to obtain the natural substrate K_M values in Section 2.5.1. For each fluoro-analogue (except 3FA), a significant increase in absorbance at 270 nm consistent with the formation of an indole ring was observed, indicating successful *Eco*-PRAI:InGPS turnover of fluoro-PRA. Control assays of the fluoro-analogues showed that when the concentration of *Eco*-PRAI:InGPS alone was increased, an increase in the rate of InGP formation was also observed (Figure 3.7). This demonstrated that *Eco*-PRAI:InGPS was limiting the formation of product even with a minimum 10-fold excess compared to *Mtu*-AnPRT. This observation indicates that *Eco*-PRAI:InGPS is less tolerant of fluoro-PRA than of regular PRA, and validates the use of the PP_i assay for determination of anthranilate-analogue kinetic parameters.

The methyl-analogues and 3FA had minimal kinetic rates difficult to distinguish from the experimental baseline, with no concrete evidence of turnover. The product of orthanilate and PRPP, sulfonyl-PRA, could theoretically undergo the rearrangement catalysed by PRAI to yield CdRP but not the decarboxylation catalysed by InGPS to form InGP as the stability of the sulfonyl moiety makes it a bad leaving group (Figure 3.8). Correspondingly, there was not a significant increase in absorbance at 270 nm on incubation of sulfonyl-PRA with *Eco*-PRAI:InGPS.

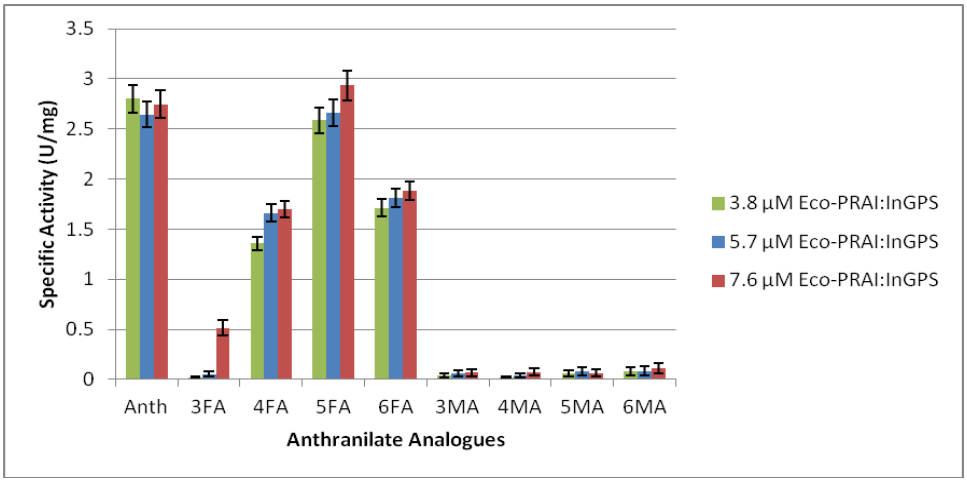

Figure 3.7 Apparent activity of *Mtu*-AnPRT when utilising anthranilate analogues as substrates, as monitored by the enzyme-coupled assay. Solutions contained 0.3 µM *Mtu*-AnPRT, 1 mM $MgCl_2$, 0.6 mM PRPP and (3 x K_M) µM fluoro/anthranilate analogues or 0.5 mM methyl analogues with varying concentrations of *Eco*-PRAI:InGPS.

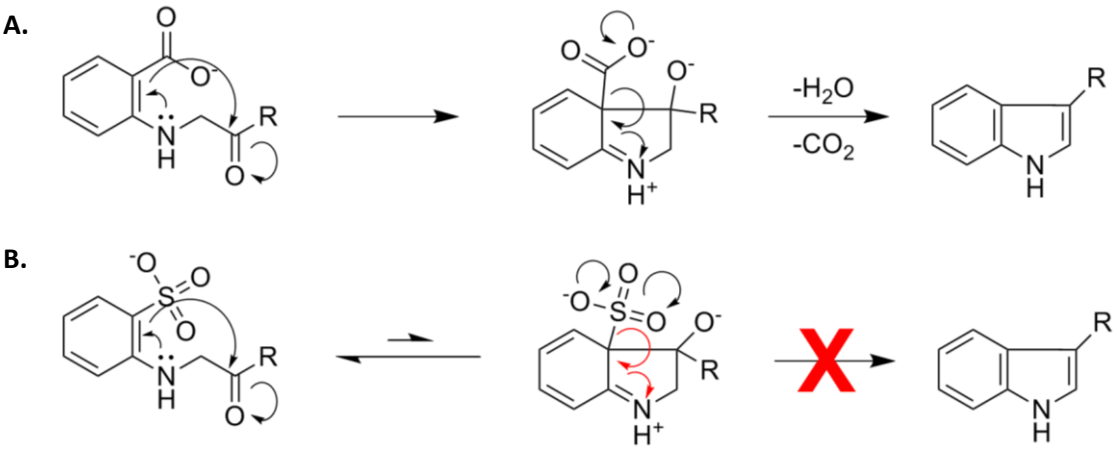

Figure 3.8 The InGPS-catalysed reaction resulting in formation of InGP. A) The reaction of the natural substrate CdRP. B) The reaction of sulfonyl-substituted CDRP cannot from the InGP product. Red curly arrows indicate electron movement that cannot take place.

3.5.1 Wavelength Scans

The enzyme-coupled assay was used in conjunction with continuous wavelength scanning to qualitatively ascertain successful turnover of substituted PRA by *Eco*-PRAI:InGPS, as described in Section 7.3.3. These wavelength scans (from 200 - 380 nm) were also used to determine whether substituted InGP shifts the wavelength at which the absorbance maximum is observed.

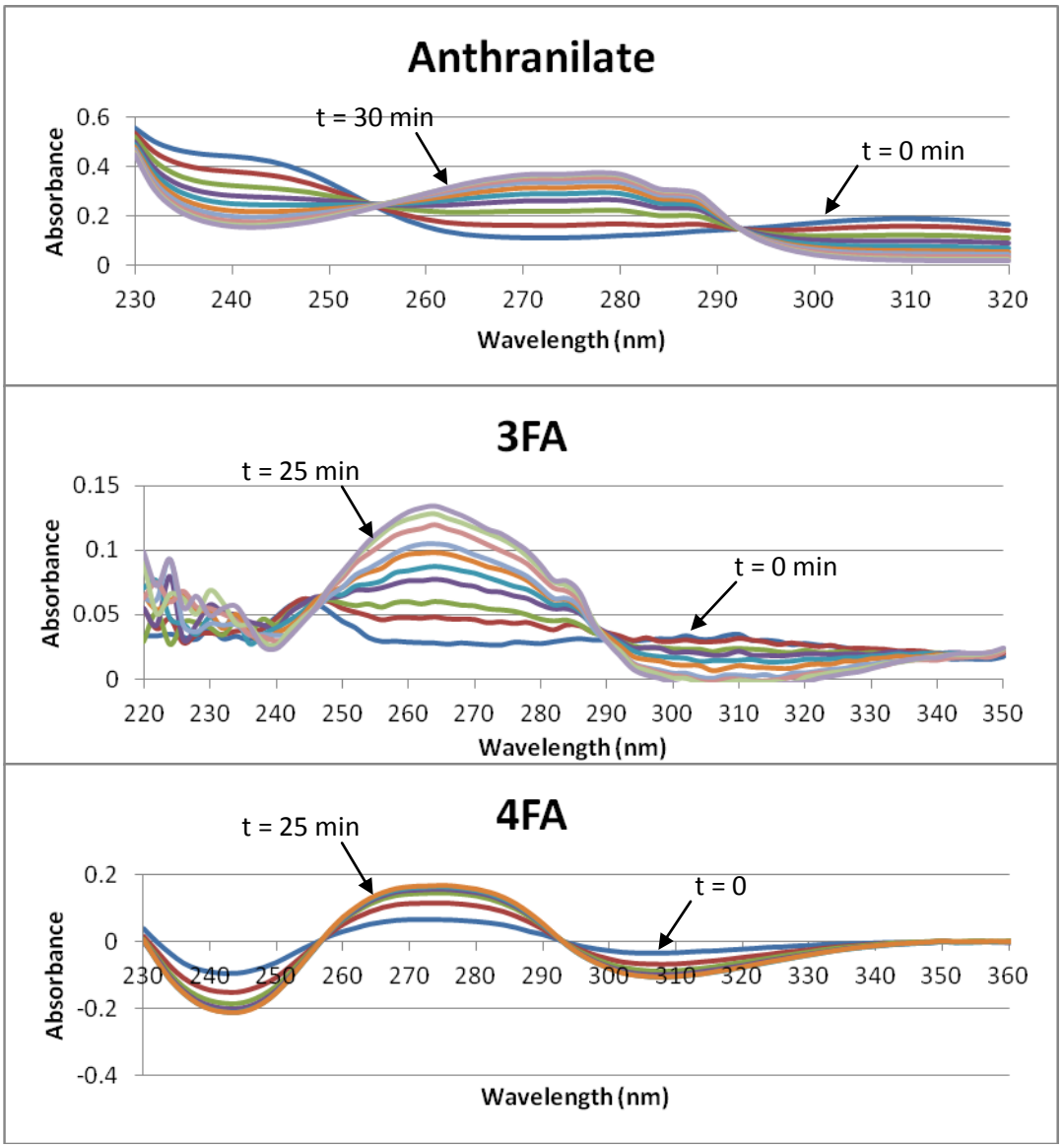

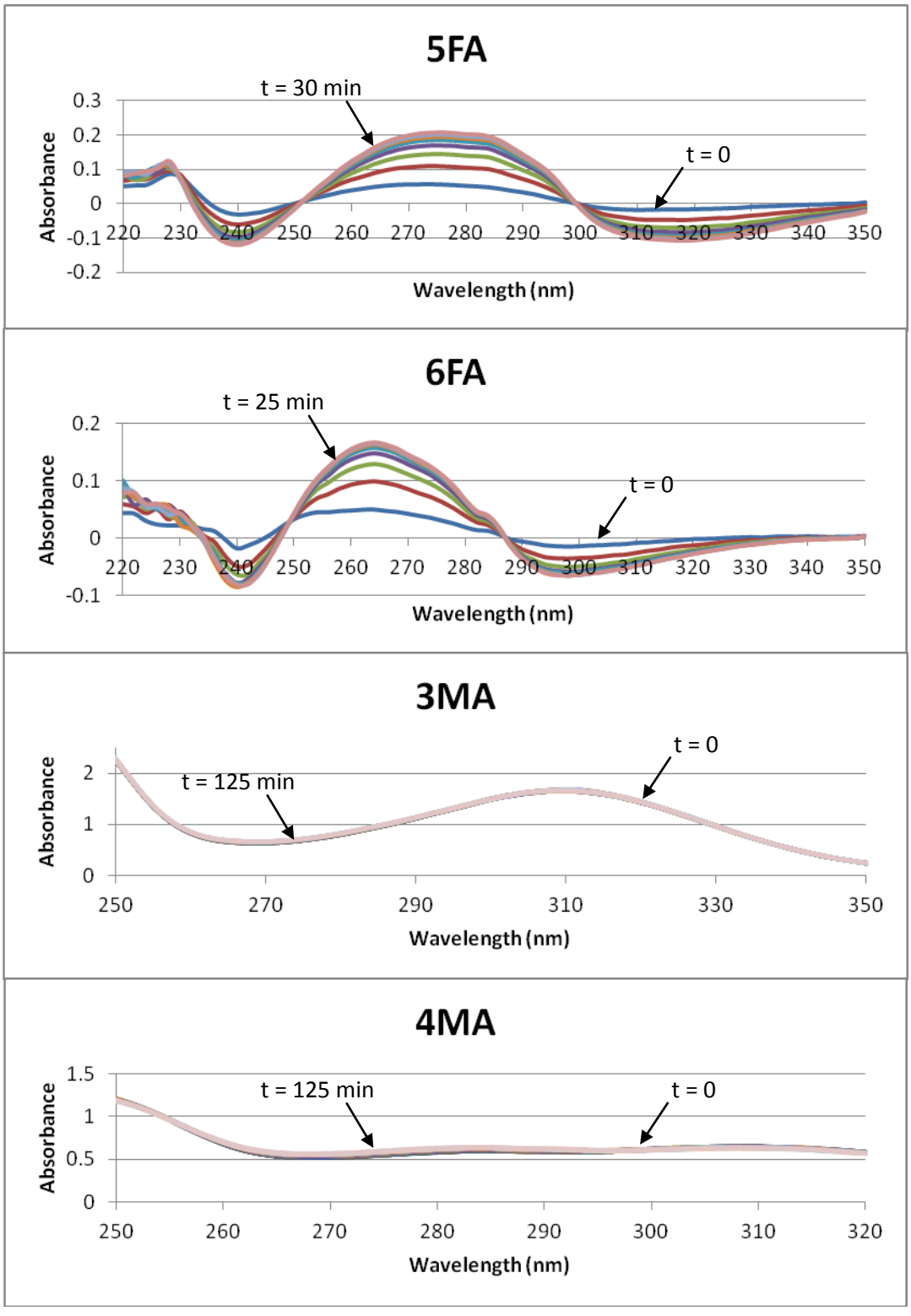
5FA
t = 30 min
t = 0
Absorbance
Wavelength (nm)
6FA
t = 25 min
t = 0
Absorbance
Wavelength (nm)
3MA
t = 0
t = 125 min
Absorbance
Wavelength (nm)
4MA
t = 125 min
t = 0
Absorbance
Wavelength (nm)

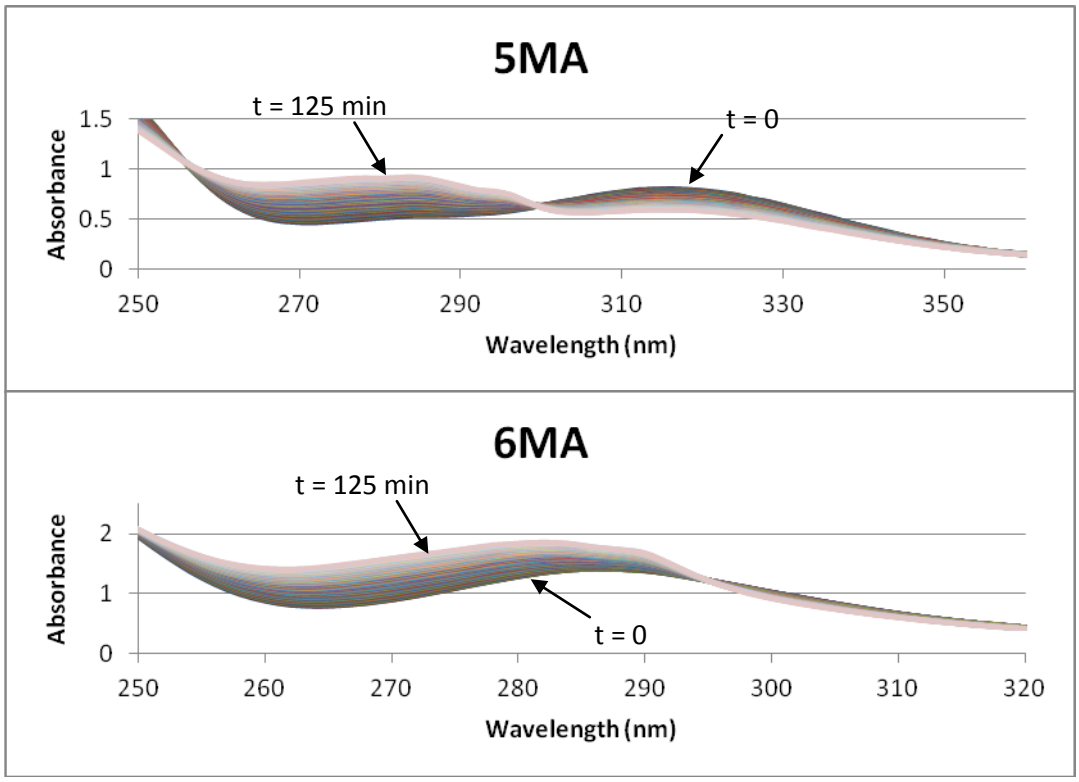

Figure 3.9 Wavelength scans of the *Mtu*-AnPRT/*Eco*-PRAI:InGPS reaction using anthranilate/analogues, with the initial scan marked by t = 0. The absorbance can be seen to increase in the range 260 – 290 nm for each substrate, indicating the formation of InGP product. Solutions for analysis of fluoro-/anthranilate contained 1 mM $MgCl_2$, 0.1 µM *Mtu*-AnPRT, 1.7 µM *Eco*-PRAI:InGPS, 0.6 mM PRPP and 100 µM fluoro-/anthranilate. Solutions for analysis of methyl-anthranilate contained 1 mM $MgCl_2$, 30 µM *Mtu*-AnPRT, 150 µM *Eco*-PRAI:InGPS, 0.6 mM PRPP and 0.5 mM methyl-anthranilate. Reactions were scanned from 360-220 nm with a cycle length time of 2.5 min. Solutions were thermally equilibrated for 5 min prior to initiation with alternate substrate and either allowed to go to completion or to a maximum of 50 cycles.

During incubation of each of the fluoro-substituted analogues with both enzymes a considerable increase in absorption from 265 - 275 nm could be observed (Figure 3.9). This is consistent with formation of the expected fluoro-InGP analogues. 6MA and 5MA also showed a significant increase in absorption in this range, though at a much slower rate. No definitive evidence of a new substituted InGP product could be detected for 3MA or 4MA using this method, as the total absorbance change observed did not exceed that of the respective blanks (containing all assay constituents minus the anthranilate analogue). However, the reactions for 3MA and 4MA with all assay constituents present did show individual scans in increasing order of reaction time, as shown by the progression from darker colours (early scans) to lighter colours (later scans) in Figure 3.10. The experiment blanks for 3MA and 4MA, however, did not show such a progression, which could

indicate that 3MA and 4MA are indeed turned over, though with an exceedingly slow reaction rate. Nonetheless, these results indicate *Eco*-PRAI:InGPS is less tolerant of methyl substitutions of the aromatic moiety of PRA, especially at the C3 and C4 positions.

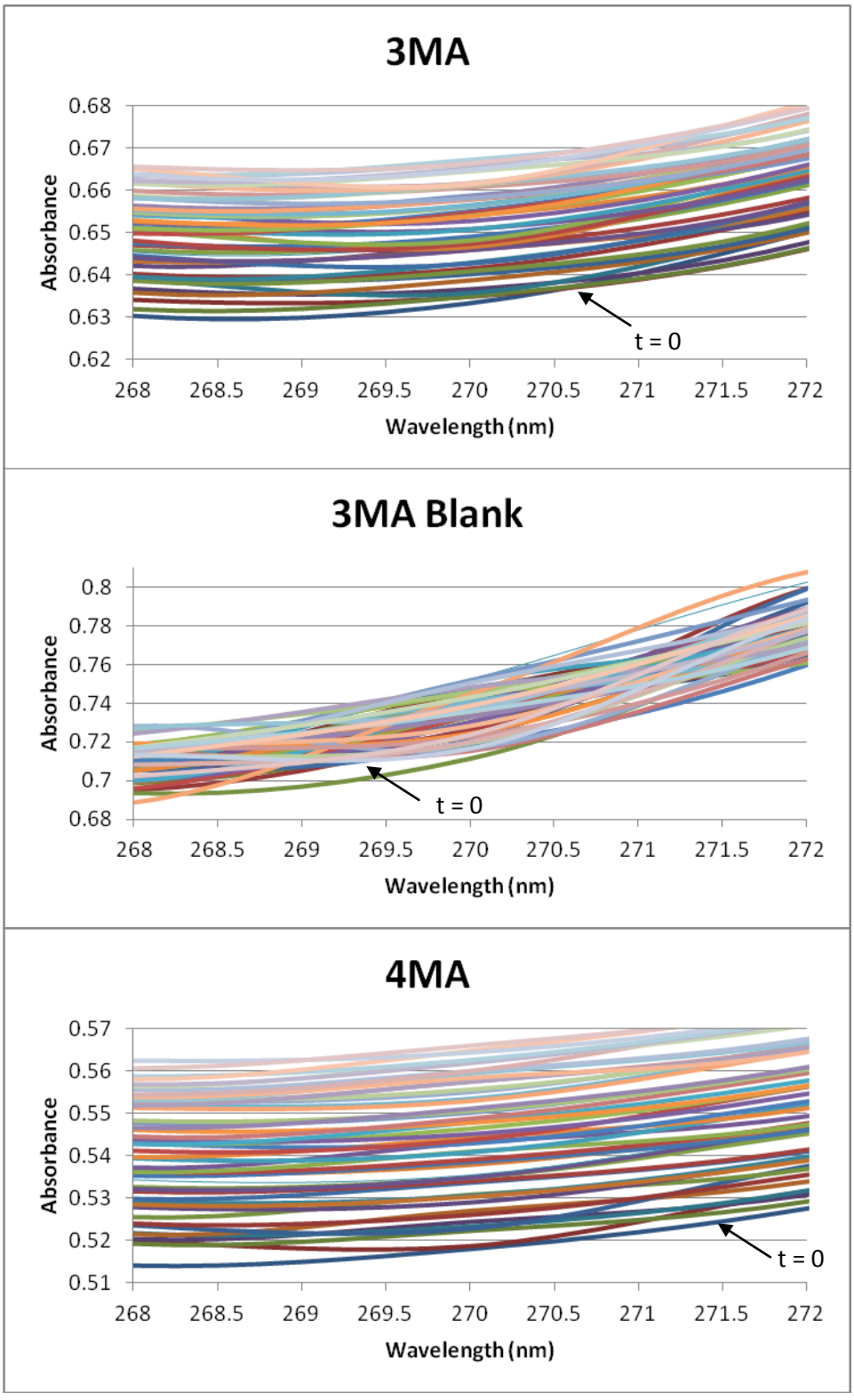

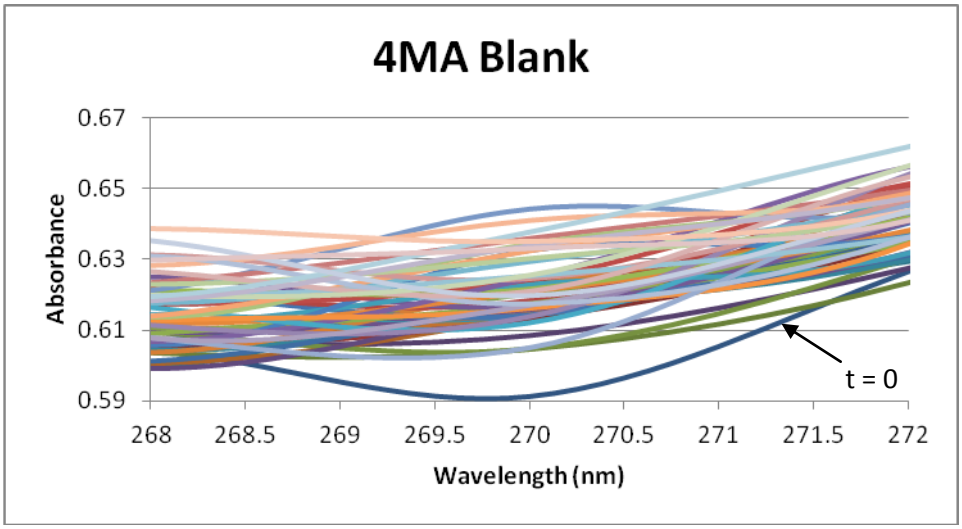

Figure 3.10 Wavelength scans of the *Mtu*-AnPRT/*Eco*-PRAI:InGPS reaction for 3MA and 4MA, with the initial scan marked as t = 0. The colours of the individual scans indicate how much time has passed, with earlier scans represented by darker colours, and later scans indicated by lighter colours. Solutions contained 1 mM $MgCl_2$, 30 µM *Mtu*-AnPRT, 150 µM *Eco*-PRAI:InGPS, 0.6 mM PRPP and 0.5 mM methyl-anthranilate. Blanks contained all constituents minus the methyl-anthranilate. Reactions were scanned from 360-220 nm for 50 cycles, with a cycle length time of 2.5 min. Solutions were thermally equilibrated for 5 min prior to initiation with alternate substrate.

3.5.2 Mass Spectrometry

To complement the findings in Section 3.5.1, mass spectrometry was utilised to detect substituted InGP formation. Using the experimental conditions described in Section 7.3.4, analysis of the alternate substrates in solution with PRPP, Mg^{2+}, *Mtu*-AnPRT and *Eco*-PRAI:InGPS confirmed the presence of all fluoro- and methyl-InGP products as sodium salts with the exclusion of 3MA (Table 3.3). The catalysis of 3-methyl-PRA by *Eco*-PRAI:InGPS is therefore either too low for detection using this method, or it does not occur. Orthanilate was not tested using this method as the sulfonyl-CdRP product has the same expected mass as its sulfonyl-PRA precursor.

Substrate	Formula of InGP Product	Expected Mass of Product (g/mol)	Observed Mass of Product (g/mol)
Anthranilate	$C_{11}H_{14}NO_6PNa$	310.0451	310.0441
6FA	$C_{11}H_{13}FNO_6PNa$	328.0357	328.0348
5FA	$C_{11}H_{13}FNO_6PNa$	328.0357	328.0349
4FA	$C_{11}H_{13}FNO_6PNa$	328.0357	328.0347
3FA	$C_{11}H_{13}FNO_6PNa$	328.0357	328.0350
6MA	$C_{12}H_{16}NO_6PNa$	324.0607	324.0597
5MA	$C_{12}H_{16}NO_6PNa$	324.0607	324.0600
4MA	$C_{12}H_{16}NO_6PNa$	324.0607	324.0605
3MA	$C_{12}H_{16}NO_6PNa$	324.0607	-

Table 3.3 Masses of the substituted InGP products resulting from analogue turnover using the enzyme-coupled assay. Solutions contained 1.2 mM PRPP, 0.6 µM *Mtu*-AnPRT, 6 µM *Eco*-PRAI:InGPS, 2 mM $MgCl_2$, and either 400 µM fluoro-/anthranilate or 2 mM methyl-anthranilate. (-) indicates that the expected product could not be observed.

3.5.3 NMR

To further characterise and confirm the substituted InGP products arising from *Mtu*-AnPRT/*Eco*-PRAI:InGPS catalysis of PRPP and anthranilate, 4FA or orthanilate, ^{1}H NMR spectroscopy was again used to follow the reactions, and was carried out by Dr Esther Bulloch at the University of Auckland.

Initially, *Mtu*-AnPRT was incubated with PRPP, Mg^{2+} and anthranilate, and upon observed PRA formation *Eco*-PRAI:InGPS was then added. Immediately after *Eco*-PRAI:InGPS addition, the complete loss of both PRA anomers (Section 3.4.1) was observed with concurrent formation of peaks corresponding to the expected InGP product (Figure 3.11). With a rate similar to PRA, 4F-PRA was also turned over by *Eco*-PRAI:InGPS, with the appearance of peaks consistent with those expected for 4F-InGP.

As expected, in experiments with sulfonyl-PRA, the PRAI:InGPS-catalysed reaction did not proceed to form an indole-containing compound. However, a small decrease in the intensity of the sulfonyl-PRA peaks was observed (Figure 3.12D) as well as the appearance of new peaks in the aromatic and ribose regions of the spectra, though the latter were highly overlapped. These new peaks may correspond to the formation of sulfonyl-CDRP from sulfonyl-PRA, however, no further analysis was performed to confirm this.

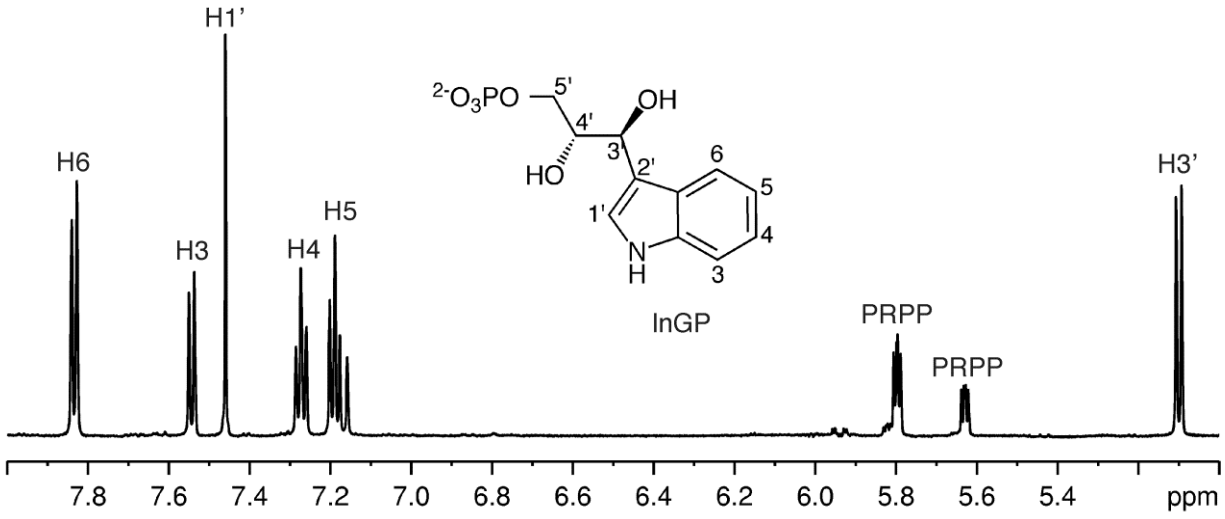

Figure 3.11 ^{1}H NMR spectrum of InGP. PRA was formed by the incubation of anthranilate (1 mM) and PRPP (2.5 mM) with *Mtu*-AnPRT (0.8 µM). Addition of *Eco*-PRAI:InGPS (2.5 µM) and incubation at 25 °C for approximately 10 min resulted in complete conversion to InGP. δ 7.83 (d, 8 Hz, H6), 7.54 (d, 8.2 Hz, H3), 7.46 (s, H1'), 7.27 (dd, 7.6 Hz, H4), 7.19 (dd, 7.5 Hz, H5), 5.10 (d, 8.2 Hz, H3'). Figure extracted from Cookson *et al.* Supplementary Material.[51]

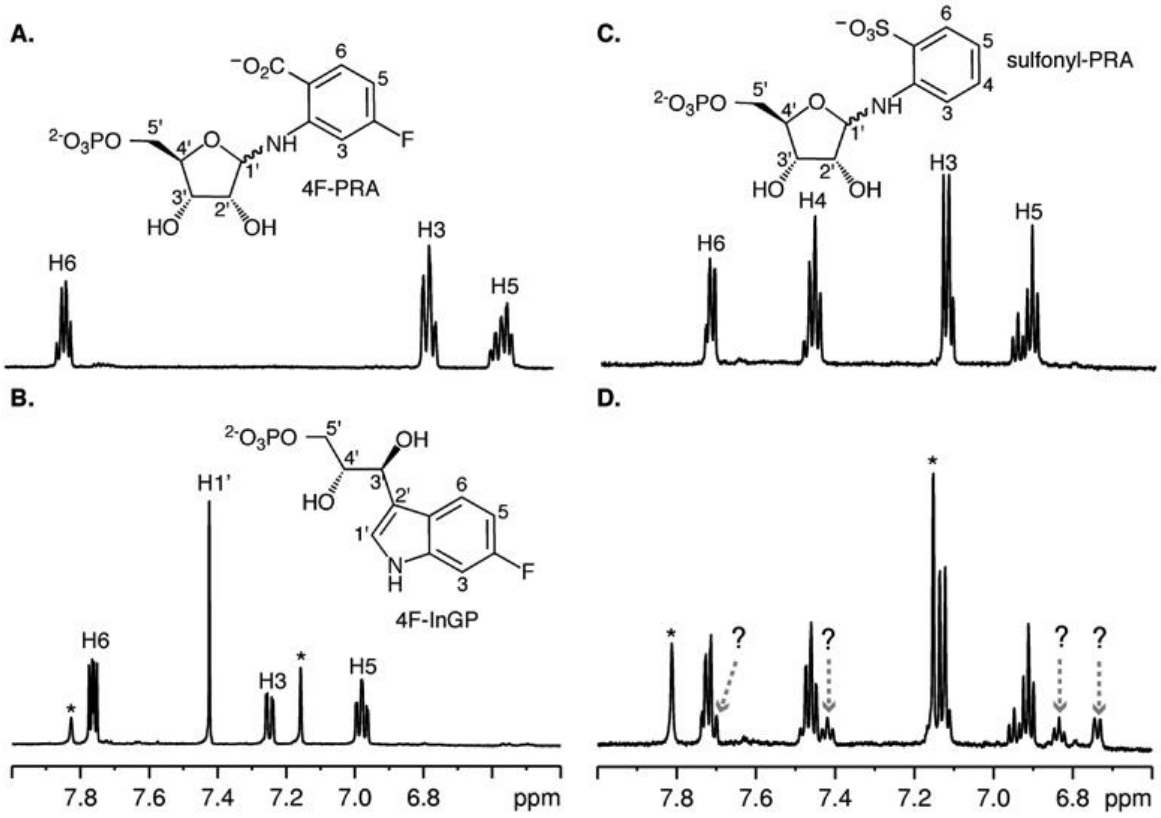

Figure 3.12 ^{1}H NMR spectra for the *Eco*-PRAI:InGPS-catalysed reaction of 4-fluoro-PRA (4F-PRA) and sulfonyl-PRA. A) 4F-PRA was formed by the incubation of 4FA (1 mM) and PRPP (2.5 mM) with *Mtu*-AnPRT (0.8 µM). B) Addition of Eco-PRAI:InGPS (2.5 µM) to this 4F-PRA sample resulted in complete conversion to 4F-InGP. δ 7.76 (dd, 5.5, 8.8 Hz, H6), 7.42 (s, H1'), 7.25 (dd, 10.1, 2.2 Hz, H3), 6.98 (ddd, 2.2, 9.4 Hz, H5), 5.06 (d, 8.2 Hz, H3') C) Sulfonyl-PRA was formed by the incubation of orthanilate (0.5 mM) and PRPP (2.5 mM) with *Mtu*-AnPRT (0.8 µM). D) Addition of *Eco*-PRAI:InGPS (2.5 µM) to this sulfonyl-PRA sample resulted in the production of a new set of minor resonances as indicates by the dashed arrows (δ 7.70, 7.42, 6.84 and 6.74 ppm), possibly corresponding to the CdRP analogue, 1-(o-sulfonylphenylamino)-1-deoxyribulose 5-phosphate. Samples were incubated at 25 °C for approximately 10 min following the addition of each enzyme. Peaks marked by an asterisk result from an imidazole impurity present in the PRAI:InGPS preparation used for these experiments. Figure extracted from Cookson *et al.* Supplementary Material.[51]

3.6 Crystal Structures of Alternate Anthranilate-like Substrates Bound to *Mtu*-AnPRT

Structures of *Mtu*-AnPRT with PRPP, Mg^{2+} and either the fluoro- or methyl-anthranilates bound were obtained by Dr Alina Castell at the School of Biological Sciences, University of Auckland. These structures provide further insight into both the ligand binding order and potential catalytic mechanism of *Mtu*-AnPRT, and are discussed and interpreted in this section. Unfortunately, not all of these structures were completely refined at the time of writing this thesis, and as such only complete structures will be discussed.

Crystals of *Mtu*-AnPRT were formed in the presence of PRPP and Mg^{2+}, and prior to structure collection were soaked in solutions of fluoro-/methyl-anthranilate for various lengths of time. Two structures were obtained from crystals soaked in 4FA, with one exposed to a 6 s soak time, and the other exposed to a 6 min soak time.

The 4FA 6 min structure (PDB ID: 4N5V) shows two 4FA molecules bound to each monomer, with one bound in the inner site and the other bound in the outer site (Figure 3.13A). This outer site has previously been identified by inhibitor binding (Section 2.7), but has not been observed in structures of *Sso*-AnPRT. [42, 50] The inner site 4FA molecule makes hydrogen bonds via its amino group to G107 and the PRPP C2 hydroxyl, with the carboxylate group hydrogen bonded to N138, R193 and four water molecules (Figure 3.13B and C). The binding mode of the inner site 4FA molecule places its amino group 4.2 Å from the C1 atom of PRPP, in a favourable orientation for nucleophilic attack on PRPP from the β position. The 4FA molecule bound in the outer site makes hydrogen bonds to R194 and three water molecules with its carboxylate group, with the amino group hydrogen bonded to H183 (Figure 3.13B and D). The aromatic ring of the outer site 4FA is also stacked parallel with the proline ring of P180, forming likely C-H···π interactions.

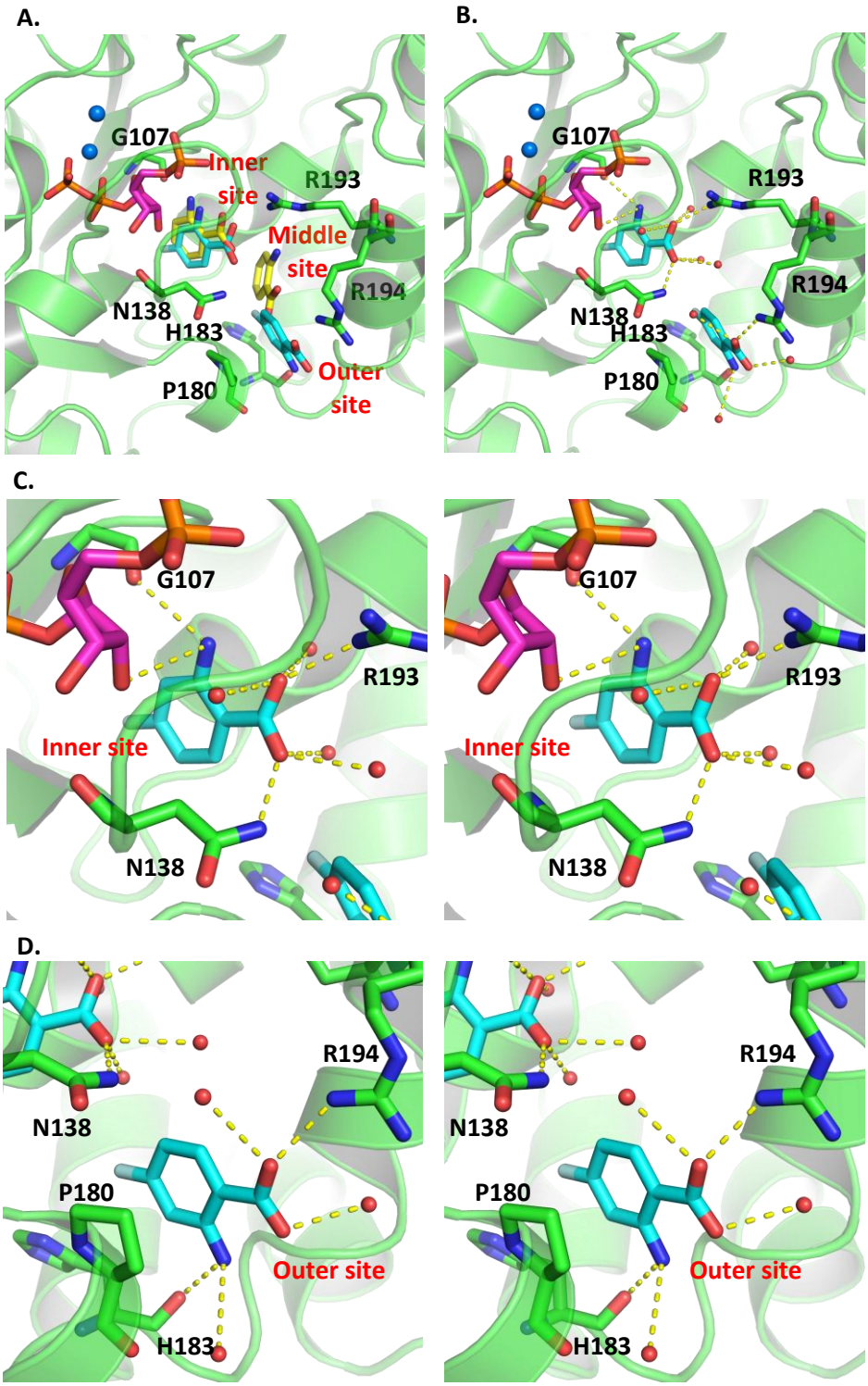

Figure 3.13 Chain A of the 4FA 6 min *Mtu*-AnPRT structure showing the 4FA binding sites. Analogous binding is observed for chain B. A) An overlay of *Sso*-AnPRT with PRPP, Mg^{2+} and anthranilate (yellow) bound with *Mtu*-AnPRT chain A (green) with PRPP (magenta), Mg^{2+} (blue spheres) and 4FA (cyan) bound. B) *Mtu*-AnPRT chain A (green) with PRPP (magenta), Mg^{2+} (blue spheres) and 4FA (cyan) bound. Polar contacts of 4FA are shown as yellow dashes. C) Stereo diagram of 4FA bound to the inner site. D) Stereo diagram of 4FA bound to the outer site.

A comparison of the 4FA molecules bound at each site highlights the positioning of the amino group; in order for the 4FA compound bound at the outer site to progress to the inner site and emulate the same binding mode, the aromatic ring of 4FA would have to flip 180°. However, the position of the fluorine group on 4FA could be forcing the amino group to point towards H183 in order to minimise steric clashes with the surrounding protein.

The structure of *Mtu*-AnPRT with PRPP, Mg^{2+} and 6MA bound (PDB ID: 4N93), obtained from a 30 min soak of 6MA, shows two 6MA molecules bound to each monomer (Figure 3.14). The 6MA molecule bound in the inner site makes hydrogen bond contacts to R193, N138 and three water molecules via its carboxylate group, with the amino group hydrogen bonded to G107 only, showing a similar binding mode to 4FA. The 6MA molecule bound in the outer site is hydrogen bonded to R194, H183 and a water molecule. Inspection of the F_o-F_c map of the 6MA structure reveals a potential third binding site between the inner and outer sites, which would be analogous to the middle site observed for the *Sso*-AnPRT structures (Figure 3.14B).[42, 50] This density indicates a possible mode of passage of 6MA through the anthranilate channel, from the outer site through the middle site to the inner site.

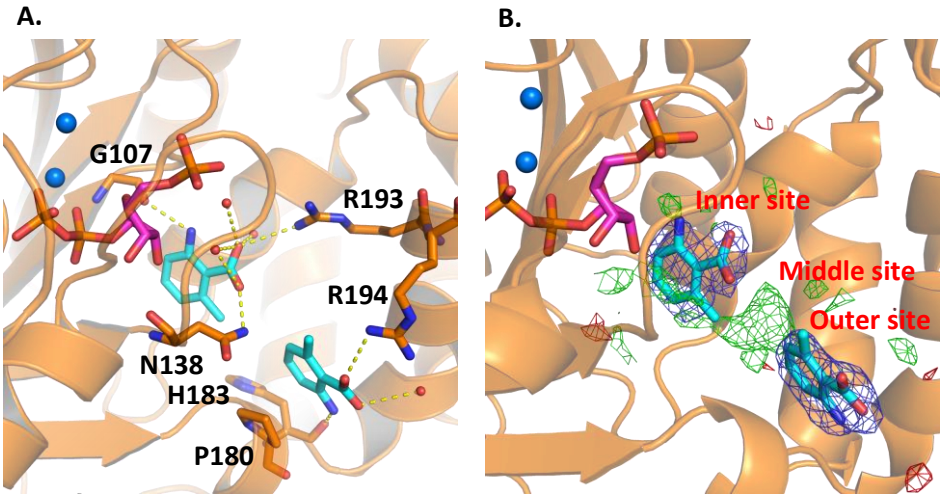

Figure 3.14 Chain B of the 6MA 30 min *Mtu*-AnPRT structure showing the 6MA binding sites. Analogous binding is observed for chain A. A) *Mtu*-AnPRT chain B (orange) with PRPP (magenta), Mg^{2+} (blue spheres) and 6MA (cyan) bound. Polar contacts of 6MA are shown as yellow dashes. B) *Mtu*-AnPRT chain B (orange) with PRPP (magenta), Mg^{2+} and 6MA (cyan) bound. The $2F_o$-F_c map for both 6MA ligands are shown as blue mesh, contoured at 1.0 σ. The F_o-F_c map is shown as green mesh, contoured at 3.0 σ.

The 4FA 6 s structure (PDB ID: 4N8Q) shows only one 4FA molecule bound to each monomer, without PRPP or Mg^{2+} bound. The analogue is bound in the outer site, and makes similar contacts to N138, H183 and R194 as described for the 4FA 6 min soak (Figure 3.15A). The β2-α6 loop, which has previously been observed to close over the PRPP binding site once PRPP has bound,[44] is folded into the anthranilate channel (Figure 3.15B), which perhaps prevents the 4FA molecule from advancing further along the channel. This structure raises the possibility that PRPP is not the first ligand to bind to the *Mtu*-AnPRT enzyme, and that anthranilate binding at the outer site could precede PRPP and Mg^{2+} binding.

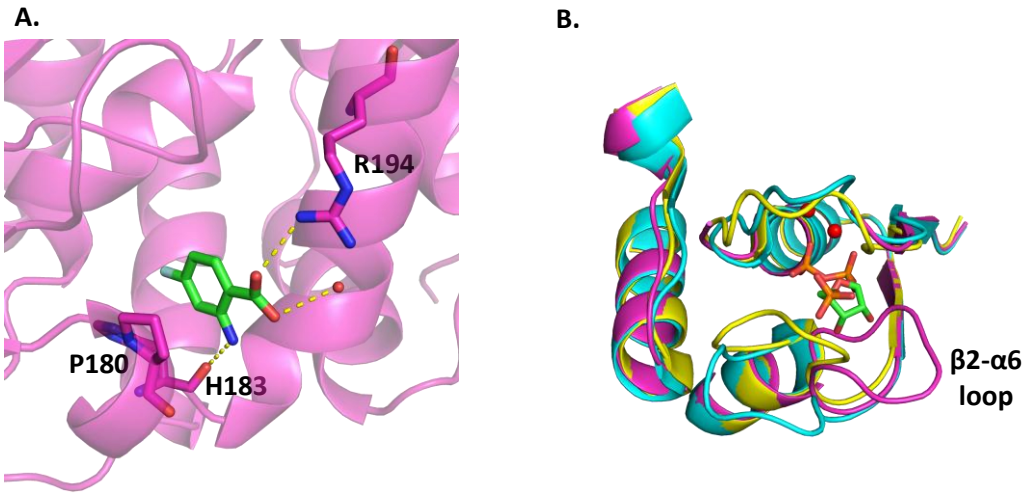

Figure 3.15 Chain B of the 4FA 6 s *Mtu*-AnPRT structure. Analogous binding and structural features are observed for chain A. A) *Mtu*-AnPRT (magenta) with 4FA (green) bound in the outer site. B) An overlay of *Mtu*-AnPRT with 4FA bound (magenta), *Mtu*-AnPRT with PRPP (green) and Mg^{2+} (red spheres) bound (yellow) and *apo Mtu*-AnPRT (cyan) depicting the differing β2-α6 loop positions.

3.7 Summary

Kinetic characterisation of *Mtu*-AnPRT with alternate anthranilate substrates was carried out using a commercially available PP_i assay. The apparent K_M value and k_{cat} values for the natural substrate anthranilate were determined as 1.7 ± 0.1 μM and 2.0 ± 0.1 s^{-1} respectively, comparing well to the values obtained in Chapter 2 (Section 2.5.1). Alternate substrates employing fluoro- or methyl-substitutions to the anthranilate aromatic ring were accepted as substrates for *Mtu*-AnPRT, as well as ACS130 which substituted the carboxylate group for a sulfonyl group. Compounds involving methoxy-substitutions or repositioning of the anthranilate amine group to C3 or C4 did not act as substrates for *Mtu*-AnPRT.

Fluoro-substitution around the aromatic ring of anthranilate had the least effect on the reaction kinetics of *Mtu*-AnPRT, with apparent K_M values ranging from 1.4 – 31 μM and k_{cat} values ranging from 1.2 – 1.4 s^{-1}. These results contrast significantly with those obtained for the methyl-substituted substrates, with higher K_M values ranging from 290 – 800 μM and lower k_{cat} values ranging from 0.15 – 0.63 s^{-1} demonstrating a dramatic decrease in *Mtu*-AnPRT tolerance for the sterically larger methyl moiety. ACS130 displayed an increased binding affinity (K_M = 130 ± 11 μM) compared to the methyl-substituted analogues, but had the lowest overall k_{cat} value of 0.1 ± 0.004 s^{-1}, highlighting the importance of the anthranilate carboxylate group for *Mtu*-AnPRT catalysis. High concentrations of the fluoro-substituted analogues caused *Mtu*-AnPRT inhibition similar to that observed for anthranilate, with K_i values ranging from 34 – 1090 μM.

Characterisation of PRA-substituted products resulting from successful *Mtu*-AnPRT catalysis of the anthranilate analogues was performed using mass spectrometry and NMR, and showed the appearance of both α and β PRA anomers in solution. Selective reduction of the suspected PRA imine species formed during anomer interconversion and subsequent mass spectrometry analysis confirmed this anomerisation mechanism.

The ability of *Eco*-PRAI:InGPS to catalyse the PRA-substituted products arising from *Mtu*-AnPRT catalysis of anthranilate analogues was investigated using the enzyme-coupled assay, mass spectrometry and NMR. Clear evidence of catalysis was observed for all substrates tested with the exception of 3MA and ACS130.

Structures of *Mtu*-AnPRT co-crystallised with PRPP, Mg^{2+} and various anthranilate analogues were obtained by Dr Alina Castell. 4FA and 6MA were seen to bind in both the inner and outer sites, with binding in the inner site replicating the previously predicted binding mode for anthranilate in *Mtu*-AnPRT[44] and which had been directly observed in *Sso*-AnPRT.[42, 50]

Chapter 4

Variants of *Mtu*-AnPRT

4.1 Overview

The first part of this chapter describes the generation of *Mtu*-AnPRT variant proteins containing point mutations of identified key residues. Mutated plasmids were synthesised using PCR, confirmed via sequencing, and successfully transformed into *E. coli* cells. Subsequent purification of the variant proteins was achieved, and physical characterisation utilising mass spectrometry, CD and DSF revealed that all variants displayed similar physical attributes to the wild-type *Mtu*-AnPRT.

Kinetic characterisation of the variants was carried out using the enzyme-coupled assay described in Chapter 2. Anthranilate inhibition was also investigated.

Finally, crystal structures of the variants in the presence of various combinations of the natural ligands PRPP, Mg^{2+} and anthranilate are described in detail.

4.2 Introduction

Prior to this study, a structure-based sequence alignment of AnPRT enzymes from *M. tuberculosis, S. solfataricus, P. carotovorum* and *T. thermophilus* was performed and used to create a multiple sequence alignment from a diverse range of bacteria - *Clostridium acetobutylicum*, *Staphylococcus aureus*, *Brucella melitensis* and *Agrobacterium tumefaciens*.[44] This alignment demonstrated the existence of several conserved sequence motifs that have since been shown to be involved in the binding of one or both substrates: including a GTGGD sequence (residues 107-111 – numbered for *Mtu* enzyme) located on the β1-α5 loop involved in PRPP binding, a ψψKHGN anthranilate binding motif (residues 133-138, where ψ stands for a hydrophobic amino acid) located on the β2-α6 loop, a conserved A179 residue located on the α8' helix and a conserved R193 residue located on the α8 helix associated with anthranilate binding.

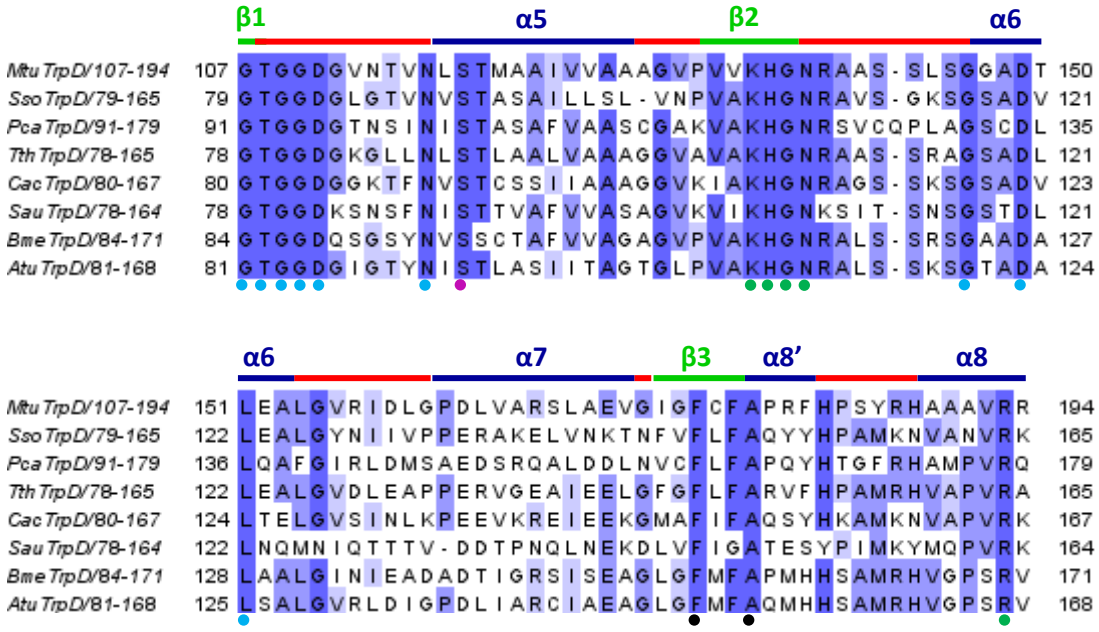

Figure 4.1 A partial sequence alignment of AnPRT enzymes from *M. tuberculosis* (*Mtu*), *S. solfataricus* (*Sso*), *P. carotovorum* (*Pca*), *T. thermophilus* (*Tth*), *C. acetobutylicum* (*Cac*), *S. aureus* (*Sau*), *B. melitensis* (*Bme*) and *A. tumefaciens* (*Atu*) recreated from Lee *et al.*[44] using TCOFFEE:Advance.[48] The diagram was made using Jalview.[49] Dots indicate residues involved with PRPP binding (blue), anthranilate binding (green) and Mg^{2+} binding (purple). Black dots indicate residues that appear to be conserved for structural reasons. Blue solid lines denote α helices, green solid lines indicate β strands and red solid lines indicate loop regions.

The crystal structure of *Sso*-AnPRT in the presence of PRPP, Mg^{2+} and anthranilate (PDB ID: 1ZYK) gave further insight into the roles of the aforementioned conserved residues in substrate binding. In

particular, the presence of two anthranilate molecules bound in the active site was surprising, as this had not been shown in a crystal structure of AnPRT previously.

In the *Sso*-AnPRT structure, the anthranilate molecules are associated with the N-terminal helical domain, with one ligand bound in an inner site and another bound in a 'middle' site, located between the inner site and the outer site discussed in Sections 2.7 and 3.6 (Figure 4.2). The anthranilate bound in the inner site creates hydrogen bonds with G79, N109, and several water molecules (numbered for the *Sso* enzyme). The carboxylate group of this anthranilate interacts with N109, with its amino group pointing towards the bound PRPP molecule and held in place by the backbone carbonyl of G79. The carboxylate group of the anthranilate bound in the middle site interacts with the protein residues R164 and N109, while the amino group interacts with a water molecule.

Several variants of the *Sso*-AnPRT enzyme were synthesised prior to this study to probe the catalytic relevance of certain conserved residues involved with substrate binding, namely K106, H107, D223, E224, R164, H154 and P178 (all mutated to alanine residues).[42] Conclusions drawn from studies of these variants state the importance of R164 alone for anthranilate binding, with R164A and K106A slightly influencing the rate of catalysis.

4.3 Residues Mutated

The residues selected for mutagenesis in *Mtu*-AnPRT were based on the sequence and structural information as well as mutations characterised from the *Sso*-AnPRT enzyme (Section 4.2). The discovery of a third potential binding site for anthranilate (Sections 2.7 and 3.6) highlighted some additional key binding residues which were also taken into consideration.

The residue G107 was chosen for its involvement in the binding of both the PP_i group of PRPP and the amino moiety of the inner catalytic anthranilate site, with the latter seen in the *Sso*-AnPRT structure[42] as the equivalent residue G79. It is also part of the conserved GTGGD motif located in the flexible β1-α5 loop which closes over the PRPP molecule after it has bound. The mutation chosen for this study is G107P, to investigate the effect on substrate binding after the flexibility of that loop has been decreased.

N138 forms part of the conserved KHGN motif on the β2-α6 loop and is another residue that binds both substrates in *Mtu*-AnPRT – the carboxylate group of anthranilate (bound in the inner site) via its side-chain nitrogen, and the PRPP C3 hydroxyl via its backbone oxygen. The equivalent residue in *Sso*-AnPRT is N109. The mutation chosen is N138A, where complete removal of the side-chain will determine if it is necessary for binding and/or catalysis.

P180 is adjacent to the conserved residue A179 as part of the α8' helix, which is located at the entrance to the anthranilate channel. The equivalent residue from the *Sso*-AnPRT enzyme is Q151. Structures of *Mtu*-AnPRT co-crystallised with inhibitors (Section 2.7) and anthranilate analogues (Section 3.6) implicate this residue in anthranilate binding at the entrance of the anthranilate channel (outer site). The mutation P180A was chosen to investigate whether removing the rigidity of the α8' helix would have any effect on the protein's structure, and will also determine the necessity of this non-conserved residue for anthranilate recruitment.

R194 is also located at the entrance to the anthranilate channel and is adjacent to the conserved R193 residue on the α8 helix. Like P180, this residue has also been implicated in anthranilate binding at the outer site and likely binds the anthranilate carboxylate group. *Sso*-AnPRT has a lysine residue (K165) present at this position. Mutating this non-conserved arginine to an alanine (R194A) will determine how crucial this residue is for anthranilate recruitment, with the additional effect of altering the overall charge of the outer site environment.

The final residue chosen for mutation is R193, a conserved residue highly involved in anthranilate binding in both the inner site and the middle site. Studies on the *Sso*-AnPRT variant R164A

(equivalent to R193 in *Mtu*-AnPRT), have previously shown this residue to be important for both anthranilate binding and reaction catalysis,[42] and structures of wild-type *Sso*-AnPRT with PRPP and anthranilate bound show the formation of a salt bridge between the R164 guanidinium moiety and the inner site anthranilate carboxylate group in some protein chains.[42] Two mutations have been chosen for this residue: R193A and R193L. R193A was selected in order to investigate the effect of completely removing the side-chain, and additionally altering the overall charge of the environment. R193L, however, will retain most of the structure of the side-chain with the functionality removed, again altering the overall charge of the environment.

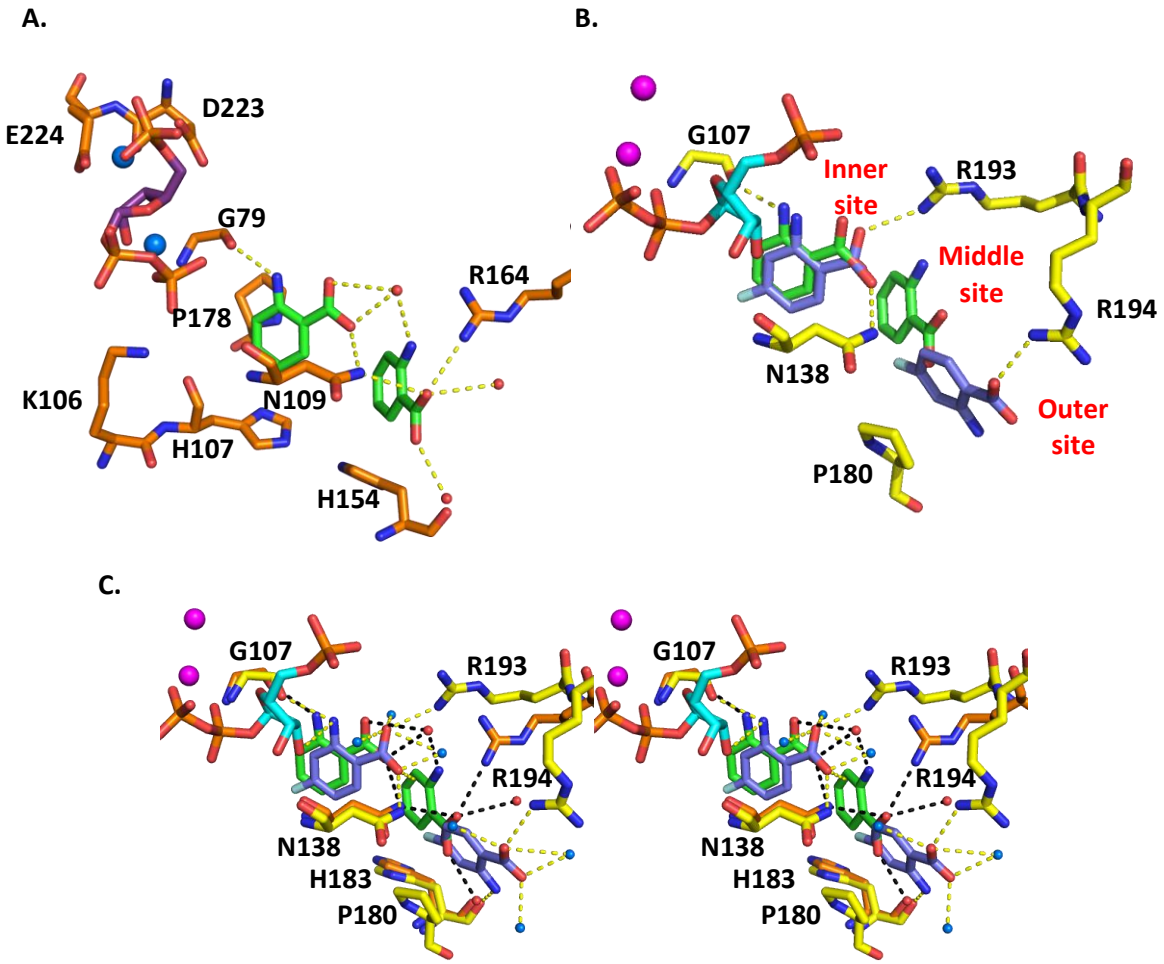

Figure 4.2 Potential *Mtu*-AnPRT anthranilate binding sites. A) *Sso*-AnPRT chain C (orange) with PRPP (purple), Mg^{2+} (blue spheres) and anthranilate (green) bound. Polar contacts for anthranilate are shown as yellow dashes, with black text indicating *Sso*-AnPRT residues. B) An overlay of *Mtu*-AnPRT (yellow) with PRPP (cyan), 4FA (purple) and Mg^{2+} (magenta spheres) bound with *Sso*-AnPRT (not shown) with PRPP (not shown), Mg^{2+} (not shown) and anthranilate (green) bound. Anthranilate binding sites are indicated by red text. Polar contacts between *Mtu*-AnPRT and the 4FA molecules are indicated by yellow dashes. C) Stereo diagram of *Sso*-AnPRT chain C (orange) with PRPP (not shown), Mg^{2+} (not shown) and anthranilate (green) bound overlaid with Mtu-AnPRT with PRPP (cyan) Mg^{2+} (magenta spheres) and 4FA (purple) bound. Polar contacts for anthranilate are shown as black dashes, with polar contacts for 4FA shown as yellow dashes. Water molecules from *Sso*-AnPRT are shown as red spheres, with *Mtu*-AnPRT water molecules as blue spheres. Black text indicates *Mtu*-AnPRT residue numbers.

4.4 Protein Isolation

4.4.1 Preparation of Mutant Plasmids

In order to form TrpD plasmids containing the required mutations, PCR reactions were carried out using the conditions outlined in Section 7.4.2. Mutant plasmids formed as a result of the PCR reaction were visualised using agarose gels (Figure 4.3).

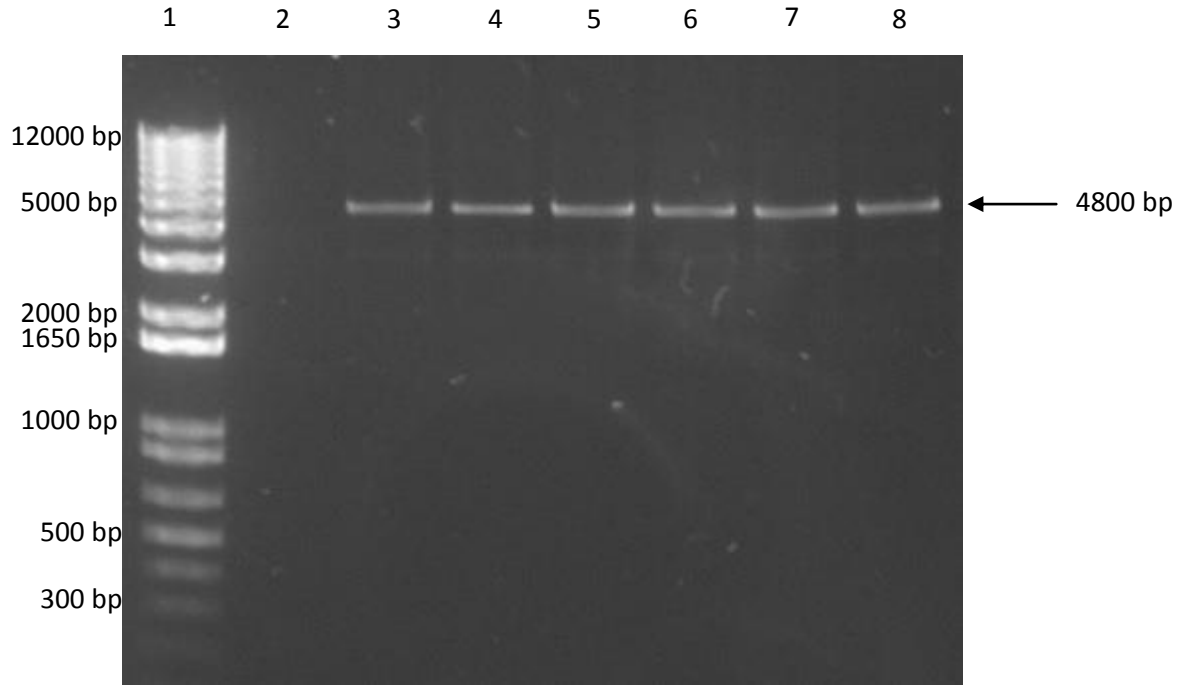

Figure 4.3 Agarose gel of TrpD mutant PCR products. Lane 1 contains the DNA ladder, with base pair sizes defined to the left. Lane 3 – R194A. Lane 4 – R193A. Lane 5 – R193L. Lane 6 – P180A. Lane 7 – N138A. Lane 8 – G107P. Lane 2 is empty.

4.4.2 Transformation

Each mutant plasmid was transformed as outlined in Section 7.1.7 into both One Shot® Top10 chemically competent *E. coli* cells and *E. coli* BL21 (DE3) pBB528/pBB541 cells. The transformed cells were then left to grow on LB/agar media overnight. Successful colony growth was observed for all six *Mtu*-AnPRT mutants, and 5 mL LB media cultures containing ampicillin were inoculated and left to grow overnight at 37 °C in a shaking incubator. Glycerol stocks of each mutant in both cell lines were made and snap frozen with liquid N_2 for storage at -80 °C.

4.4.3 Protein Expression and Purification

After verification of successful gene mutations via sequencing, the variant proteins were expressed and purified exactly as described for wild-type *Mtu*-AnPRT. Samples of each pure *Mtu*-AnPRT variant were analysed via an SDS-PAGE gel, as depicted in Figure 4.4. These variant proteins will be referred to by their mutation: *Mtu*-N138A, *Mtu*-P180A, *Mtu*-G107P, *Mtu*-R194A, *Mtu*-R193A and *Mtu*-R193L.

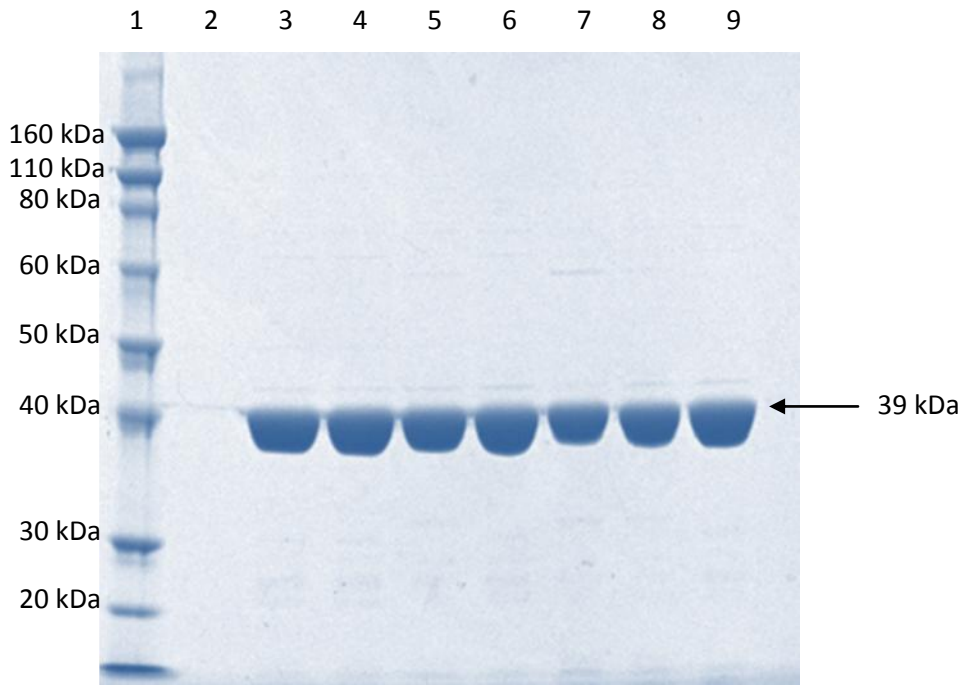

Figure 4.4 SDS-PAGE gel of purified wild-type/variant *Mtu*-AnPRTs. Lane 1 contains the protein ladder, with molecular weights defined to the left. Lane 3 – wild-type *Mtu*-AnPRT. Lane 4 – *Mtu*-R194A. Lane 5 – *Mtu*-R193A. Lane 6 – *Mtu*-R193L. Lane 7 – *Mtu*-P180A. Lane 8 – *Mtu*-N138A. Lane 9 – *Mtu*-G107P. Lane 2 is empty.

4.5 Physical Characterisation

4.5.1 Secondary Structure

To determine whether the *Mtu*-AnPRT variant proteins had folded correctly, a CD spectrum was obtained for each variant and compared to the wild-type *Mtu*-AnPRT spectrum (Figure 4.5).

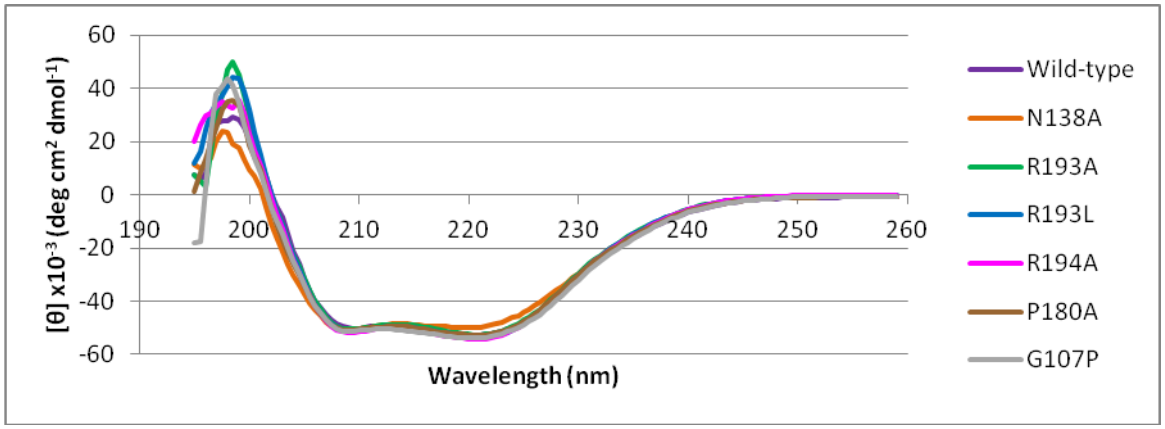

Figure 4.5 CD spectra of wild-type/variant *Mtu*-AnPRTs. Solutions contained 0.03 mg/mL enzyme in 20 mM sodium phosphate buffer (pH 8.0).

An inspection of the CD spectra for both wild-type and variant *Mtu*-AnPRTs illustrates a clear similarity between the proteins, and thus that the mutations to *Mtu*-AnPRT have not introduced significant changes to the secondary structure.

4.5.2 Molecular Mass

The masses of the *Mtu*-AnPRT variant proteins were obtained via mass spectrometry under the same conditions as wild-type *Mtu*-AnPRT (Table 4.1). All masses obtained were similar to the values predicted by the website tool ProtParam.[62]

Mtu-AnPRT variant	Expected Mass (Da)	Observed Mass (Da)
R193A	38588.6	38587.5
R193L	38630.7	38628.9
R194A	38588.6	38587.5
P180A	38647.7	38646.6
N138A	38630.7	38629.5
G107P	38713.8	38712.9

Table 4.1 Masses of *Mtu*-AnPRT variants as obtained via mass spectrometry.

4.5.3 Thermal Stability

The temperature of denaturation for the *Mtu*-AnPRT variants was determined via DSF using the same protocol outlined for wild-type *Mtu*-AnPRT (Figure 4.6, Table 4.2). Raw data from DSF scans can be observed in Appendix 1. *Mtu*-N138A and *Mtu*-R194A had denaturation temperatures most similar to that of wild-type enzyme, demonstrating that while these residues may be important for substrate capture (Section 3.6) they have no impact on the thermal stability of the protein. Mutations to the residue R193, however, show a surprising increase in the denaturation temperature of approximately 10 °C. *Mtu*-P180A and *Mtu*-G107P show a decrease in the denaturation temperature of 4 °C and 9 °C respectively. For *Mtu*-P180A, this decrease is perhaps unsurprising given the substitution of the conformationally restricted proline ring for the relatively unrestricted methyl moiety of alanine, although this reasoning does not explain why the introduction of a proline group in *Mtu*-G107P should also cause a decrease in the denaturation temperature.

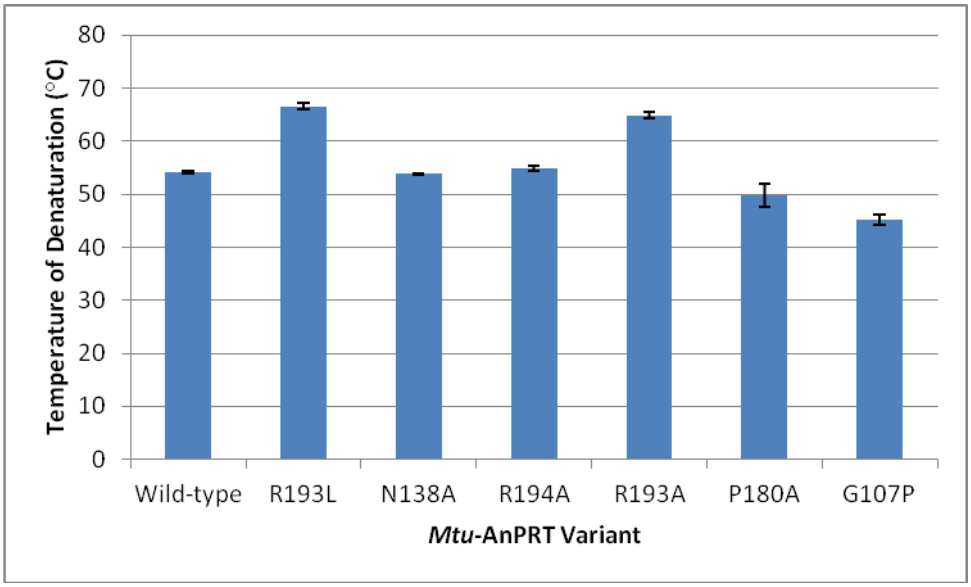

Figure 4.6 DSF denaturation temperatures of wild-type/variant *Mtu*-AnPRTs. Enzymes were analysed in Tris.HCl buffer (pH 8.0), at concentrations of 1 mg/mL.

Mtu-AnPRT	Temperature of Denaturation (°C)
Wild-type	54.1 ± 0.3
R193L	66.5 ± 0.6
N138A	53.8 ± 0.2
R194A	54.7 ± 0.5
R193A	64.9 ± 0.6
P180A	50 ± 2
G107P	45 ± 1

Table 4.2 DSF denaturation temperatures of wild-type/variant *Mtu*-AnPRTs.

4.6 Kinetic Characterisation

4.6.1 Michaelis-Menten Kinetics

Using the enzyme-coupled assay as outlined in Section 7.1.24/7.4.4, the turnover number and apparent K_M values were found for all variants of *Mtu*-AnPRT (Figure 4.7, Table 4.3) with the exception of *Mtu*-G107P, which was catalytically inactive. The apparent K_M values for PRPP for the variants are comparable to the wild-type value of 48 ± 2 μM, with the exception of *Mtu*-N138A, which has an increased K_M value of 160 ± 20 μM. As N138 is observed to hydrogen bond to the C3 hydroxyl of PRPP via its backbone oxygen,[44] it is possible that the introduction of alanine causes increased flexibility of this region, located at the C-terminal end of the β2 sheet. *Mtu*-N138A also displays a 5-fold increase in the apparent K_M of anthranilate and a 50% decrease in the k_{cat} value, indicating a role for this residue in both anthranilate binding and catalysis.

Mutations to the residue R193 have the greatest impact on the apparent K_M of anthranilate, with a 240- and 150-fold increase observed for *Mtu*-R193A and *Mtu*-R193L respectively. *Mtu*-R193A and *Mtu*-R193L also have the largest effect on the turnover number, with a 25- and 54-fold decrease observed respectively, indicating that residue R193 is not only crucial for anthranilate binding but also for catalysis between anthranilate and PRPP. Similar results have been observed for the equivalent *Mtu*-R193A variant in *Sso*-AnPRT (*Sso*-R164A), with a 7000-fold increase in the apparent K_M value of anthranilate, and a 7-fold decrease in the turnover number.[42]

Mtu-AnPRT variant	K_M Anth (μM)	K_M PRPP (μM)	k_{cat} (s^{-1})	k_{cat}/K_M Anth ($\mu M^{-1}\ s^{-1}$)	k_{cat}/K_M PRPP ($\mu M^{-1}\ s^{-1}$)
Wild-type	2.0 ± 0.2	48 ± 2	1.9 ± 0.06	0.95 ± 0.13	0.04 ± 0.003
N138A	8.0 ± 0.6	160 ± 20	1.0 ± 0.02	0.13 ± 0.01	0.006 ± 0.0007
R193A	480 ± 24	40 ± 4	0.075 ± 0.002	0.0002 ± 0.00002	0.002 ± 0.0003
R193L	300 ± 18	48 ± 5	0.035 ± 0.001	0.0001 ± 0.000009	0.0007 ± 0.00009
P180A	4.0 ± 0.3	68 ± 5	1.7 ± 0.05	0.43 ± 0.045	0.025 ± 0.003
R194A	5.8 ± 0.4	46 ± 3	1.9 ± 0.05	0.33 ± 0.031	0.041 ± 0.0038
G107P	-	-	-	-	-

Table 4.3 Kinetic data for wild-type/variant *Mtu*-AnPRTs. (-) indicates that activity could not be detected above 0.001 s^{-1}.

A.

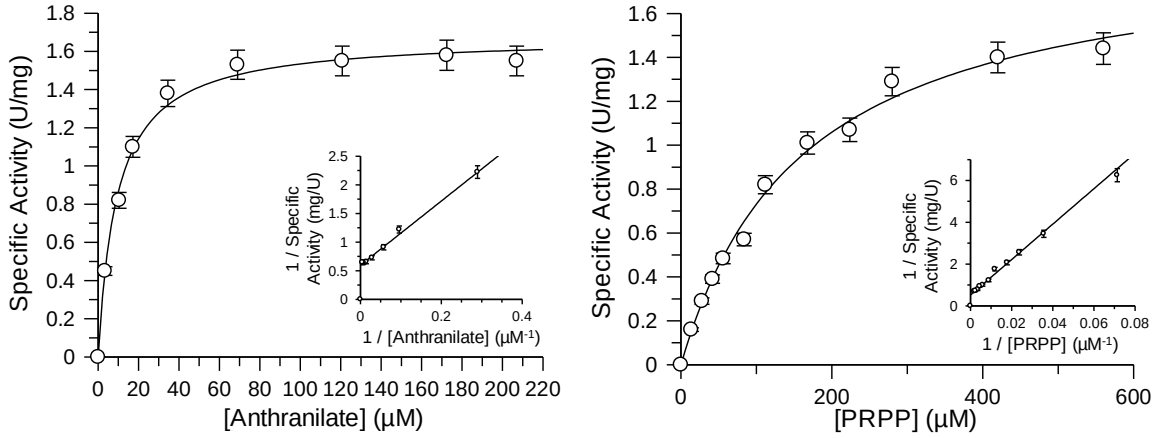
Specific Activity (U/mg)
[Anthranilate] (μM)
1 / Specific Activity (mg/U)
1 / [Anthranilate] (μM-1)
Specific Activity (U/mg)
[PRPP] (μM)
1 / Specific Activity (mg/U)
1 / [PRPP] (μM-1)

B.

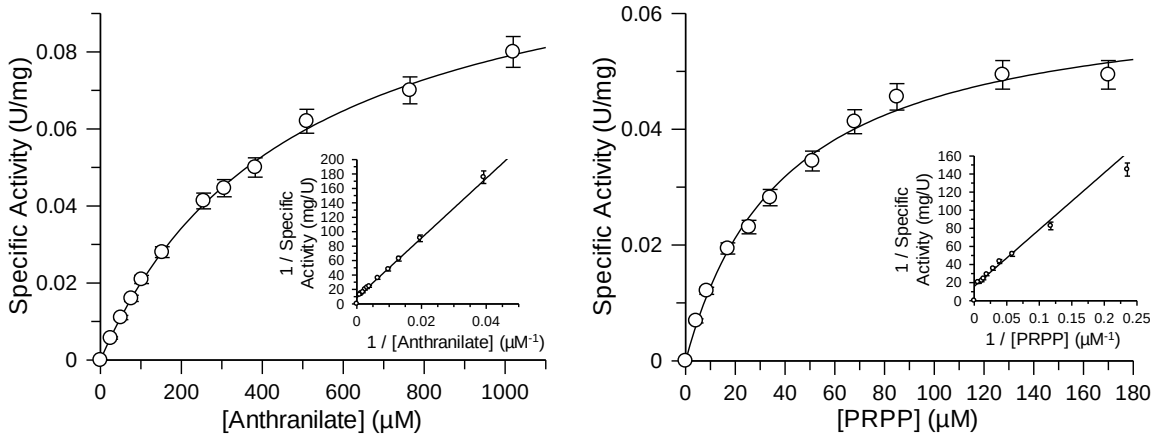
Specific Activity (U/mg)
[Anthranilate] (μM)
1 / Specific Activity (mg/U)
1 / [Anthranilate] (μM-1)
Specific Activity (U/mg)
[PRPP] (μM)
1 / Specific Activity (mg/U)
1 / [PRPP] (μM-1)

C.

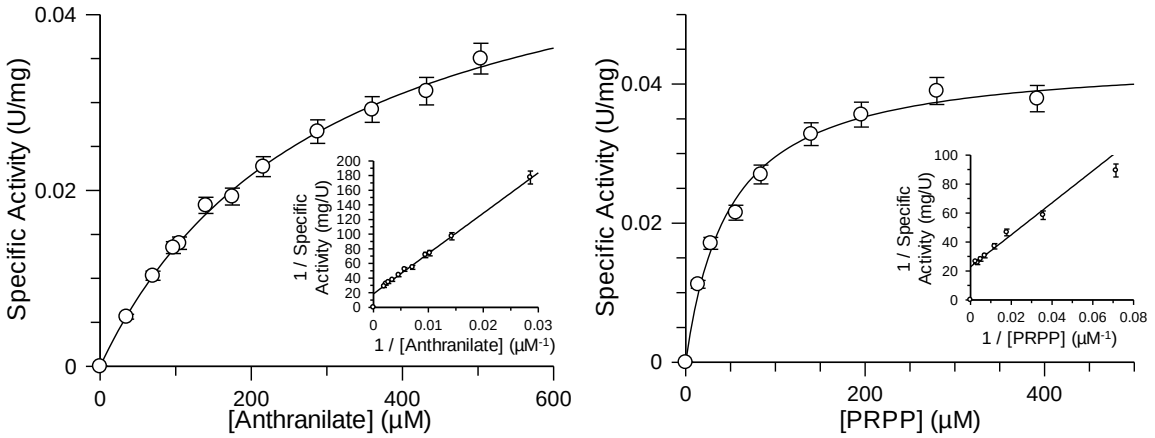
Specific Activity (U/mg)
[Anthranilate] (μM)
1 / Specific Activity (mg/U)
1 / [Anthranilate] (μM-1)
Specific Activity (U/mg)
[PRPP] (μM)
1 / Specific Activity (mg/U)
1 / [PRPP] (μM-1)

D.

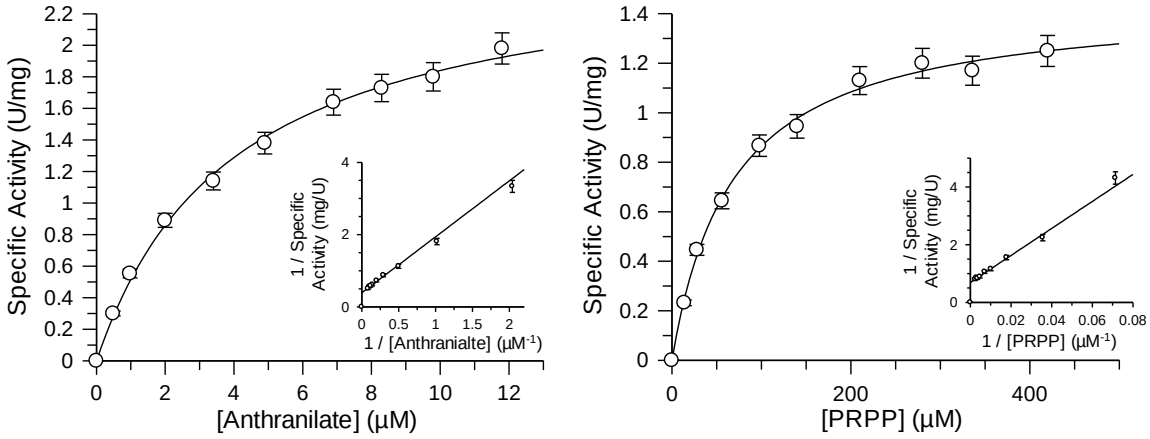

E.

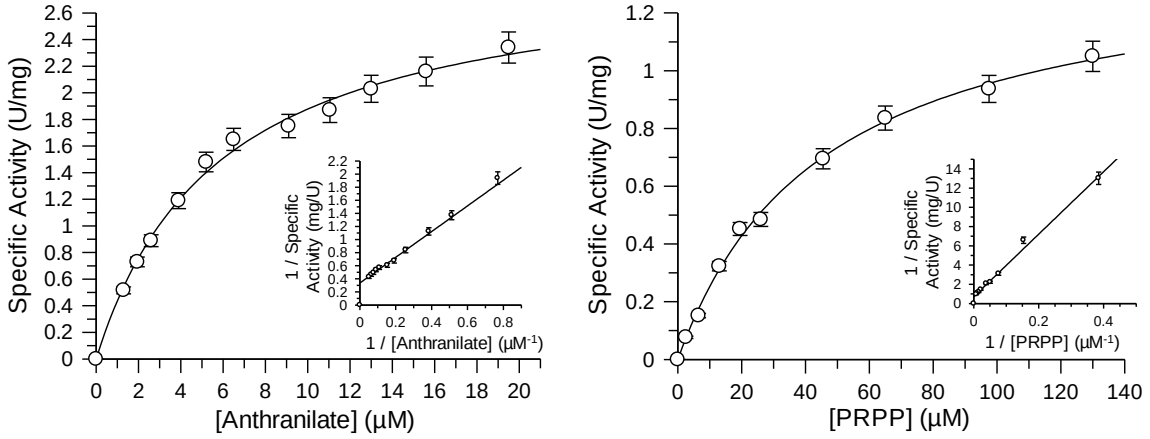

Figure 4.7 Michaelis-Menten plots for *Mtu*-AnPRT variants. Insets: Lineweaver-Burk plots. Solutions for analysis of the kinetic parameters of anthranilate contained PRPP held at a concentration of 0.6 mM, with all solutions incubated at 25 °C at pH 8.0. A) *Mtu*-N138A. Solutions for analysis of the kinetic parameters of PRPP contained anthranilate held at a concentration of 200 μM. B) *Mtu*-R193A. Solutions for analysis of the kinetic parameters of PRPP contained anthranilate held at a concentration of 200 μM. C) *Mtu*-R193L. Solutions for analysis of the kinetic parameters of PRPP contained anthranilate held at a concentration of 200 μM. D) *Mtu*-P180A. Solutions for analysis of the kinetic parameters of PRPP contained anthranilate held at a concentration of 25 μM. E) *Mtu*-R194A. Solutions for analysis of the kinetic parameters of PRPP contained anthranilate held at a concentration of 25 μM.

4.6.2 Anthranilate Inhibition

To investigate whether any of the residues mutated were involved in the mechanism of anthranilate inhibition, *Mtu*-N138A, *Mtu*-P180A and *Mtu*-R194A were tested with higher concentrations of anthranilate (0 – 220 μM) using the enzyme-coupled assay (Table 4.4, Figure 4.8). *Mtu*-R193A and

Mtu-R193L were not tested as their higher K_M values (Table 4.3) suggested that significantly higher concentrations of anthranilate would be required, thereby causing high absorbance readings that would impair accurate rate measurements. *Mtu*-P180A and *Mtu*-R194A both still demonstrated a capacity for anthranilate inhibition, though both showed a marked increase in K_i value of 9- and 2-fold respectively. Interestingly, *Mtu*-N138A showed no signs of inhibition up to 220 μM of anthranilate, indicating a clear role for the conserved N138 residue in *Mtu*-AnPRT anthranilate inhibition. All three variants tested showed weaker anthranilate inhibition, and N138, P180 and R194 have also been identified in Section 3.6 as residues involved with the binding of anthranilate analogues in the outer site. Thus it is highly likely that anthranilate binding at this outer site is instrumental for successful anthranilate inhibition.

Mtu-AnPRT variant	K_i value (μM)
Wild-type	47 ± 7
N138A	-
P180A	440 ± 110
R194A	89 ± 11

Table 4.4 K_i values for wild-type/variant *Mtu*-AnPRTs. (-) indicates that the variant was not subject to anthranilate inhibition.

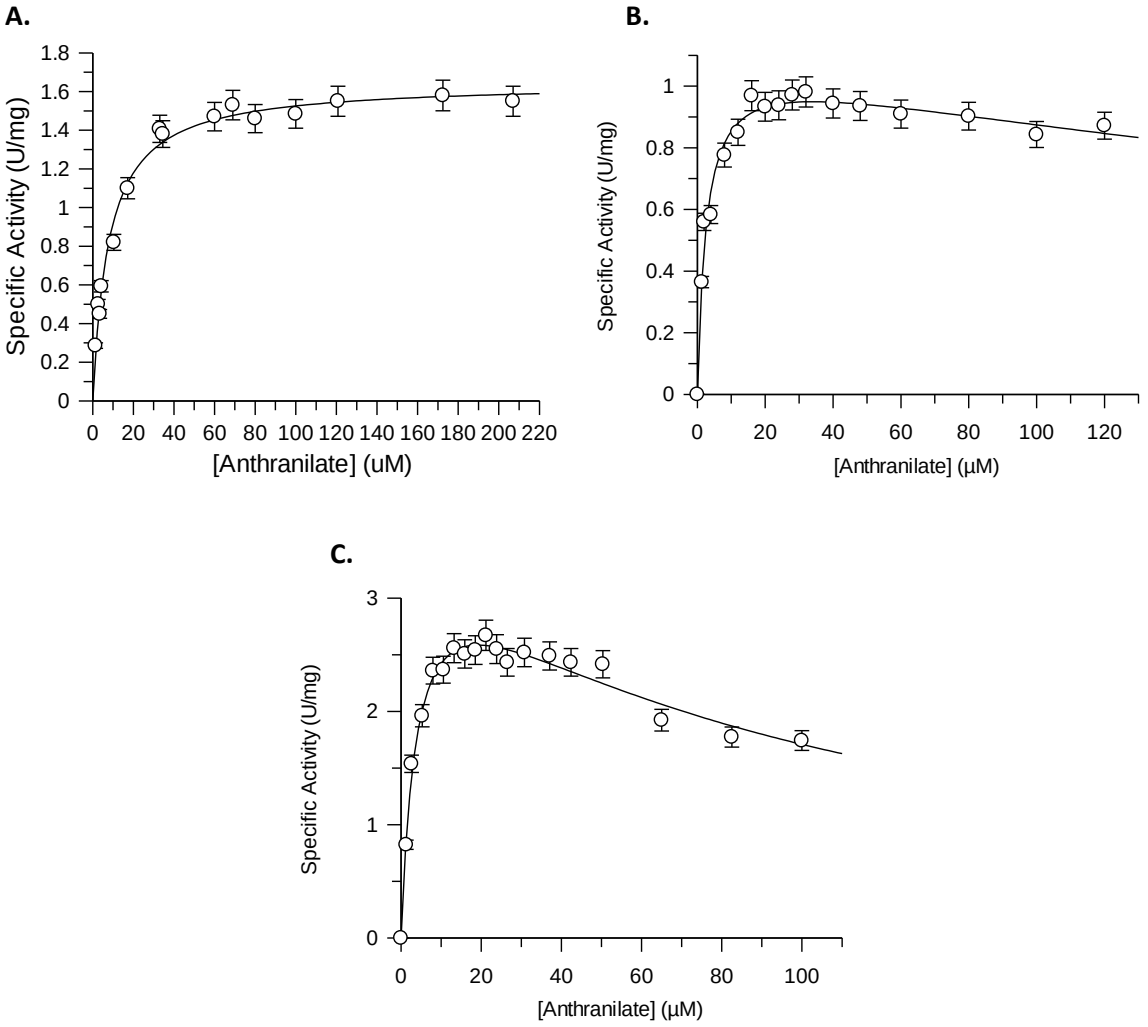

Figure 4.8 Anthranilate inhibition plots for *Mtu*-AnPRT variants. All solutions contained PRPP held at a concentration of 0.6 mM, and were incubated at 25 °C at pH 8.0. A) *Mtu*-N138A as fitted to the Michaelis-Menten equation. B) *Mtu*-P180A as fitted to the substrate inhibition equation. C) *Mtu*-R194A as fitted to the substrate inhibition equation. All graphs fitted using Grafit 5 software.[67]

4.7 Structural Characterisation

Crystals were obtained for all *Mtu*-AnPRT variants with the exception of *Mtu*-G107P, which could not be concentrated enough to facilitate crystal growth due to protein precipitation. Attempts were made to grow crystals at low *Mtu*-G107P concentrations of approximately 13 µM, however, no crystal formation was observed. Variants were co-crystallised in the presence of 10 mM PRPP and 10 mM $MgCl_2$, with some exposed to 10 mM anthranilate soaks for various lengths of time. All crystals grew within 24 hours, and showed the same diamond morphology seen for wild-type *Mtu*-AnPRT crystals (Figure 4.9). All data processing and refinement data for each structure can be found in Appendix 3, while all omit maps for ligands present in structures can be observed in Appendix 4.

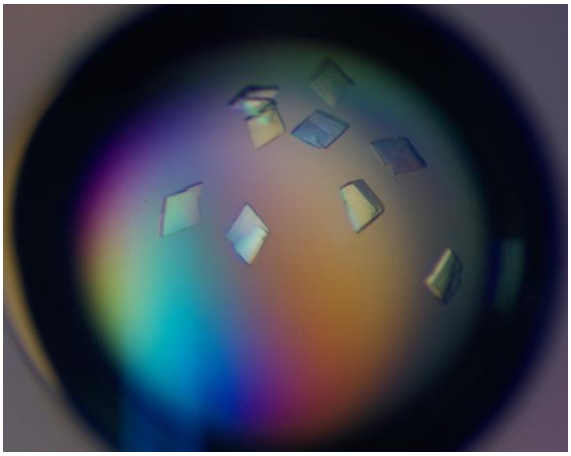

Figure 4.9 Crystals of *Mtu*-R194A co-crystallised with 10 mM PRPP and 10 mM $MgCl_2$ in the presence of 0.2 M imidazole malate (pH 7.0) and 7% PEG-4000 (w/v).

In all structures obtained during this project, both *apo* and ligand bound, the positions of the α8 and α9 helices overlaid almost exactly with the positions observed in the wild-type *Mtu*-AnPRT *apo* structure without benzamidine (PDB ID: 3QR9), not the positions observed in the wild-type *Mtu*-AnPRT PRPP/Mg^{2+} bound structure with benzamidine (PDB ID: 1ZVW) (Figure 4.10). It is therefore likely that the presence of the crystal additive benzamidine does cause the rearrangement of these helices, as has been suggested by Castell *et al.*[41a]

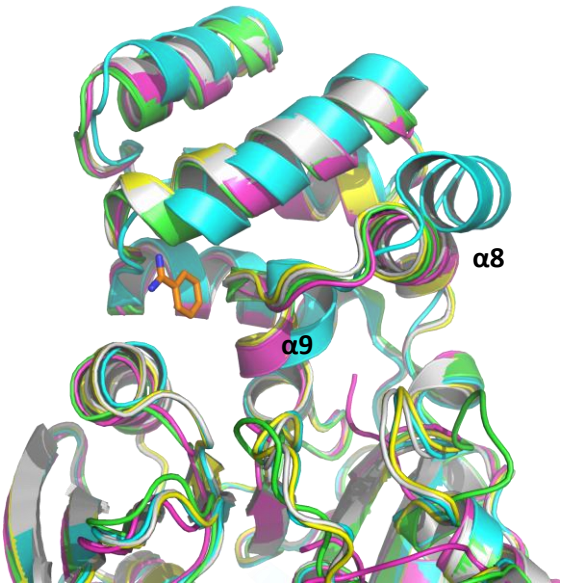

Figure 4.10 Structures of PRPP/Mg^{2+} bound *Mtu*-AnPRT variants overlaid with wild-type *apo* and PRPP/Mg^{2+}/benzamidine bound structures. Wild-type *apo Mtu*-AnPRT is shown in green, wild-type *Mtu*-AnPRT with PRPP/Mg^{2+}/benzamidine bound is shown in cyan, *Mtu*-N138A is shown in magenta, *Mtu*-P180A is shown in yellow, and *Mtu*-R193L is shown in white. Benzamidine is shown in orange.

4.7.1 Structures Co-crystallised with PRPP and Mg^{2+}

Crystals were grown and structural information obtained for *Mtu*-N138A, *Mtu*-P180A, *Mtu*-R193A and *Mtu*-R193L in the presence of PRPP and Mg^{2+}. These structures are compared to the wild-type *Mtu*-AnPRT *apo* structure (PDB ID: 3QR9) as well as the wild-type *Mtu*-AnPRT structure co-crystallised with PRPP, Mg^{2+} and benzamidine (PDB ID: 1ZVW).

4.7.1.1 *Mtu*-N138A/PRPP/Mg^{2+}

The structure of *Mtu*-N138A was obtained in the presence of PRPP and Mg^{2+} at a resolution of 1.72 Å, with four monomers in the asymmetric unit. Chains A and C were associated as a dimer, with chains B and D located on either side of chain A as monomers. Chains A and B crystallised with no ligands present, while chains C and D both showed clear density for PRPP and Mg^{2+}. Chains A and B overlaid well with chain A of both the wild-type *Mtu*-AnPRT *apo* and PRPP/Mg^{2+} bound structures, with RMSD values of 0.514 Å and 0.516 Å respectively for chain A, and 0.530 Å and 0.480 Å respectively for chain B. An obvious shift in position towards the active site can be observed for the α11'' helix, the α11'' - α11 loop and the α11 helix in both chains A and B of the *Mtu*-N138A structure (Figure 4.11), with a displacement of 3.7 Å and 2.0 Å respectively (as measured between G291 of the *Mtu*-N138A and the wild-type *Mtu*-AnPRT PRPP/Mg^{2+} bound structures). Finite density was not

observed for the β1-α5 loop for chains A or B, however, chain B showed clear density for the β2-α6 loop folded into the anthranilate channel, a phenomenon which has been previously observed in *Mtu*-AnPRT wild-type structures (Section 3.6). The β2-α6 loop in Chain A was partially disordered, though enough density was present to also indicate folding into the anthranilate channel. Some extra coiling of the α5 helix N-terminus is also seen in both chains A and B.

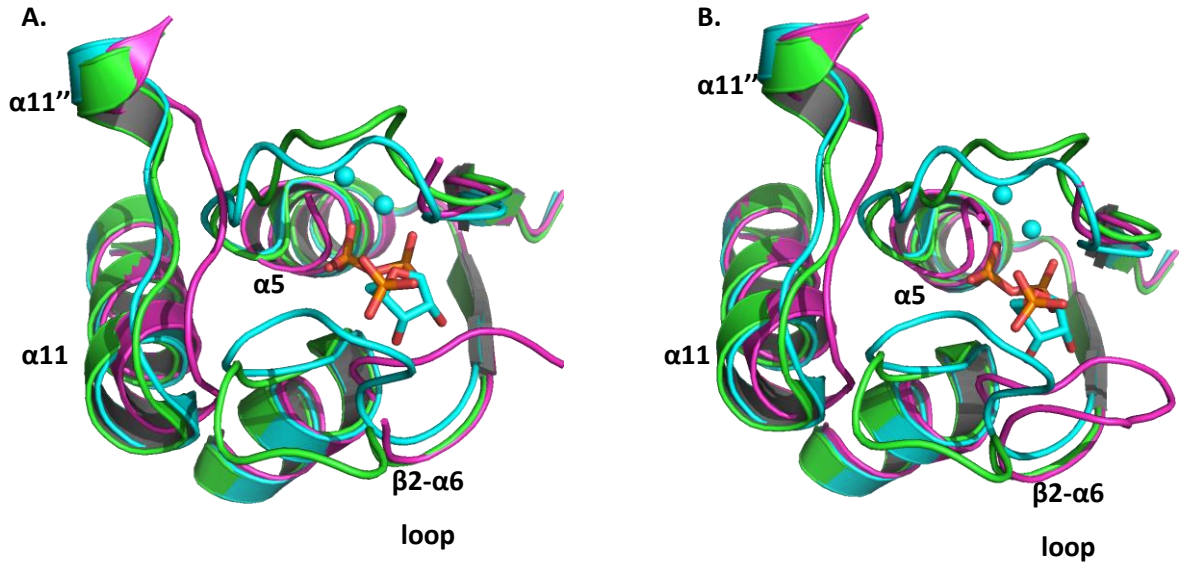

Figure 4.11 An active site comparison of *Mtu*-N138A and wild-type *Mtu*-AnPRT structures. *Mtu*-N138A (magenta), wild-type *Mtu*-AnPRT *apo* chain A (green) and wild-type *Mtu*-AnPRT chain A with PRPP (cyan) and Mg^{2+} (cyan spheres) bound. A) Chain A of *Mtu*-N138A. B) Chain B of *Mtu*-N138A.

Chains C and D overlay almost perfectly with chain A of the wild-type *Mtu*-AnPRT PRPP/Mg^{2+} structure (with the exception of the helices displaced due to benzamidine), with RMSD values of 0.355 Å and 0.371 Å respectively. PRPP and two Mg^{2+} ions are bound in each chain, in positions almost identical to those observed for the wild-type *Mtu*-AnPRT PRPP/Mg^{2+} structure (Figure 4.12). The PRPP molecules in each chain make contacts via the phosphate moiety to A141, S142, S143 and G110, with the ribose ring making contacts with A138 and G147. The PP_i group is the most tightly bound of the molecule, hydrogen bonding to G107, N117, S119, T120, K135 and both Mg^{2+} ions. The two Mg^{2+} ions are co-ordinated to S119, D251 and E252. All of these contacts are identical to those made in the wild-type *Mtu*-AnPRT PRPP/Mg^{2+} structure.[44]

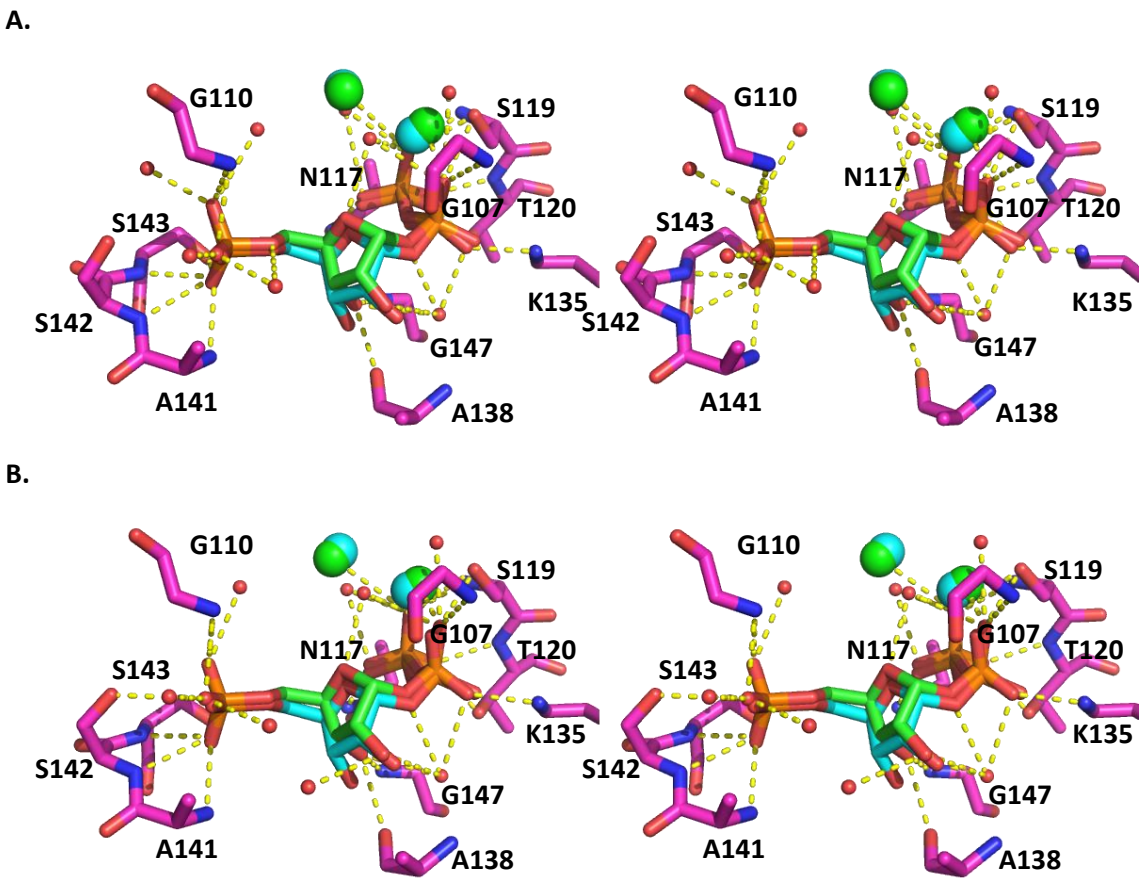

Figure 4.12 Stereo diagrams of PRPP binding in *Mtu*-N138A and wild-type *Mtu*-AnPRT. *Mtu*-N138A (magenta) with PRPP (green) and Mg^{2+} (green spheres) bound is overlaid with wild-type *Mtu*-AnPRT chain A (not shown) with PRPP (cyan) and Mg^{2+} (cyan spheres) bound. Polar contacts for *Mtu*-N138A PRPP are shown as yellow dashes. Water molecules are shown as red spheres. A) Chain C of *Mtu*-N138A. B) Chain D of *Mtu*-N138A.

4.7.1.2 *Mtu*-P180A/PRPP/Mg^{2+}

The structure of *Mtu*-P180A was determined at 1.80 Å in the presence of PRPP and Mg^{2+}, with two non-associated monomers in the asymmetric unit. The *Mtu*-P180A dimers could be generated via crystallographic symmetry. Chain A had one PRPP molecule bound, however, no density for Mg^{2+} was observed. Interestingly, when overlaid with chain A of the wild-type *Mtu*-AnPRT *apo* structure (RMSD = 0.545 Å), the β2-α6 loop from *Mtu*-P180A chain A is shown to be in the open position (Figure 4.13A). When superimposed with chain A of the wild-type *Mtu*-AnPRT PRPP/Mg^{2+} bound structure (RMSD = 0.446 Å), however, it can be seen that the *Mtu*-P180A PRPP molecule is oriented differently, with the outermost phosphate of the PP_i group overlapping with the binding site of one of the wild-type Mg^{2+} ions. In this orientation, the ribose ring is rotated approximately 180°

compared to wild-type PRPP, with the phosphate group pointing towards the anthranilate channel (Figure 4.13A and C). This PRPP orientation is also observed in the *Sso*-AnPRT D83G/F149S variant structure (PDB ID: 3GBR) (Figure 4.13B) though the PP_i group is oriented differently, which is most likely due to the lack of extra coiling of the α5 helix N-terminus. Other structural features of chain A include the displacement of the α11'' helix, α11''-α11 loop and the α11 helix, which is similar to that observed for *Mtu*-N138A PRPP/Mg^{2+} bound structure.

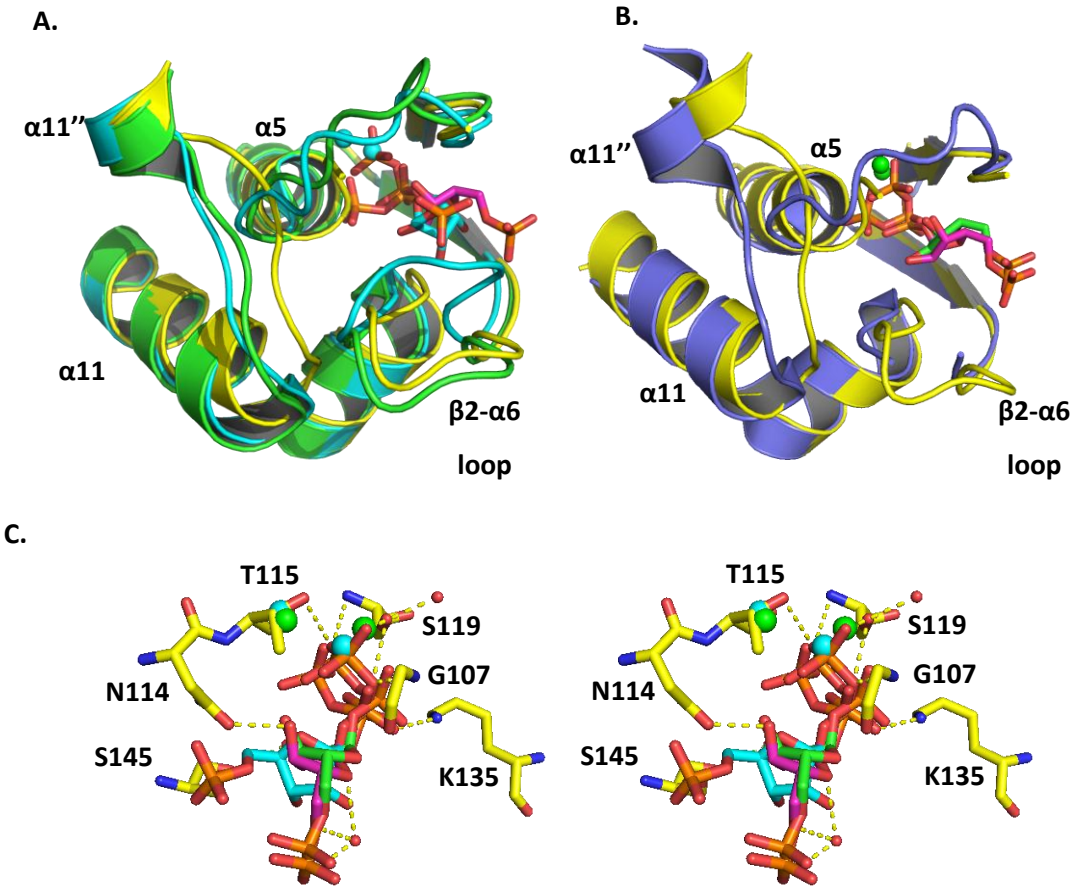

Figure 4.13 PRPP binding in *Mtu*-P180A, wild-type *Mtu*-AnPRT and *Sso*-AnPRT D83G/F149S. A) An overlay of *Mtu*-P180A chain A (yellow) with PRPP (magenta) bound, wild-type *Mtu*-AnPRT *apo* chain A (green) and wild-type *Mtu*-AnPRT chain A with PRPP (cyan) and Mg^{2+} (cyan spheres) bound. B) An overlay of *Mtu*-P180A chain A (yellow) with PRPP (magenta) bound and *Sso*-AnPRT D83G/F149S chain A with PRPP (green) and Mn^{2+} (green spheres) bound. C) Stereo diagram of *Mtu*-P180A chain A (yellow), PRPP (magenta) and Mg^{2+} (magenta spheres) overlaid with wild-type *Mtu*-AnPRT (not shown) with PRPP (cyan) and Mg^{2+} (cyan spheres) bound and *Sso*-AnPRT D83G/F149S with PRPP (green) and Mn^{2+} (green spheres) bound. Polar contacts for *Mtu*-P180A PRPP are shown as yellow dashes. Water molecules are shown as red spheres.

Chain B of *Mtu*-P180A shows the β2-α6 loop in the closed position, similar to chain A of the wild-type *Mtu*-AnPRT PRPP/Mg^{2+} structure (RMSD = 0.358 Å) (Figure 4.14). This chain has PRPP bound in two alternate conformations with two Mg^{2+} ions co-ordinated. The primary conformation of PRPP has an occupancy of 0.8 and overlays well with the wild-type PRPP, making the same hydrogen bond contacts as seen in Figure 4.12 for *Mtu*-N138A. The secondary conformation has an occupancy of 0.2 and is similar in position to the PRPP molecule in chain A. However, the difference in position of the β2-α6 loop in this chain provides different contacts for the ribose ring, with only one contact to G147, and the phosphate group, bound only to N138.

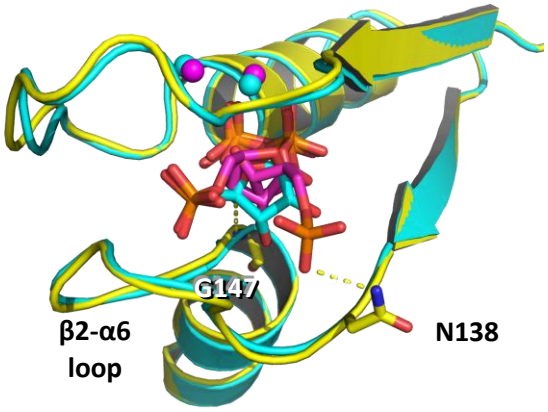

Figure 4.14 Multiple PRPP binding modes in *Mtu*-P180A. *Mtu*-P180A chain B (yellow) with PRPP (magenta) and Mg^{2+} (magenta spheres) bound is overlaid with wild-type *Mtu*-AnPRT chain A with PRPP (cyan) and Mg^{2+} (cyan spheres) bound. Polar contacts between the phosphate and ribose ring of the *Mtu*-P180A PRPP (occupancy = 0.2) are shown as yellow dashes.

4.7.1.3 *Mtu*-R193L/PRPP/Mg^{2+}

The structure of *Mtu*-R193L was elucidated in the presence of PRPP and Mg^{2+} to a resolution of 2.47 Å. Two separate monomers are within the asymmetric unit, though dimers could be generated via crystallographic symmetry. Chain A of *Mtu*-R193L contained PRPP in the active site, but no Mg^{2+} ions. An overlay of this chain with chain A of the wild-type *Mtu*-AnPRT PRPP/Mg^{2+} structure (RMSD = 0.464 Å) (Figure 4.15A) shows the β2-α6 loop in the closed position, with the PRPP molecules overlapping almost exactly, with the exception of the PP_i group. In Figure 4.15A, the PP_i group can be seen to project upwards where it overlaps with a Mg^{2+} ion from the wild-type *Mtu*-AnPRT PRPP/Mg^{2+} structure, making different contacts with G107, T115 and S119. Chain A also shows a displacement of the α11'' and α11 helices of 2.5 Å from the wild-type *Mtu*-AnPRT PRPP/Mg^{2+} structure (as measured between G291 residues), as well as extra coiling of the α5 helix N-terminus.

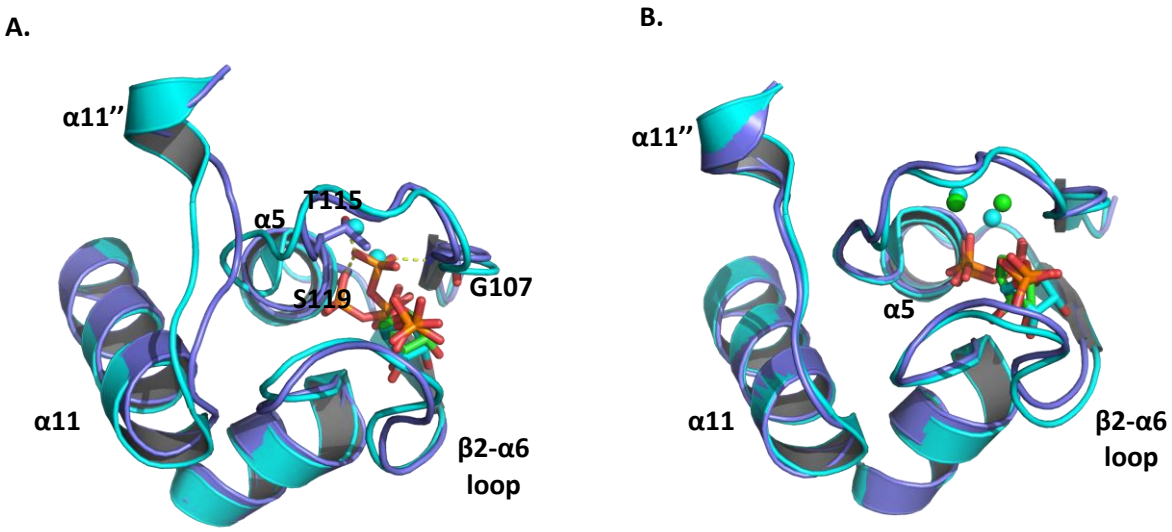

Figure 4.15 An active site comparison of PRPP/Mg^{2+}-bound *Mtu*-R193L and wild-type *Mtu*-AnPRT structures. *Mtu*-R193L (purple) with PRPP (green) and Mg^{2+} (green spheres) bound is overlaid with wild-type *Mtu*-AnPRT chain A (cyan) with PRPP (cyan) and Mg^{2+} (cyan spheres) bound. Polar contacts for the R193L PRPP shifted PP_i are shown as yellow dashes. A) Chain A of *Mtu*-R193L. B) Chain B of *Mtu*-R193L.

Chain B of *Mtu*-R193L also shows the β2-α6 loop in the closed position when overlaid with chain A of the wild-type *Mtu*-AnPRT PRPP/Mg^{2+} structure (RMSD = 0.412 Å). Two Mg^{2+} ions are present in this chain along with PRPP, all co-ordinated in the same manner as for the wild-type *Mtu*-AnPRT PRPP/Mg^{2+} structure (Figure 4.15B). Extra coiling of the α5 helix and displacement of the α11'' and α11 helices are not observed in this chain.

4.7.1.4 *Mtu*-R193A/PRPP/Mg^{2+}

Mtu-R193A was co-crystallised with PRPP and Mg^{2+}, with the crystal structure solved at a resolution of 1.93 Å. However, no ligands were observed in either of the two monomers in the asymmetric unit. The two monomers are non-associated in the asymmetric unit, however, dimers can be generated via crystallographic symmetry. Superimposing chain A of *Mtu*-R193A onto chain A of the wild-type *Mtu*-AnPRT PRPP/Mg^{2+} structure (RMSD = 0.468 Å) and chain A of the wild-type *Mtu*-AnPRT *apo* structure (RMSD = 0.492 Å) showed the *Mtu*-R193A β2-α6 loop folded into the anthranilate channel. Extra coiling of the α5 helix N-terminus was also observed, along with displacement of the α11'' and α11 helices (Figure 4.16A). The same structural features were also present in *Mtu*-R193A chain B (Figure 4.16B), which had an RMSD value of 0.599 Å when overlaid with chain A of the wild-type *Mtu*-AnPRT PRPP/Mg^{2+}, and 0.690 Å when overlaid with chain A of the wild-type *Mtu*-AnPRT *apo* structure. Chain B also showed some stabilisation of the β2-α6 loop, when compared to *Mtu*-R193A

chain A and to the wild-type *Mtu*-AnPRT *apo* and wild-type *Mtu*-AnPRT PRPP/Mg^{2+} structures (Figure 4.16C-F).

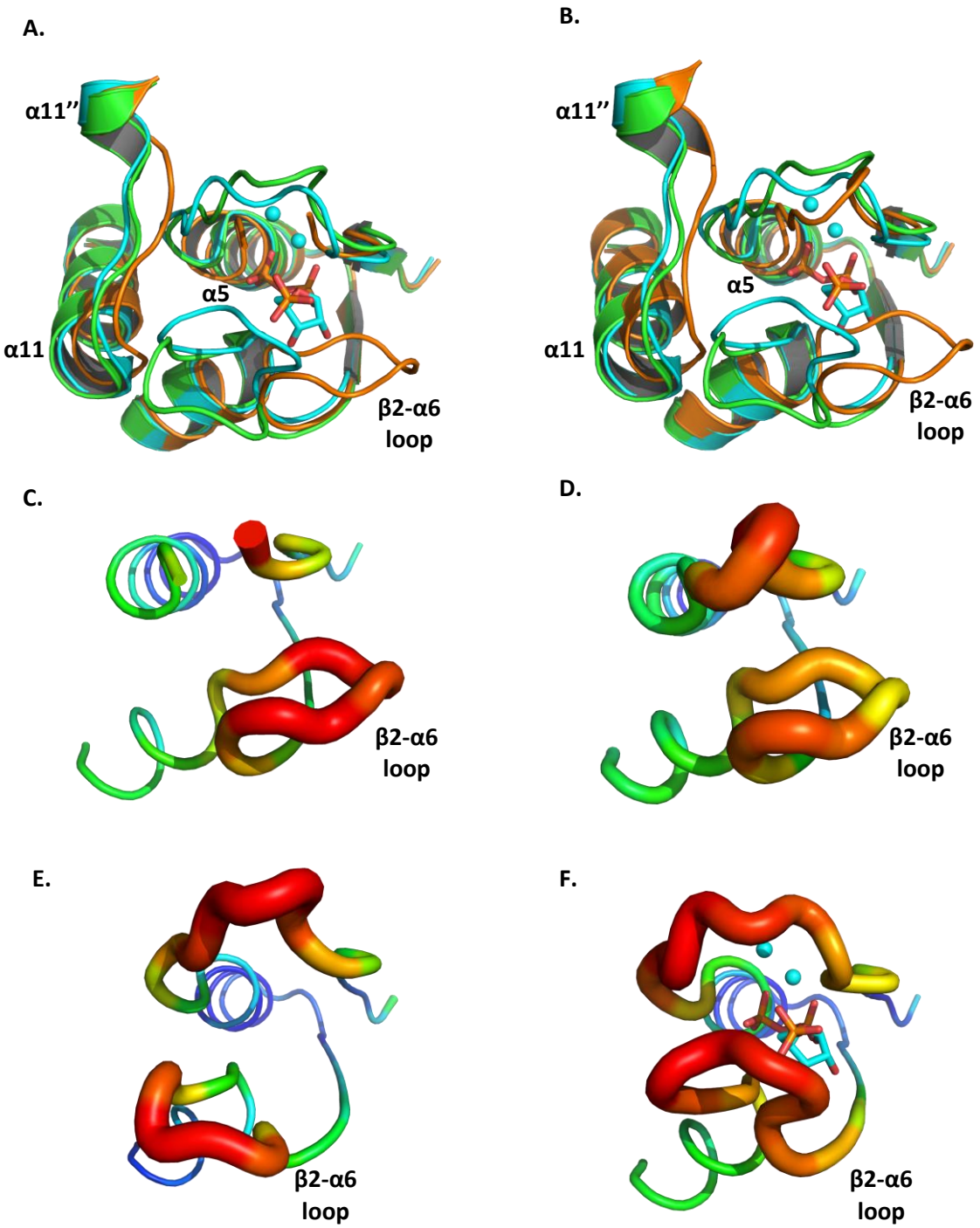

Figure 4.16 A comparison of the active site and β2-α6 loop stability in PRPP/Mg^{2+}-bound *Mtu*-R193A and wild-type *Mtu*-AnPRT. A) *Mtu*-R193A chain A (orange) or B) *Mtu*-R193A chain B (orange) overlaid with wild-type *Mtu*-AnPRT *apo* chain A (green) and wild-type *Mtu*-AnPRT chain A (cyan) with PRPP (cyan) and Mg^{2+} (cyan spheres) bound. Panels C-F depict B-factor putty models for residues 101-154 of wild-type/variant *Mtu*-AnPRTs generated using PyMOL software,[53] where larger red regions indicate residues with high B-factors, and smaller blue regions indicate residues with low B-factors. The average B-factors for the compared proteins range from 23.9 – 26.0. C) *Mtu*-R193A chain A. D) *Mtu*-R193A chain B. E) Wild-type *Mtu*-AnPRT *apo* chain A. F) Wild-type *Mtu*-AnPRT chain A with PRPP (cyan) and Mg^{2+} (cyan spheres) bound.

4.7.1.5 Interpretation of Structures

A comparison of all four variant structures (*Mtu*-N138A, *Mtu*-P180A, *Mtu*-R193L and *Mtu*-R193A) obtained in the presence of PRPP and Mg^{2+} raises some interesting questions about the order of binding of these two ligands. Chain A of the *Mtu*-P180A structure shows PRPP bound in a completely different conformation to that observed for wild-type *Mtu*-AnPRT with PRPP and Mg^{2+} bound (Figure 4.14); a pose that could be illustrating how PRPP initially binds to the active site. Chain B of the *Mtu*-P180A structure correlates with this hypothesis, as the same pose is present at an occupancy of 0.2 together with the 'final' binding mode at an occupancy of 0.8. However, it is important to note that the rigidity present within the *Mtu*-AnPRT crystal structures could be influencing the mechanism by which PRPP binds, and as such the alternative PRPP binding observed in *Mtu*-P180A may not represent the binding events of a dynamic protein in solution.

Further to this, it can be observed that Mg^{2+} is not present in chain A of the *Mtu*-R193L structure where the β2-α6 loop is in the 'closed' position. However, DSF experiments outlined in Section 2.4.3 show a decided increase in *Mtu*-AnPRT stability when both Mg^{2+} and PRPP are present, which is likely attributable to the closure of the β2-α6 loop causing an increase to the global stability of the enzyme. This increase in stability was not observed when PRPP was present without Mg^{2+}. As the DSF experiments are performed in solution, they are more likely to reflect the events associated with ligand binding. The crystal structure of *Mtu*-R193L, where the β2-α6 loop is 'closed' despite the absence of Mg^{2+}, could therefore be a result of crystal packing.

Three structural changes can be observed to contribute to the suggested order of binding of PRPP and Mg^{2+}. Firstly, the β2-α6 loop curling into the anthranilate channel, which is observed in the unliganded chains of *Mtu*-N138A and *Mtu*-R193A. Secondly, the extra coiling of the α5 helix N-terminus, which is present in the unliganded chains of the *Mtu*-N138A and *Mtu*-R193A structures, chain A of *Mtu*-R193L and chain A of *Mtu*-P180A. Thirdly, the displacement of the α11'' helix, the α11''-α11 loop and the α11 helix towards the PRPP binding site, which is also present in the unliganded chains of the *Mtu*-N138A and *Mtu*-R193A structures, chain A of *Mtu*- R193L and chain A of *Mtu*-P180A. Upon inspection of these structures, it appears that prior to PRPP binding the β2-α6 loop is folded into the anthranilate channel. It is unclear whether movement of this loop to the 'open' position (observed in the wild-type *Mtu*-AnPRT *apo* structure) appears to facilitate the initial stages of PRPP binding, or vice versa. As the binding of PRPP progresses, the α5 helix likely uncoils and becomes part of the β1-α5 loop. These PRPP binding events may somehow trigger the uncoiling of the α5 helix, which would also allow the binding of Mg^{2+} ions in the positions observed in the wild-

type *Mtu*-AnPRT PRPP/Mg^{2+} bound structure. PRPP binding may also cause the movement of the α11'' and α11 helices away from the PRPP binding site, though the mechanism for this is unclear.

It is possible that the mutations made to *Mtu*-AnPRT have somehow facilitated these binding events and structural movements, however, similar observations were made between different variants, and superimposition of the structures onto wild-type proteins show little gross conformational changes. The folding of the β2-α6 loop into the anthranilate channel has previously been observed in wild-type *Mtu*-AnPRT structures in the presence of 4-fluoro-anthranilate (Section 3.6).

The variant most likely to affect PRPP binding is *Mtu*-N138A, which binds the ribose ring of PRPP via the C3 hydroxyl group, and has been shown to increase the apparent K_M value of PRPP (Section 4.6.1). However, the structure obtained for *Mtu*-N138A has shown that PRPP is able to bind in the same manner as wild-type, and maintains the hydrogen bond interaction between the backbone oxygen of A138 and the PRPP C3 hydroxyl. The reason for the increase in the K_M value is therefore not likely to be caused by the protein's inability to accept a PRPP conformation similar to wild-type.

4.7.2 Structures Soaked with Anthranilate

Looped crystals of the variants *Mtu*-N138A, *Mtu*-P180A, *Mtu*-R193A, *Mtu*-R193L and *Mtu*-R194A, which were co-crystallised with PRPP and Mg^{2+}, were soaked for various time periods with solutions containing 10 mM anthranilate before snap-freezing with liquid N_2. Structural information was obtained for all five variants in the presence of different combinations of ligands, subject to the *Mtu*-AnPRT-catalysed reaction of the two substrates PRPP and anthranilate. These structures are compared to the wild-type *Mtu*-AnPRT *apo* structure (PDB ID: 3QR9) as well as the wild-type *Mtu*-AnPRT structure co-crystallised with PRPP, Mg^{2+} and benzamidine (PDB ID: 1ZVW).

4.7.2.1 *Mtu*-N138A/PRPP/Mg^{2+}/Anthranilate

Structural data was obtained for *Mtu*-N138A, which had been soaked for 10 s with anthranilate, at a resolution of 2.23 Å. Two non-associated monomers were present in the asymmetric unit, though no evidence of bound ligands was observed in either protein chain. Both chains have unresolved density for the β2-α6 loop, suggesting this loop is flexible within the crystal lattice. Extra coiling of the α5 helix is observed for both chains, however, only chain B shows some displacement of the α11''-α11 loop towards the PRPP binding site (Figure 4.17).

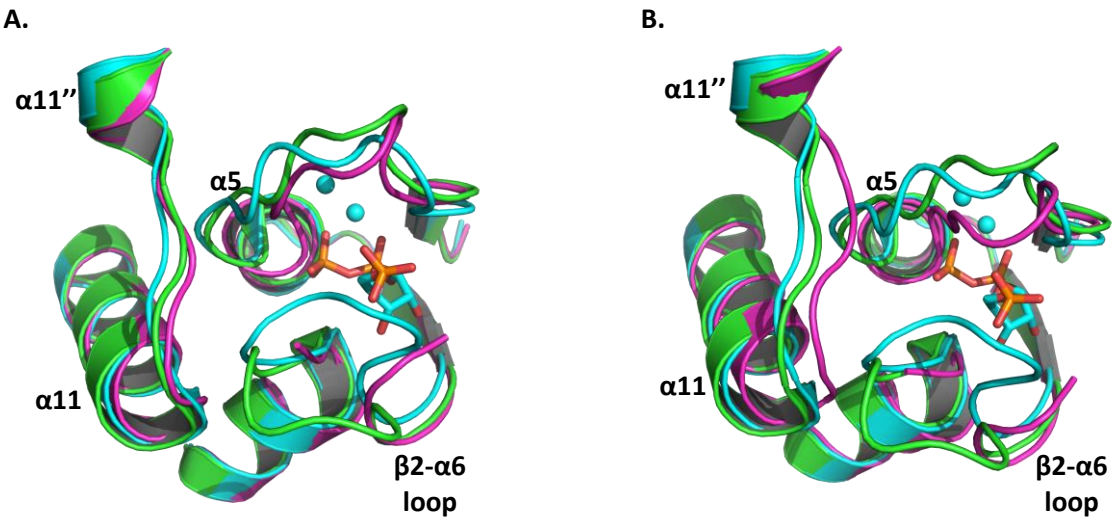

Figure 4.17 An active site comparison of the *Mtu*-N138A (10 s anth soak) and wild-type *Mtu*-AnPRT structures. *Mtu*-N138A (10 s Anth soak) (magenta) is overlaid with wild-type *Mtu*-AnPRT *apo* chain A (green) and wild-type *Mtu*-AnPRT chain A (cyan) with PRPP (cyan) and Mg^{2+} (cyan spheres) bound. A) Chain A of *Mtu*-N138A (10 s Anth soak). B) Chain B of *Mtu*-N138A (10 s Anth soak).

4.7.2.2 *Mtu*-P180A/PRPP/Mg^{2+}/Anthranilate

Mtu-P180A was soaked in a solution containing anthranilate for 1 s before snap-freezing in liquid N_2. A crystal structure was obtained at a resolution of 2.04 Å, containing two monomers in the asymmetric unit associated as a dimer. Unfortunately, no ligands were observed bound to either protein chain, with the exception of one Mg^{2+} ion bound to chain A. Chain A overlays well with chain A of the *Mtu*-AnPRT *apo* structure (RMSD = 0.194 Å), with the β2-α6 loop shown clearly in the open position (Figure 4.18A). If the previous assumption of PRPP binding preceding Mg^{2+} binding is correct, the presence of the lone Mg^{2+} ion in chain A may indicate the state of the enzyme post-reaction after PP_i has departed.

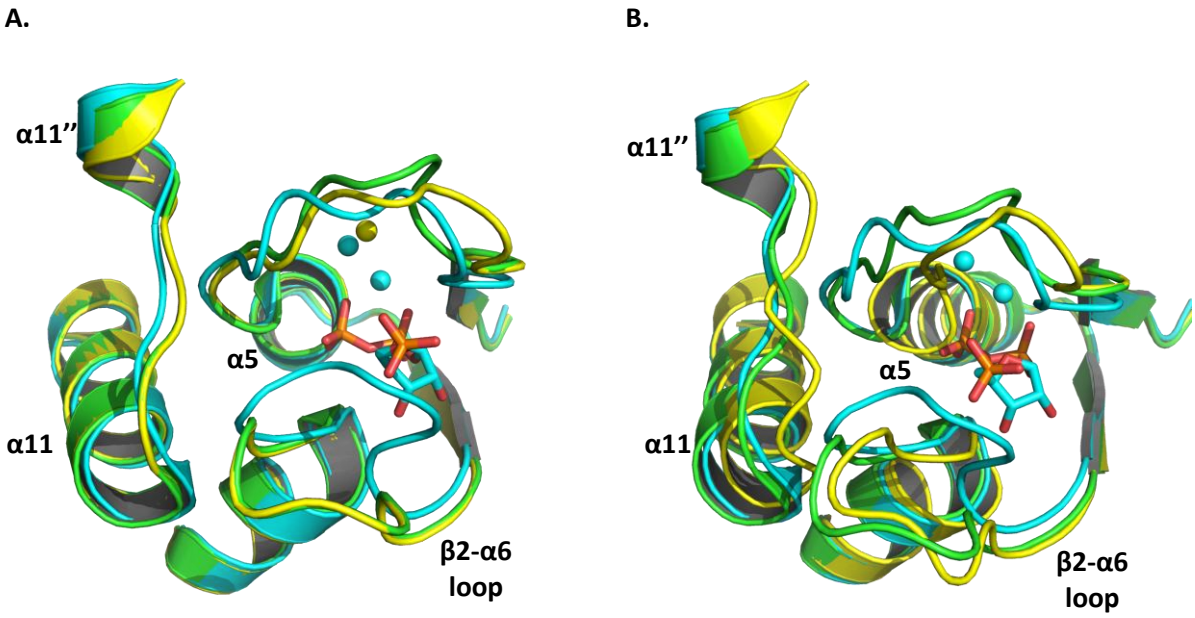

Figure 4.18 An active site comparison of the *Mtu*-P180A (1 s anth soak) and wild-type *Mtu*-AnPRT structures. *Mtu*-P180A (1 s Anth soak) (yellow) with Mg^{2+} bound (yellow spheres) is overlaid with wild-type *Mtu*-AnPRT *apo* chain A (green) and wild-type *Mtu*-AnPRT chain A (cyan) with PRPP (cyan) and Mg^{2+} (cyan spheres) bound. A) Chain A of *Mtu*-P180A (1 s Anth soak). B) Chain B of *Mtu*-P180A (1 s Anth soak).

An overlay of chain B of *Mtu*-P180A with chain A of the wild-type *Mtu*-AnPRT *apo* structure also shows the β2-α6 loop clearly in the open position, however, the RMSD value has increased to 0.402 Å. This is likely due to the extra coiling of the α5 helix and displacement of the α11'' and α11 helices, which may also explain why there are no Mg^{2+} ions present in this chain (Figure 4.18B).

4.7.2.3 *Mtu*-R193L/PRPP/Mg^{2+}/Anthranilate

The structure of *Mtu*-R193L was obtained at a resolution of 2.47 Å with two separate monomers in the asymmetric unit. *Mtu*-R193L was first co-crystallised in the presence of PRPP and Mg^{2+}, and was soaked in a solution containing anthranilate for 5 s prior to snap-freezing with liquid N_2. Chain A of R193L had both PRPP and two Mg^{2+} ions bound, and overlays well with chain A of the wild-type *Mtu*-AnPRT PRPP/Mg^{2+} structure (RMSD = 0.380 Å). As can be seen in Figure 4.19A, the PRPP and Mg^{2+} ions are bound in a similar manner to the ligands in the wild-type *Mtu*-AnPRT PRPP/Mg^{2+} structure, with the β2-α6 loop in the closed position.

Chain B of *Mtu*-R193L had both PP_i and Mg^{2+} ions bound, with these ligands shown to overlay well with the positions occupied by the PP_i moiety and the Mg^{2+} ions in chain A of the wild-type *Mtu*-AnPRT PRPP/Mg^{2+} structure (RMSD = 0.473 Å) (Figure 4.19B). Interestingly, this chain showed the β2-

α6 loop folded into the anthranilate channel, as was previously observed for the *Mtu*-R193A structure in Section 4.7.1.4. As with *Mtu*-R193A chain B, *Mtu*-R193L chain B also shows some stabilisation of the β2-α6 loop in this folded position (Figure 4.19C).

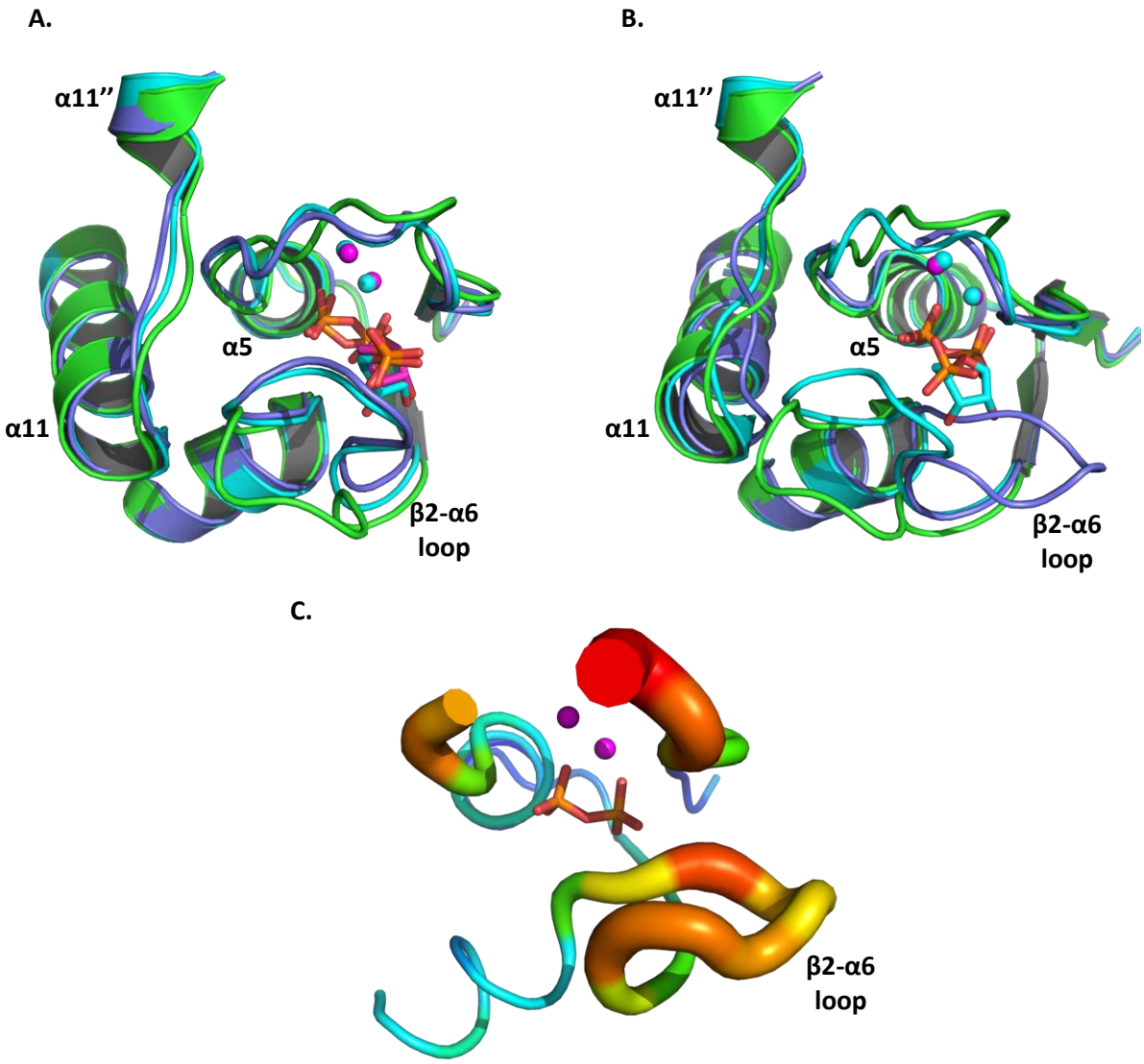

Figure 4.19 A comparison of the active site and β2-α6 loop stability in the *Mtu*-R193L (5 s anth soak) and wild-type *Mtu*-AnPRT structures. A) *Mtu*-R193L chain A (5 s Anth soak) (purple) with PRPP (magenta) and Mg^{2+} (magenta spheres) bound or B) *Mtu*-R193L chain B (5 s Anth soak) (purple) with PP_i and Mg^{2+} (magenta spheres) bound overlaid with wild-type *Mtu*-AnPRT *apo* chain A (green) and wild-type *Mtu*-AnPRT chain A (cyan) with PRPP (cyan) and Mg^{2+} (cyan spheres) bound. C) B-factor putty model of *Mtu*-R193L chain B with PP_i (orange) and Mg^{2+} (magenta spheres) bound showing residues 101-154. Larger red regions indicate residues with high B-factors, while smaller blue regions indicate residues with low B-factors.

4.7.2.4 *Mtu*-R193A/PRPP/Mg^{2+}/Anthranilate

Two structures were obtained of *Mtu*-R193A in the presence of PRPP, Mg^{2+} and anthranilate. The first structure was obtained from a crystal that had been soaked in a solution containing anthranilate for 3 s before snap-freezing with liquid N_2, and has a resolution of 2.20 Å. The second structure arose from a crystal soaked for 1 min and 10 s in anthranilate solution, and has a resolution of 2.50 Å.

The *Mtu*-R193A 3 s structure has two monomers associated as a dimer in the asymmetric unit. Each monomer has one anthranilate bound, with both molecules bound in the same position in the outer site. The anthranilate molecules in each chain make the same hydrogen bond contacts to N138, R194 and a water molecule via the carboxylate group. The aromatic ring of anthranilate also has C-H···π interactions to P180 via its proline ring (Figure 4.20C). Both chains also show extra coiling of the α5 helix, with the β2-α6 loop definitely folded into the anthranilate channel in chain B (Figure 4.20B and D). The β2-α6 loop in chain A is partially disordered, but has sufficient density present to suggest folding into the anthranilate channel (Figure 4.20A). Chain B also shows some slight displacement of the α11'' and α11 helices.

The *Mtu*-R193A 1 min 10 s structure has two non-associated monomers in the asymmetric unit, with both chains showing similar structural features to chain B of the *Mtu*-R193A structure soaked with anthranilate for 3 s (Figure 4.21A). Both monomers show one anthranilate molecule bound in the outer site, but with slightly different hydrogen bond contacts. Chain A shows the anthranilate hydrogen bonded to N138 and a water molecule via the amino group, and forming a salt bridge to R194 via the carboxylate group (Figure 4.21B). Chain B has the anthranilate molecule hydrogen bonded to N138 via the amino group, and hydrogen bonded to R194 and a water molecule via the carboxylate group (Figure 4.21C). The aromatic rings of the anthranilate molecules in each chain form C-H···π interactions to the proline ring of P180. The stability of the β2-α6 loop in each chain has a similar B-factor profile to that shown in Figure 4.20D.

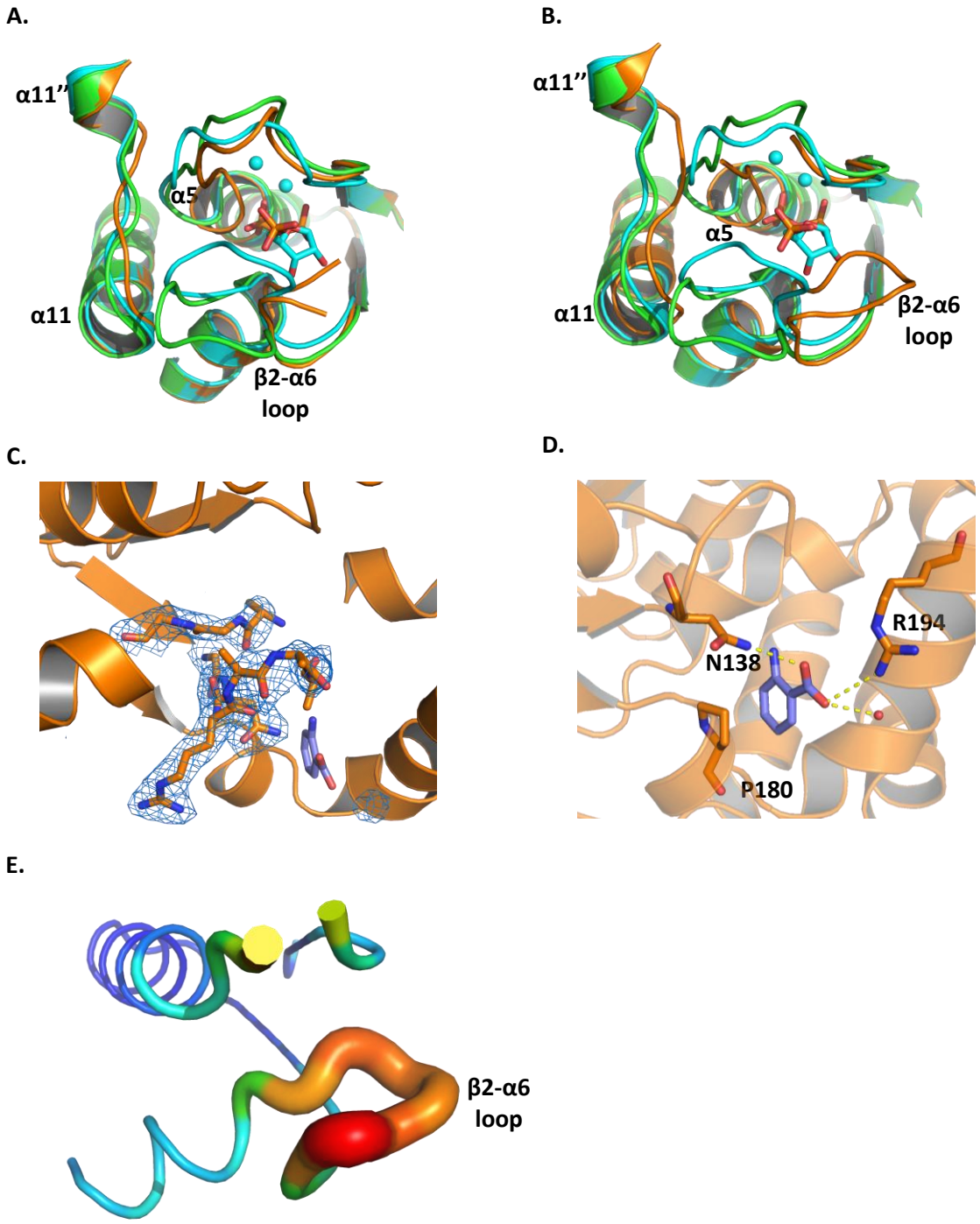

Figure 4.20 A comparison of the active site and β2-α6 loop stability in the *Mtu*-R193A (3 s anth soak) and wild-type *Mtu*-AnPRT structures. A) *Mtu*-R193A chain A (3 s anth soak) (orange) or B) *Mtu*-R193A chain B (3 s Anth soak) (orange) overlaid with wild-type *Mtu*-AnPRT *apo* chain A (green) and wild-type *Mtu*-AnPRT chain A (cyan) with PRPP (cyan) and Mg^{2+} (cyan spheres) bound. C) $2F_o$-F_c map (blue, contoured at 1 σ) of the β2-α6 loop in chain A of *Mtu*-R193A (3s anth soak), showing likely folding into the anthranilate channel. D) *Mtu*-R193A chain B (3 s anth soak) (orange) with anthranilate (purple) bound in the outer site. Polar contacts are shown as yellow dashes, with water molecules shown as red spheres. E) B-factor putty model of *Mtu*-R193A chain B showing residues 101-154, where larger red regions indicate residues with high B-factors and smaller blue regions indicated residues with low B-factors.

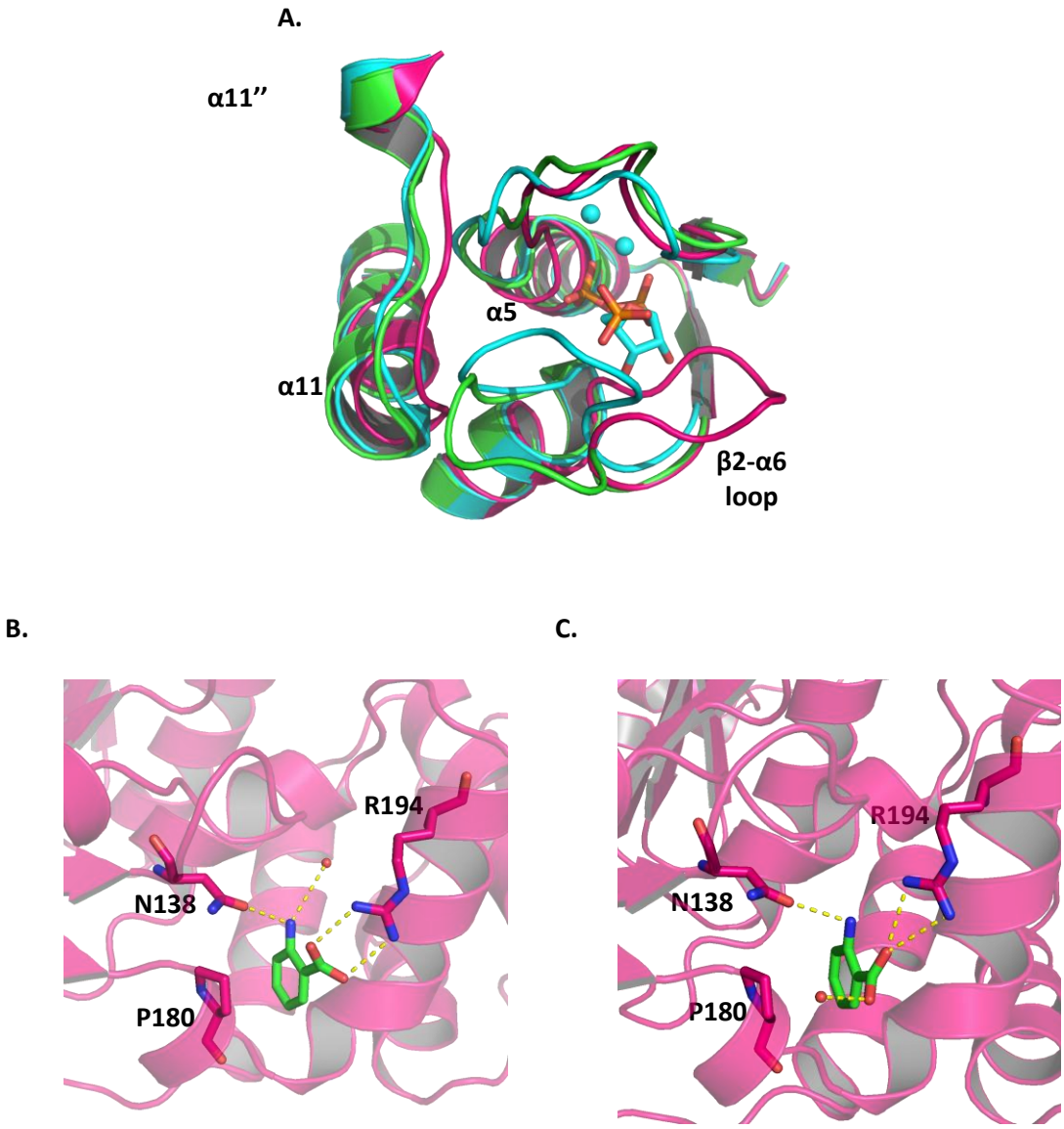

Figure 4.21 An active site comparison of the *Mtu*-R193A (1 min 10 s anth soak) and wild-type *Mtu*-AnPRT structures. A) *Mtu*-R193A chain A (1 min 10 s anth soak) (pink) overlaid with wild-type *Mtu*-AnPRT *apo* chain A (green) and wild-type *Mtu*-AnPRT chain A (cyan) with PRPP (cyan) and Mg^{2+} (cyan spheres) bound. B) *Mtu*-R193A chain A (1 min 10 s anth soak) (pink) with anthranilate (green) bound in the outer site. C) *Mtu*-R193A chain B (1 min 10 s anth soak) (pink) with anthranilate (green) bound in the outer site. Polar contacts are shown as yellow dashes, with water molecules shown as red spheres.

The structures elucidated from both *Mtu*-R193A soaks with anthranilate bound and the wild-type *Mtu*-AnPRT structure with 4FA (6 s soak) bound (PDB ID: 4N8Q) are overlaid in Figure 4.22. A comparison of these structures shows both anthranilate and 4FA bound in similar positions in the outer site, with the residues involved in this outer site (N138, P180 and R194) also in analogous orientations. The β2-α6 loop is positioned differently in the *Mtu*-R193A structures when compared to the 4FA-bound wild-type structure, which is likely due to the absence of the steric bulk of the R193 side-chain in the variant protein. This absence of R193 would allow further projection of the β2-α6 loop into the anthranilate channel.

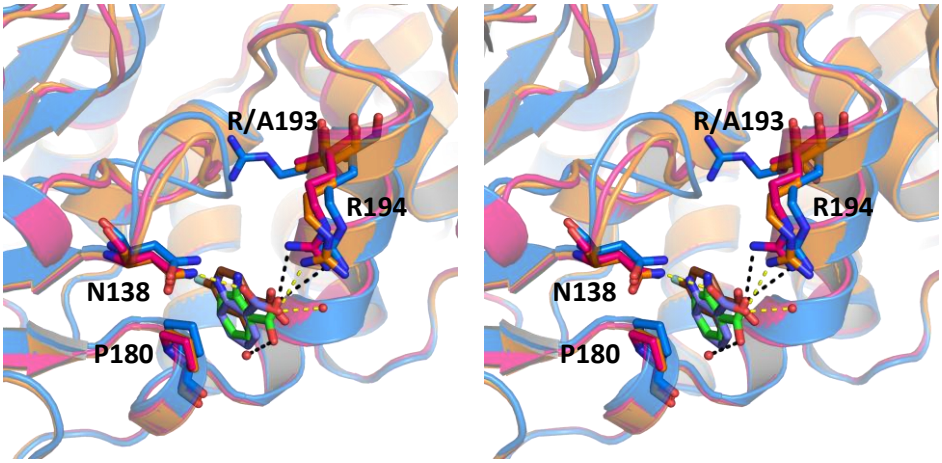

Figure 4.22 Stereo diagram of the anthranilate/4FA binding modes in *Mtu*-R193A (anth soaked) and wild-type *Mtu*-AnPRT structures. *Mtu*-R193A (3 s anth soak) (orange) with anthranilate (purple) bound is overlaid with *Mtu*-R193A (1 min 10 s anth soak) (pink) with anthranilate (green) bound and wild-type *Mtu*-AnPRT (6 s 4FA soak) (blue) with 4FA (brown) bound. Polar contacts for anthranilate from the *Mtu*-R193A 3 s soak and 1 min 10 s soak are shown as yellow and black dashes respectively.

4.7.2.5 *Mtu*-R194A/PRPP/Mg^{2+}/Anthranilate

The final crystal structure in this section is of *Mtu*-R194A, co-crystallised with PRPP and Mg^{2+} and soaked with anthranilate for 5 min at 4 °C. The structure has a resolution of 1.77 Å and has two monomers associated as a dimer in the asymmetric unit. Both monomers show PP_i, two Mg^{2+} ions and two anthranilate molecules bound in the anthranilate channel. Both chains overlay well with chain A of the wild-type *Mtu*-AnPRT PRPP/Mg^{2+} bound structure (RMSD = 0.393 Å for chain A, RMSD = 0.409 Å for chain B), though neither show density for the β2-α6 loop. Both chains show the PP_i molecules and Mg^{2+} ions overlaid in the same positions as those observed for PP_i moiety and the Mg^{2+} ions in chain A of the wild-type *Mtu*-AnPRT PRPP/Mg^{2+} bound structure (Figure 4.23A and B).

Although both chains of *Mtu*-R194A have two anthranilate molecules bound, each chain has them bound in different positions (Figure 4.23C and D). Chain A has one anthranilate bound in the inner site, making hydrogen bond contacts to G107 and T108 via the amino group, and to R193, N138, the amino group of the second anthranilate and three water molecules via the carboxylate group. The second anthranilate molecule in chain A is bound in the middle site, and is hydrogen bonded to the carboxylate group of the first anthranilate molecule and a water molecule via its amino group, and to N138 and three water molecules via its carboxylate group. Chain B also has one anthranilate molecule bound in the inner site, but with different hydrogen bond contacts. The amino group of the inner anthranilate makes contacts to a single water molecule, with the carboxylate group making four contacts to N138 and three water molecules. The second anthranilate molecule in chain B is bound in the outer site, hydrogen bonded to a single water molecule and making C-H···π interactions to the P180 residue.

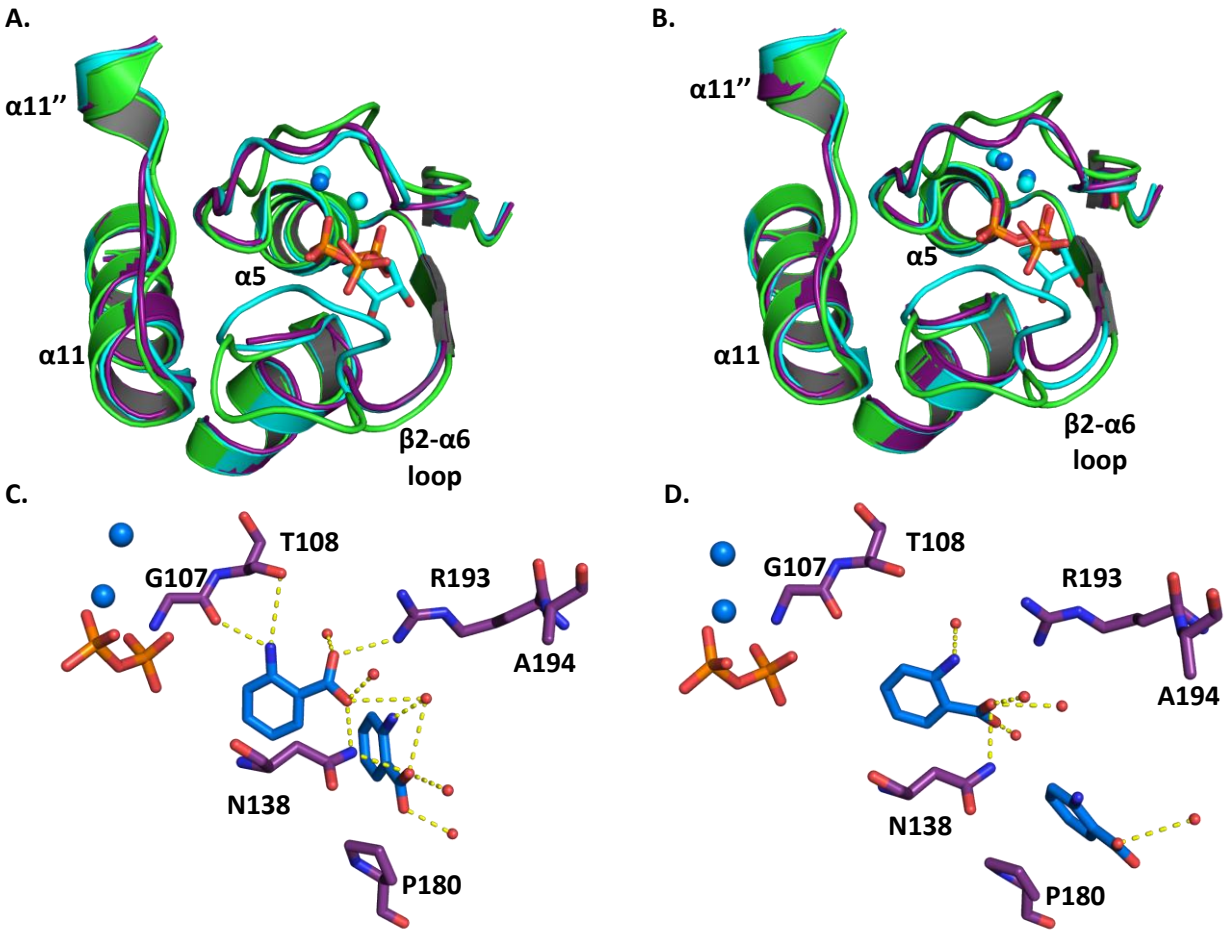

Figure 4.23 An active site comparison of the *Mtu*-R194A (5 min anth soak) and wild-type *Mtu*-AnPRT structures. A) *Mtu*-R194A chain A (5 min anth soak) (purple) or B) *Mtu*-R194A chain B (5 min anth soak) (purple) is overlaid with wild-type *Mtu*-AnPRT *apo* chain A (green) and wild-type *Mtu*-AnPRT chain A (cyan) with PRPP (cyan) and Mg^{2+} (cyan spheres) bound. C) *Mtu*-R194A chain A (5 min anth soak) with anthranilate (blue) bound in both the inner site and middle site. D) *Mtu*-R194A chain B (5 min anth soak) with anthranilate (blue) bound in both the inner site and the outer site.

An overlay of *Mtu*-R194A chain A with the wild-type *Mtu*-AnPRT structures containing the alternate substrates 4FA (6 min soak) (PDB ID: 4N5V), 4FA (6 s soak) (PDB ID: 4N8Q) and 6MA (30 min soak) (PDB ID: 4N93) shows the identical positioning of anthranilate, 4FA and 6MA in the inner site (Figure 4.24A). The active site residues contributing hydrogen bonds to the inner site anthranilate are also in the same positions, indicating that the mutation R194A has not caused any significant changes to the anthranilate binding in the inner site. The *Mtu*-AnPRT structures containing the alternate substrates do not show additional anthranilate binding in the middle site, contrary to what is observed in *Mtu*-R194A chain A, and instead have the second anthranilate-like substrate bound in the outer site. This observation suggests a possible role for R194 in the shuttling of anthranilate from the outer site to

the middle site. However, when *Mtu*-R194A chain A is overlaid with the *Sso*-AnPRT enzyme (PDB ID: 2GVQ) (RMSD = 1.358 Å), it can be seen that the two anthranilate positions overlay almost exactly with the positions observed in the *Sso*-AnPRT protein (Figure 4.24A & C).

When overlaid with the wild-type *Mtu*-AnPRT alternate substrate structures, *Mtu*-R194A chain B can be observed to have a similar anthranilate binding pattern (Figure 4.24B & D). The inner site anthranilate is in a slightly different position to the wild-type *Mtu*-AnPRTs with alternate substrates bound, with the amino group oriented towards R193 as opposed to G107/T108. This position also differs from the *Sso*-AnPRT structures with anthranilate bound (PDB IDs: 2GVQ and 1ZYK). The outer site anthranilate of *Mtu*-R194A aligns with the 4FA and 6MA molecules also bound in this site in wild-type *Mtu*-AnPRT, though there is a key discrepancy. The 4FA and 6MA molecules bound in the outer site have their amino groups oriented towards H183, while in *Mtu*-R194A the anthranilate amino group is pointing towards N138. It is likely that anthranilate binds in the outer site with its amino group facing towards N138, negating the necessary ring flip (discussed in Section 3.6) that would be required for 4FA and 6MA to adopt their inner site binding modes.

Figure 4.24 also shows that residues from the wild-type *Mtu*-AnPRT 4FA 6 s soak structure are slightly displaced compared to *Mtu*-R194A and the other alternate substrate structures, which is likely caused by the folding of the β2-α6 loop into the anthranilate channel.

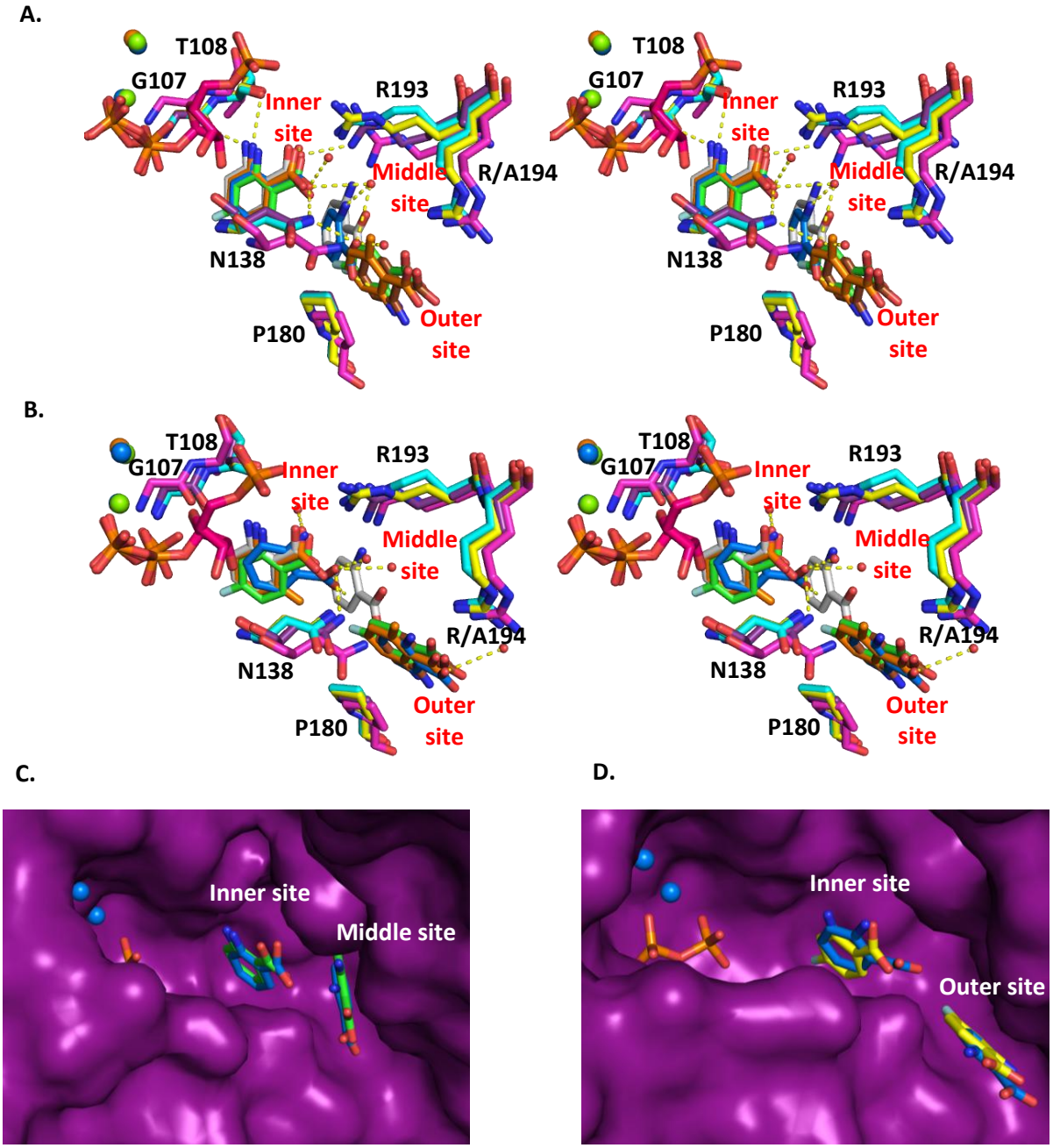

Figure 4.24 A comparison of anthranilate/analogue binding sites in *Mtu*-R194A, wild-type *Mtu*-AnPRT and wild-type *Sso*-AnPRT. Stereo diagram of A) *Mtu*-R194A chain A or B) *Mtu*-R194A chain B with anthranilate (blue) bound overlaid with wild-type *Mtu*-AnPRT (cyan) with 4FA (6 min soak) (green) bound, wild-type *Mtu*-AnPRT (magenta) with 4FA (6 s soak) (brown) bound, wild-type *Mtu*-AnPRT (yellow) with 6MA (30 min soak) (orange) bound and *Sso*-AnPRT (not shown) with anthranilate (white) bound. All PRPP/PP_i molecules are shown in pink, with Mg^{2+} colours mimicking the colour of the anthranilate-like ligand bound. Polar contacts are shown as yellow dashes, with water molecules shown as red spheres. (C) Surface representation of *Mtu*-R194A chain A (5 min anth soak) (purple) with anthranilate (blue) bound, overlaid with *Sso*-AnPRT (not shown) with anthranilate (green) bound. D) Surface representation of *Mtu*-R194A chain B (5 min anth soak) (purple) with anthranilate (blue) bound, overlaid with wild-type *Mtu*-AnPRT (not shown) with 4FA (6 min soak) (yellow) bound. Mg^{2+} (blue spheres) and PP_i (orange) from *Mtu*-R194A are also shown.

4.7.2.6 Interpretation of Structures

By comparing all of the variant *Mtu*-AnPRT structures that were captured in the presence of PRPP, Mg^{2+} and anthranilate, one can begin to form an understanding of the possible order of ligand binding events. As has been observed before in Section 4.7.1 and in the wild-type *Mtu*-AnPRT PRPP/Mg^{2+} bound structure, PRPP has the ability to bind to the *Mtu*-AnPRT *apo* enzyme. Additionally, the *Mtu*-R193A variant has demonstrated that anthranilate can bind to the enzyme in the non-productive Site 3 without PRPP or Mg^{2+} binding first, and corroborates with the wild-type *Mtu*-AnPRT structure with 4FA soaked in for 6 s, which has a single 4FA molecule bound in the outer site (Section 3.6). These observations indicate that the first substrate binding event in the ligand-free *Mtu*-AnPRT protein is either one of two options: either PRPP, or anthranilate in the non-productive outer site. The β2-α6 loop would be in the 'open' position for PRPP binding, or folded into the anthranilate channel for anthranilate binding in the outer site. The flexibility of the β2-α6 loop is evident in all structures obtained in this study, and would be a necessary feature for random binding events of PRPP or anthranilate in *Mtu*-AnPRT.

However, the concentration of PRPP (10 mM) used in the crystallisation conditions is very high when compared to the apparent K_M value, and it is possible that this high concentration artificially shifts the equilibrium between the solvent and *Mtu*-AnPRT towards a PRPP-bound state. This would create a situation in which PRPP is already bound to *Mtu*-AnPRT prior to anthranilate exposure, and thus would not give an accurate insight into the natural order of binding events. In the presence of PRPP and Mg^{2+}, *Mtu*-R193A showed the β2-α6 loop folded into the active site in both chains, with no ligands bound. However, when anthranilate is also present a single anthranilate molecule alone is bound in the outer site, despite the presence of PRPP and Mg^{2+}. Given the decrease in catalytic turnover and anthranilate binding ability of *Mtu*-R193A (Section 4.6.1) coupled with the short anthranilate soak time of 3 s, it is reasonable to assume that the binding of anthranilate in the outer site is the first ligand binding event in this variant, and perhaps in *Mtu*-AnPRT. The positioning of the β2-α6 loop in the anthranilate channel likely prevents the anthranilate bound in the outer site from progressing further until PRPP is bound, whereupon it could simultaneously assist in moving the outer site anthranilate along the channel towards the catalytically relevant inner site.

The structure of *Mtu*-R193L shows PP_i and Mg^{2+} bound in chain B, with the β2-α6 loop again folded into the anthranilate channel. It is possible that this variant has been captured in a post-reaction pose, and it could be suggested that movement of the β2-α6 loop back into this position somehow assists the product PRA in leaving the active site, leaving only PP_i and Mg^{2+} behind. This structure strengthens the argument for anthranilate binding prior to PRPP, as the β2-α6 loop has moved into a

conformation that has been seen to accommodate anthranilate binding. This leaves *Mtu*-AnPRT primed for further anthranilate binding before PP_i has left the active site.

The structure of *Mtu*-R194A, captured in the presence of PP_i, Mg^{2+} and anthranilate, is the only *Mtu*-AnPRT structure to be obtained with two anthranilate molecules bound. This can be explained in two ways, depending on the order of ligand-binding events for *Mtu*-AnPRT. If the enzyme does allow PRPP to bind first *in vivo*, it is likely that the β2-α6 loop would be closed over the PRPP molecule, and thus be unable to fold into the anthranilate channel. Without the β2-α6 loop blocking the anthranilate channel, anthranilate could likely diffuse along the channel unimpeded, which would also allow for the presence of at least two anthranilate molecules in the channel at once. If it is anthranilate that binds to *Mtu*-AnPRT first, the β2-α6 loop is likely to be folded into the anthranilate channel, based on the *Mtu*-R193A structure with anthranilate bound and the wild-type *Mtu*-AnPRT structure with 4FA soaked in for 6 s. When positioned in the anthranilate channel, the β2-α6 loop could shuttle anthranilate to the active site as required. If the latter scenario is correct, the *Mtu*-R194A structure could have potentially captured binding events pertaining to anthranilate inhibition, which is still possible for this variant (Section 4.6.2). If, as the *Mtu*-R193L variant suggests, the β2-α6 loop is required to fold into the anthranilate channel for PP_i release, the presence of two anthranilate molecules in the channel would prevent this loop movement from occurring. It is possible that the PP_i in *Mtu*-R194A is stuck in the active site for this reason.

If the binding of PRPP to *Mtu*-AnPRT facilitates the dissociation of PP_i, it seems likely that the anthranilate nucleophile would be appropriately positioned in the active site prior to PRPP. If PRPP did bind first, it could be assumed that the β2-α6 loop would stay in the closed position until the reaction is complete. This loop closure leaves no obvious alternative mechanism for anthranilate regulation or to stop nucleophilic attack from water molecules diffusing into the anthranilate channel. However, if anthranilate binds first at the outer site with the β2-α6 loop folded into the channel, PRPP could subsequently bind and immediately react with the available anthranilate, reducing the risk of unproductive catalysis.

Finally, the crystal structures discussed in this section also corroborate with the observation that *Mtu*-AnPRT utilises a sequential mechanism. The ternary mechanism equation describes substrate binding in their catalytically relevant sites; in this case the PRPP binding site and the catalytically relevant inner anthranilate site. As stated in Section 2.5.4, crystal structures of *Mtu*-AnPRT have indicated that the contacts for the catalytically relevant inner anthranilate site are only formed upon the binding of PRPP, where the β2-α6 loop is in the closed position.[44] The proposal that anthranilate

binding in the outer site precedes PRPP binding in the active site still conforms to this observation, as the outer anthranilate site is not catalytically relevant.

4.8 Summary

Point mutations to the TrpD gene were successfully carried out using PCR, with the formation of the *Mtu* mutants N138A, P180A, G107P, R193A, R193L and R194A confirmed via plasmid sequencing. These mutated plasmids were then successfully transformed into BL21 (DE3) pBB528/pBB541 cells. All six variant proteins were purified successfully, with CD spectra indicating they were all properly folded. Mass spectrometry was utilised to confirm that the masses of the variants were of the expected size, with DSF used to determine their temperatures of denaturation. *Mtu*-N138A, *Mtu*-P180A and *Mtu*-R194A showed similar melting temperatures to the wild-type value of 54.1 ± 0.3 °C, whereas *Mtu*-G107P showed a decrease in protein stability with a melting temperature of 45 ± 1 °C. Interestingly, *Mtu*-R193L and *Mtu*-R193A showed an increase in stability, with melting temperatures of 66.5 ± 0.6 °C and 64.9 ± 0.6 °C respectively.

Kinetic characterisation of all six *Mtu*-AnPRT variants was carried out using the UV enzyme-coupled assay developed in this study, with *Eco*-PRAI:InGPS as the coupling enzyme. *Mtu*-G107P was found to be totally inactive in this study. The apparent K_M values for the natural substrate PRPP, as catalysed by the remaining variants, showed little variation from the wild-type value of 48 ± 2 μM, with the exception of *Mtu*-N138A which had an increased K_M value of 160 ± 20 μM. The apparent K_M values for anthranilate for *Mtu*-R193A and *Mtu*-R193L were drastically increased when compared to the wild-type value of 2.0 ± 0.2 μM, with values of 480 ± 24 μM and 300 ± 18 μM respectively. The turnover numbers of *Mtu*-R193A and *Mtu*-R193L were also affected, with k_{cat} values of 0.075 ± 0.002 s^{-1} and 0.035 ± 0.001 s^{-1}. Anthranilate inhibition was observed for *Mtu*-P180A and *Mtu*-R194A, with K_i values of 440 ± 110 μM and 89 ± 11 μM respectively. Anthranilate inhibition was absent for *Mtu*-N138A.

Crystal structures were obtained for all *Mtu*-AnPRT variants with the exception of *Mtu*-G107P. *Mtu*-N138A, *Mtu*-P180A, *Mtu*-R193L and *Mtu*-R193A were co-crystallised in the presence of PRPP and Mg^{2+}. *Mtu*-N138A, *Mtu*-P180A, *Mtu*-R193L, *Mtu*-R193A and *Mtu*-R194A were also soaked with anthranilate for various time periods after co-crystallisation with PRPP and Mg^{2+}. *Mtu*-R193A and *Mtu*-R194A structures were obtained with clear evidence of anthranilate bound, with other variants captured in differing stages of catalysis.

Chapter 5

Inhibition of Variant *Mtu*-AnPRTs

5.1 Overview

Chapter 5 explores the potential inhibition of the AnPRT variants *Mtu*-N138A, *Mtu*-P180A and *Mtu*-R194A using the inhibitor compounds ACS172 and ACS142, previously tested on wild-type *Mtu*-AnPRT in Chapter 2.

The inhibition of these three variants by the anthranilate-like inhibitors ACS172 and ACS142 was successfully characterised using the enzyme-coupled assay described in Chapter 2. *Mtu*-N138A, *Mtu*-P180A and *Mtu*-R194A were each co-crystallised in the presence of PRPP, Mg^{2+} and either ACS172 or ACS142, with crystal structures obtained for all three variants bound to ACS172. A crystal structure of *Mtu*-R194A bound to ACS142 was also solved.

5.2 Introduction

The inhibition of wild-type *Mtu*-AnPRT using anthranilate-like inhibitor compounds has previously been investigated and discussed in Chapter 2. It was observed in structures of wild-type *Mtu*-AnPRT with inhibitors bound that many inhibitors utilised the outer site at the entrance to the anthranilate channel, making contacts to N138, R194 and P180. The inhibitors tested can be categorised into two groups: those with one aromatic ring, and those with multiple aromatic rings. Of the inhibitors that fall into the first category, ACS142 (Figure 5.1A) displayed the greatest inhibitory effect, with a K_i value of 8.5 ± 0.7 μM, and showed multiple binding modes to *Mtu*-AnPRT along the anthranilate channel. ACS172 (Figure 5.1B) had the lowest K_i value of the inhibitors defined by multiple aromatic rings (K_i = 5.5 ± 0.3 μM), though this inhibitor was the only compound to display pure non-competitive inhibition. ACS172 was also observed to bind in different sites along the anthranilate channel, with a total of three binding modes.

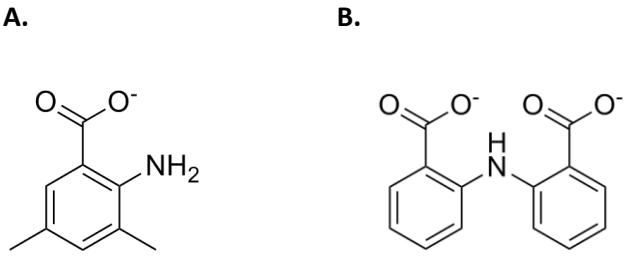

Figure 5.1 The chemical structure of A) ACS142 and B) ACS172.

As has been discussed in Chapter 4, the residues N138, P180 and R194 provide contacts for anthranilate binding at the outer site of *Mtu*-AnPRT, which is likely the first recognition site for anthranilate upon *Mtu*-AnPRT binding, and thus also for any anthranilate-like inhibitor compounds. The inhibitor compounds ACS142 and ACS172 were chosen to be tested with the variant *Mtu*-N138A, *Mtu*-P180A and *Mtu*-R194A, with the aim of investigating the effect of these outer site residues on inhibitor potency.

5.3 Kinetic Characterisation

The compounds ACS142 and ACS172 were tested for inhibition against the *Mtu*-AnPRT variants *Mtu*-N138A, *Mtu*-P180A and *Mtu*-R194A using the enzyme-coupled assay (Section 7.1.24/7.5.1), with K_i values listed in Table 5.1. Results were fitted to each of four inhibition equations (competitive, pure non-competitive, uncompetitive and mixed inhibition) and the χ^2 values compared to determine which fit best described the data.

Mtu-AnPRT variant	Inhibitor compound	K_i value (μM)	Type of inhibition
Wild-Type	ACS172	5.5 ± 0.3	Pure non-competitive
	ACS142	8.5 ± 0.7	Competitive
N138A	ACS172	16 ± 1	Pure non-competitive
	ACS142	563 ± 58	Uncompetitive
P180A	ACS172	45 ± 3	Pure non-competitive
	ACS142	1100 ± 60	Pure non-competitive
R194A	ACS172	35 ± 2	Pure non-competitive
	ACS142	348 ± 48	Competitive

Table 5.1 K_i values for ACS142 and ACS72 against wild-type/variant *Mtu*-AnPRTs.

The anthranilate channel present in *Mtu*-AnPRT complicates the understanding of the kinetically determined inhibition profiles. Crystal structures of wild-type *Mtu*-AnPRT have shown that ACS172 and ACS142 have the potential to bind in multiple sites along the channel, however, it is likely that these inhibitors first bind at the outer site prior to diffusion further along the channel. The diffusion of these inhibitors along the channel would then leave the same outer binding site available for subsequent inhibitor/anthranilate molecules to bind.

Traditionally, pure non-competitive inhibition occurs when an inhibitor compound can bind reversibly either to the free enzyme or to the enzyme-substrate complex, with identical dissociation constants (Figure 5.2). Usually, this would indicate that the inhibitor and substrate bind at different sites on the enzyme, and that this binding site has the same affinity for the inhibitor whether or not anthranilate was bound. However, the unique anthranilate channel present in *Mtu*-AnPRTs likely allows anthranilate or the inhibitors to bind in the outer site and then progress towards the inner site, leaving the outer site again open for anthranilate/inhibitor binding. The wild-type *Mtu*-AnPRT enzyme displays this type of inhibition behaviour with ACS172, which is postulated to occur due to the simultaneous presence of ACS172 and anthranilate within the anthranilate channel (discussed in Section 2.6.1). *Mtu*-N138A, *Mtu*-P180A and *Mtu*-R194A had no effect on the mode of inhibition of ACS172, demonstrating pure non-competitive inhibition for all three variants. This observation indicates that removing any one of the residues N138, P180 or R194 does not detract from the enzyme's ability to accommodate both ACS172 and anthranilate within the anthranilate channel.

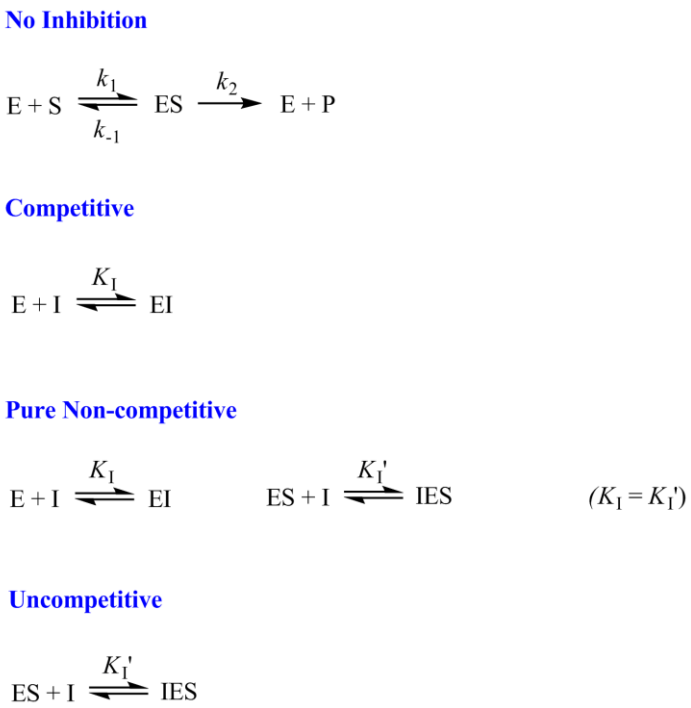

Figure 5.2 Reaction schemes describing uninhibited enzyme turnover as well as competitive, pure non-competitive and uncompetitive inhibition. Abbreviations are as follows: E = enzyme, S = substrate, I = inhibitor, k = rate constant, K_I = dissociation constant.

A decrease in inhibitor potency for ACS172 was observed for all three variants. The P180A mutation had the greatest effect on ACS172 potency, with an 8-fold increase in K_i value. *Mtu*-P180A showed a 2-fold increase in the K_M value of anthranilate, and had no effect on the maximum rate of catalysis.

Taken in this context, the decrease in ACS172 potency against *Mtu*-P180A is not largely significant. *Mtu*-R194A also demonstrated a decrease in ACS173 potency, though to a lesser extent than *Mtu*-P180A. *Mtu*-N138A had a negligible effect on ACS172 potency with a 3-fold increase in the K_i value, and showed a similar 4-fold increase in the K_M value of anthranilate. The absence of any significant differences between ACS172 potency against wild-type *Mtu*-AnPRT and *Mtu*-N138A is a surprising result, given that of the three residues P180, R194 and N138, the latter is the only one conserved.

The inhibition behaviour for ACS142 differed greatly between the three variants, with only *Mtu*-R194A still able to maintain the competitive inhibition demonstrated for wild-type *Mtu*-AnPRT. *Mtu*-R194A also showed the smallest change in the K_i value for this inhibitor, with a 40-fold increase. This 40-fold increase for *Mtu*-R194A is significant when compared to its relatively small 3-fold decrease in the binding affinity of anthranilate, as compared to wild-type *Mtu*-AnPRT.

Interestingly, the substitution of residue N138 changed the type of inhibition behaviour observed for ACS142 to uncompetitive, which indicates that an inhibitor can only bind to an enzyme-substrate complex, thus rendering the complex incapable of product formation (Figure 5.2). If it is assumed that ACS142 binds in the outer site of *Mtu*-N138A after anthranilate is already bound, a complex would be formed in which *Mtu*-N138A has anthranilate bound in the inner site and ACS142 bound in the outer site. The traditional definition of uncompetitive inhibition states that product formation does not occur, however, the unusual nature of the anthranilate channel in *Mtu*-AnPRT may allow anthranilate and PRPP to react, though product release could be prevented (Figure 5.3).

Mtu-N138A displays a 3-fold decrease in the binding affinity of PRPP, and therefore an alternative explanation for the uncompetitive inhibition observed for ACS142 could be that ACS142 binding in the outer site of *Mtu*-N138A instigates a further reduction in the binding affinity for PRPP. Thus, PRPP may not bind to *Mtu*-N138A at all in this scenario. Binding events outlined in Figure 5.3 also imply that prior to anthranilate binding, *Mtu*-N138A is in a conformation that cannot support ACS142 binding, perhaps caused by a higher intolerance of the additional methyl groups. *Mtu*-N138A also causes a decrease in ACS142 potency, with a 66-fold increase in K_i value.

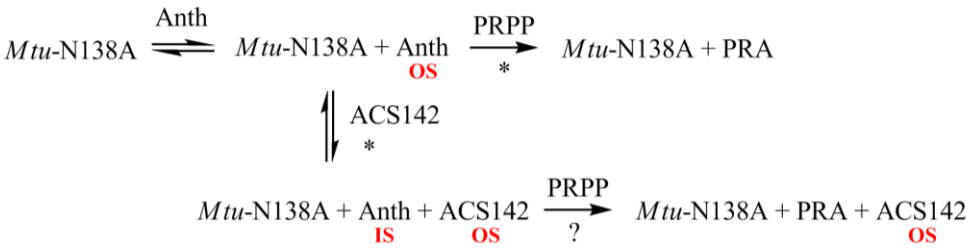

Figure 5.3 A possible inhibition scheme for *Mtu*-N138A in the presence of anthranilate (Anth), PRPP and ACS142. IS and OS denote inner site and outer site binding respectively. * indicates the diffusion of anthranilate from the outer site to the inner site. ? indicates that it is unclear whether this reaction occurs. Binding of anthranilate/ACS142 in the middle site is excluded for clarity.

The largest K_i value for ACS142 was observed with *Mtu*-P180A, which displayed a 130-fold increase compared to wild-type *Mtu*-AnPRT. This implies that the P180 residue is critical for the binding of this inhibitor. The substitution of the P180 residue for A180 has also changed the type of inhibition from competitive to pure non-competitive, which indicates that ACS142 can bind to *Mtu*-P180A either with or without anthranilate already bound (Figure 5.4), and that the preferred binding site of this inhibitor in this enzyme variant is not the catalytic site (inner site) for anthranilate.

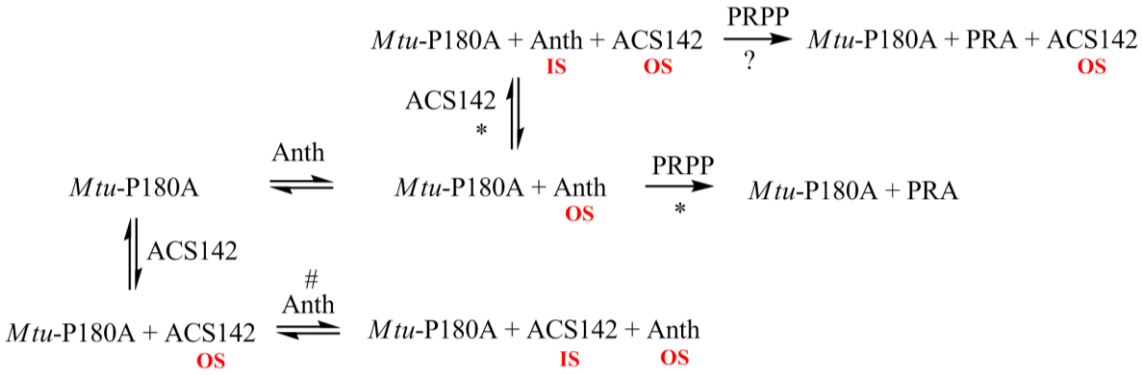

Figure 5.4 A possible inhibition scheme for *Mtu*-P180A in the presence of anthranilate (Anth), PRPP and ACS142. IS and OS denote inner site and outer site binding respectively. * indicates the diffusion of anthranilate from the outer site to the inner site. # indicates the diffusion of ACS142 from the outer site to the inner site. ? indicates that it is unclear whether this reaction occurs. Binding of anthranilate/ACS142 in the middle site is excluded for clarity.

Overall, *Mtu*-N138A, *Mtu*-P180A and *Mtu*-R194A have a more pronounced effect for the smaller inhibitor molecule ACS142 than for ACS172. This is likely due to the difference in size of the two

compounds, with the extra aromatic ring and carboxylate group on ACS172 able to make more contacts to *Mtu*-AnPRT, which would hold it more firmly in place when one contact is removed. The wild-type *Mtu*-AnPRT structure with ACS142 bound (PDB ID: 3UU1) shows that the ACS142 molecule makes a total of two hydrogen bonds to the surrounding protein when bound in the outer site. These hydrogen bonds are to R194 and N138, with a third C-H···π interaction between the ACS142 aromatic ring and the P180 proline ring. Removing any one of these residues would eliminate one third of the potential binding interactions for ACS142. In comparison, the wild-type *Mtu*-AnPRT structure with ACS172 bound (PDB ID: 3QQS) demonstrates ACS172 forming an additional salt bridge to R193 via its inner carboxylate group, when bound in Mode 1.

Of the three residues tested, P180 is the most crucial for the potency of these two inhibitors, as evidenced by the K_i values, highlighting the importance of the C-H···π interactions between the inhibitor aromatic rings and the proline ring.

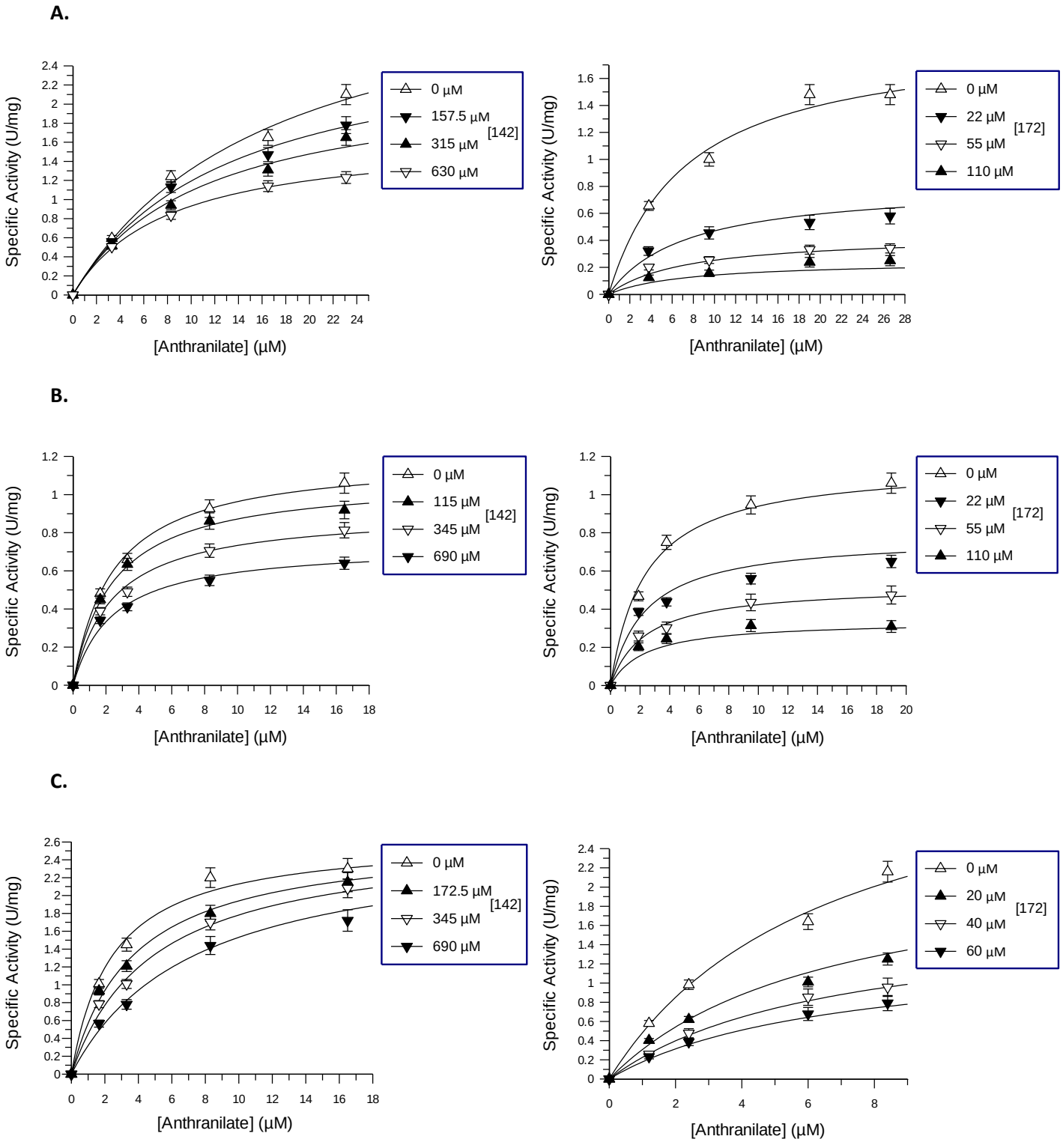

Figure 5.5 Inhibition graphs for determination of K_i values for ACS142 and ACS172 in the presence of variant *Mtu*-AnPRTs as calculated by the graphing software Grafit 5.[67] A) *Mtu*-N138A. B) *Mtu*-P180A. C) *Mtu*-R194A. Solutions contained PRPP held at a concentration of 0.6 mM, at a temperature of 25 °C, pH 8.0.

5.4 Structural Characterisation

The variants *Mtu*-N138A, *Mtu*-P180A and *Mtu*-R194A were co-crystallised with 10 mM PRPP, 10 mM $MgCl_2$ and either 10 mM ACS172 or 10 mM ACS142. The inhibitor concentrations used in this study differs to the 1-5 mM used for obtaining wild-type *Mtu*-AnPRT inhibitor bound structures (Section 2.7). Equimolar concentrations of PRPP, Mg^{2+} and inhibitor were used in an attempt to remove the potential for an artificial *Mtu*-AnPRT PRPP-bound state driven by high concentrations of PRPP. All crystals grew with the same diamond morphology observed for wild-type *Mtu*-AnPRT crystals (Figure 5.6), and had formed within 24 hours. The data processing and refinement statistics for the crystals described in this section can be found in Appendix 3, with ligand omit maps located in Appendix 4.

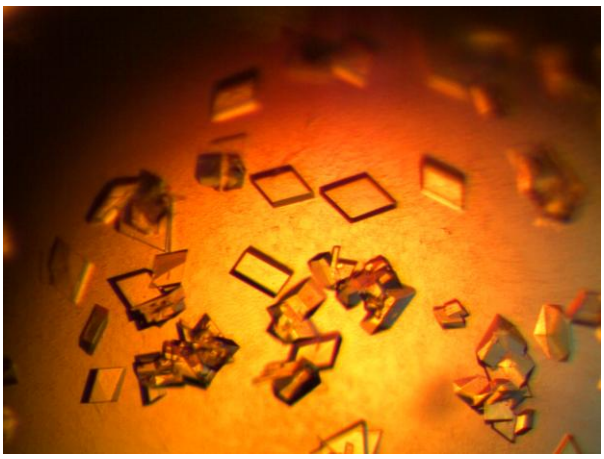

Figure 5.6 Crystals of *Mtu*-R194A co-crystallised with 10 mM PRPP, 10 mM $MgCl_2$ and 10 mM ACS172 in the presence of 0.2 M imidazole malate (pH 8.5) and 13% PEG-4000 (w/v).

5.4.1 Structures Containing ACS172

Crystal structures of the variants *Mtu*-N138A, *Mtu*-P180A and *Mtu*-R194A were successfully obtained in the presence of ACS172. PRPP and Mg^{2+} were also present in the crystal conditions, but none of the structures showed positive density for these ligands bound anywhere in the asymmetric unit. Inspection of the asymmetric units of these structures showed the presence of two separate *Mtu*-AnPRT monomers, however, dimers could be generated via crystallographic symmetry. These structures are compared to the wild-type *Mtu*-AnPRT structure with PRPP, Mg^{2+} and ACS172 bound (PDB ID: 3QQS).

5.4.1.1 *Mtu*-N138A/PRPP/Mg^{2+}/ACS172

The structure of *Mtu*-N138A was elucidated in the presence of ACS172 to a resolution of 2.4 Å. Chain A of *Mtu*-N138A shows ACS172 bound in the anthranilate outer site, in a mode similar to that of 'Mode 3' as described for wild-type *Mtu*-AnPRT (Section 2.7). An overlay of chain A with chain C from the wild-type structure (RMSD = 0.392 Å) shows the Mode 3 ligands bound in a slightly different conformation, with the two carboxylate groups of the *Mtu*-N138A ACS172 molecule making hydrogen bonds to R194 as well as C-H···π interactions to P180 (Figure 5.7A). The wild-type ACS172 molecule also makes these contacts, though the carboxylate group of the inner aromatic ring makes an extra hydrogen bond with N138. Another significant difference between the two structures is the presence of an additional ACS172 molecule further into the anthranilate channel in the wild-type structure. The absence of this second molecule in *Mtu*-N138A could point to the importance of residue N138 for ACS172 movement up the anthranilate channel, and thus also for anthranilate movement. The position of the R193 side-chain in *Mtu*-N138A chain A could not be determined with confidence due to a lack of electron density, and has been modelled in as an alanine.

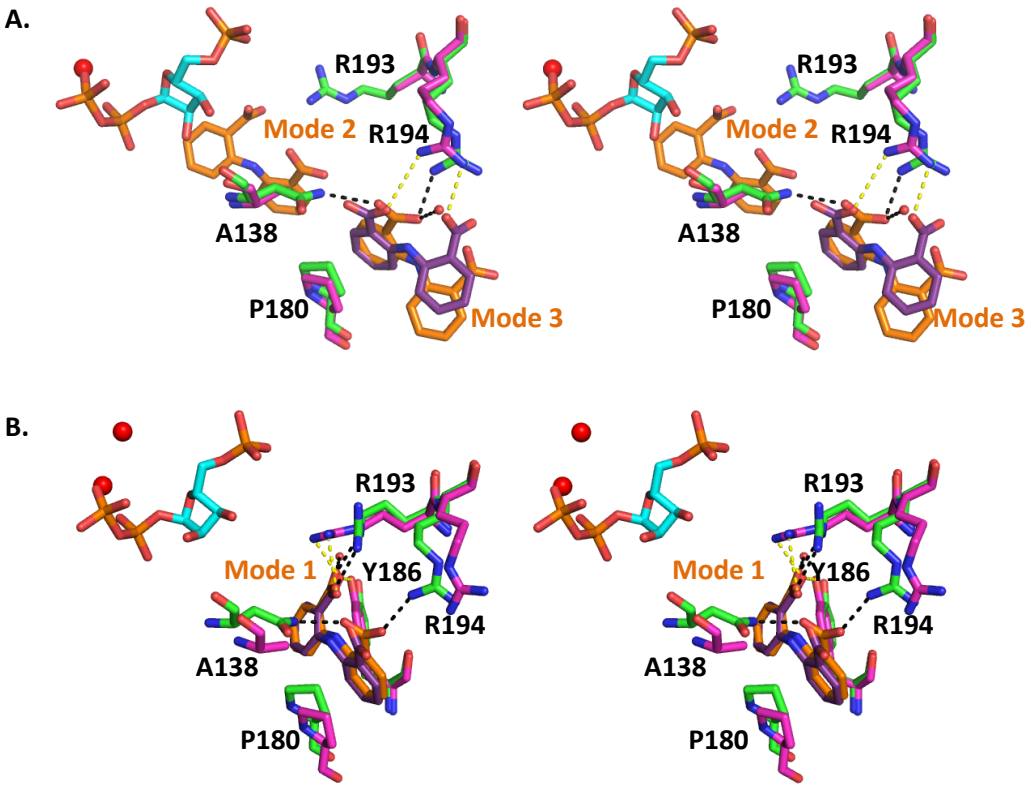

Figure 5.7 Stereo diagrams of ACS172 binding in *Mtu*-N138A and wild-type *Mtu*-AnPRT. Wild-type *Mtu*-AnPRT (green) with PRPP (cyan), Mg^{2+} (red spheres) and ACS172 (orange) bound is overlaid with *Mtu*-N138A (magenta) with ACS172 (purple) bound. Polar contacts for wild-type *Mtu*-AnPRT bound ACS172 and *Mtu*-N138A bound ACS172 are shown as black and yellow dashes respectively. The binding modes of wild-type *Mtu*-AnPRT bound ACS172 are indicated by orange text. Residue numbers for *Mtu*-N138A are indicated by black text. A) *Mtu*-N138A chain A overlaid with wild-type chain C. B) *Mtu*-N138A chain B overlaid with wild-type chain A.

Chain B of *Mtu*-N138A shows ACS172 (occupancy = 0.8) bound in a position almost identical to 'Mode 1' of ACS172 bound to wild-type, however, differing hydrogen bond contacts are made between the two molecules (Figure 5.7B). The *Mtu*-N138A structure has the carboxylate group of the inner aromatic ring hydrogen bonded to Y186, with a salt bridge formed with R193. No contacts are made by the carboxylate group of the outer aromatic ring. The ACS172 molecule bound in chain A of the wild-type structure is hydrogen bonded to R194 and N138 via the carboxylate group of the outer aromatic ring, and forms a salt bridge with R193 via the carboxylate group of the inner aromatic ring.

5.4.1.2 *Mtu*-P180A/PRPP/Mg^{2+}/ACS172

The crystal structure of *Mtu*-P180A was obtained with one ACS172 molecule bound in each of the two monomers present, at a resolution of 1.95 Å. An overlay of *Mtu*-P180A chain A with wild-type chain A (RMSD = 0.269 Å) shows the positions of the two ACS172 molecules (in Mode 1) to be almost identical (Figure 5.8A). Both ACS172 molecules make hydrogen bond contacts with R194 and N138 via their outer aromatic ring carboxylate groups; two residues which appear to hold the outer aromatic ring in place despite the lack of C-H···π interactions caused by the absence of P180. The *Mtu*-P180A-bound ACS172 carboxylate group on the inner aromatic ring is hydrogen bonded to N138, with a salt bridge formed with R193.

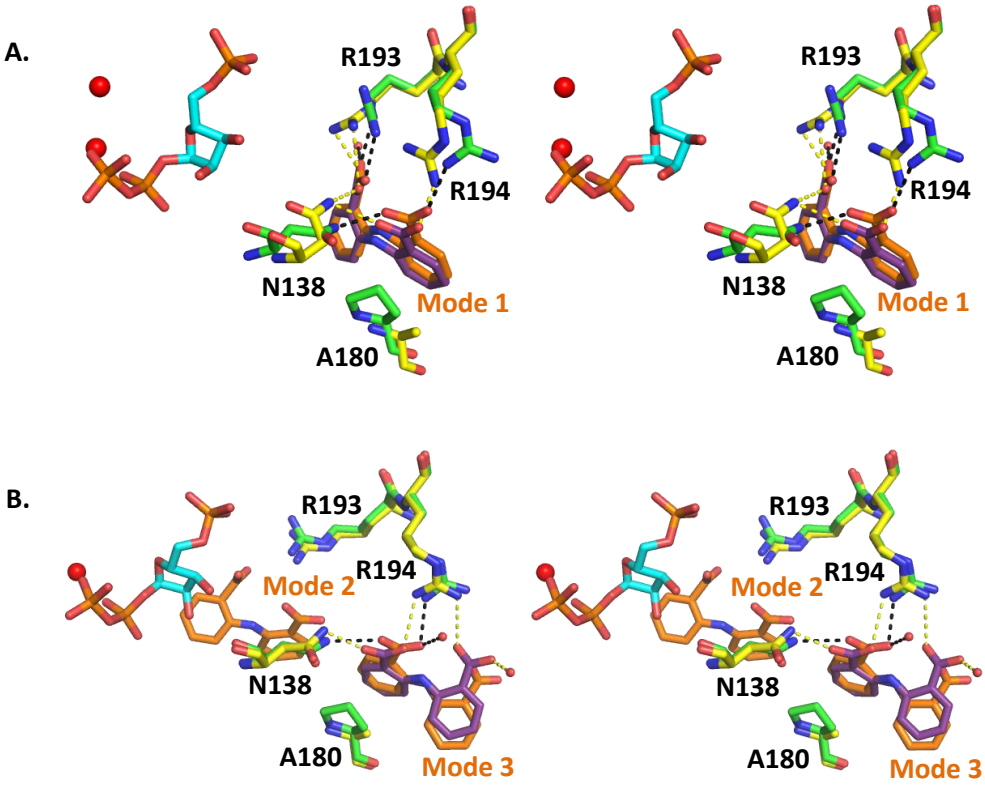

Figure 5.8 Stereo diagrams of ACS172 binding in *Mtu*-P180A and wild-type *Mtu*-AnPRT. Wild-type *Mtu*-AnPRT (green) with PRPP (cyan) Mg^{2+} (red spheres) and ACS172 (orange) bound is overlaid with *Mtu*-P180A (yellow) with ACS172 (purple) bound. Polar contacts for wild-type *Mtu*-AnPRT bound ACS172 and *Mtu*-P180A bound ACS172 are shown as black and yellow dashes respectively. The binding modes of wild-type *Mtu*-AnPRT bound ACS172 are indicated by orange text. Residue numbers for *Mtu*-P180A are indicated by black text. A) *Mtu*-P180A chain A overlaid with wild-type chain A. B) *Mtu*-P180A chain B overlaid with wild-type chain C.

An overlay of *Mtu*-P180A chain B with wild-type chain C (RMSD = 0.274 Å) shows ACS172 bound in Mode 3 (Figure 5.8B). The carboxylate group on the outer aromatic ring makes hydrogen bond contacts to R194 and a water molecule, while the carboxylate group on the inner aromatic ring hydrogen bonds to R194 and N138. The ACS172 molecule bound to the wild-type structure shows the inner aromatic ring in an almost identical position to the ACS172 molecule from *Mtu*-P180A, with similar hydrogen bonds made. This indicates that the replacement of P180 with A180 has little effect on the orientation of the inner aromatic ring of Mode 3, and that hydrogen bonds to R194 and N138 are sufficient to hold this ring in the position displayed in wild-type *Mtu*-AnPRT. The outer aromatic ring of the ACS172 molecule bound to *Mtu*-P180A is slightly displaced relative to the position observed in the wild-type *Mtu*-AnPRT ACS172, which is likely due to the lack of potential hydrogen bonds available for this ring, rendering it more mobile.

5.4.1.3 *Mtu*-R194A/PRPP/Mg^{2+}/ACS172

The structure of *Mtu*-R194A with ACS172 bound was solved at a resolution of 2.06 Å, with one ACS172 molecule bound in each monomer. Both chain A and chain B of *Mtu*-R194A show ACS172 bound in Mode 1 (Figure 5.9), making it the only variant structure to have both ACS172 molecules in the same binding mode, though the ACS172 in chain B is at an occupancy of 0.8. An overlay of *Mtu*-R194A chain A with wild-type *Mtu*-AnPRT chain A (RMSD = 0.298 Å) shows a similarity in the position of both ACS172 and the surrounding residues, with the inner carboxylate group hydrogen bonded to R193, Y186 and a water molecule, with the outer carboxylate group hydrogen bonded to N138 only.

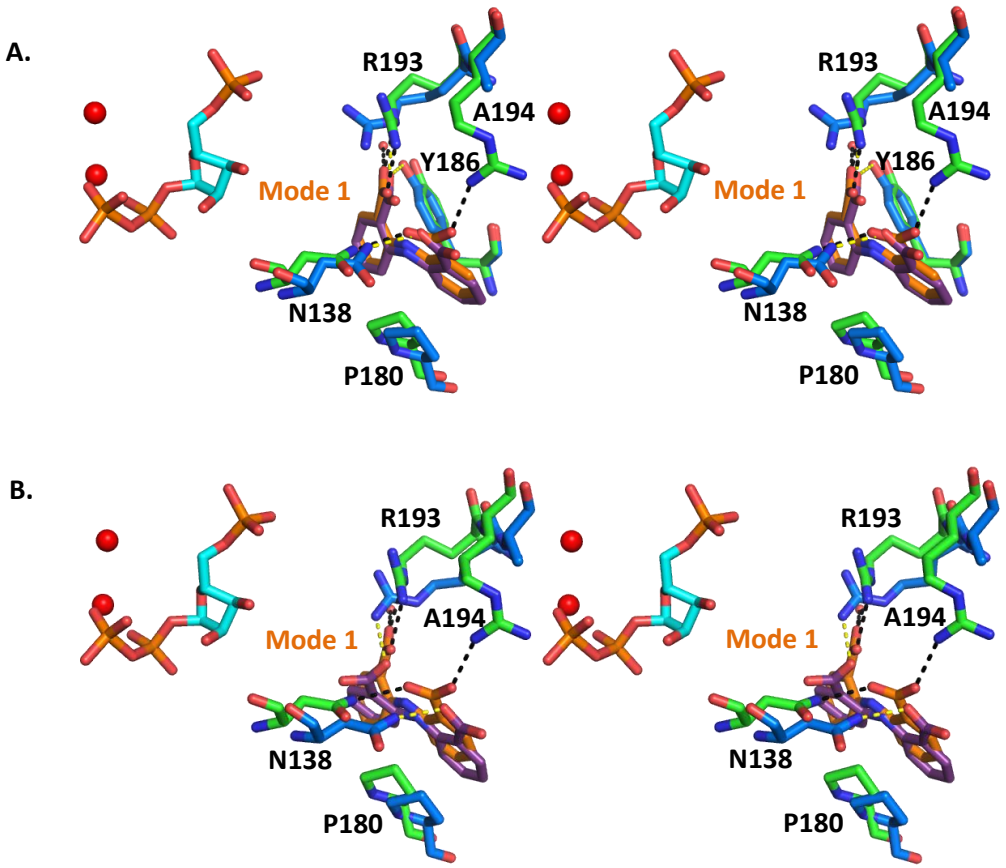

Figure 5.9 Stereo diagrams of ACS172 binding in *Mtu*-R194A and wild-type *Mtu*-AnPRT. Wild-type *Mtu*-AnPRT (green) with PRPP (cyan) Mg^{2+} (red spheres) and ACS172 (orange) bound is overlaid with *Mtu*-R194A (blue) with ACS172 (purple) bound. Polar contacts for wild-type *Mtu*-AnPRT bound ACS172 and *Mtu*-R194A bound ACS172 are shown as black and yellow dashes respectively. The binding modes of wild-type *Mtu*-AnPRT bound ACS172 are indicated by orange text. Residue numbers for *Mtu*-R194A are indicated by black text. A) *Mtu*-R194A chain A overlaid with wild-type chain A. B) *Mtu*-R194A chain B overlaid with wild-type chain A.

An overlay of *Mtu*-R194A chain B with wild-type *Mtu*-AnPRT (RMSD = 0.629 Å) shows an apparent difference in the positions of N138 and P180, which could be due to the disordered nature of the *Mtu*-R194A β2-α6 loop. Despite this residue displacement, the hydrogen bond contacts formed between ACS172 and *Mtu*-R194A are still similar to those made between ACS172 and wild-type, with the former hydrogen bonded to N138 and R193. Interestingly, a salt bridge between R193 and the inner carboxylate group of the ACS172 molecule bound to *Mtu*-R194A is not observed in either chain of this structure. This observation could indicate the importance of the hydrogen bond between R194 and the outer carboxylate group of ACS172 in positioning the ACS172 molecule correctly for effectual channel shuttling.

5.4.1.4 Interpretation of Structures

In all three of the variant structures obtained with ACS172 bound, it is interesting to notice that none of them have either PRPP or Mg^{2+} bound, despite their presence in the crystallisation conditions in an equimolar ratio with ACS172. Extra coiling at the N-terminus of the α5 helix and displacement of the α11''-α11 loop is present in every variant protein chain with ACS172 bound, with the exception of *Mtu*-R194A chain A. These structural features are present in several crystal structures discussed in Chapter 4, where PRPP is absent or atypically bound. As discussed in Section 4.7.1.5, it is possible that the β2-α6 loop movement from the anthranilate channel to the open position could facilitate the initial stages of PRPP binding, which could simultaneously cause the uncoiling of the α5 helix. If this hypothesis is correct, it is possible that these variant structures with ACS172 bound have captured events preceding PRPP and Mg^{2+} binding. There do not seem to be any structural features preventing PRPP or Mg^{2+} from binding to *Mtu*-R194A chain A, however, as the β2-α6 loop is in the open conformation (Figure 5.10). Density for the β2-α6 loop is undefined in all other chains of the variant structures.

If *Mtu*-AnPRT requires anthranilate binding in the outer site to precede PRPP binding, it could be assumed that the anthranilate-like inhibitor ACS172 would also precede PRPP binding. Despite the presence of PRPP and Mg^{2+} in the crystallisation conditions, only one ACS172 molecule is bound per monomer in either Mode 1 or Mode 3 (where one aromatic ring is bound in the outer site), indicating that ACS172 binding is likely the first binding event. Adding weight to this suggestion are the observations that the variants *Mtu*-N138A, *Mtu*-P180A and *Mtu*-R194A all have the ability to bind PRPP as was observed in the crystal structures described in Section 4.7, but in these experimental conditions they do not.

The structures outlined in Section 5.4.1 were obtained in the presence of equimolar concentrations of PRPP, Mg^{2+} and ACS172 (10 mM), yet only the presence of ACS172 was observed in a bound state. Previous structures of wild-type *Mtu*-AnPRT with ACS172 bound were obtained by co-crystallisation with 10 mM PRPP, 10 mM $MgCl_2$ and 1-5 mM ACS172, and occupancy for all three ligands was observed.[41a] Assuming that PRPP, Mg^{2+} and ACS172 have similar binding affinities for wild-type *Mtu*-AnPRT, the excess concentrations of PRPP and Mg^{2+} in the crystal drop may have driven the *Mtu*-AnPRT protein towards a PRPP/Mg^{2+} bound state, according to Le Chatelier's principle.[76] If this assumption is correct, it could explain the differences in ligand binding observed between the wild-type and variant *Mtu*-AnPRT structures in the presence of PRPP, Mg^{2+} and ACS172.

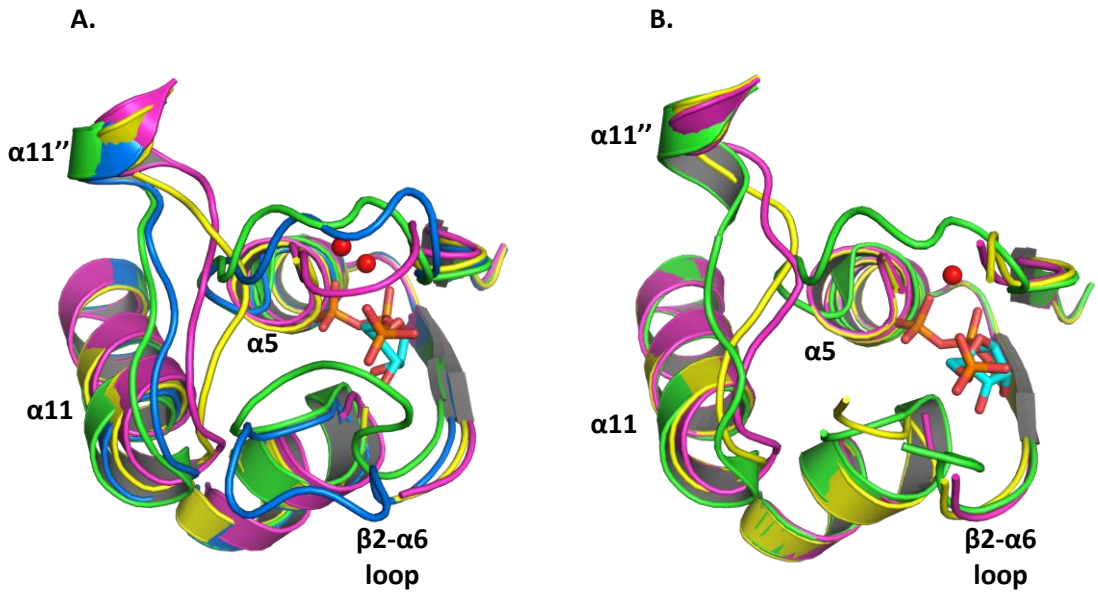

Figure 5.10 An active site comparison of wild-type/variant *Mtu*-AnPRT structures with ACS172 bound. A) An overlay of chain A wild-type *Mtu*-AnPRT (green) with PRPP (cyan), Mg^{2+} (red spheres) and ACS172 bound with *Mtu*-N138A chain A (magenta), *Mtu*-P180A chain B (yellow), and *Mtu*-R194A chain A (blue). B) An overlay of chain C wild-type *Mtu*-AnPRT (green) with PRPP (cyan), Mg^{2+} (red spheres) and ACS172 bound with *Mtu*-N138A chain B (magenta) and *Mtu*-P180A chain A (yellow).

5.4.2 Structures Containing ACS142

Crystals were grown of *Mtu*-N138A, *Mtu*-P180A and *Mtu*-R194A co-crystallised with PRPP, Mg^{2+} and ACS142. Unfortunately, *Mtu*-N138A and *Mtu*-P180A did not yield diffraction-quality crystals, and thus only the structure of *Mtu*-R194A with ACS142 bound was obtained during this study. This structure showed *Mtu*-R194A bound to ACS142 alone, with no positive density to signify PRPP or Mg^{2+} bound anywhere in the asymmetric unit. This structure is compared to the wild-type *Mtu*-AnPRT structure with PRPP, Mg^{2+} and ACS142 bound (PDB ID: 3UU1).

5.4.2.1 *Mtu*-R194A/PRPP/Mg^{2+}/ACS142

The crystal structure of *Mtu*-R194A with ACS142 bound was solved at a resolution of 2.23 Å, and contained two separate monomers in the asymmetric unit, with dimers generated via crystallographic symmetry. Chain A of *Mtu*-R194A has two ACS142 molecules bound within the anthranilate channel: one in the outer site, and one in the inner site at 0.8 occupancy. When overlaid with chain B of the wild-type *Mtu*-AnPRT structure with ACS142 bound (RMSD=0.364 Å) it can be observed that both ACS142 molecules in the outer site are almost identical in their positions (Figure 5.11A). The *Mtu*-R194A ACS142 molecule in the outer site is hydrogen bonded to N138 via its

carboxylate group, and is oriented parallel to P180. The wild-type ACS142 molecule in the outer site makes additional hydrogen bonds to R194 and three water molecules. The *Mtu*-R194A ACS142 inhibitor bound in the outer site is hydrogen bonded to R193 alone via its carboxylate group, whereas the wild-type ACS142 is hydrogen bonded via its carboxylate group to R193 and a water molecule, and is hydrogen bonded to two water molecules via its amino group. The ACS142 molecules bound in the inner site are significantly different in their positions, with the amino group of the *Mtu*-R194A ACS142 molecule pointing away from the PRPP binding site instead of towards it, as can be seen for the wild-type ACS142 molecule. However, the wild-type *Mtu*-AnPRT structure shows the outer site ACS142 molecule with its amino group pointing away from N138, in a different orientation to the inner site ACS142 molecule. This could indicate that ACS142 has the ability to diffuse through the channel in either orientation, which is perhaps warranted by the symmetry of the ACS142 methyl groups relative to the carboxylate group.

It is possible that the *Mtu*-R194A ACS142 molecule present in the inner site cannot be modelled in at full occupancy due to movement of this molecule from the middle site to the inner site. The F_o-F_c map for chain A of *Mtu*-R194A shows large areas of density at 3.0 σ, which are not present in the $2F_o$-F_c map, indicating a possible transition of ACS142 from the middle site towards the inner site (Figure 5.11B).

Chain B of the *Mtu*-R194A structure has only one ACS142 molecule bound within the anthranilate channel, located in the outer site (Figure 5.11C). By superimposing *Mtu*-R194A chain B onto wild-type chain A, it can be seen that the position of *Mtu*-R194A ACS142 is positioned closer to H183, presumably caused by the removal of the potential hydrogen bond between the ACS142 carboxylate group and the absent R194 side-chain. The positions of the *Mtu*-R194A residues N138 and P180 have also shifted, possibly to accommodate this different ACS142 binding position. In this outer site binding mode, the *Mtu*-R194A ACS142 molecule makes hydrogen bond contacts to N138 via its carboxylate group, and to a single water molecule via its amino group. In comparison, the wild-type ACS142 molecule makes hydrogen bonds to R193, R194 and N138 via its carboxylate group.

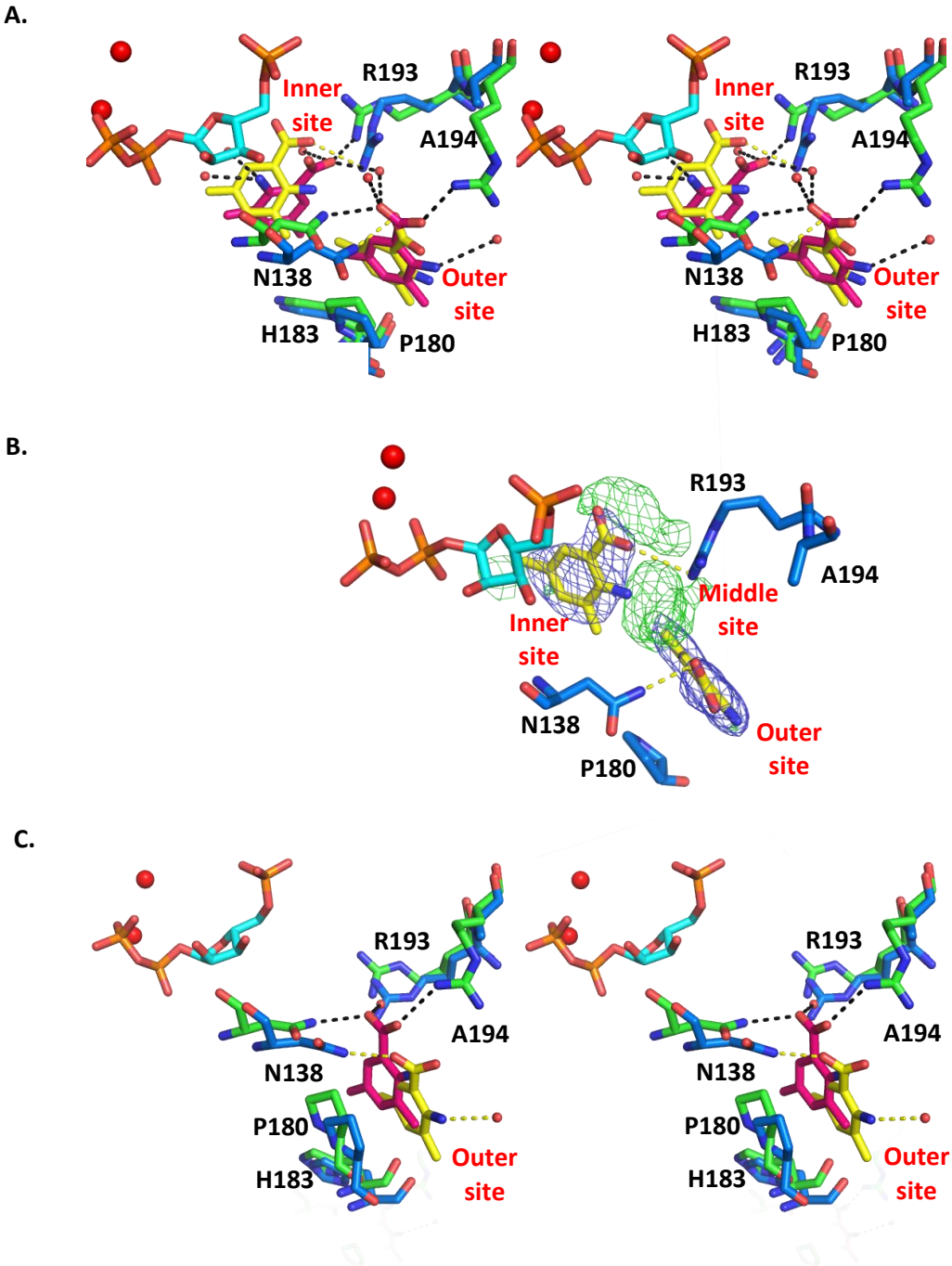

Figure 5.11 A comparison of ACS142 binding in *Mtu*-R194A and wild-type *Mtu*-AnPRT. A) *Mtu*-R194A chain A (blue) with ACS142 (yellow) bound overlaid with wild-type chain B (green) with PRPP (cyan), Mg^{2+} (red spheres) and ACS142 (pink) bound. Polar contacts for wild-type *Mtu*-AnPRT bound ACS142 and *Mtu*-R194A bound ACS142 are shown as black and yellow dashes respectively. Residue numbers for *Mtu*-R194A are indicated by black text. B) *Mtu*-R194A chain A overlaid with wild-type chain B. The $2F_o$-F_c map for *Mtu*-R194A is shown as blue mesh, contoured at 1.0 σ. The F_o-F_c map for *Mtu*-R194A is shown as green mesh, contoured at 3.0 σ. C) *Mtu*-R194A chain B overlaid with wild-type chain A.

5.4.2.2 Interpretation of Structure

It can again be noticed in the *Mtu*-R194A structure that neither PRPP nor Mg^{2+} are bound, despite their presence in the crystallisation conditions. Extra coiling of the α5 helix can be observed in both chains which would likely preclude these ligands from binding, as well as the displacement of the α11''-α11 loop present in chain B (Figure 5.12). As was discussed in Section 5.4.1.4, it is possible that the β2-α6 loop movement from the anthranilate channel to the open position could facilitate the initial stages of PRPP binding, which could simultaneously cause the uncoiling of the α5 helix. The *Mtu*-R194A structure with ACS142 bound is therefore likely to have captured events preceding PRPP and Mg^{2+} binding, underlining the enzyme's preference for binding the anthranilate-like ACS142 molecule prior to the PRPP/Mg^{2+} ligands.

The presence of two ACS142 molecules within the anthranilate channel without PRPP or Mg^{2+} bound indicates that the closing of the β2-α6 loop upon PRPP binding is not required for this inhibitor to move from the outer site to the inner site in the *Mtu*-R194A variant. The role of residue R194 could be to assist in holding anthranilate-like compounds in the outer site until PRPP is bound which, if correct, could also explain the presence of two anthranilate molecules within the anthranilate channel in the *Mtu*-R194A structure discussed in Chapter 4.

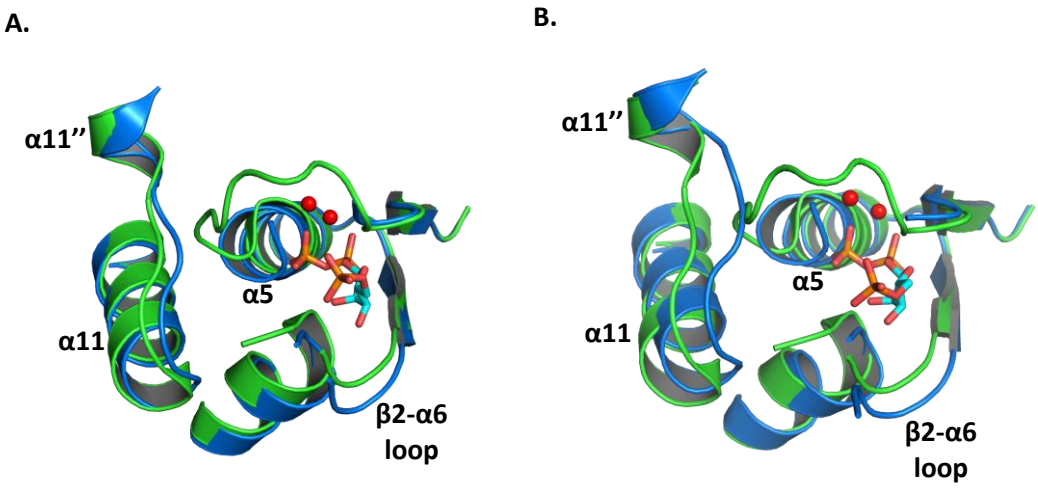

Figure 5.12 An active site comparison of *Mtu*-R194A and wild-type *Mtu*-AnPRT structures with ACS142 bound. A) An overlay of wild-type *Mtu*-AnPRT chain B (green) with PRPP (cyan), Mg^{2+} (red spheres) and ACS142 (not shown) bound with *Mtu*-R194A chain A (blue) with ACS142 bound (not shown). B) An overlay of wild-type *Mtu*-AnPRT chain A (green) with PRPP (cyan), Mg^{2+} (red spheres) and ACS142 (not shown) bound with *Mtu*-R194A chain B (blue) with ACS142 (not shown) bound.

The *Mtu*-R194A structure with ACS142 bound also suggests that R194 plays a key role in orientating the inhibitor for efficient shuttling further through the anthranilate channel, as evidenced by the differences in ACS142 binding poses between the wild-type and *Mtu*-R194A structures. As ACS142 has a similar structure to anthranilate, it can be assumed that this would apply to wild-type *Mtu*-AnPRT also. The binding of ACS142 to *Mtu*-R194A was disrupted to a greater extent than the larger ACS172 inhibitor, which again suggests an important hydrogen bonding role for the non-conserved R194 residue.

5.5 Summary

The inhibitors ACS172 and ACS142 were tested against the *Mtu*-N138A, *Mtu*-P180A and *Mtu*-R194A variants using the enzyme-coupled assay. None of the variants changed the mode of inhibition of ACS172, with all displaying pure non-competitive behaviour. The absence of residue P180 had the greatest effect on the inhibitor potency of ACS172, with *Mtu*-P180A showing an 8-fold increase in the K_i value. *Mtu*-N138A and *Mtu*-P180A both changed the mode of inhibition of ACS142 from competitive to uncompetitive and pure non-competitive respectively. *Mtu*-P180A had the greatest effect on inhibitor potency for ACS142 also, with a 130-fold increase in the K_i value.

Crystal structures were obtained for *Mtu*-N138A, *Mtu*-P180A and *Mtu*-R194A in the presence of PRPP, Mg^{2+} and ACS172, with the inhibitor found to bind in the anthranilate outer site either in Mode 1 or Mode 3. A crystal structure was also solved for *Mtu*-R194A in the presence of PRPP, Mg^{2+} and ACS142, with two inhibitor molecules bound to chain A of the structure, and one inhibitor molecule bound to chain B. Interestingly, neither PRPP nor Mg^{2+} were observed to bind to any of the structures obtained in this chapter.

Chapter 6

Discussion

6.1 Key Findings of This Thesis

The aim of this research was to provide further insight into the active site machinery of *Mtu*-AnPRT, in order to aid future tuberculosis drug development. To achieve this goal, the wild-type *Mtu*-AnPRT enzyme was successfully purified and physically characterised using a range of techniques including DSF and CD. The kinetic characterisation of *Mtu*-AnPRT was accomplished using a novel enzyme-coupled UV-based assay, incorporating *Mtu*-AnPRT and *Eco*-PRAI:InGPS, which monitored the formation of InGP. Subjecting *Mtu*-AnPRT to high concentrations of anthranilate revealed a substantial decrease in enzyme activity, indicative of anthranilate inhibition. The successful characterisation of several inhibitor compounds was achieved using this assay, which revealed a 'bi-anthranilate'-like inhibitor (ACS172) as the most potent against *Mtu*-AnPRT. Crystal structures of *Mtu*-AnPRT with these compounds bound identified several common inhibitor binding residues (N138, P180, R193 and R194) as well as a third potential binding site for anthranilate located at the entrance to the anthranilate channel. A new *apo* structure of *Mtu*-AnPRT was also elucidated in the absence of the crystal additive benzamidine, which highlights the rearrangement of several *Mtu*-AnPRT helices to accommodate this compound in previous *Mtu*-AnPRT structures.

The substrate specificity of *Mtu*-AnPRT was probed using a range of fluoro-, methyl- and methoxy-substituted anthranilate analogues. The ability of *Mtu*-AnPRT to utilise these analogues as substrates was tested using a commercially available PP_i assay. All fluoro-analogues were turned over by *Mtu*-AnPRT at a catalytic rate comparable to the natural substrate anthranilate, with analogue inhibition of *Mtu*-AnPRT displayed at high concentrations. Methyl-substituted analogues were also accepted as substrates for *Mtu*-AnPRT, though with heavily decreased binding affinities and at relatively slow catalytic rates. The methoxy-substituted compounds were not viable substrates. *Mtu*-AnPRT is therefore able to tolerate small additional functional groups on the aromatic ring of anthranilate. The products formed by the reaction of *Mtu*-AnPRT with anthranilate and the substrate analogues were characterised using ^{1}H NMR spectroscopy, which confirmed that *Mtu*-AnPRT catalysed production of PRA-substituted compounds and also revealed the presence of PRA anomers. These α and β anomers were found to interconvert via an imine intermediate using mass spectrometry experiments. The PRA-substituted products, formed via the *Mtu*-AnPRT catalysis of PRPP and anthranilate analogues, were also confirmed as viable substrates for *Eco*-PRAI:InGPS, with the exception of 3M-PRA.

Six variant *Mtu*-AnPRT proteins were generated in order to examine the necessity of several active site residues identified as contributing to substrate binding. The variant proteins *Mtu*-G107P, *Mtu*-N183A, *Mtu*-P180A, *Mtu*-R193A, *Mtu*-R193L and *Mtu*-R194A were all successfully expressed and

purified, and displayed similar physical attributes to the wild-type *Mtu*-AnPRT enzyme. Kinetic characterisation of these variants showed that *Mtu*-G107P was the only variant that did not display catalytic activity. Wild-type *Mtu*-AnPRT, *Mtu*-N138A, *Mtu*-P180A and *Mtu*-R194A had similar binding affinities for both natural substrates, with comparable catalytic rates. *Mtu*-R193A and *Mtu*-R193L, on the other hand, demonstrated a substantial decrease both in the binding affinity of anthranilate and the catalytic rate when compared to wild-type *Mtu*-AnPRT, indicating a vital role for R193 in these events. Crystal structures of the variants in the presence of PRPP and Mg^{2+} showed an intact active site which retained the ability to bind these ligands, with the exceptions of *Mtu*-R193A, which remained ligand-free, and *Mtu*-G107P, which could not be crystallised. The crystal structures of *Mtu*-P180A and *Mtu*-R193L also revealed alternate binding modes for PRPP. Anthranilate soaking of these variants yielded structures in varying stages of catalysis, with only *Mtu*-R193A and *Mtu*-R194A showing positive density for anthranilate. These are the first structures of a *Mtu*-AnPRT variant with anthranilate bound, and show anthranilate bound in the outer site. *Mtu*-R194A also shows anthranilate bound in the middle site and inner site, and confirms the existence of three anthranilate binding sites.

Mtu-N138A, *Mtu*-P180A and *Mtu*-R194A were kinetically characterised in the presence of either ACS142, an anthranilate-like inhibitor with two additional methyl groups on the C3 and C5 positions, or ACS172, a 'bi-anthranilate'-like inhibitor. These variants were found not to have a significant effect on the potency of ACS172, with increases in K_i values similar to increases in the apparent K_M values for anthranilate, caused by the introduction of the N138A, P180A or R194A mutations. Consequently, no major differences were observed between the ACS172 binding modes of the variant and wild-type *Mtu*-AnPRT structures with ACS172 bound. *Mtu*-N138A, *Mtu*-P180A and *Mtu*-R194A did have a significant effect on the potency of ACS142, causing a minimum 40-fold increase in the K_i values. The structure of *Mtu*-R194A with ACS142 bound showed some inconsistencies in the binding modes of ACS142 in both the inner and outer sites, which could explain the reduction in potency of this inhibitor. The structures of *Mtu*-N138A and *Mtu*-P180A were not obtained in the presence of ACS142. PRPP and Mg^{2+} were not observed to bind to the variant structures with either ACS172 or ACS142 bound.

6.2 Reaction Mechanism

Both the structures of *Mtu*-AnPRT with alternate anthranilate-like substrates bound and the variant *Mtu*-AnPRT structures with anthranilate bound have confirmed the presence of three binding sites (inner, middle and outer) for anthranilate within the anthranilate channel of *Mtu*-AnPRT (Figure 6.1). The inner and middle anthranilate sites in these *Mtu*-AnPRT structures also confirm a correspondence in anthranilate binding sites to those of the *Sso*-AnPRT enzyme, that was suspected prior to this research. The *Mtu*-AnPRT structure with PRPP, Mg^{2+} and 4FA bound (6 min soak) (PDB ID: 4N5V) has 4FA bound in the inner site, in a pose that indicates the nucleophilic attack of 4FA at the C1 carbon of PRPP from the β-position. The distance from the 4FA amino group nitrogen to the C1 carbon of PRPP in the 4N5V structure is approximately 4.2 Å.

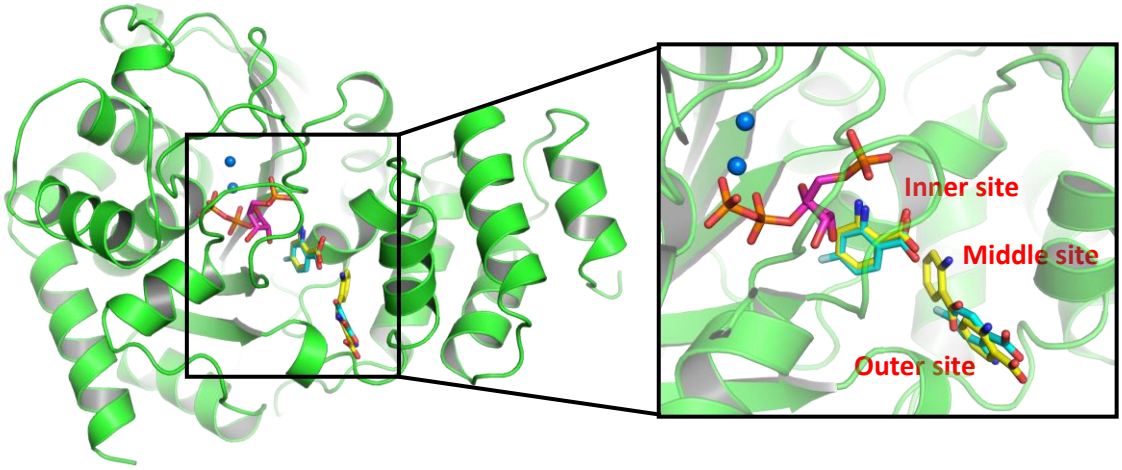

Figure 6.1 The three anthranilate binding sites within *Mtu*-AnPRT. Wild-type *Mtu*-AnPRT (green) with PRPP (magenta), Mg^{2+} (blue spheres) and 4FA (cyan) bound (PDB ID: 4N5V) is overlaid with the anthranilate molecules (yellow) from *Mtu*-R194A (5 min anth soak).

It is unclear whether the nucleophilic attack of anthranilate on PRPP takes place via an S_N1 or S_N2 mechanism, as the inversion of stereochemistry from the α-PRPP to the β-PRA product is dictated by the chiral active site of *Mtu*-AnPRT, and is characteristic of both reaction mechanisms. As yet, a detailed characterisation of the reaction mechanism of AnPRTs has not been carried out, however, the proposal that AnPRTs may have evolved from PyNPs due to structural similarities[43, 45] could suggest a similarity in the reaction mechanisms between these two enzymes. It has been proposed that some purine and pyrimidine NPs undergo an S_N1 mechanism, via ribosyl-oxocarbenium ion

migration between the phosphate and the purine/pyrimidine base. The structure of purine NP with the transition state mimic immucillin-H bound (PDB ID: 1B8O) supports this hypothesis (Figure 6.2).[71]

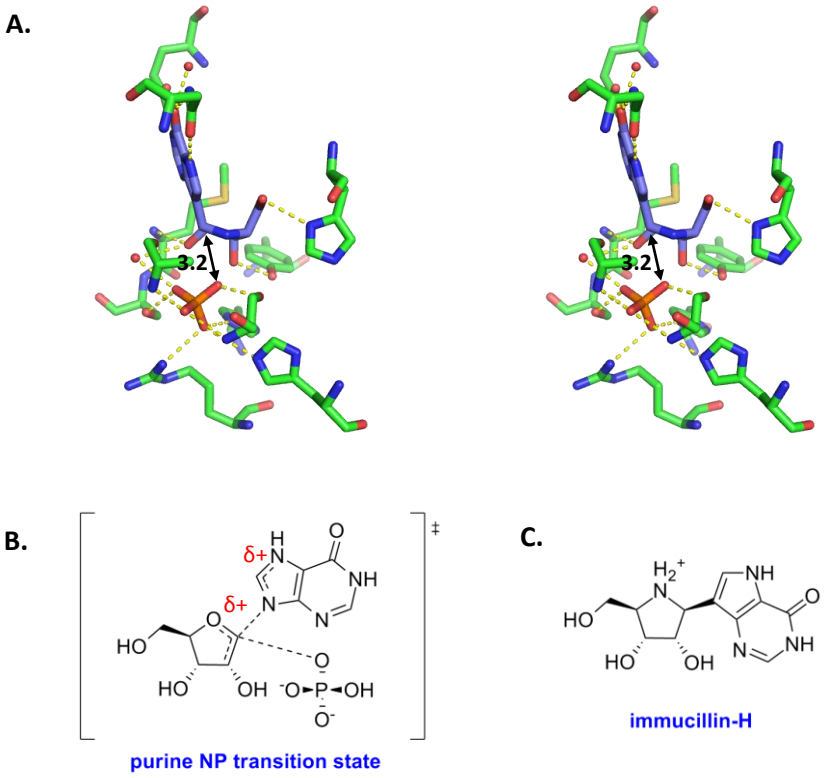

Figure 6.2 The bovine purine NP active site with the inhibitor immucillin-H bound. A) Stereo diagram of purine NP (green) (PDB ID: 1B8O) shown bound to the inhibitor immunocillin-H (purple) and a phosphate ion (orange). Polar contacts are shown as yellow dashes, with bond distances indicated in Å. The path of migration between the C1' carbon of immucillin-H and the phosphate oxygen, which would occur with the natural substrates, is outlined. B) The purine NP transition state,[77] which is mimicked by C) immucillin-H.

The purine/pyrimidine NPs catalyse the reversible phosphorolysis of purine/pyrimidine nucleosides to the free purines/pyrimidines and the corresponding ribose 1-phosphates, similar to the reaction catalysed by AnPRTs (Figure 6.3). The ribosyl-oxocarbenium ion migration mechanism is thought to be facilitated by the anchoring of the phosphate moiety by protein interactions and Mg^{2+} ion co-ordination, and the anchoring of the purine/pyrimidine moiety via protein interactions. In comparison, the ribose sugar of the purine/pyrimidine nucleoside creates few protein interactions. Upon formation of the ribosyl-oxocarbenium ion intermediate, the phosphate and the purine/pyrimidine moieties remain in place, while the relatively 'free' ribose sugar group migrates to/from the phosphate molecule, forming the free purine/pyrimidine and α-D-ribose 1-phosphate.[71]

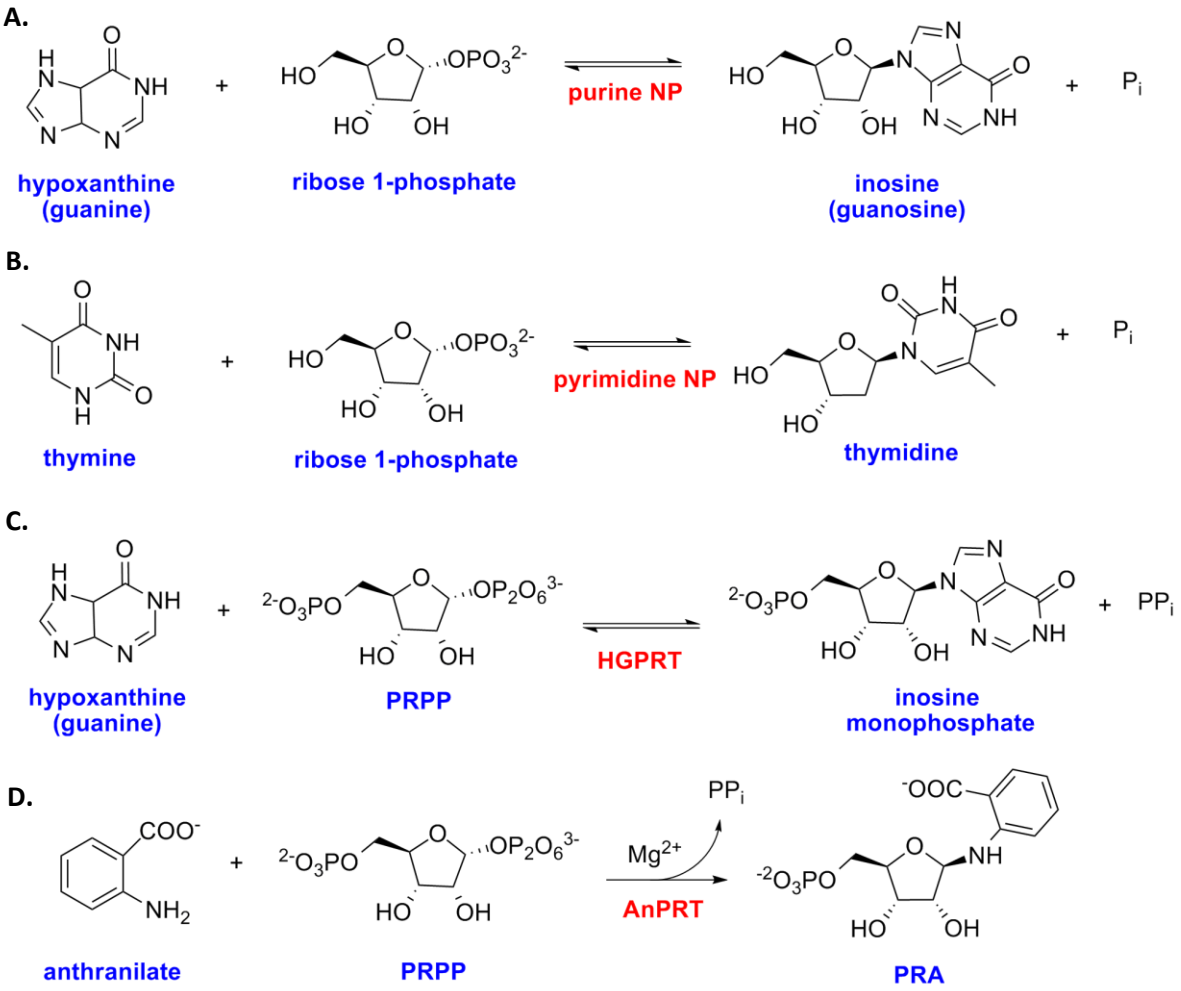

Figure 6.3 A comparison of the reactions catalysed by A) purine NP, B) pyrimidine NP, C) hypoxanthine-guanine PRT (HGPRT) and D) *Mtu*-AnPRT.

Type I PRTs have shown a propensity for S_N1 mechanisms, as evidenced by kinetic isotope effect experiments on orotate and hypoxanthine-guanine PRTs.[31b, 71] It has been suggested that the type I AnPRTs also utilise ribosyl-oxocarbenium ion migration in their S_N1 mechanisms. For example, in hypoxanthine-guanine PRTs the ribose ring of PRPP could migrate from the PP_i moiety to hypoxanthine-guanine, forming a bond between the C1' carbon of the ribose ring and the N9 nitrogen of the hypoxanthine-guanine (Figure 6.3).[31b, 78] It is entirely possible that the type III *Mtu*-AnPRT also uses this mechanism, based on the crystal structures of this enzyme (Figure 6.4). It is reasonable to assume that the PP_i moiety of PRPP, when bound to *Mtu*-AnPRT, would be held firmly in place during the *Mtu*-AnPRT-catalysed reaction. This thesis has described numerous *Mtu*-AnPRT crystal structures that have displayed virtually identical PRPP binding modes, in which the PP_i moiety is anchored by several hydrogen bonds to the surrounding protein residues, as well as by co-ordination to two Mg^{2+} ions. The phosphate group on the C5 position of PRPP is also stabilised by

several hydrogen bonds to the flexible β2-α6 loop and the β1-α5 loop. The ribose ring of PRPP hydrogen bonds to the backbone carbonyls of N138 and R139 via the C2 hydroxyl, and to the backbone nitrogen of G147 via the C3 hydroxyl, which are all located on the flexible β2-α6 loop. The ribose ring is therefore the least protein-interactive element of PRPP.

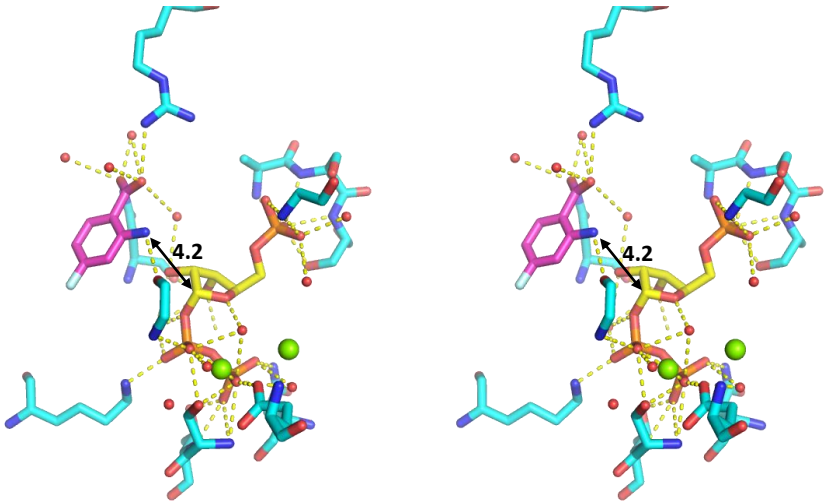

Figure 6.4 Stereo diagram of PRPP, Mg^{2+} and 4FA bound to *Mtu*-AnPRT with the potential ribosyl-oxocarbenium ion path of migration outlined. *Mtu*-AnPRT (PDB ID: 4N5V) residues are shown in cyan, with PRPP in yellow, Mg^{2+} as green spheres and 4FA in magenta. Polar contacts are shown as yellow dashes, with bond distances indicated in Å.

The crystal structure of *Mtu*-R193L co-crystallised with PRPP and Mg^{2+} and soaked for 5 s with anthranilate shows PP_i and Mg^{2+} bound, indicating that a reaction between PRPP and anthranilate has taken place. When overlaid with the wild-type *Mtu*-AnPRT structure with PRPP and Mg^{2+} ions bound, the *Mtu*-R193L-bound PP_i molecule can be seen to overlay well with the PP_i moiety of the PRPP molecule bound to the wild-type structure, indicating that it does not move during catalysis. The structure of *Sso*-AnPRT with PP_i and Mg^{2+} bound has been solved (PDB ID: 1GXB), and shows these ligands bound in identical positions to those found in the *Sso*-AnPRT structure with PRPP and Mg^{2+} bound (PDB ID: 1ZXY). The 1GXB structure arose from the soaking of *Sso*-AnPRT with 10 mM PRPP, 10 mM $MgCl_2$ and 5 mM aniline-2-arsenic acid for 15 mins. The presence of PP_i in the active site of *Sso*-AnPRT was attributed to the hydrolysis of PRPP, however, aniline-2-arsenic acid was not tested as a substrate or inhibitor of *Sso*-AnPRT.[45a] The ability of *Mtu*-AnPRT to utilise orthanilate as a substrate could indicate that *Sso*-AnPRT has the ability to utilise aniline-2-arsenic acid as a substrate, given the similarity of their chemical structures (Figure 6.5). If correct, the presence of PP_i in the active site of *Sso*-AnPRT could be the result of the catalytic turnover of PRPP and aniline-2-arsenic

acid by *Sso*-AnPRT, which would provide further evidence that PP_i is the final product to leave the AnPRT active site post-reaction.

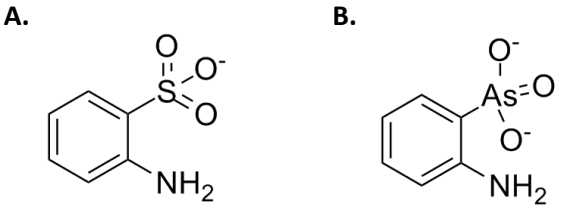

Figure 6.5 The chemical structures of A) orthanilate and B) aniline-2-arsenic acid.

The structure of *Mtu*-AnPRT with PRPP, Mg^{2+} and 4FA (6 min soak) bound (PDB ID: 4N5V) has 4FA bound in the inner site, with hydrogen bonds to R193 via the 4FA carboxylate group in each active site of the dimer. Kinetic analysis of the *Mtu*-R193A and *Mtu*-R193L variants has established the necessity of the R193 residue in both the binding of anthranilate and for catalytic turnover. The role of the R193 residue could be to assist in anchoring the inner site anthranilate during catalysis while the ribosyl-oxocarbenium ion migrates towards it. This hypothesis for the role of R193 would explain both the decrease in anthranilate binding affinity and catalytic turnover rate observed for *Mtu*-R193A and *Mtu*-R193L. The structures of wild-type *Mtu*-AnPRT with PRPP, Mg^{2+} and 6MA (30 min soak) bound (PDB ID: 4N93) and of *Mtu*-R194A with PP_i, Mg^{2+} and anthranilate bound also show the side-chain of R193 hydrogen bonded to the inner site anthranilate/6MA molecule.

The structures of *Mtu*-AnPRT with PRPP, Mg^{2+} and 4FA (6 min soak)/6MA (30 min soak) bound and *Mtu*-R194A with PP_i, Mg^{2+} and anthranilate bound highlight the involvement of the G107 residue in binding the anthranilate/4FA/6MA molecule bound in the inner site. A hydrogen bond between the anthranilate/4FA/6MA amino group and the backbone carbonyl of G107 is observed in all three structures. The G107 residue is also observed to hydrogen bond to the PP_i moiety in PRPP and in PP_i. The G107 residue likely anchors both the inner site anthranilate molecule and the PP_i moiety of PRPP during catalysis, which would provide some explanation towards the total inactivity observed for *Mtu*-G107P. The introduction of a proline mutation at position 107 (Figure 6.6) highlights several unfavourable interactions between the proline ring and Mg1, the Mg-binding residue D251, and the PP_i moiety of PRPP, which could conceivably disrupt the binding of PRPP and Mg^{2+}.

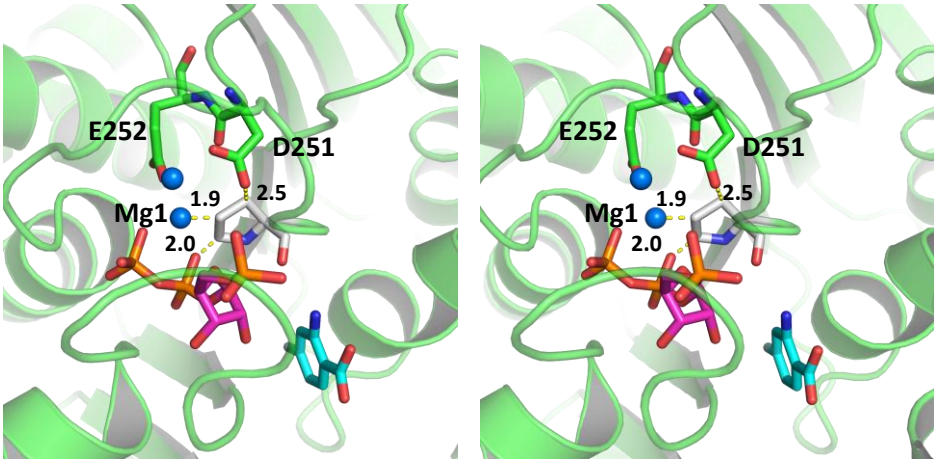

Figure 6.6 Stereo diagram of the possible effects of a G107P mutation in *Mtu*-AnPRT. *Mtu*-AnPRT (green) with PRPP (magenta), Mg^{2+} (blue spheres) and 4FA (cyan) bound (PDB ID: 4N5V) is shown with a proline residue (white) at position 107. Potentially unfavourable interactions between the proline residue and surrounding ligands/residues are indicated by yellow dashes, with bond lengths shown in Å.

The presence of both α and β anomers of PRA in solution post-reaction can be detected by NMR spectroscopy, and this anomerisation is also reported for similar compounds such as phosphoribosyl amine.[75a] By trapping the reduced PRA product through selective reduction with $CNBH_3$, it is clear that anomerisation occurs via an imine intermediate. It seems improbable that *Mtu*-AnPRT catalyses the formation of both anomers, as the direction from which anthranilate approaches PRPP through the anthranilate channel clearly promotes the inversion of stereochemistry. The product of the *Mtu*-AnPRT reaction is most likely β-PRA, which then rapidly interconverts in solution between α and β anomers without enzyme facilitation.

6.3 Substrate Specificity

Fluoro-analogues of anthranilate are more readily accepted as *Mtu*-AnPRT substrates than methyl-analogues. The trend shown by the apparent K_M values of the fluoro-analogues indicates that 4FA and 6FA have a higher, anthranilate-like affinity for *Mtu*-AnPRT than 3FA and 5FA. This difference in tolerance to the position of the fluorine substitution is likely caused by the electrostatic interactions made within the anthranilate channel. It is also of interest to note that 4FA and 6FA are the only two fluorinated analogues so far that can be observed to bind in the inner site of *Mtu*-AnPRT. The *Mtu*-AnPRT structure with 4FA bound in the inner site shows this compound bound in almost identical positions to the anthranilate molecules bound in the inner site in the *Sso*-AnPRT (PDB IDs: 1ZYK & 2GVQ) and *Mtu*-R194A enzymes, and is a strong indication that these fluoro-analogues are turned over via the equivalent mechanism that *Mtu*-AnPRT utilises for anthranilate.

Structures of 3FA and 5FA obtained by Dr Alina Castell are yet to be completely refined, and will hopefully provide further insight towards the reason for the reduced binding affinity of *Mtu*-AnPRT for these analogues. However, if we compare the *Mtu*-R194A and *Mtu*-R193A structures with anthranilate bound in the outer site, it can be seen that any substituent in the C3 position of anthranilate would project towards the β2-α6 loop when it is folded into the channel (Figure 6.7). If it is assumed that the β2-α6 loop is required to fold into the channel for efficient anthranilate binding in the outer site, it is entirely possible that an anthranilate analogue containing a fluoro- or methyl-group moiety at C3 would encounter steric hindrances when binding at the outer site. Any substitutions to the C5 position of anthranilate would project towards the backbone carbonyl of H183, potentially creating unfavourable steric and/or electrostatic interactions with *Mtu*-AnPRT.

On the other hand, if we use the *Mtu*-AnPRT structure with 4FA bound (6 s soak) as a template, the amino group of 4FA points towards the backbone carbonyl of H183. If the 3FA and 5FA molecules bind in this orientation, the C3 fluorine would project towards the side-chain of H183, with the C5 fluorine projecting towards the β2-α6 loop when folded into the anthranilate channel. Regardless of whether these analogues bind with the amino group oriented towards N138 or H183, there are potentially unfavourable interactions that could explain this decrease in their binding affinity for *Mtu*-AnPRT.

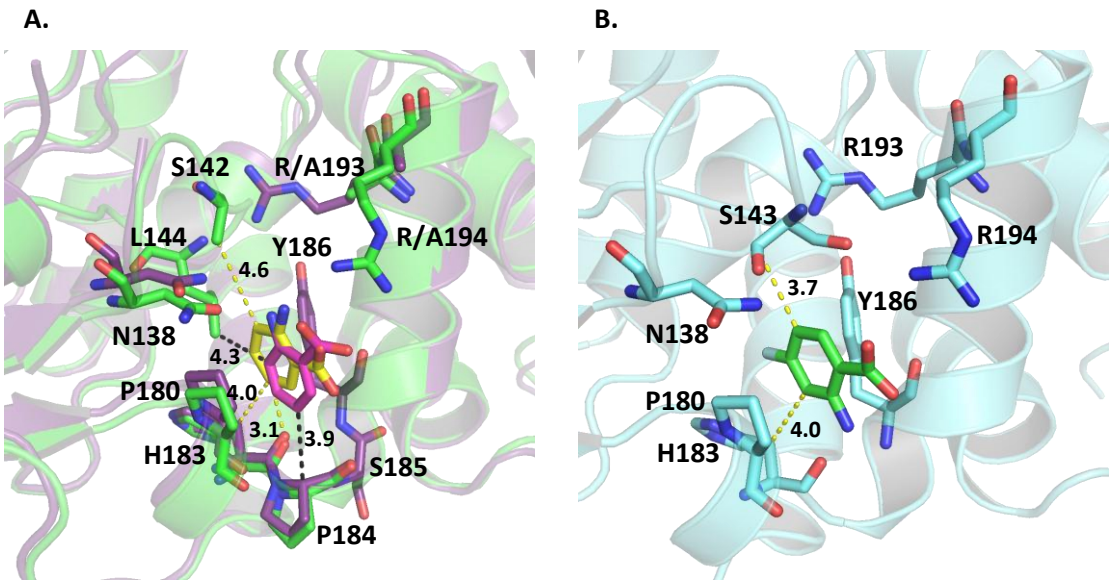

Figure 6.7 The outer binding site for anthranilate in *Mtu*-AnPRT. A) *Mtu*-R194A (purple) with anthranilate (yellow) bound overlaid with *Mtu*-R193A (1 min 10 s soak) (green) with anthranilate (magenta) bound. Potential steric clashes for C3 and C5 substitutions are shown as yellow and black dashes for *Mtu*-R194A and *Mtu*-R193A (1 min 10 s soak) respectively. B) *Mtu*-AnPRT (6 s soak) (cyan) with 4FA (green) bound. Potential steric clashes for C3 and C5 substitutions are shown as yellow dashes. Bond distances are indicated in Å.

Methy-substituted anthranilate analogues are not favourably tolerated by *Mtu*-AnPRT, as indicated by the dramatic increases in the K_M values and decreases in the k_{cat} values recorded for these compounds. The overall reduction in the ability of *Mtu*-AnPRT to accept any of the methyl-analogues as substrates points to unfavourable steric interactions within the anthranilate channel, rather than electronic interactions, as the root cause. Orthanilate, which has a sulfonyl group in place of the anthranilate carboxylate group, is also accepted as a poor *Mtu*-AnPRT substrate, which indicates the allowance for extra steric bulk at this position. The sulfonate functional group present in orthanilate is larger than the carboxylate group of anthranilate in two ways: firstly, there are three oxygens present on the sulfonate group, and only two on the carboxylate group, and secondly, sulfur has a larger atomic radius of 100 pm compared to the 70 pm atomic radius of carbon.[79]

6.4 Substrate Inhibition

The anthranilate inhibition observed in wild-type *Mtu*-AnPRT is perhaps a means of regulating the production of PRA, and subsequently the formation of the pathway end-product tryptophan. Inhibition of an AnPRT due to anthranilate alone has not been reported for any other AnPRT enzymes to the author's knowledge. At anthranilate concentrations above 15 μM the activity of *Mtu*-AnPRT steadily decreases, with the specific activity of the enzyme dropping to approximately 50% of its maximum at 100 μM. It has been reported that anthranilate is a metabolic intermediate not normally accumulated within the cell,[80] although as the exact cellular concentration of this compound is not currently known, it is difficult to confidently assert the relevance of the anthranilate inhibition observed in this study.

Substitutions to the key residues thought to be involved with binding anthranilate in the outer site of *Mtu*-AnPRT identified the absolute importance of the interaction between N138 and anthranilate for intact anthranilate inhibition. *Mtu*-N138A showed a complete lack of anthranilate inhibition up to 220 μM, and could indicate why 3FA and 4FA showed a significant decrease in their ability to cause substrate inhibition. Structures of *Mtu*-AnPRT with 4FA bound (both the 6 min and 6 s soaks) showed the 4FA compounds bound in the outer site with their amino groups oriented towards H183 rather than N138, which effectively removes any hydrogen bonding interactions with N138, and thus the ability to effectively inhibit *Mtu*-AnPRT. It is possible that 3FA also binds with its amino group oriented towards H183, which would both cause steric clashes with H183 (Section 6.3) and remove any hydrogen bonding with N138. If correct, the extra steric hindrance caused by 3FA would explain the increase in the K_i value compared to 4FA.

Mtu-P180A and *Mtu*-R194A also showed decreases in their ability to facilitate anthranilate inhibition, and several structures described in this research have demonstrated the involvement of P180 and R194 in binding anthranilate or its analogues in the outer site. These kinetic and structural observations further indicate the binding of anthranilate in the outer site as a key event in the inhibition of *Mtu*-AnPRT by anthranilate.

6.5 Effect of Mutations to *Mtu*-AnPRT

The thermal stabilities of the *Mtu*-AnPRT variants *Mtu*-N138A, *Mtu*-P180A and *Mtu*-R194A were not significantly different to that of the wild-type enzyme. However, *Mtu*-R193A and *Mtu*-R193L both showed a dramatic increase in thermal stability of approximately 10 °C. Crystal structures of the *Mtu*-R193A enzyme all displayed a common structural feature whereby the β2-α6 loop was folded into the anthranilate channel, indicating a possible preference for this loop conformation in this variant. Structures of *Mtu*-R193L showed more variety in the position of the β2-α6 loop, which could be observed both in the 'closed' position or folded into the anthranilate channel depending on the ligands present in the crystal condition.

A comparison of the *Mtu*-R193A and *Mtu*-R193L structures with the wild-type *Mtu*-AnPRT structure with 4FA (6 s soak) bound (which also shows the β2-α6 loop folded into the anthranilate channel) shows a slight difference in the β2-α6 loop position (Figure 6.8). This discrepancy is possibly due to the removal of the full R193 side-chain in *Mtu*-R193A and *Mtu*-R193L. The alternate β2-α6 loop positions observed in the *Mtu*-R193A and *Mtu*-R193L structures allow for a hydrogen bond between S143 and Y186, which is not present in the wild-type structure with 4FA bound. This extra hydrogen bond between S143 and Y186 may tether the β2-α6 loop in a thermodynamically favourable position, which could possibly result in an overall increase in the variants' stability.

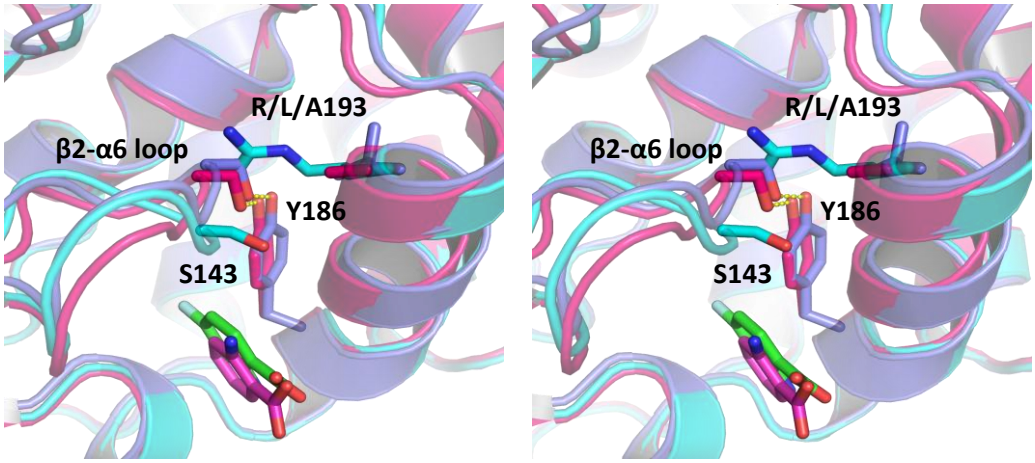

Figure 6.8 Stereo diagram of β2-α6 loop folding into the anthranilate channel in wild-type *Mtu*-AnPRT, *Mtu*-R193A and *Mtu*-R193L. Wild-type *Mtu*-AnPRT (cyan) with 4FA (6 s soak) (green) bound is overlaid with *Mtu*-R193A (pink) with anthranilate (1 min 10 s soak) (magenta) bound and *Mtu*-R193L (purple) with PP_i (orange) and Mg^{2+} (red spheres) bound (5 s anth soak). Polar contacts are shown as yellow dashes.

Mtu-G107P shows a decrease in thermal stability of 9 °C when compared to the wild-type *Mtu*-AnPRT enzyme. The G107 residue is the first residue of the β1-α5 loop, located adjacent to the C-terminus of the β1 strand. The introduction of a proline residue at this position near to the β1 strand, which is approximately central to the seven-stranded β-sheet of *Mtu*-AnPRT (Figure 6.9), could create unfavourable electrostatic/steric interactions at the centre of the β-sheet that propagate outwards. If correct, the G107P mutation would cause a slight shift in the *Mtu*-AnPRT secondary structure, which could also explain the decrease in thermal stability of the *Mtu*-G107P variant.

Figure 6.9 The position of residue 107 within *Mtu*-AnPRT. *Mtu*-AnPRT (green) with PRPP, Mg^{2+} and 4FA (not shown) bound (PDB ID: 4N5V) is shown with a proline residue (magenta) at position 107.

6.6 Drug Design and Future Work

The structures of several variant and wild-type *Mtu*-AnPRTs have indicated that anthranilate binding precedes PRPP/Mg^{2+} binding (Section 4.7.2). If anthranilate is used as a template for drug design, there are several different approaches that could be used to block the biosynthesis of tryptophan using *Mtu*-AnPRT. Such tactics involve the design of drugs that will effectively bind to and subsequently block the active site/anthranilate channel of *Mtu*-AnPRT, as well as the catalysis of anthranilate-like compounds by *Mtu*-AnPRT to form prodrugs. Other avenues of drug design include transition state mimicry and allosteric inhibition.

Crystal structures of wild-type and variant *Mtu*-AnPRTs with anthranilate-like inhibitors bound (Section 2.7/Section 5.3) have elucidated several key residues involved with inhibitor binding in the anthranilate channel: N138, P180, R193 and R194. Kinetic analysis of these inhibitors with the enzyme-coupled UV-based assay elucidated the 'bi-anthranilate'-like inhibitor ACS172 as the most potent inhibitor, followed by ACS142. Further substitutions/additions of chemical groups to these inhibitors to enhance their potency would be a worthwhile investment, and is currently being investigated for ACS172 at the University of Auckland. A 'tri-anthranilate'-like inhibitor is also under investigation, which could potentially bind to all three anthranilate binding sites within the anthranilate channel.

The discovery of alternate anthranilate-like substrates for *Mtu*-AnPRT illuminates the possibility of a prodrug that could travel through the tryptophan biosynthetic pathway, creating tryptophan analogues that might conceivably be incorporated into protein synthesis within *Mtu*. With the exception of 3MA and orthanilate, this study has shown that *Eco*-PRAI:InGPS does have the ability to completely turn over both the fluoro- and methyl-substituted PRA products of the *Mtu*-AnPRT reaction. 4FA is the best example in this study of a potential prodrug, with K_M and k_{cat} values similar to that of the natural substrate anthranilate, a significantly higher K_i value, and the ability of its *Mtu*-AnPRT product 4F-PRA to be turned over relatively quickly by *Eco*-PRAI:InGPS. Further investigation into alternate substitutions at this C4 position may yield even better candidates, which could then be tested *in vivo* against *Mycobacterium smegmatis*, for example, as a next step in prodrug development. *Mycobacterium smegmatis* is a relatively easy strain of mycobacteria to work with, as it grows faster than other strains, is non-pathogenic and has similar characteristics to *Mtu*.[81]

Compounds that mimic the transition states of reacting substrates have also been shown to be potent inhibitors of enzymes.[71, 82] Compounds mimicking the transition state of *Mtu*-AnPRT are likely to have a greater potency than those that imitate just one substrate, as they may resemble a species

that has a high affinity for the enzyme.[77] Additionally, a greater number of contacts would be made to the enzyme both in the PRPP and inner site anthranilate binding sites. Regardless of the catalytic mechanism that *Mtu*-AnPRT utilises, it can be asserted that anthranilate approaches PRPP from the β position, which has been observed in several structures of wild-type and variant *Mtu*-AnPRT structures described in this thesis. A transition state mimic compound could therefore be based on the basic template outlined in Figure 6.10. Kinetic isotope effect studies of the *Mtu*-AnPRT reaction could lead to a more accurate prediction of the transition state of this enzyme, and thus to the design of more potent drug compounds. However, measurements of the kinetic isotope effects may be difficult to obtain due to the instabilities of the PRPP and PRA molecules.

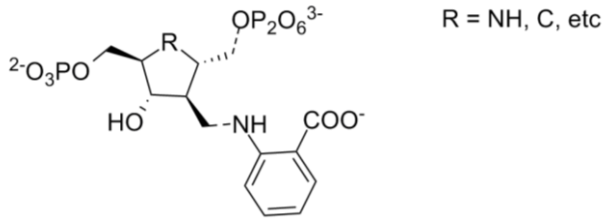

Figure 6.10 A potential transition state analogue of *Mtu*-AnPRT, which would act as a template for further drug design. Dashed lines indicate linker regions.

Allosteric inhibition of *Mtu*-AnPRT by tryptophan has not been examined, however, there is some evidence within the literature that this occurs with other AnPRT orthologues.[66b, 68, 83] The AnPRT enzyme in *Salmonella typhimurium* is covalently linked to the preceding AS enzyme in the tryptophan pathway, due to gene fusion. Experiments to disrupt this covalent linkage were successful, and the AS-linked and separate AnPRT enzymes were tested for tryptophan inhibition and compared. Both forms of AnPRT showed inhibition by tryptophan, though the AS-linked form was more significantly inhibited than the separate form.[83a] It is possible that the mode of tryptophan inhibition is allosteric, as structures of *Mtu*-AnPRT have been shown to bind benzamidine in a location removed from the active site near the hinge region of the protein. Tryptophan could conceivably bind in this hinge region and disrupt the *Mtu*-AnPRT dynamics, which may also hinder the enzyme catalysis. Further studies would need to be conducted in this area to confirm tryptophan inhibition of *Mtu*-AnPRT. If *Mtu*-AnPRT is allosterically inhibited by tryptophan, compounds similar in structure to this aromatic amino acid could be used as allosteric site drug compounds.

6.7 Concluding Remarks

Discovering novel drugs that will successfully target *Mycobacterium tuberculosis* is becoming ever more crucial as drug-resistant strains emerge, with the constant concern of a completely drug-resistant 'superbug' looming on the horizon. Knowledge of the active site mechanisms of enzymes proved necessary to *Mtu* virulence is a key ingredient in further drug-discovery for tuberculosis, as essential protein-substrate interactions can be identified and replicated in the synthesis of potential inhibitor compounds. This thesis has provided considerable insight into the active site mechanism of *Mtu*-AnPRT, and highlights significant features of the enzyme that have assisted in the conception of several potential drug design strategies.

Chapter 7

Methods and Materials

7.1 General Methods

7.1.1 Water

All water used in these experiments was from a Millipore Milli-Q system. This water is referred to as Milli-Q water. All water used for PCRs and crystal formation was autoclaved prior to use.

7.1.2 pH Measurements

pH solutions were measured using a Denver Instruments UB-10 Ultra-Basic pH meter, with a standard probe. Solutions were made more acidic by addition of 1 M or 10 M HCl and basic by addition of either 1 M or 10 M NaOH.

7.1.3 Plasmids

M. tuberculosis genomic DNA containing the ORF that encodes the TrpD gene (Rv2192c) was previously amplified by PCR, and subsequently cloned into the pET-23a(+) vector. *E. coli* genomic DNA containing the ORF that encodes the TrpFC gene was also previously amplified by PCR, and cloned into both pProEX-HTb and pET-42a(+)rTEV vectors.[56] The pET-23a (+) vector is a 3666 bp cloning vector containing a T7/*lac* promoter for *E. coli* expression under high lactose conditions, and introduces a non-cleavable C-terminal His-tag. pProEX-HTb is a 4779 bp cloning vector containing a T7/*lac* promoter, a cleavable N-terminal His-tag, and an rTEV site which can be recognised by TEV protease for selective His-tag cleavage. The pET-42a(+)rTEV 5930 bp cloning vector contains a T7/*lac* promoter, an rTEV site, and introduces an N-terminal GST-tag, two N-terminal His-tags and an S-tag. All three plasmids have an ampicillin resistance gene included to allow for selective growth of cells containing these plasmids when ampicillin is present.

7.1.4 Antibiotics

Ampicillin was added to all growth media to a final concentration of 0.1 mg/mL. Stock solutions of ampicillin at 100 mg/mL dissolved in Milli-Q were created, filter sterilised and stored at -80 °C, and freeze-thawed a maximum of two times. The chaperone 3 cell line used contains resistance to chloramphenicol and spectinomycin. When this cell line was used, these antibiotics were added to all growth media in addition to ampicillin, to a final concentration of 25 µg/mL for chloramphenicol and 0.1 mg/mL for spectinomycin. Stock solutions of chloramphenicol at 25 mg/mL dissolved in ethanol and spectinomycin at 10 mg/mL dissolved in Milli-Q were created, filter sterilised and stored at -80 °C, and freeze-thawed a maximum of two times.

7.1.5 Cell Lines

The cell lines used for plasmid propagation were either *E. coli* XL1-Blue or TOP10 (Invitrogen). For protein expression *E.coli* BL21 (DE3) cells or *E. coli* BL21 (DE3) cells containing the plasmids pBB528 and pBB541for co-expression of the chaperonins GroEL and GroES were used.

7.1.6 Preparation of Chemically Competent Cells

Chemically competent cells were prepared using the method of Hanahan[84]. An overnight culture of the cells to be made competent was grown in the presence of the appropriate antibiotic(s). The following day lysogeny broth (LB) medium with the appropriate antibiotic was inoculated with one hundredth the volume of the overnight culture. Cells were grown at 37 °C until reaching an OD_{600} of 0.3 AU to 0.6 AU. The culture medium was then incubated on ice for 10 - 15 min, before being harvested by centrifugation for 15 min at 4 000 rpm and 4 °C, in a pre-chilled centrifuge and rotor. The pellet was then resuspended in 18 mL of RF1 solution and incubated on ice for 30 min. The cells were then harvested again by the same centrifugation method, and resuspended in 4 mL of RF2 solution. Suspended cells were then split into 50 µL to 100 µL aliquots, flash-frozen in liquid nitrogen and stored at -80 °C.

RF1 solution: 100 mM $RbCl_2$, 50 mM $MnCl_2$, 30 mM KOAc, 10 mM $CaCl_2$, pH 5.8 (adjusted using concentrated acetic acid).

RF2 solution: 10 mM $RbCl_2$, 10 mM MOPS, 75 mM $CaCl_2 \cdot 6H2O$, 15% (v/v) glycerol, pH 5.8 (adjusted using NaOH).

The RF1 and RF2 solutions were filter-sterilised (0.2 µm) rather than autoclaved to avoid formation of a Rb precipitate, and stored at 4 °C.

7.1.7 Transformation

Chemically competent cells (100 µL to 200 µL aliquots) were thawed on ice before addition of 2 µL of either PCR product or purified plasmid. The mixture was left on ice for 30 min then placed in a 42 °C water bath for 30 s to 45 s before being placed on ice again for 2 min. Cells were then outgrown for 1 hr at 37 °C while shaking after addition of 250 µL super optimal broth (SOC) or LB medium. A portion (50 µL to 200 µL) of the transformed cells was spread directly onto an LB-agar plate containing the appropriate antibiotic(s) and left to grow on the inverted medium overnight at 37 °C.

SOC medium: 2% (w/v) tryptone, 0.5% (w/v) yeast extract, 10 mM NaCl, 2.5 mM KCl, 10 mM $MgSO_4$, 20 mM glucose. Filter sterilised in aliquots.

7.1.8 Glycerol Stocks

In order to keep cells viable, all strains of *E. coli* cells containing plasmids were flash frozen and stored at -80 °C as glycerol stocks. Glycerol stocks were created by adding 400 µL of 50% (v/v) glycerol with 800 µL of an overnight culture in either a 1.6 mL eppendorf or screw-top tube.

7.1.9 Culture Media

LB-agar was prepared by dissolving LB (Lennox L) (20 g L^{-1}) and agar (15 g L^{-1}) base in Milli-Q water and sterilised by autoclaving. The LB-agar solution was then heated in a microwave oven until boiling, and left to cool in a 60 °C oven. The LB-agar solution was then further cooled to 50 °C before antibiotic(s) were added immediately prior to pouring into round petri dishes.

LB media for plasmid extraction and pre-cultures were prepared by dissolving 20 g L^{-1} LB (Lennox L) base in Milli-Q water and sterilised by autoclaving. Antibiotic(s) were added immediately prior to use.

7.1.10 Plasmid Extraction and Purification

Plasmids were extracted using a High Pure Plasmid Isolation Kit (Roche). Small cultures (5 mL) of plasmid-containing cells were grown overnight with the appropriate antibiotic(s). The cultures were harvested the following morning and plasmids extracted and purified as per the kit instructions. The concentration of purified plasmid was measured by absorption at 260 nm using an appropriately blanked Nanodrop ND-1000 spectrophotometer.

7.1.11 Protein Expression Cultures

Autoinduction of protein expression was used for larger cultures, based on the methods of Studier.[85] For 1 L of culture, 10 g tryptone and 5 g yeast extract in 960 mL of water was autoclaved in a 2 L to 3 L baffled conical flask. Added to this was 20 mL of a 50 x 5052 stock solution, 20 mL of a 50 x M stock solution, 1 mL of 1 M $MgSO_4$, 0.2 mL of a trace metal solution, and the appropriate antibiotic(s). The complete medium was then inoculated with 10 mL of an overnight pre-culture and placed in a shaking incubator (170 rpm to 180 rpm) for 4 hrs at 37 °C before being transferred to 20 °C for 20 - 36 hrs. The amounts and volumes were appropriately scaled depending on the culture volume.

50 x 5052 stock: 25% (w/v) glycerol, 2.5% (w/v) glucose, and 10% (w/v) lactose. Filter sterilised (0.2 µm).

50 x M stock: 500 mL, 1.25 M Na_2HPO_4, 1.25 M KH_2PO_4, 2.5 M NH_4Cl, 0.25 M Na_2SO_4. Autoclaved.

Trace metal solution: 50 mM $FeCl_3$, 20 mM $CaCl_2$, 10 mM $MnCl_2$/$ZnSO_4$, 2 mM $CoCl_2$, $CuCl_2$, $NiCl_2$, $NaMoO_4$, Na_2SeO_3 and H_3Bo_3 in 60 mM HCl.

7.1.12 Cell Harvesting

The method used to harvest cells from cultures used for protein expression varied depending on rotor and centrifuge availability. Typically, large cultures were harvested in 0.8 L or 1 L bottles at 14 000 *g* for 30 min at 4 °C. The supernatant liquid was removed and pellets were then transferred to 50 mL centrifuge tubes and stored at -80 °C. Alternatively, cultures were sometimes progressively harvested in 50 mL centrifuge tubes at 12 000 *g* for 10 min at 4 °C, or in 0.4 L buckets at 4 618 *g* for 40 min at 4 °C before being transferred to 50 mL centrifuge tubes and stored at -80 °C. Small volume cultures (5 mL) were progressively harvested in 1.6 mL micro-centrifuge tubes at 17 000 *g* for 3 min.

7.1.13 Cell Lysis

Cells were lysed by one of two methods. The first method using sonication was performed with an Omni-Ruptor 4000 Ultrasonic Homogenizer (Omni International). Cell pellets were resuspended in chilled lysis buffer (typically 50 mL to 100 mL) on ice, and sonicated in a beaker surrounded by packed ice by one of two sonication protocols. Cells were sonicated at 70 – 80% power either for 6 - 8 multiples of 10 s with 1 min pauses between bursts, or by 30 ms pulses for 25 - 35 min with 70 – 80% pulsation.

The second method utilised a Microfluidics Lab Homogeniser M-110P, and was performed by resuspending the cell pellet as mentioned above and passing cells through the homogeniser twice to ensure complete lysis. The lysis buffer for *Mtu*-AnPRT and *Eco*-PRAI:InGPS was either 50 mM Tris.HCl pH 8.0, 200 mM NaCl and 25 mM imidazole, or 20 mM Na_2SO_4, pH 8.0 for CD analysis. Cellular debris were removed by centrifugation either at 12 000 *g* or 19 500 *g* for 30 min at 4 °C depending on rotor and centrifuge availability.

7.1.14 Protein Purification

All proteins were purified by a two- or three- step procedure composed of IMAC chromatography followed by desalting, with an additional SEC chromatography step depending on protein purity. The chromatography was performed on Bio-Rad Biologic DuoFlow and GE Healthcare ÄKTApurifier™ 10 machines.

Before use, all buffers were filtered (0.2 µm) under vacuum. Samples were all likewise filtered before being loaded on either a 50 mL or 200 mL Superloop™ (GE Healthcare). The eluate was fractionated in 2 mL fractions collected in 96-well plates. On ÄKTApurifier™ 10 machines, the eluate

from injection of the sample onto the column (flow-through) was collected in 50 mL centrifuge tubes. Elution from the columns was monitored principally at 280 nm, and depending on the machine being used, also at 260nm and 214 nm. When the fractions corresponding to *Mtu*-AnPRT/*Eco*-PRAI:InGPS could not be deduced from the chromatogram, suspected AnPRT/PRAI:InGPS-containing fractions were analysed by sodium dodecyl sulfate polyacrylamide gel electrophoresis (SDS-PAGE) and/or for AnPRT/PRAI:InGPS activity. Fractions containing AnPRT/PRAI:InGPS were then pooled and prepared for the next chromatographic step.

7.1.15 Immobilized Metal Affinity Chromatography (IMAC)

IMAC was performed using a precharged Ni Sepharose™ High Performance resin packed in a HisTrap™ HP column (GE Healthcare), normally at 4 °C. The supernatant liquid (resulting from removal of the cellular debris by centrifugation after cell lysis) was passed onto the column in lysis buffer, and elution from the column was performed using a gradient of increasing imidazole concentration (linear) from 25mM to 200 mM over 50 mL at a flow rate of 2 - 3 mL min^{-1}.

7.1.16 Desalting

Fractions of interest containing high concentrations of imidazole were desalted prior to storage. Desalting was performed using a HiPrep 26/10 Desalting column prepacked with Sephadex G-25 Fine (GE Healthcare), usually at 4 °C in either low imidazole buffer or crystal buffer (50 mM Tris.HCl, 150 mM NaCl, 5% glycerol) depending on the future use of the protein. The elution flow rate was 2 - 5 mL min^{-1}.

7.1.17 Size Exclusion Chromatography (SEC)

Fractions containing *Mtu*-AnPRT/*Eco*-PRAI:InGPS from either IMAC or desalting were pooled and loaded into a loop. SEC was performed using a HiLoad™ 26/60 Superdex™ 200 prep grade column (GE Healthcare), usually at 4 °C in either low imidazole buffer or crystal buffer depending on the future use of the protein. The elution flow rate was 0.5 - 1 mL min^{-1}.

7.1.18 Sodium Dodecyl Sulfate-Polyacrylamide Gel Electrophoresis (SDS-PAGE)

SDS-PAGE was performed using pre-cast gels using NuPAGE® 10% Bis-Tris Gel 1.0mm × 12-well pre-cast gels (Invitrogen) in NuPAGE® MOPS SDS Running Buffer (Invitrogen). Electrophoresis was performed using a XCell SureLock™ Electrophoresis Cell (Invitrogen), at 200 V for 50 min. Samples were mixed with NuPAGE® LDS Sample Buffer (4×) and DTT, and boiled before loading.

7.1.19 Visualisation

All SDS-PAGE gels were stained in square petri dishes by coomassie brilliant blue R-250, for at least 1 hour before being destained to remove excess dye.

Stain: 0.1% (w/v) coomassie brilliant blue R-250, 10% (v/v) acetic acid and 40% (v/v) methanol

Destain: 10% (v/v) acetic acid and 40% (v/v) methanol

Molecular weight standards (Novex® Sharp Pre-Stained Protein Standards (Invitrogen)) were run as the sample in one lane of each gel. Photographs of gels were taken on a white light transilluminator in a Molecular Imager® Gel Doc™ XR (Bio-Rad).

7.1.20 Concentrating and Buffer Exchanging of Protein Solutions

Protein solutions were concentrated using 10 000 Da molecular weight cut-off (MWCO) devices (Vivaspin 2 (GE Healthcare), Vivaspin 500 and Vivaspin 20 (Sartorius Stedim Biotech) and Amicon® Ultra-4 (Millipore)). All filtration units were rinsed before use with Milli-Q water. Protein solutions were buffer exchanged by repeatedly concentrating in a MWCO device and diluting with desired buffer.

7.1.21 Enzyme Storage

Purified protein was divided into aliquots in either 0.6 mL or 1.2 mL micro-centrifuge tubes in 0.2 mL to 1.2 mL aliquots, flash-frozen in liquid nitrogen, and stored at -80 °C. All protein samples were rapidly thawed immediately before use and kept on ice. Protein solutions were stored at 0.5 mg mL^{-1} to 10 mg mL^{-1}.

7.1.22 Protein Concentration Determination

Protein concentrations were measured by their absorbance at 280nm by an appropriately blanked Nanodrop ND-1000 spectrophotometer, using 2 µL samples of purified protein solution. The concentration was calculated from the absorption using molar extinction coefficient values of 34 615 M^{-1} cm^{-1} and 40 715 M^{-1} cm^{-1} for *Mtu*-AnPRT and *Eco*-PRAI:InGPS respectively. The coefficient values, calculated from protein sequences using the ProtParam tool on the ExPASy Proteomics Server,[62] were the same for both wild-type and mutant proteins.

7.1.23 Agarose Gel Electrophoresis

Separation of DNA was performed by agarose gel electrophoresis, using either 1% (w/v) agarose gels or pre-cast E-Gel® 1.2% (w/v) agarose gels (Invitrogen). DNA was stained for both self-poured and

pre-cast gels by inclusion of SYBR® Safe DNA stain. Agarose gels were created by dissolving 1% (w/v) agarose in 40 mL of Tris-acetate-EDTA (TAE) buffer and heating in a microwave oven until the agarose was dissolved. The hot agarose solution was left to cool in a 60 °C oven. Immediately before pouring, 4 µL SYBR® Safe DNA stain was added. Samples were mixed with a (6×) sample loading dye. Electrophoresis was performed for 45 min at 85 V in TAE buffer using a Mini-Sub® Cell GT (Bio-Rad).

TAE buffer: 50 mM Tris, 1 mM EDTA, 20 mM acetic acid

Sample loading dye (6×): 60 mM Tris-HCl, 60 mM EDTA, 0.2% (w/v) orange G, 0.05% (w/v) xylene cyanol ff, 60% (v/v) glycerol

The E-Gel® agarose gels were used according to the manufacturer's instructions. Samples were loaded without a sample loading dye directly into the wells, and separation could be monitored in real-time during electrophoresis using the E-Gel® iBase™ Safe Imager™ systems at 480 nm.

Typically 20 µL from 50 µL PCR reactions were loaded onto the agarose gels for visualisation of amplification products. To one well of each agarose gel, 2 µL of DNA ladder (1 kb Plus DNA Ladder (Invitrogen)) was used to estimate DNA size. Stained DNA was visualised and photographed under UV (302 nm) using a Molecular Imager® Gel Doc™ XR (Bio-Rad).

7.1.24 Enzyme-Coupled Activity Assay

All kinetic measurements were made using a Varian Cary 100 UV-visible spectrophotometer, stoppered 1 cm pathlength quartz cuvettes and a total assay volume of 1 mL. All assay solutions were equilibrated to 25 °C and baseline absorbance before initialisation with either *Mtu*-AnPRT or anthranilate. Standard reaction mixtures contained 50 mM Tris.HCl pH 8.0, 200 mM NaCl, 1 mM $MgCl_2$ (except when testing the effect of Mg^{2+} concentration), and a variable concentration of anthranilate, PRPP, *Mtu*-AnPRT, *Eco*-PRAI:InGPS and inhibitors (when tested). Assay buffers were treated with Chelex® 100 resin (Bio-Rad) prior to use to remove metal ions, and Chelex-treated buffer solution was used to create concentrated stock solutions of PRPP and anthranilate. $MgCl_2$ solutions were created using either Chelex-treated buffer or Milli-Q water.

Initial rates of reaction were measured as a least-squares fit of the initial rate data using Cary WinUV Kinetics Application (version 3.00, Varian). A unit of enzyme activity was defined as the formation of 1 µmol min^{-1} of InGP at 25 °C, and could be calculated from the measured gain of absorbance (at 270 nm) using Beer's Law (ε is 7500 L mol^{-1} cm^{-1}). The values of the kinetic parameters were determined by fitting data to the Michaelis-Menten equation $v = \frac{V_{max}[S]}{K_M + [S]}$ using the software GraFit

5[67] (Erithacus Software Limited). For determination of the *Mtu*-AnPRT mechanism, data were fitted to the ternary mechanism equation: $v = \frac{V_{max}\,[A][B]}{K_A K_B + K_B[A] + K_A[B] + [A][B]}$. Substrate inhibition data were fitted to the substrate inhibition equation: $v = \frac{V_{max}\,[S]}{K_M + [S]\left(1 + \left(\frac{[S]}{K_i}\right)\right)}$. For determination of K_i values, data were fitted to four inhibition equations: competitive: $v = \frac{V_{max}[S]}{([S] + K_M\left(1 + \frac{[I]}{K_i}\right))}$, pure non-competitive: $v = \frac{\frac{V_{max}[S]}{1+\frac{[I]}{K_i}}}{K_M + [S]}$, uncompetitive: $v = \frac{V_{max}[S]}{K_M + [S](1+\frac{[I]}{K_i})}$ and mixed: $v = \frac{V_{max}[S]}{\left(1+\frac{[I]}{K_i}\right)K_M + \left(1+\frac{[I]}{K_i'[S]}\right)}$. A statistical F-test was performed on data fitted to each inhibition equation using Grafit 5[67] and the χ^2 values compared for selection of the best fit equation.

7.1.25 Determination of Substrate Concentrations

The concentrations of natural substrate solutions (PRPP and anthranilate) were determined using the enzyme-coupled assay system. The concentration of the substrate not being measured was used in excess and the substrate for which the concentration was being measured was used at a limiting concentration. That the correct substrate was limiting was checked by addition of more of it after the reaction had reached completion. The change in absorbance, between that before initiation of the reaction and that at completion, was measured as ΔA_1. A control reaction, absent in one of the substrates, was used to measure the change in absorbance due to the addition of enzyme to the cuvette at initiation of the reaction (ΔA_2). The total change in absorbance ($\Delta A_1 + \Delta A_2$), was converted using Beer's Law to a concentration of the limiting substrate in the cuvette, and the stock substrate concentration calculated.

7.1.26 Pyrophosphate Activity Assay

All kinetic measurements were made using a Varian Cary 100 UV-visible spectrophotometer, stoppered 1 cm pathlength quartz cuvettes and a total assay volume of 1 mL. All assay solutions were equilibrated to 22 °C and baseline absorbance before initialisation with anthranilate. Standard reaction mixtures contained MESG (200 µM), PNP (1 U), inorganic pyrophosphatase (0.03 U) 50 µL of 20X reaction buffer (1 M Tris.HCl, 20 mM $MgCl_2$, pH 7.5, containing 2 mM sodium azide) from the commercially available EnzChek® Pyrophosphate Assay Kit E-6645 (Invitrogen™) as well as PRPP (120 µM), $MgCl_2$ (1 mM) and varying concentrations of anthranilate or anthranilate analogues, *Mtu*-

AnPRT and *Eco*-PRAI:InGPS. Solutions were made up to 1 mL total volume with autoclaved Milli-Q water.

Initial rates of reaction were measured as a least-squares fit of the initial rate data using the Cary WinUV Kinetics Application (version 3.00, Varian). A unit of enzyme activity was defined as the formation of 1 µmol min^{-1} of 2-amino-6-mercapto-7-methylpurine at 22 °C, and could be calculated from the measured gain of absorbance (at 360 nm) using Beer's Law (ε is 26 200 L mol^{-1} cm^{-1}). The values of the kinetic parameters were determined by fitting data to the Michaelis-Menten equation $v = \frac{V_{max}[S]}{K_M + [S]}$ using the software GraFit 5[67] (Erithacus Software Limited). Substrate inhibition data were fitted to the substrate inhibition equation $v = \frac{V_{max}[S]}{K_M + [S]\left(1 + \left(\frac{[S]}{K_i}\right)\right)}$.

7.1.27 Mass Spectrometry for Determination of Protein Mass

The masses of purified proteins were measured by Bruker maXis 3G UHF-TOF tandem mass spectrometer. Proteins were either buffer exchanged into 5 mM ammonium bicarbonate, or were diluted from stored concentrations to 1 mg mL^{-1} with water.

7.1.28 Differential Scanning Fluorimetry (DSF)

Melt temperatures of the proteins were determined both with and without the presence of different additives by DSF, using an iCycler iQ5 Multicolour Real-Time PCR Detection System (Bio-Rad). The method used was based on that of Ericsson *et al*.[64] Triplicate protein samples were added with mixing to buffer (potentially containing additives) and SYPRO orange dye (Invitrogen) in a 96-well microplate (*vide infra*), which was then sealed. The melt proceeded in 0.2 °C increments from 20 - 95 °C, with a 20 s dwell time after each temperature rise. Measurements of the fluorescence were made at the end of each dwell time.

For each sample (three replicates and blank) 100 µL of buffer (50 mM Tris.HCl pH 8.0, 200 mM NaCl) including any additive(s) was prepared, to which 5 µL of 250x SYPRO orange dye was added (condition solution). In the blank well for the sample, 21 µL of the condition solution was added to 4 µL of water. Then, 16 µL of protein (at 1 mg mL^{-1}) was added to the remaining condition solution before 25 µL was dispensed into three replicate wells. Additives used in experiments were as follows: PRPP (0.6 mM) Mg^{2+} (1 mM) or anthranilate (15 µM, 100 µM, 1 mM or 5 mM).

For analysis an Excel spreadsheet with custom VBA-scripted macro was created by Dr Timothy Allison to toggle and dynamically display melt and derivative curves for each sample. The melt

temperatures were calculated as the temperature of maximum inflection of the melting curve after subtracting the reading of a blank well containing buffer and dye but lacking protein.

7.1.29 Circular Dichroism (CD)

CD experiments were performed using a JASCO J-815 Spectropolarimeter. All CD spectra were recorded from 260 nm to 195 nm using a 0.5 nm data pitch, 1 s response, 1 nm bandwidth at 25 °C. A 3 mL protein solution at a concentration of 0.03 mg mL^{-1} in a 3 mL quartz cuvette with 1 cm path length was used for each measurement. The buffer for all experiments was 20 mM sodium phosphate pH 8.0. Blank spectra were recorded of buffer alone for each experiment before addition of protein. Data were smoothed using the Savitzky-Golay algorithm of the Jasco Spectra Manager™ (version 1.5) with a convolution width of 15.

7.1.30 Crystallisation of Variant *Mtu*-AnPRT

Crystals of variant *Mtu*-AnPRTs were grown by hanging-drop vapour diffusion in 24-well VDX plates (Hampton Research). Protein solutions (3 mg mL^{-1} to 7 mg mL^{-1}), in 50 mM Tris.HCl (pH 8.0), 150 mM NaCL and 5% glycerol (v/v)) were mixed 1:1 (v/v) with a reservoir solution containing 200 mM sodium imidazole malate (pH 6.5 – 8.0), 5% - 15% PEG-4000, and Milli-Q. The additives (PRPP, $MgCl_2$, anthranilate, ACS172 and ACS142) were all present at a concentration of 10 mM unless otherwise stated. All additives were co-crystallised with *Mtu*-AnPRT with the exception of anthranilate, which was soaked into the crystal in the presence of 26% glycerol and the crystal's mother liquor. Droplets were seeded with wild-type *Mtu*-AnPRT crystals using a cat whisker. Droplet sizes were 2 µL, and the reservoir solution volume 500 µL. Unless otherwise stated, the crystallisation trays were left at 20 °C until immediately before data collection, with crystals being transferred briefly into a cryoprotectant composed of 26% glycerol in the respective reservoir solution. Crystals typically began to form after 4 h and were fully formed in 24 h.

7.1.31 X-Ray Data Collection and Data Processing

X-Ray diffraction data were collected at the Australian Synchrotron. Protein was transported frozen to Melbourne the day before collection. Crystals were mounted on loops, flash-frozen in liquid nitrogen and placed in a sample storage cassette (Crystal Positioning Systems), which was stored in a dry shipper (Taylor-Wharton CX100) and transported as checked-in luggage. Data collection at the Australian Synchrotron used either the Macromolecular Crystallography (MX1) or Micro Crystallography (MX2) beamlines[86] and were processed using XDS,[87] iMosflm,[88] Scala or Aimless (CCP4 suite[89]). Resolution cutoffs were determined based on a CC½ value of > 0.5.[90]

7.1.32 Structure Determination and Refinement

Structures of *Mtu*-AnPRT variant proteins were solved by molecular replacement using PhaserMR (CCP4 suite), using chain A of the structure of wild-type *Mtu*-AnPRT (PDB ID: 3QR9) as a starting model (with all non-protein molecules removed) and performing ten rounds of rigid-body refinement using Refmac5.[91] Each structure had the same set of reflections for calculation of R_{free} as the starting model 3QR9, and these were carried through the refinement process for each structure. Further refinements were conducted with Refmac5,[91] and electron-density maps were analysed with Coot.[92] The validation tools of Coot and MolProbity[93] were used to check for, and correct, conformation infelicities.

In the refinement of ligand-bound structures, the model of the protein in the absence of any ligands was refined and rebuilt until the model was in close agreement with the electron density map. At this stage, waters and ligands other than the ligands of interest (eg. glycerol) were added to the model, except for the regions of the structure where the electron density suggested the presence of the ligands of interest. Waters were added into appropriate electron density if the water would have at least one hydrogen bond to the protein. Waters in secondary and higher shells were only added if the position of the water molecule allowed the establishment of an uninterrupted chain of interactions to a protein atom. Solvent ligands (eg. glycerol) were modelled into appropriate density and their occupancy refined by inspection of electron density maps after refinement.

After the model and electron density was judged in good agreement in all regions apart from the ligand binding site(s) of interest, the electron density in the ligand binding site(s) was examined. If appropriate electron density was present, the ligand(s) of interest and water molecules were added to the model and the final rounds of refinement carried out. Ligand restraints were generated by using the PRODRG server.[94] The occupancies of ligands of interest were refined by inspection of the electron density maps after refinement. The $2F_o-F_c$ omit maps shown in figures were generated using the program FFT (CCP4 suite) before addition of the ligands to the model.

7.2 Methods in Chapter 2

7.2.1 Kinetics

The assays for determining the kinetic parameters kept the concentration of one substrate constant while varying that of the other and vice versa. The concentration of *Mtu*-AnPRT used in each assay ranged from 0.1 – 0.3 μM in the cuvette depending on the experiment. *Eco*-PRAI:InGPS was always held at a concentration with a minimum 10-fold excess compared to *Mtu*-AnPRT, and ranged from 3

– 6 μM in the cuvette. To determine the kinetic parameters for wild-type *Mtu*-AnPRT, the following concentrations of substrates and metal were used in the enzyme-coupled assay: $MgCl_2$ (1 mM), PRPP (either held at 0.6 mM for determination of anthranilate parameters, or varied from 0 – 320 μM) and anthranilate (either held at 15 μM for determination of PRPP parameters, or varied from 0 – 11 μM).

For determination of Mg^{2+} inhibition, all other components were held at the concentrations mentioned in the above paragraph, with a range of 0 – 12 mM for $MgCl_2$. For determination of anthranilate inhibition, all other components were held at the concentrations mentioned in the above paragraph, with a range of 0 – 100 μM for anthranilate. For determination of the *Mtu*-AnPRT mechanism, all components were held at the concentrations mentioned in the above paragraph, except for anthranilate and PRPP which varied from 0 – 20 μM and 0 – 62.5 μM respectively.

K_i values of inhibitors thought to compete with anthranilate were determined using the enzyme-coupled assay, with PRPP held at a saturating concentration of 0.6 mM, $MgCl_2$ at 1 mM, *Mtu*-AnPRT ranging from 0.1 – 0.3 μM, and *Eco*-PRAI:InGPS ranging from 3 – 6 μM. The inhibitor ACS172 was tested from 0 – 8 μM, with an anthranilate range of 0 – 12 μM. The inhibitor ACS142 was tested from 0 – 20 μM, with an anthranilate range of 0 – 12 μM. The inhibitor ACS145 was tested from 0 – 90 μM, with an anthranilate range of 0 – 6 μM. The inhibitor ACS174 was tested from 0 – 13 μM, with an anthranilate range of 0 – 7.5 μM. The inhibitor ACS10 was tested from 0 – 60 μM, with an anthranilate range of 0 – 5.5 μM. The inhibitor ACS126 was tested from 0 – 104 μM, with an anthranilate range of 0 – 5.5 μM. The inhibitor ACS165 was tested from 0 – 43.8 μM, with an anthranilate range of 0 – 5.5 μM. The inhibitor ACS179 was tested from 0 – 14.4 μM, with an anthranilate range of 0 – 7.5 μM.

K_i values of inhibitors thought to compete with PRPP were determined using the enzyme-coupled assay, with anthranilate held at a saturating concentration of 15 μM, $MgCl_2$ at 1 mM, *Mtu*-AnPRT ranging from 0.1 – 0.3 μM, and *Eco*-PRAI:InGPS ranging from 3 – 6 μM. The inhibitor R5P was tested from 0 – 240 μM, with a PRPP range of 0 – 25 mM.

7.3 Methods in Chapter 3

7.3.1 Kinetics – PP_i Assay

The final concentrations of the following components were included in the PP_i assay and held at these concentrations: PRPP (120 μM), $MgCl_2$ (1 mM), *Mtu*-AnPRT (0.1 – 0.3 μM), *Eco*-PRAI-InGPS (3 - 6 μM), MESG (200 μM), PNP (1 U), inorganic pyrophosphatase (0.03 U), 50 μL of 20X reaction buffer

(1 M Tris-HCl, 20 mM $MgCl_2$, pH 7.5, containing 2 mM sodium azide) and sterile Milli Q water to 1 mL. Anthranilate was tested from 0 – 16 μM. 3FA was tested from 0 – 400 μM. 4FA was tested from 0 – 16 μM. 5FA was tested from 0 – 20 μM. 6FA was tested from 0 – 10 μM. 3MA was tested from 0 – 500 μM. 4MA was tested from 0 – 660 μM. 5MA was tested from 0 – 840 μM. 6MA was tested from 0 – 700 μM. ACS130 was tested from 0 – 250 μM.

K_i values of anthranilate analogues were obtained using the PP_i assay and contained the same components at the same concentrations as mentioned in the above paragraph. Anthranilate was tested from 0 – 100 μM. 3FA was tested from 0 – 700 μM. 4FA was tested from 0 – 100 μM. 5FA was tested from 0 – 100 μM. 6FA was tested from 0 – 60 μM.

7.3.2 Mass Spectrometry - Anomerisation

Solutions for determination of the mode of anomerization of PRA via mass spectroscopy contained 2 mM PRPP, 2 mM anthranilate, 1 mM $MgCl_2$, and 20 mM $NaCNBH_3$ made up to 2 mL with Tris.HCl buffer (50 mM Tris.HCl, 150 mM NaCl; pH 8.0). Solutions were mixed by inversion and 0.2 μM *Mtu*-AnPRT added. After 5 mins reaction time, solutions were spun through Vivaspin 10 000 MWCO concentrators to remove the enzyme present, flash frozen with liquid nitrogen, and left to freeze dry (FreeZone 2.5, Labconco) for 4 - 5 days. Dried products were then resuspended in Milli Q and analysed via Ultra High Resolution Time Of Flight (UHR-TOF) tandem mass spectrometry (Bruker maXis 3G).

7.3.3 Kinetics – Enzyme Coupled Assay

To detect turnover of anthranilate analogues by both *Mtu*-AnPRT and *Eco*-PRAI:InGPS, the enzyme-coupled assay was utilised. The following compounds were included in the assay: $MgCl_2$ (1 mM), PRPP (0.6 mM), *Mtu*-AnPRT (0.1 μM), anthranilate/analogue (200 μM) and *Eco*-PRAI:InGPS (4 – 8 μM).

Solutions for wavelength scan analysis of fluoro-/anthranilate contained 1 mM $MgCl_2$, 0.1 μM *Mtu*-AnPRT, 1.7 μM *Eco*-PRAI:InGPS, 0.6 mM PRPP and 100 μM fluoro-/anthranilate. Solutions for wavelength scan analysis of methyl-anthranilate contained 1 mM $MgCl_2$, 30 μM *Mtu*-AnPRT, 150 μM *Eco*-PRAI:InGPS, 0.6 mM PRPP and 0.5 mM methyl-anthranilate. Reactions were scanned from 360 - 220 nm with a cycle length time of 2.5 mins. Solutions were thermally equilibrated for 5 min prior to initiation with alternate substrate and either allowed to go to completion or to a maximum of 50 cycles.

7.3.4 Mass Spectrometry – *Eco*-PRAI:InGPS Turnover

Solutions for analysis of *Mtu*-AnPRT/*Eco*-PRAI:InGPS reaction products contained 1.2 mM PRPP, 400 µM fluoro-/anthranilate or 2 mM methyl-anthranilate, 2 mM $MgCl_2$, 0.6 µM *Mtu*-AnPRT, 6 µM *Eco*-PRAI:InGPS made up to 500 µL with H_2O for fluoro-/anthranilate or 5 mM NH_4HCO_3 for methyl-anthranilate. Reactions for fluoro-/anthranilate were initiated with *Mtu*-AnPRT immediately prior to analysis via mass spectrometry, whereas reactions for methyl-anthranilate were incubated with all substituents present for 1 hr prior to analysis.

7.4 Methods in Chapter 4

7.4.1 Primer Design

Primers for the mutations described in Section 4.3 were designed using the web-based QuikChange Primer Design tool by Agilent Technologies[95] and were ordered from Invitrogen™.

R193A Forward Primer	5’ CACGCGGCCGCGGTAGCCCGCGAGATC 3’
R193A Reverse Primer	5’ GATCTCGCGGGCTACCGCGGCCGCGTG 3’
N138A Forward Primer	5’ GGTCAAGCACGGCGCCCGAGCGGCGTCC 3’
N138A Reverse Primer	5’ GGACGCCGCTCGGGCGCCGTGCTTGACC 3’
G107P Forward Primer	5’ CGTCGACGTCGTCCCCACCGGTGGCGAC 3’
G107P Reverse Primer	5’ GTCGCCACCGGTGGGGACGACGTCGACG 3’
P180A Forward Primer	5’ GTTCTGCTTCGCGGCGCGGTTCCATCC 3’
P180A Reverse Primer	5’ GGATGGAACCGCGCCGCGAAGCAGAAC 3’
R194A Forward Primer	5’ GGCCGCGGTACGCGCCGAGATCGGTGTG 3’
R194A Reverse Primer	5’ CACACCGATCTCGGCGCGTACCGCGGCC 3’
R193L Forward Primer	5’ GGCCGCGGTACTCCGCGAGATCG 3’
R193L Reverse Primer	5’ CGATCTCGCGGAGTACCGCGGCC 3’

7.4.2 Site-Directed Mutagenesis

Mutagenesis was performed using either a Quikchange® Lightning Mutagenesis Kit (Stratagene) or Phusion® High-Fidelity DNA Polymerase (Thermo Fisher Scientific) with dNTPs from Invitrogen. PCRs

were performed in a Veriti® 96-well Thermal Cycler (Applied Biosystems) or an iCycler (Bio-Rad). Primers for mutagenesis were synthesised by Invitrogen and resuspended in sterilised Milli-Q water to a concentration of 100 µM. Each PCR reaction solution was 50 µL and typicially 85 ng of plasmid template and 200 ng of each primer was used. Initially, the cycling protocols used were those recommended by each kit or polymerase. If the use of these protocols did not yield the desired product, touchdown PCR was utilised with components from the Quikchange® Lightning Mutagenesis Kit (Stratagene) (see below). Template DNA (which is methylated) was digested by treatment with the restriction enzyme Dpn1 according to the protocols of the kit.

Touchdown PCR Protocol

1 x	denaturation	95 °C	2 min
21 x	denaturation	95 °C	30 s
	annealing	72 °C*	30 s
	extension	72 °C	6 min
14 x	denaturation	95 °C	30 s
	annealing	40 °C	30 s
	extension	72 °C	6 min
1 x	final extension	72 °C	10 min
	Hold	4 °C	∞

*This temperature drops 1.5 °C every cycle.

7.4.3 DNA Sequencing

All DNA sequencing was performed at Canterbury Sequencing and Genotyping using an Applied Biosystems 3130xl Genetic Analyzer with BigDye Terminator 189 v3.1 (Applied Biosystems) sequencing chemistry. Typically 300 ng to 700 ng of purified double-stranded plasmid and 3.2 µM of primer were supplied for each sample. As all AnPRT genes were in the pET-23a(+) vector containing a T7 promoter, TOPO forward and reverse primers from Invitrogen or Geneworks were used for all sequencing.

Forward: 5’ TAA TAC GAC TCA CTA TAG GG

Reverse: 5’ TAG TTA TTG CTC AGC GGT GG

7.4.4 Kinetics

The enzyme-coupled assay for determining the kinetic parameters of *Mtu*-AnPRT variants kept the concentration of one substrate constant while varying that of the other and vice versa. The following components were used in the assay: $MgCl_2$ (1 mM), *Eco*-PRAI:InGPS (3 – 10 µM - held at a minimum 10-fold excess), PRPP (either held at 0.6 mM for determination of anthranilate parameters, or varied), anthranilate (either held at saturating concentration for determination of PRPP parameters, or varied) and *Mtu*-AnPRT variant. PRPP, anthranilate and *Mtu*-AnPRT variant concentrations are as described below:

N138A (0.46 µM)	Anthranilate range: 0 – 220 µM
	PRPP range: 0 – 560 µM (anthranilate held at 200 µM)
R194A (0.1 µM)	Anthranilate range: 0 – 20 µM
	PRPP range: 0 – 130 µM (anthranilate held at 25 µM)
R193A (0.6 µM)	Anthranilate range: 0 – 1 mM
	PRPP range: 0 – 170 µM (anthranilate held at 200 µM)
R193L (1 µM)	Anthranilate range: 0 – 500 µM
	PRPP range: 0 – 400 µM (anthranilate held at 200 µM)
P180A (0.1 µM)	Anthranilate range: 0 – 12 µM
	PRPP range: 0 – 420 µM (anthranilate held at 25 µM)

The concentration of the inactive variant G107P was increased from 0.5 – 1.2 µM during experiments and was tested in the presence of up to 1 mM PRPP and up to 1 mM anthranilate.

7.4.5 Crystallisation and Data Collection

N138A/PRPP/Mg

The X-ray diffraction data for *Mtu*-AnPRT N138A was collected at the Australian Synchrotron on the Macromolecular Crystallography (MX1) beamline. Data were collected for crystals grown in 0.2 M imidazole malate (pH 6.5) with 7% PEG-4000. N138A crystallised in the monoclinic space group $P12_11$ and diffracted to 1.72 Å, with unit cell dimensions of a = 94.7 Å, b = 78.0 Å and c = 101.3 Å.

P180A/PRPP/Mg

The X-ray diffraction data for *Mtu*-AnPRT P180A was collected at the Australian Synchrotron on the Macromolecular Crystallography (MX1) beamline. Data were collected for crystals grown in 0.2 M imidazole malate (pH 7.0) with 11% PEG-4000. P180A crystallised in the monoclinic space group $C121$ and diffracted to 1.80 Å, with unit cell dimensions of a = 95.2 Å, b = 78.3 Å and c = 102.2 Å.

R193L/PRPP/Mg

The X-ray diffraction data for *Mtu*-AnPRT R193L was collected at the Australian Synchrotron on the Macromolecular Crystallography (MX1) beamline. Data were collected for crystals grown in 0.2 M imidazole malate (pH 6.5) with 7% PEG-4000. R193L crystallised in the monoclinic space group $C121$ and diffracted to 2.47 Å, with unit cell dimensions of a = 94.4 Å, b = 78.1 Å and c = 100.4 Å.

R193A/PRPP/Mg

The X-ray diffraction data for *Mtu*-AnPRT R193A was collected at the Australian Synchrotron on the Macromolecular Crystallography (MX1) beamline. Data were collected for crystals grown in 0.2 M imidazole malate (pH 8.0) with 7% PEG-4000. R193A crystallised in the orthorhombic space group $P2_12_12_1$ and diffracted to 2.04 Å, with unit cell dimensions of a = 79.6 Å, b = 92.5 Å and c = 120.3 Å.

N138A/PRPP/Mg/anth soaked for 10 s

The X-ray diffraction data for *Mtu*-AnPRT N138A was collected at the Australian Synchrotron on the Macromolecular Crystallography (MX1) beamline. Data were collected for crystals grown in 0.2 M imidazole malate (pH 7.5) with 9% PEG-4000. N138A crystallised in the orthorhombic space group $P2_12_12_1$ and diffracted to 2.23 Å, with unit cell dimensions of a = 79.7 Å, b = 91.7 Å and c = 119.4 Å.

P180A/PRPP/Mg/anth soaked for 1 s

The X-ray diffraction data for *Mtu*-AnPRT P180A was collected at the Australian Synchrotron on the Micro Crystallography (MX2) beamline. Data were collected for crystals grown in 0.2 M imidazole malate (pH 8.0) with 7% PEG-4000. P180A crystallised in the orthorhombic space group $P2_12_12_1$ and diffracted to 2.04 Å, with unit cell dimensions of a = 79.6 Å, b = 92.5 Å and c = 120.3 Å.

R193L/PRPP/Mg/anth soaked for 5 s

The X-ray diffraction data for *Mtu*-AnPRT R193L was collected at the Australian Synchrotron on the Macromolecular Crystallography (MX1) beamline. Data were collected for crystals grown in 0.2 M imidazole malate (pH 6.5) with 9% PEG-4000. R193L crystallised in the monoclinic space group $C121$ and diffracted to 2.33 Å, with unit cell dimensions of a = 94.5 Å, b = 78.1 Å and c = 100.6 Å.

R193A/PRPP/Mg/anth soaked for 3 s

The X-ray diffraction data for *Mtu*-AnPRT R193A was collected at the Australian Synchrotron on the Macromolecular Crystallography (MX1) beamline. Data were collected for crystals grown in 0.2 M imidazole malate (pH 6.5) with 9% PEG-4000. R193A crystallised in the orthorhombic space group $P2_12_12_1$ and diffracted to 2.20 Å, with unit cell dimensions of a = 80.0 Å, b = 91.7 Å and c = 120.8 Å.

R193A/PRPP/Mg/anth soaked for 1 min 10 s

The X-ray diffraction data for *Mtu*-AnPRT R193A was collected at the Australian Synchrotron on the Macromolecular Crystallography (MX1) beamline. Data were collected for crystals grown in 0.2 M imidazole malate (pH 6.5) with 7% PEG-4000. R193A crystallised in the orthorhombic space group $P2_12_12_1$ and diffracted to 2.50 Å, with unit cell dimensions of a = 79.7 Å, b = 91.4 Å and c = 119.1 Å.

R194A/PRPP/Mg/anth soaked for 5 min

The X-ray diffraction data for *Mtu*-AnPRT R194A was collected at the Australian Synchrotron on the Macromolecular Crystallography (MX1) beamline. Data were collected for crystals grown in 0.2 M imidazole malate (pH 7.0) with 11% PEG-4000. R194A crystallised in the monoclinic space group $C121$ and diffracted to 1.77 Å, with unit cell dimensions of a = 94.9 Å, b = 78.6 Å and c = 101.3 Å.

7.5 Methods in Chapter 5

7.5.1 Kinetics

K_i values of the inhibitors ACS172 and ACS142 for the *Mtu*-AnPRT variants N138A, P180A and R194A were determined using the enzyme-coupled assay, with PRPP held at a saturating concentration of 0.6 mM, $MgCl_2$ at 1 mM, and *Eco*-PRAI:InGPS ranging from 3 – 6 µM.

N138A (0.46 µM) ACS172 was tested from 0 - 110 µM, with an anthranilate range of 0 – 27 µM

ACS142 was tested from 0 – 630 µM with an anthranilate range of 0 – 24 µM

P180A (0.1 µM) ACS172 was tested from 0 - 110 µM, with an anthranilate range of 0 – 19 µM

ACS142 was tested from 0 – 690 µM with an anthranilate range of 0 – 18 µM

R194A (0.1 µM) ACS172 was tested from 0 - 60 µM, with an anthranilate range of 0 – 9 µM

ACS142 was tested from 0 – 690 µM with an anthranilate range of 0 – 18 µM

7.5.2 Crystallisation and Data Collection

N138A/PRPP/Mg/ACS172

The X-ray diffraction data for *Mtu*-AnPRT N138A was collected at the Australian Synchrotron on the Macromolecular Crystallography (MX1) beamline. Data were collected for crystals grown in 0.2 M imidazole malate (pH 6.5) with 7% PEG-4000. N138A crystallised in the monoclinic space group *C*121 and diffracted to 2.40 Å, with unit cell dimensions of *a* = 94.7 Å, *b* = 78.1 Å and *c* = 102.5 Å.

P180A/PRPP/Mg/ACS172

The X-ray diffraction data for *Mtu*-AnPRT P180A was collected at the Australian Synchrotron on the Macromolecular Crystallography (MX1) beamline. Data were collected for crystals grown in 0.2 M imidazole malate (pH 6.5) with 5% PEG-4000. P180A crystallised in the monoclinic space group *C*121 and diffracted to 1.95 Å, with unit cell dimensions of *a* = 95.5 Å, *b* = 78.1 Å and *c* = 101.9 Å.

R194A/PRPP/Mg/ACS172

The X-ray diffraction data for *Mtu*-AnPRT R194A was collected at the Australian Synchrotron on the Macromolecular Crystallography (MX1) beamline. Data were collected for crystals grown in 0.2 M

imidazole malate (pH 7.0) with 7% PEG-4000. R194A crystallised in the monoclinic space group *C*121 and diffracted to 2.06 Å, with unit cell dimensions of *a* = 95.1 Å, *b* = 78.1 Å and *c* = 102.8 Å.

R194A/PRPP/Mg/ACS142

The X-ray diffraction data for *Mtu*-AnPRT R194A was collected at the Australian Synchrotron on the Macromolecular Crystallography (MX1) beamline. Data were collected for crystals grown in 0.2 M imidazole malate (pH 6.5) with 9% PEG-4000. R194A crystallised in the monoclinic space group *C*121 and diffracted to 2.23 Å, with unit cell dimensions of *a* = 95.0 Å, *b* = 78.5 Å and *c* = 102.5 Å.

Appendix 1

Differential Scanning Fluorimetry Raw Data

This appendix contains raw DSF data for *Eco*-PRAI:InGPS, *Mtu*-AnPRT with and without ligands present, and for variant *Mtu*-AnPRT proteins. The differentiated relative fluorescence units (RFU) are plotted against temperature in °C. The denaturation temperature is derived from the local minimum for each data set.

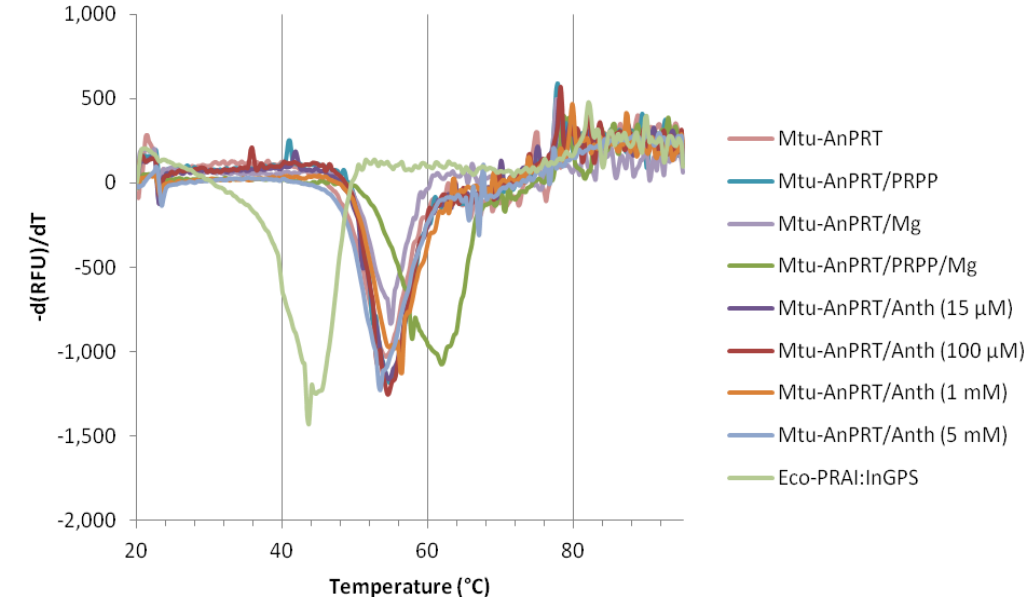

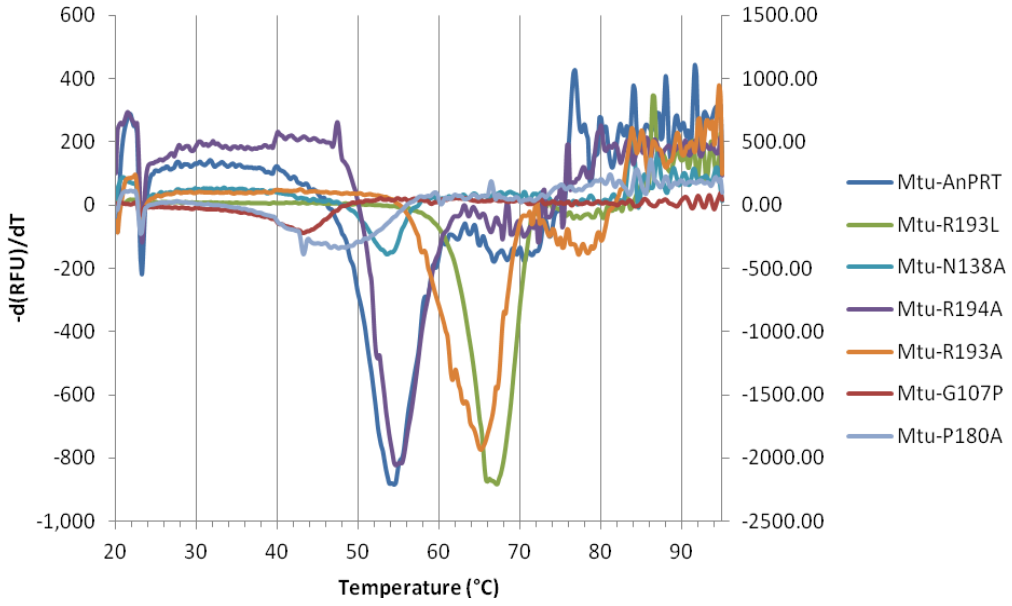

Appendix 2

^{1}H NMR Spectra for *Mtu*-AnPRT Catalysis of Anthranilate Analogues

This appendix contains the ^{1}H NMR spectra obtained by Dr Esther Bulloch at the University of Auckland, and shows the successful conversion of each alternate substrate into the respective PRA substituted product with the exception of 3MA.

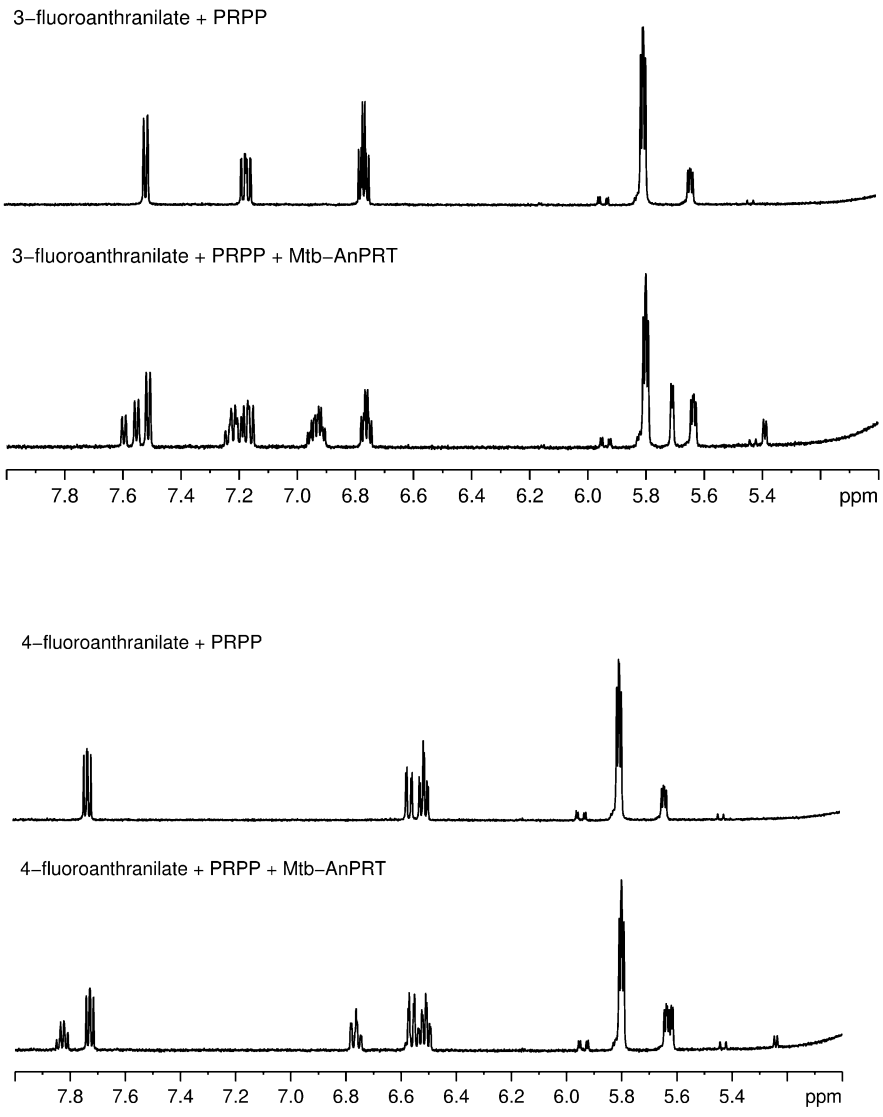

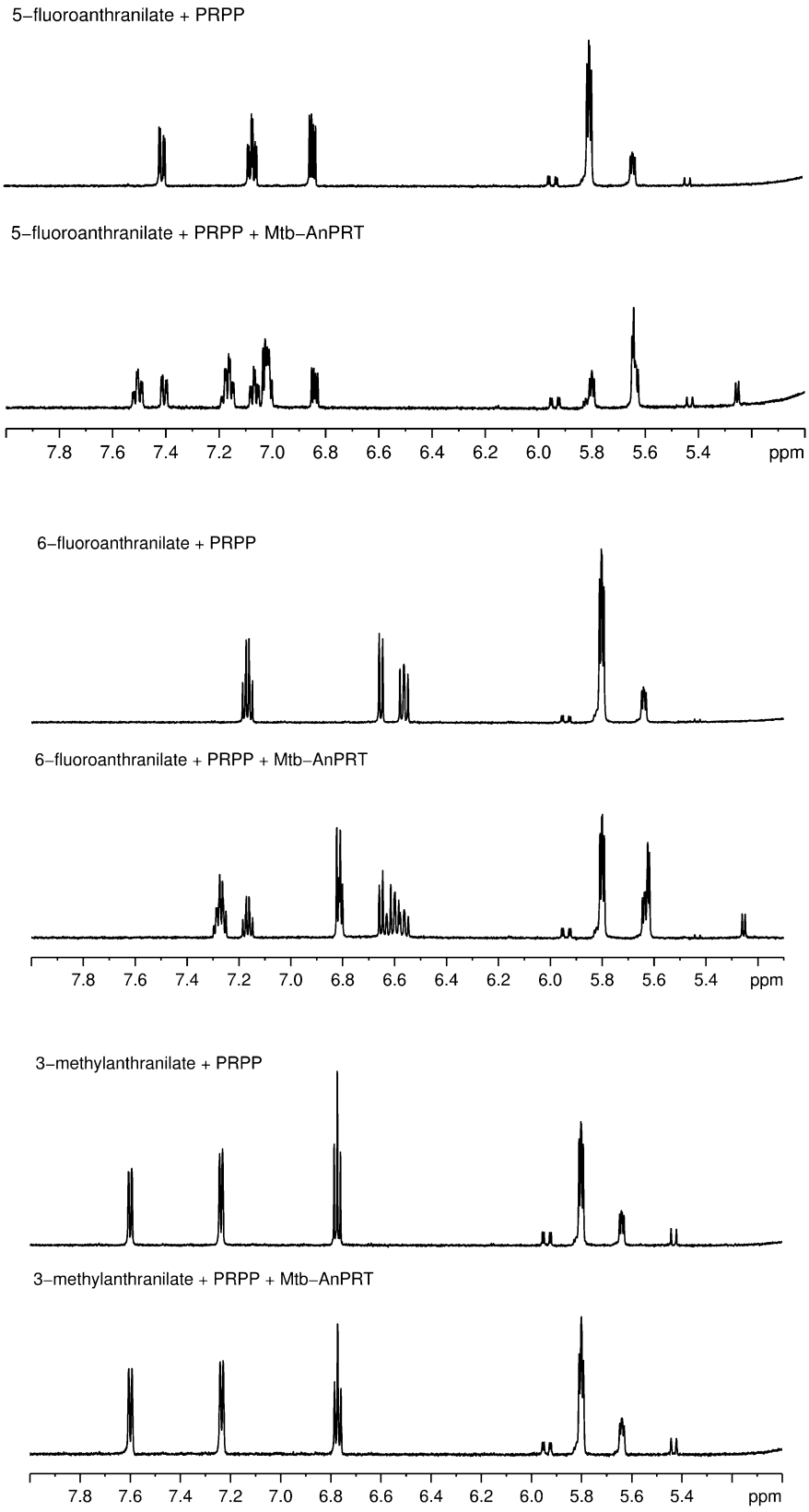
5–fluoroanthranilate + PRPP
5–fluoroanthranilate + PRPP + Mtb–AnPRT
7.8 7.6 7.4 7.2 7.0 6.8 6.6 6.4 6.2 6.0 5.8 5.6 5.4 ppm
6–fluoroanthranilate + PRPP
6–fluoroanthranilate + PRPP + Mtb–AnPRT
7.8 7.6 7.4 7.2 7.0 6.8 6.6 6.4 6.2 6.0 5.8 5.6 5.4 ppm
3–methylanthranilate + PRPP
3–methylanthranilate + PRPP + Mtb–AnPRT
7.8 7.6 7.4 7.2 7.0 6.8 6.6 6.4 6.2 6.0 5.8 5.6 5.4 ppm

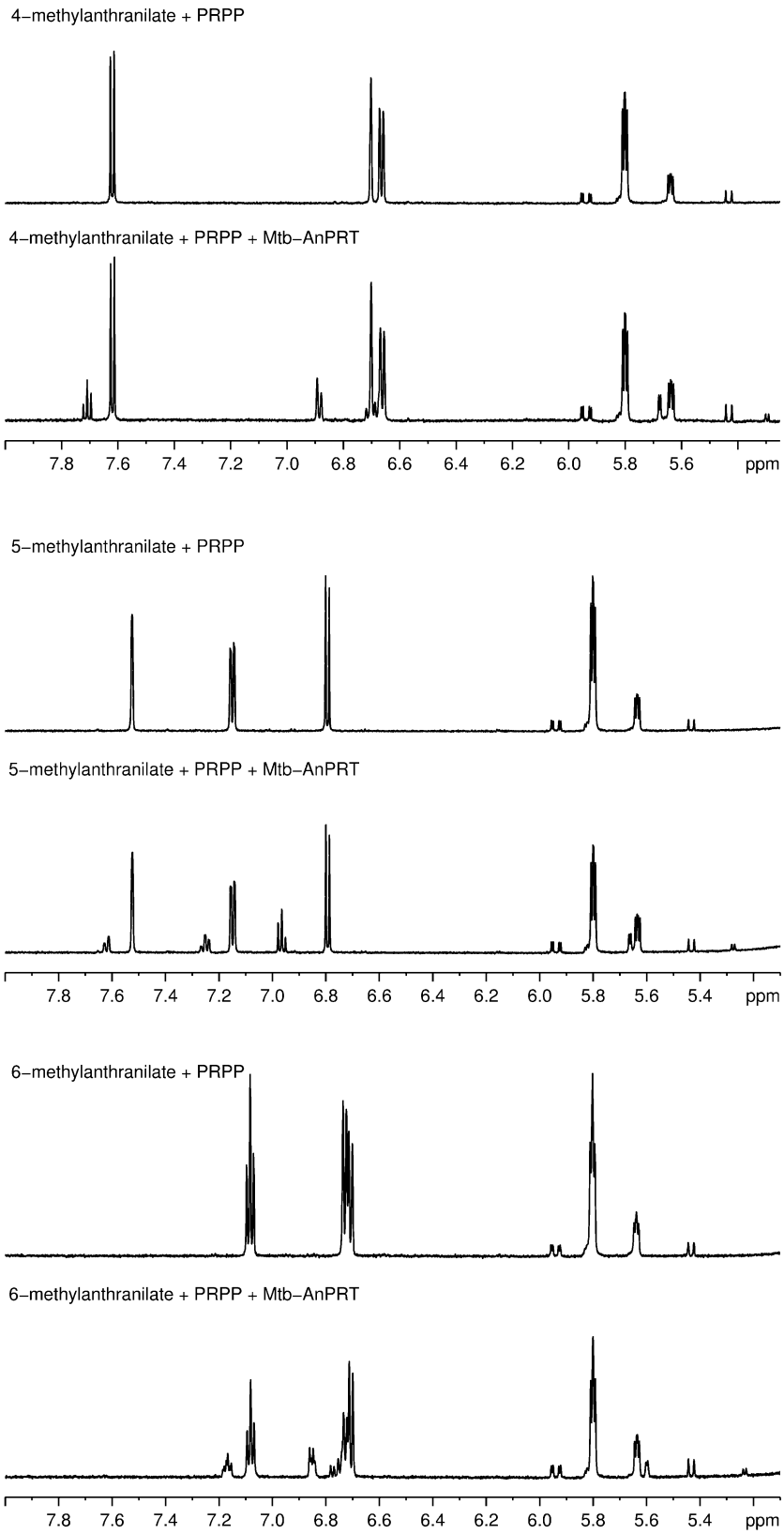
4–methylanthranilate + PRPP
4–methylanthranilate + PRPP + Mtb–AnPRT
7.8 7.6 7.4 7.2 7.0 6.8 6.6 6.4 6.2 6.0 5.8 5.6 ppm
5–methylanthranilate + PRPP
5–methylanthranilate + PRPP + Mtb–AnPRT
7.8 7.6 7.4 7.2 7.0 6.8 6.6 6.4 6.2 6.0 5.8 5.6 5.4 ppm
6–methylanthranilate + PRPP
6–methylanthranilate + PRPP + Mtb–AnPRT
7.8 7.6 7.4 7.2 7.0 6.8 6.6 6.4 6.2 6.0 5.8 5.6 5.4 ppm

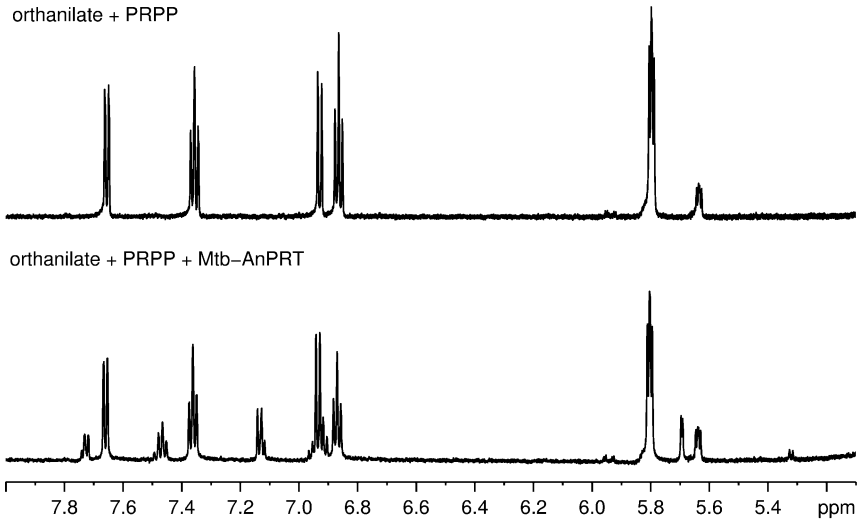
orthanilate + PRPP
orthanilate + PRPP + Mtb−AnPRT
7.8
7.6
7.4
7.2
7.0
6.8
6.6
6.4
6.2
6.0
5.8
5.6
5.4
ppm

Appendix 3

Crystal Structure Data Tables

This appendix contains the final statistics for each crystal structure solved in this thesis, obtained from structure processing and refinement using CCP4 software.[89]

Complex	N138A/PRPP/Mg	P180A/PRPP/Mg	R193L/PRPP/Mg
	Data Collection		
Space group	$P12_11$	$C121$	$C121$
Cell dimensions			
a, b, c (Å)	94.7, 78.0, 101.3	95.2, 78.3, 102.2	94.4, 78.1, 100.4
α, β, γ (°)	90.0, 111.3, 90.0	90.0, 111.7, 90.0	90.0, 110.5, 90.0
No. of unique reflections	145346	64672	24299
Resolution range[a] (Å)	94.38-1.72 (1.75-1.72)	58.65-1.80 (1.85-1.80)	39.95-2.47 (2.59-2.47)
CC½	0.998 (0.583)	0.999 (0.583)	0.988 (0.569)
R_{merge}[a,b]	0.214 (2.82)	0.239 (3.79)	0.186 (1.08)
I/σ(I)[a]	8.2 (0.9)	20.0 (1.7)	7.5 (1.9)
Completeness[a] (%)	99.7 (98.5)	100 (100)	98.8 (98.9)
Redundancy[a]	14.3 (12.3)	28.7 (23.6)	5.0 (5.1)
	Refinement		
No. of atoms, *B* factor[c]			
Protein	9910, 17.9	4930, 21.3	4936, 20.7
Solvent	660, 26.9	236, 31.7	46, 34.4
PRPP	44, 22.9	66, 26.6	44, 53.2
Mg^{2+}	4, 23.7	2, 23.0	2, 43.9
R_{work}[a,d] (%), R_{free}[a,e] (%)	26.9, 30.2 (48.8, 51.4)	19.1, 22.0 (28.4, 31.3)	21.1, 26.1 (31.7 , 35.6)
Ramachandran outliers[f] (%)	0.29	0.15	0.15
RMSD[g]			
Bond lengths (Å)	0.009	0.010	0.007
Bond angles (°)	1.465	1.484	1.377

[a] – Data for the outer resolution shell are shown in parentheses.
[b] – $R_{merge} = \sum_{hkl} I(hkl) - \langle I(hkl)\rangle / \sum_{hkl} I(hkl)$, where $\langle I(hkl)\rangle$ is the mean of the symmetry-equivalent reflections of $I(hkl)$.
[c] –Å^2 The average atomic temperature factor.
[d] – $R_{work} = (|F_{obs}| - |F_{calc}|) / |F_{obs}|$.
[e] – $R_{free} = \sum_T (|F_{obs}| - |F_{calc}|) / \sum_T |F_{obs}|$, where T is a test data set of 5% of the total reflections randomly chosen and set aside before refinement.
[f] – Ramachandran outliers calculated using Molprobity.[93]
[g] - Ideal values from Engh and Huber (1991).[96]

Complex Anth Soak Time	R193A/PRPP/Mg	N138A/PRPP/Mg/Anth (10 s)	P180A/PRPP/Mg/Anth (1 s)
		Data Collection	
Space group	*C*121	$P2_12_12_1$	$P2_12_12_1$
Cell dimensions			
a, b, c (Å)	94.5, 77.8, 101.9	79.7, 91.7, 119.4	79.6, 92.5, 120.3
α, β, γ (°)	90.0, 111.8, 90.0	90.0, 90.0, 90.0	90.0, 90.0, 90.0
No. of unique reflections	50966	43292	56304
Resolution range[a] (Å)	47.31-1.93 (1.98-1.93)	119.4-2.23 (2.30-2.23)	120.3-2.04 (2.10-2.04)
CC½	0.996 (0.560)	0.995 (0.581)	0.998 (0.576)
R_{merge}[a,b]	0.129 (1.66)	0.267 (2.17)	0.183 (1.59)
$I/\sigma(I)$[a]	8.2 (0.9)	12.4 (1.1)	14.5 (1.0)
Completeness[a] (%)	99.0 (98.3)	99.7 (97.3)	98.6 (82.2)
Redundancy[a]	4.7 (4.7)	13.9 (8.0)	13.6 (4.2)
		Refinement	
No. of atoms, *B* factor[c]			
Protein	4962, 25.8	4985, 26.2	5008, 32.2
Solvent	148, 33.7	154, 38.5	224, 36.9
PRPP	N/A	N/A	N/A
Mg^{2+}	N/A	N/A	1, 49.6
Anthranilate	N/A	N/A	N/A
R_{work}[a,d] (%), R_{free}[a,e] (%)	24.1, 28.3 (38.4, 40.6)	21.4, 25.5 (39.5, 44.9)	20.8, 24.3 (42.5, 47.5)
Ramachandran outliers[f] (%)	0.29	0.29	0.43
RMSD[g]			
Bond lengths (Å)	0.011	0.010	0.010
Bond angles (°)	1.432	1.460	1.424

[a] – Data for the outer resolution shell are shown in parentheses.

[b] – $R_{merge} = \sum_{hkl} I(hkl) - \langle I(hkl)\rangle / \sum_{hkl} I(hkl)$, where $\langle I(hkl)\rangle$ is the mean of the symmetry-equivalent reflections of $I(hkl)$.

[c] –Å^2 The average atomic temperature factor.

[d] – $R_{work} = (|F_{obs}| - |F_{calc}|) / |F_{obs}|$.

[e] – $R_{free} = \sum_T (|F_{obs}| - |F_{calc}|) / \sum_T |F_{obs}|$, where T is a test data set of 5% of the total reflections randomly chosen and set aside before refinement.

[f] – Ramachandran outliers calculated using Molprobity.[93]

[g] - Ideal values from Engh and Huber (1991).[96]

Complex Anth Soak Time	R193L/PRPP/Mg/Anth (5 s)	R193A/PRPP/Mg/Anth (3 s)	R193A/PRPP/Mg/Anth (1 min 10 s)
		Data Collection	
Space group	*C*121	$P2_12_12_1$	$P2_12_12_1$
Cell dimensions			
a, b, c (Å)	94.5, 78.1, 100.6	80.0, 91.7, 120.8	79.7, 91.4, 119.1
α, β, γ (°)	90.0, 110.6, 90.0	90.0, 90.0, 90.0	90.0, 90.0, 90.0
No. of unique reflections	29405	44908	30694
Resolution range[a] (Å)	94.12-2.33 (2.41-2.33)	120.8-2.20 (2.27-2.20)	119.1-2.50 (2.60-2.50)
CC½	0.996 (0.576)	0.999 (0.938)	0.995 (0.689)
R_{merge}[a,b]	0.182 (1.72)	0.068 (0.254)	0.255 (1.40)
I/σ(I)[a]	10.2 (1.2)	37.9 (7.0)	13.2 (1.9)
Completeness[a] (%)	100 (99.9)	98.1 (81.2)	99.5 (95.5)
Redundancy[a]	7.4 (7.5)	13.8 (5.6)	14.1 (11.2)
		Refinement	
No. of atoms, *B* factor[c]			
Protein	4938, 32.5	4976, 27.8	4987, 28.1
Solvent	60, 40.6	235, 35.2	102, 33.6
PRPP	22, 52.4	N/A	N/A
Mg^{2+}	4, 53.1	N/A	N/A
Anthranilate	N/A	20, 63.1	20, 57.0
Pyrophosphate	9, 75.7	N/A	N/A
R_{work}[a,d] (%), R_{free}[a,e] (%)	20.1, 25.7 (31.5, 36.1)	20.4, 23.5 (49.5, 47.4)	20.1, 26.1 (26.7, 33.8)
Ramachandran outliers[f] (%)	0.00	0.44	0.29
RMSD[g]			
Bond lengths (Å)	0.010	0.011	0.010
Bond angles (°)	1.442	1.435	1.455

[a] – Data for the outer resolution shell are shown in parentheses.
[b] – $R_{merge} = \sum_{hkl} I(hkl) - \langle I(hkl)\rangle / \sum_{hkl} I(hkl)$, where $\langle I(hkl)\rangle$ is the mean of the symmetry-equivalent reflections of $I(hkl)$.
[c] –Å^2 The average atomic temperature factor.
[d] – $R_{work} = (|F_{obs}| - |F_{calc}|) / |F_{obs}|$.
[e] – $R_{free} = \sum_T (|F_{obs}| - |F_{calc}|) / \sum_T |F_{obs}|$, where T is a test data set of 5% of the total reflections randomly chosen and set aside before refinement.
[f] – Ramachandran outliers calculated using Molprobity.[93]
[g] - Ideal values from Engh and Huber (1991).[96]

Complex Anth Soak Time	R194A/PRPP/Mg/Anth (5 min)	N138A/PRPP/Mg/172	P180A/PRPP/Mg/172
		Data Collection	
Space group	*C*121	*C*121	*C*121
Cell dimensions			
a, b, c (Å)	94.9, 78.6, 101.3	94.7, 78.1, 102.5	95.5, 78.1, 101.9
α, β, γ (°)	90.0, 110.2, 90.0	90.0, 111.9, 90.0	90.0, 111.5, 90.0
No. of unique reflections	68018	27281	50366
Resolution range[a] (Å)	95.1-1.77 (1.87-1.77)	47.6-2.40 (2.49-2.40)	47.4-1.95 (2.00-1.95)
CC½	0.998 (0.502)	0.998 (0.829)	0.991 (0.532)
R_{merge}[a,b]	0.136 (2.28)	0.117 (0.692)	0.139 (1.75)
I/σ(I)[a]	12.0 (1.2)	16.4 (3.3)	15.3 (1.3)
Completeness[a] (%)	99.8 (99.4)	100 (100)	100 (99.9)
Redundancy[a]	12.2 (9.1)	7.5 (7.6)	7.6 (7.6)
		Refinement	
No. of atoms, *B* factor[c]			
Protein	5027, 26.8	4857, 26.3	4849, 25.8
Solvent	520, 39.8	67, 28.6	150, 34.3
Mg^{2+}	4, 35.4	N/A	N/A
Anthranilate	40, 39.1	N/A	N/A
Pyrophosphate	18, 26.3	N/A	N/A
172	N/A	38, 46.4	38, 48.1
R_{work}[a,d] (%), R_{free}[a,e] (%)	18.7/22.1(39.4/42.2)	21.9, 26.8 (28.2, 38.3)	25.4, 29.9 (34.9 , 36.3)
Ramachandran outliers[f] (%)	0.15	0.30	0.30
RMSD[g]			
Bond lengths (Å)	0.010	0.009	0.010
Bond angles (°)	1.455	1.373	1.409

[a] – Data for the outer resolution shell are shown in parentheses.

[b] – $R_{merge} = \sum_{hkl} I(hkl) - \langle I(hkl)\rangle / \sum_{hkl} I(hkl)$, where $\langle I(hkl)\rangle$ is the mean of the symmetry-equivalent reflections of $I(hkl)$.

[c] –Å^2 The average atomic temperature factor.

[d] – $R_{work} = (|F_{obs}| - |F_{calc}|) / |F_{obs}|$.

[e] – $R_{free} = \sum_T (|F_{obs}| - |F_{calc}|) / \sum_T |F_{obs}|$, where T is a test data set of 5% of the total reflections randomly chosen and set aside before refinement.

[f] – Ramachandran outliers calculated using Molprobity.[93]

[g] - Ideal values from Engh and Huber (1991).[96]

Complex	R194A/PRPP/Mg/172	R194A/PRPP/Mg/142
	Data Collection	
Space group	*C*121	*C*121
Cell dimensions		
a, b, c (Å)	95.1, 78.1, 102.8	95.0, 78.5, 102.5
α, β, γ (°)	90.0, 111.8, 90.0	90.0, 111.8, 90.0
No. of unique reflections	43298	34186
Resolution range[a] (Å)	47.7-2.06 (2.12-2.06)	47.6-2.23 (2.30-2.23)
CC½	0.998 (0.542)	0.998 (0.665)
R_{merge}[a,b]	0.151 (1.43)	0.146 (1.39)
$I/\sigma(I)$[a]	13.8 (1.5)	12.2 (1.7)
Completeness[a] (%)	100 (100)	100 (99.9)
Redundancy[a]	7.6 (7.6)	7.5 (7.5)
	Refinement	
No. of atoms, *B* factor[c]		
Protein	4934, 24.6	4828, 30.1
Solvent	158, 31.8	58, 38.9
172	38, 52.5	N/A
142	N/A	36, 64.2
R_{work}[a,d] (%), R_{free}[a,e] (%)	18.6, 22.3 (27.9, 28.6)	20.0, 23.3 (34.0, 37.8)
Ramachandran outliers[f] (%)	0.29	0.30
RMSD[g]		
Bond lengths (Å)	0.010	0.010
Bond angles (°)	1.411	1.436

[a] – Data for the outer resolution shell are shown in parentheses.
[b] – $R_{merge} = \sum_{hkl} I(hkl) - \langle I(hkl)\rangle / \sum_{hkl} I(hkl)$, where $\langle I(hkl)\rangle$ is the mean of the symmetry-equivalent reflections of $I(hkl)$.
[c] –Å^2 The average atomic temperature factor.
[d] – $R_{work} = (|F_{obs}| - |F_{calc}|) / |F_{obs}|$.
[e] – $R_{free} = \sum_T (|F_{obs}| - |F_{calc}|) / \sum_T |F_{obs}|$, where T is a test data set of 5% of the total reflections randomly chosen and set aside before refinement.
[f] – Ramachandran outliers calculated using Molprobity.[93]
[g] - Ideal values from Engh and Huber (1991).[96]

Appendix 4

Crystal Structure Omit Maps

This appendix contains the difference and post-refinement maps for all ligands bound to variant *Mtu*-AnPRTs. The left-hand side panels depict the difference maps prior to the addition of ligands to the structures, with the F_o-F_c maps contoured at 3.0 σ, and coloured green for positive density and red for negative density. The right-hand side panels depict the post-refinement maps for the ligands, with the $2F_o$-F_c maps contoured at 1.0 σ and coloured blue, and the F_o-F_c maps contoured at 3.0 σ and coloured green for positive density and red for negative density. Water molecules are not included.

N138A/PRPP/Mg

Chain C – PRPP (green), Mg (green spheres)

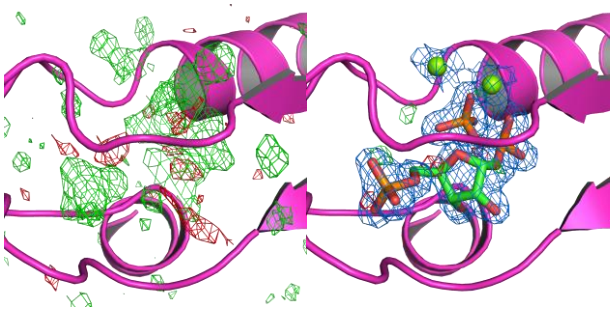

Chain D – PRPP (green), Mg (green spheres)

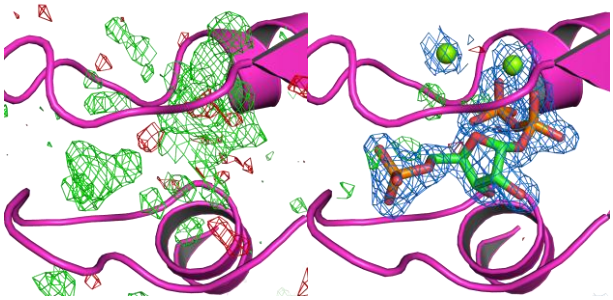

P180A/PRPP/Mg

Chain A – PRPP (magenta), Mg (magenta spheres)

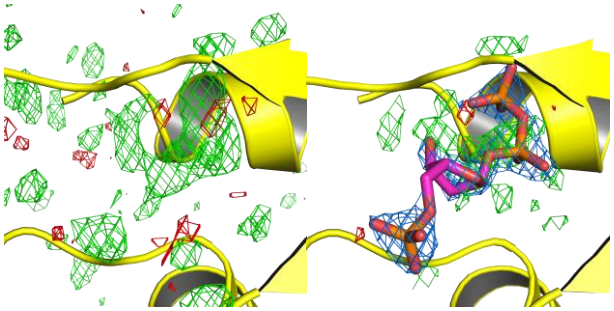

Chain B – PRPP (magenta), Mg (magenta spheres)

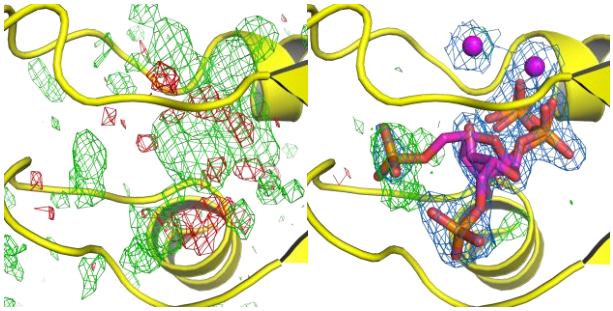

R193L/PRPP/Mg

Chain A – PRPP (green), Mg (green spheres)

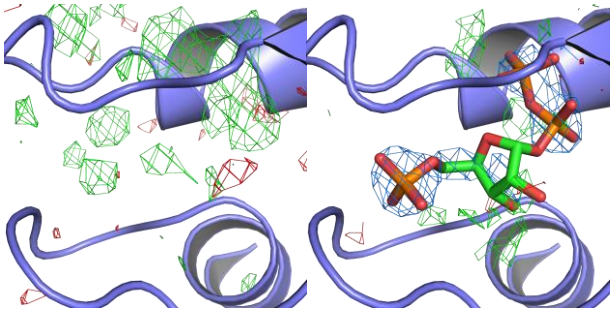

Chain B – PRPP (green), Mg (green spheres)

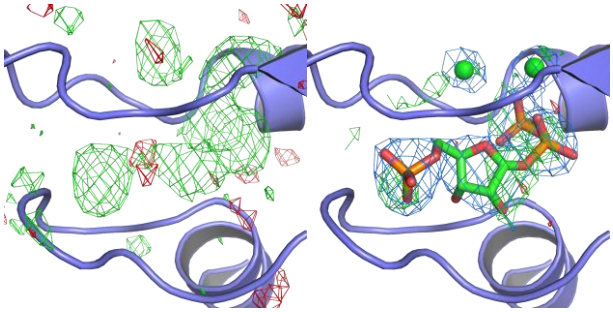

R193L/PRPP/Mg/Anth (5 s soak)

Chain A – PRPP (magenta), Mg (magenta spheres)

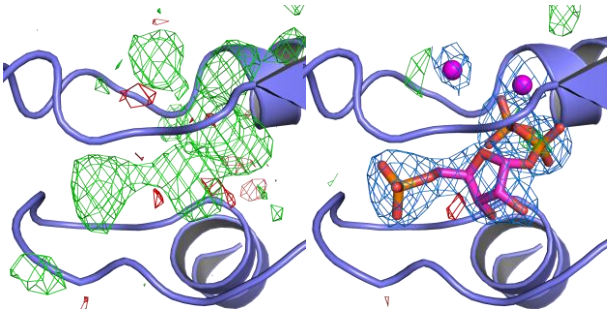

Chain B – PRPP (magenta), Mg (magenta spheres)

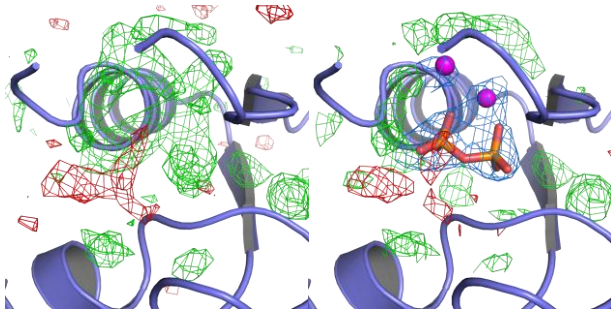

R193A/PRPP/Mg/Anth (3 s soak)

Chain A – Anth (purple)

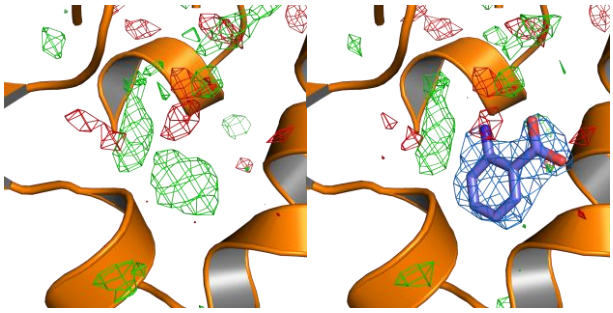

Chain B – Anth (purple)

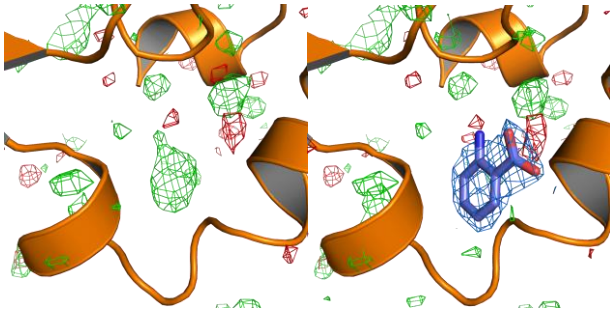

R193A/PRPP/Mg/Anth (1 min 10 s soak)

Chain A – Anth (green)

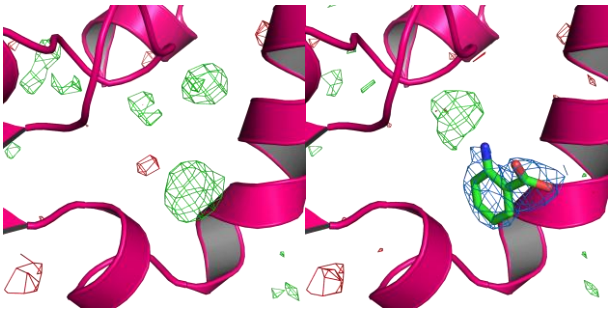

Chain B – Anth (green)

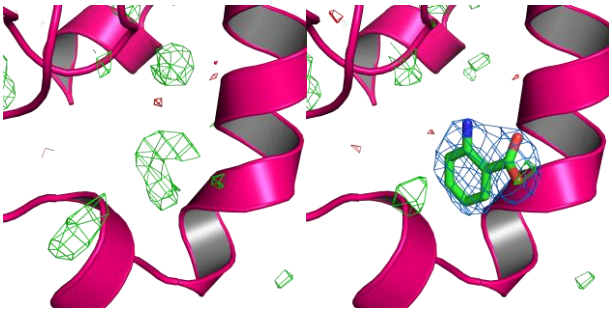

R194A/PRPP/Mg/Anth (5 min soak)

Chain A – Anth (blue), PP_i (orange),

Mg (blue spheres)

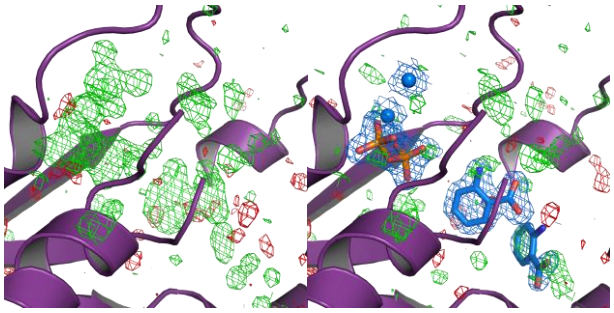

Chain B – Anth (blue), PP_i (orange),

Mg (blue spheres)

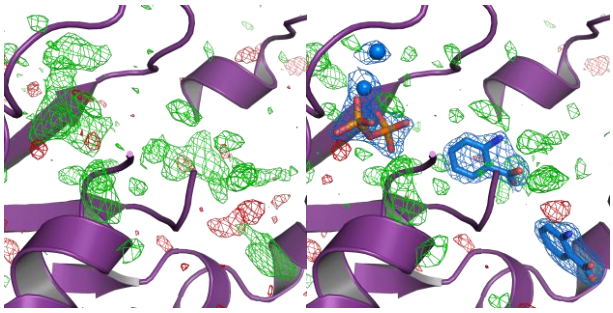

N138A/PRPP/Mg/ACS172

Chain A – ACS172 (purple)

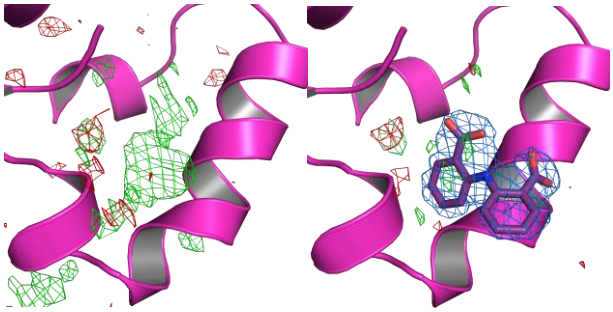

Chain B – ACS172 (purple)

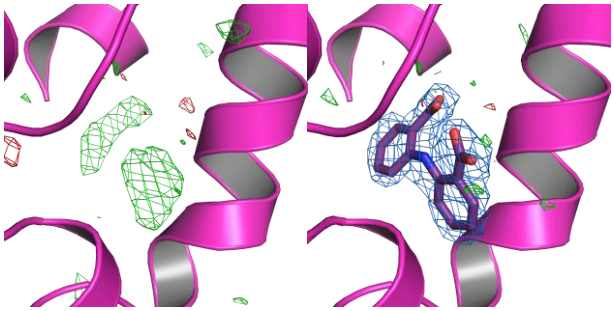

P180A/PRPP/Mg/ACS172

Chain A – ACS172 (purple)

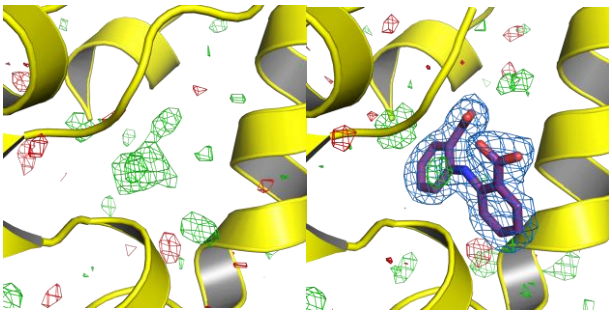

Chain B – ACS172 (purple)

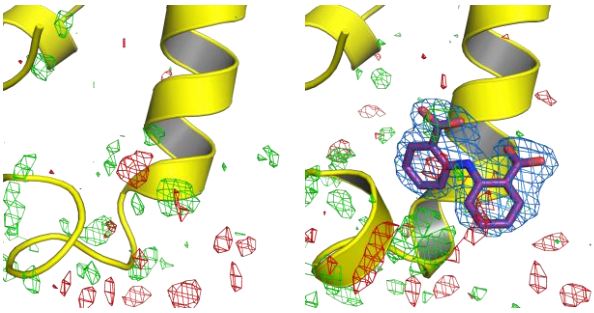

R194A/PRPP/Mg/ACS172

Chain A – ACS172 (purple)

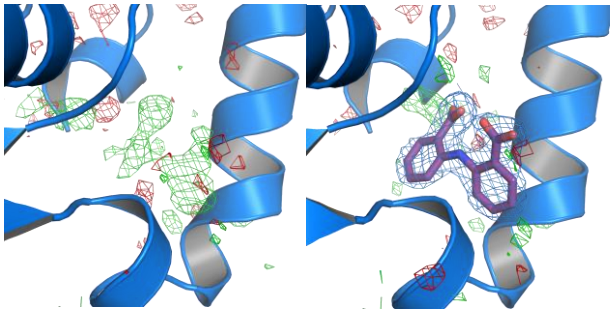

Chain B – ACS172 (purple)

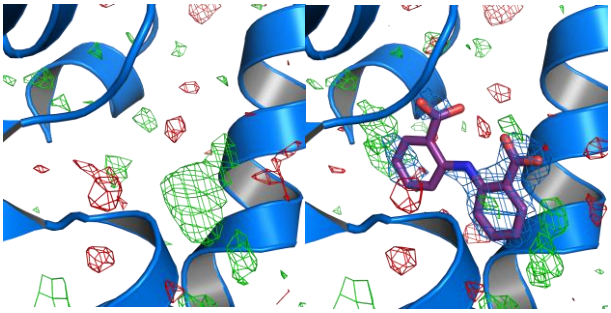

R194A/PRPP/Mg/ACS142

Chain A – ACS142 (yellow)

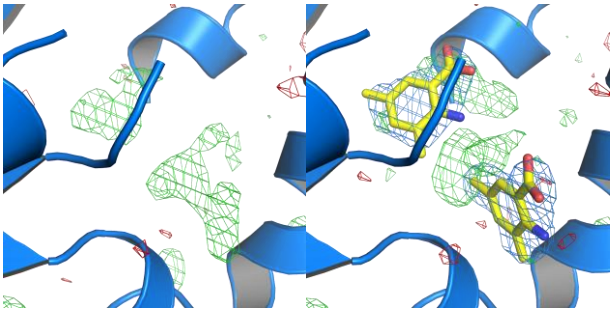

Chain B – ACS142 (yellow)

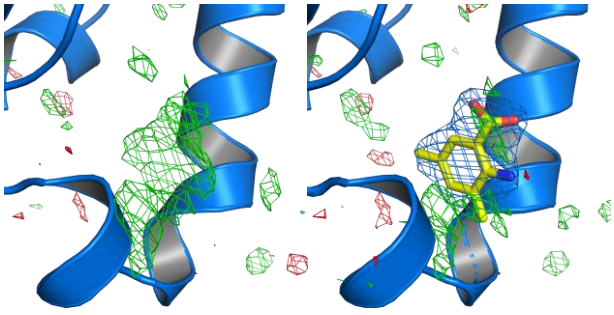

Bibliography

1. Dormandy, T., The white death: a history of tuberculosis. New York University Press: NY, USA, **1999**.

2. Russell, D. G.; Barry, C. E.; Flynn, J. L., Tuberculosis: What we don't know can, and does, hurt us. *Science* **2010,** 328 (5980), 852-856.

3. (a) Clemens, D. L., Characterization of the *Mycobacterium tuberculosis* phagosome. *Trends Microbiol.* **1996,** 4 (3), 113-118; (b) Flynn, J. L.; Chan, J., Immune evasion by *Mycobacterium tuberculosis*: living with the enemy. *Curr. Opin. Immunol.* **2003,** 15 (4), 450-455.

4. Kapoor, N.; Pawar, S.; Sirakova, T. D.; Deb, C.; Warren, W. L.; Kolattukudy, P. E., Human granuloma in vitro model for TB dormancy and resuscitation. *PLoS One* **2013,** 8 (1).

5. Crowley, L., An introduction to human disease: pathology and pathophysiology correlations. 8 ed.; Jones and Bartlett: Massachusetts, USA, **2010**.

6. Smith, I., *Mycobacterium tuberculosis* pathogenesis and molecular determinants of virulence. *Clin. Microbiol. Rev.* **2003,** 16 (3), 463-+.

7. Davis, A. L., History of the sanatorium movement. Little, Brown and Company: Boston, USA, **1996**.

8. Gradmann, C., Robert Koch and the white death: from tuberculosis to tuberculin. *Microbes Infect.* **2006,** 8 (1), 294-301.

9. Rom, W. N. G., S. M., Tuberculosis. 2 ed.; Lippincott, Williams & Wilkins: Philadelphia, USA, **2004**.

10. Development, G. A. f. T. D. http://www.tballiance.org.

11. Baciewicz, A. M.; Chrisman, C. R.; Finch, C. K.; Self, T. H., Update on rifampin, rifabutin, and rifapentine drug interactions. *Curr. Med. Res. Opin.* **2013,** 29 (1), 1-12.

12. Organization, W. H. Global Tuberculosis Report; Geneva, Switzerland, **2012**.

13. Cole, S. T., Comparative and functional genomics of the *Mycobacterium tuberculosis* complex. Microbiology-(UK) **2002,** 148, 2919-2928.

14. (a) Gehre, F.; Otu, J.; DeRiemer, K.; de Sessions, P. F.; Hibberd, M. L.; Mulders, W.; Corrah, T.; de Jong, B. C.; Antonio, M., Deciphering the growth behaviour of *Mycobacterium africanum*. *Plos Neglect. Trop. Dis.* **2013,** 7 (5); (b) Miltgen, J.; Morillon, M.; Koeck, J. L.; Varnerot, A.; Briant, J. F.; Nguyen, G.; Verrot, D.; Bonnet, D.; Vincent, W., Two cases of pulmonary tuberculosis caused by *Mycobacterium canetti*. *Emerg. Infect. Dis* **2002,** 8 (11), 1350-1352.

15. Guzman, J. D.; Gupta, A.; Bucar, F.; Gibbons, S.; Bhakta, S., Antimycobacterials from natural sources: ancient times, antibiotic era and novel scaffolds. *Front. Biosci.* **2012,** 17, 1861-1881.

16. Lee, R. E.; Brennan, P. J.; Besra, G. S., *Mycobacterium tuberculosis* cell envelope. In Tuberculosis, Shinnick, T. M., Ed. Springer-Verlag Berlin: Berlin, **1996**; Vol. 215, pp 1-27.

17. (a) Murohash.T; Kondo, E.; Yoshida, K., Role of lipids in acid-fastness of mycobacteria. *Am. Rev. Respir. Dis.* **1969,** 99 (5), 794-&; (b) Matsuba, T.; Nakajima, C.; Suzuki, Y., Envelope structure and components of *Mycobacterium tuberculosis. JPN J. Bact.* **2010,** 65 (2-4), 355-68.

18. (a) Voskuil, M. I.; Bartek, I. L.; Visconti, K.; Schoolnik, G. K., The response of *Mycobacterium tuberculosis* to reactive oxygen and nitrogen species. *Front. Microbiol.* **2011,** 2, 105; (b) Ehrt, S.; Schnappinger, D., Mycobacterial survival strategies in the phagosome: defence against host stresses. *Cell Microbiol.* **2009,** 11 (8), 1170-1178.

19. (a) Favrot, L.; Ronning, D. R., Targeting the mycobacterial envelope for tuberculosis drug development. *Expert Rev. Anti-Infect. Ther.* **2012,** 10 (9), 1023-1036; (b) Coxon, G. D.; Cooper, C. B.; Gillespie, S. H.; McHugh, T. D., Strategies and challenges involved in the discovery of new chemical entities during early-stage tuberculosis drug discovery. *J. Infect. Dis.* **2012,** 205, S258-S264; (c) Boshoff, H. I. M.; Myers, T. G.; Copp, B. R.; McNeil, M. R.; Wilson, M. A.; Barry, C. E., The transcriptional responses of *Mycobacterium tuberculosis* to inhibitors of metabolism - novel insights into drug mechanisms of action. *J. Biol. Chem.* **2004,** 279 (38), 40174-40184.

20. (a) Davis, B. D., Intermediates in amino acid biosynthesis. *Adv. Enzymol. Rel. S. Bi.* **1955,** 16, 247-312; (b) Sprinson, D. B., The biosynthesis of aromatic compounds from D-glucose. *Adv. Carbohyd. Chem.* **1960,** 15, 235-270; (c) Roberts, F.; Roberts, C. W.; Johnson, J. J.; Kyle, D. E.; Krell, T.; Coggins, J. R.; Coombs, G. H.; Milhous, W. K.; Tzipori, S.; Ferguson, D. J. P.; Chakrabarti, D.; McLeod, R., Evidence for the shikimate pathway in apicomplexan parasites. *Nature* **1998,** 393 (6687), 801-805.

21. Herrmann, K. M.; Weaver, L. M., The shikimate pathway. *Annu. Rev. Plant Physiol. Plant Molec. Biol.* **1999,** 50, 473-503.

22. Bentley, R., The shikimate pathway - a metabolic tree with many branches. *Crit. Rev. Biochem. Mol. Biol.* **1990,** 25 (5), 307-384.

23. Smith, D. A.; Parish, T.; Stoker, N. G.; Bancroft, G. J., Characterization of auxotrophic mutants of *Mycobacterium tuberculosis* and their potential as vaccine candidates. *Infect. Immun.* **2001,** 69 (2), 1142-1150.

24. (a) Crawford, I. P., Evolution of a biosynthetic-pathway - the tryptophan paradigm. *Annu. Rev. Microbiol.* **1989,** 43, 567-600; (b) Yanofsky, C., Tryptophan biosynthesis in *Escherichia coli* - genetic determination of proteins involved. *J. Amer. Med. Assoc.* **1971,** 218 (7), 1026-&; (c) Yanofsky, C., Using studies on tryptophan metabolism to answer basic biological questions. *J. Biol. Chem.* **2003,** 278 (13), 10859-10878; (d) Yanofsky, C., Advancing our knowledge in biochemistry, genetics, and microbiology through studies on tryptophan metabolism. *Annu. Rev. Biochem.* **2001,** 70, 1-37.

25. Lin, X. H.; Xu, S. F.; Yang, Y. P.; Wu, J. C.; Wang, H. J.; Shen, H. B.; Wang, H. H., Purification and characterization of anthranilate synthase component I (TrpE) from *Mycobacterium tuberculosis* H37Rv. *Protein Expr. Purif.* **2009,** 64 (1), 8-15.

26. (a) Barona-Gomez, F.; Hodgson, D. A., Occurrence of a putative ancient-like isomerase involved in histidine and tryptophan biosynthesis. *EMBO Rep.* **2003,** 4 (3), 296-300; (b)

Jurgens, C.; Strom, A.; Wegener, D.; Hettwer, S.; Wilmanns, M.; Sterner, R., Directed evolution of a $(\beta/\alpha)_8$-barrel enzyme to catalyze related reactions in two different metabolic pathways. *Proc. Natl. Acad. Sci.* U. S. A. **2000,** 97 (18), 9925-9930.

27. Yanofsky, C.; Platt, T.; Crawford, I. P.; Nichols, B. P.; Christie, G. E.; Horowitz, H.; Vancleemput, M.; Wu, A. M., The complete nucleotide sequence of the tryptophan operon of *Escherichia coli*. *Nucleic Acids Res.* **1981,** 9 (24), 6647-6668.

28. Sterner, R.; Dahm, A.; Darimont, B.; Ivens, A.; Liebl, W.; Kirschner, K., (beta-alpha)(8)-barrel proteins of tryptophan biosynthesis in the hyperthermophile *Thermotoga maritima. Embo J*. **1995,** 14 (18), 4395-4402.

29. (a) Smith, J. L., Forming and inhibiting PRT active sites. *Nat. Struct. Biol.* **1999,** 6 (6), 502-504; (b) Musick, W. D. L., Structural features of the phosphoribosyltransferases and their relationship to the human deficiency disorders of purine and pyrimidine metabolism. *Crit. Rev. Biochem.* **1981,** 11 (1), 1-34.

30. Pugmire, M. J.; Ealick, S. E., Structural analyses reveal two distinct families of nucleoside phosphorylases. *Biochem. J.* **2002,** 361, 1-25.

31. (a) Sharma, V.; Grubmeyer, C.; Sacchettini, J. C., Crystal structure of quinolinic acid phosphoribosyltransferase from *Mycobacterium tuberculosis*: a potential TB drug target. *Struct. Fold. Des.* **1998,** 6 (12), 1587-1599; (b) Tao, W.; Grubmeyer, C.; Blanchard, J. S., Transition state structure of *Salmonella typhimurium* orotate phosphoribosyltransferase. *Biochemistry* **1996,** 35 (1), 14-21; (c) Sinha, S. C.; Smith, J. L., The PRT protein family. *Curr. Opin. Struct. Biol.* **2001,** 11 (6), 733-739.

32. Hershey, H. V.; Taylor, M. W., Nucleotide-sequence and deduced amino-acid-sequence of *Escherichia coli* adenine phosphoribosyltransferase and comparison with other analogous enzymes. *Gene* **1986,** 43 (3), 287-293.

33. Chen, S. H.; Tomchick, D. R.; Wolle, D.; Hu, P.; Smith, J. L.; Switzer, R. L.; Zalkin, H., Mechanism of the synergistic end-product regulation of *Bacillus subtilis* glutamine phosphoribosylpyrophosphate amidotransferase by nucleotides. *Biochemistry* **1997,** 36 (35), 10718-10726.

34. Krahn, J. M.; Kim, J. H.; Burns, M. R.; Parry, R. J.; Zalkin, H.; Smith, J. L., Coupled formation of an amidotransferase interdomain ammonia channel and a phosphoribosyltransferase active site. *Biochemistry* **1997,** 36 (37), 11061-11068.

35. Scapin, G.; Ozturk, D. H.; Grubmeyer, C.; Sacchettini, J. C., The crystal structure of the orotate phosphoribosyltransferase complexed with orotate and α-D-5-phosphoribosyl-1-pyrophosphate. *Biochemistry* **1995,** 34 (34), 10744-10754.

36. Eads, J. C.; Scapin, G.; Xu, Y. M.; Grubmeyer, C.; Sacchettini, J. C., The crystal-structure of human hypoxanthine-guanine phosphoribosyltransferase with bound gmp. *Cell* **1994,** 78 (2), 325-334.

37. Jensen, K. F.; Mygind, B., Different oligomeric states are involved in the allosteric behavior of uracil phosphoribosyltransferase from *Escherichia coli. Eur. J. Biochem*. **1996,** 240 (3), 637-645.

38. Eads, J. C.; Ozturk, D.; Wexler, T. B.; Grubmeyer, C.; Sacchettini, J. C., A new function for a common fold: the crystal structure of quinolinic acid phosphoribosyltransferase. *Structure* **1997,** 5 (1), 47-58.

39. Chappie, J. S.; Canaves, J. M.; Han, G. W.; Rife, C. L.; Xu, C. P.; Stevens, R. C., The structure of a eukaryotic nicotinic acid phosphoribosyltransferase reveals structural heterogeneity among type II PRTases. *Structure* **2005,** 13 (9), 1385-1396.

40. Okuno, E.; White, R. J.; Schwarcz, R., Quinolinic acid phosphoribosyltransferase - purification and partial characterization from human-liver and brain. *J. Biochem.* **1988,** 103 (6), 1054-1059.

41. (a) Castell, A.; Short, F. L.; Evans, G. L.; Cookson, T. V. M.; Bulloch, E. M. M.; Joseph, D. D. A.; Lee, C. E.; Parker, E. J.; Baker, E. N.; Lott, J. S., The substrate capture mechanism of Mycobacterium tuberculosis anthranilate phosphoribosyltransferase provides a mode for inhibition. *Biochemistry* **2013,** 52 (10), 1776-1787; (b) Schramm, V. L.; Grubmeyer, C., Phosphoribosyltransferase mechanisms and roles in nucleic acid metabolism. *Prog. Nucleic Acid Re.* Vol 78 **2004,** 78, 261-+.

42. Marino, M.; Deuss, M.; Svergun, D. I.; Konarev, P. V.; Sterner, R.; Mayans, O., Structural and mutational analysis of substrate complexation by anthranilate phosphoribosyltransferase from *Sulfolobus solfataricus*. *J. Biol. Chem.* **2006,** 281 (30), 21410-21421.

43. Kim, C.; Xuong, N. H.; Edwards, S.; Madhusudan; Yee, M. C.; Spraggon, G.; Mills, S. E., The crystal structure of anthranilate phosphoribosyltransferase from the enterobacterium *Pectobacterium carotovorum*. *FEBS Lett*. **2002,** 523 (1-3), 239-246.

44. Lee, C. E.; Goodfellow, C.; Javid-Majd, F.; Baker, E. N.; Lott, J. S., The crystal structure of TrpD, a metabolic enzyme essential for lung colonization by *Mycobacterium tuberculosis*, in complex with its substrate phosphoribosylpyrophosphate. *J. Mol. Biol.* **2006,** 355 (4), 784-797.

45. (a) Mayans, O.; Ivens, A.; Nissen, L. J.; Kirschner, K.; Wilmanns, M., Structural analysis of two enzymes catalysing reverse metabolic reactions implies common ancestry. *Embo J*. **2002,** 21 (13), 3245-3254; (b) Mushegian, A. R.; Koonin, E. V., Unexpected sequence similarity between nucleosidases and phosphoribosyltransferases of different specificity. *Protein Sci*. **1994,** 3 (7), 1081-1088.

46. (a) Cho, Y.; Sharma, V.; Sacchettini, J. C., Crystal structure of ATP phosphoribosyltransferase from *Mycobacterium tuberculosis*. *J. Biol. Chem.* **2003,** 278 (10), 8333-8339; (b) Lohkamp, B.; McDermott, G.; Campbell, S. A.; Coggins, J. R.; Lapthorn, A. J., The structure of *Escherichia coli* ATP-phosphoribosyltransferase: identification of substrate binding sites and mode of AMP inhibition. *J. Mol. Biol.* **2004,** 336 (1), 131-144.

47. (a) Bovee, M. L.; Champagne, K. S.; Demeler, B.; Francklyn, C. S., The quaternary structure of the HisZ-HisG N-1-(5 '-phosphoribosyl)-ATP transferase from *Lactococcus lactis. Biochemistry* **2002,** 41 (39), 11838-11846; (b) Sissler, M.; Delorme, C.; Bond, J.; Ehrlich, S. D.; Renault, P.; Francklyn, C., An aminoacyl-tRNA synthetase paralog with a catalytic role in histidine biosynthesis. *Proc. Natl. Acad. Sci. U. S. A.* **1999,** 96 (16), 8985-8990; (c) Champagne, K. S.; Piscitelli, E.; Francklyn, C. S., Substrate recognition by the hetero-octameric ATP phosphoribosyltransferase from *Lactococcus lactis. Biochemistry* **2006,** 45 (50), 14933-14943.

48. Poirot, O.; O'Toole, E.; Notredame, C., Tcoffee@igs: a web server for computing, evaluating and combining multiple sequence alignments. *Nucleic Acids Res.* **2003,** 31 (13), 3503-3506.

49. Waterhouse, A. M.; Procter, J. B.; Martin, D. M. A.; Clamp, M.; Barton, G. J., Jalview Version 2-a multiple sequence alignment editor and analysis workbench. *Bioinformatics* **2009,** 25 (9), 1189-1191.

50. Schlee, S.; Deuss, M.; Bruning, M.; Ivens, A.; Schwab, T.; Hellmann, N.; Mayans, O.; Sterner, R., Activation of anthranilate phosphoribosyltransferase from *Sulfolobus solfataricus* by removal of magnesium inhibition and acceleration of product release. *Biochemistry* **2009,** 48 (23), 5199-5209.

51. Cookson, T. V. M.; Castell, A.; Bulloch, E. M. M.; Evans, G. L.; Baker, E. N.; Lott, J. S.; Parker, E. J., Alternative substrates reveal catalytic cycle and key binding events in the reaction catalysed by anthranilate phosphoribosyltransferase from *Mycobacterium tuberculosis*. **manuscript in preparation**.

52. Schwab, T.; Skegro, D.; Mayans, O.; Sterner, R., A rationally designed monomeric variant of anthranilate phosphoribosyltransferase from *Sulfolobus solfataricus* is as active as the dimeric wild-type enzyme but less thermostable. *J. Mol. Biol.* **2008,** 376 (2), 506-516.

53. The PyMOL Molecular Graphics System, Version 1.5.0.4; Schrodinger, LLC.

54. Stemmer, W. P. C., DNA shuffling by random fragmentation and reassembly - in-vitro recombination for molecular evolution. *Proc. Natl. Acad. Sci. U. S. A.* **1994,** 91 (22), 10747-10751.

55. (a) Mendieta, J.; Martin-Santamaria, S.; Priego, E. M.; Balzarini, J.; Camarasa, M. J.; Perez-Perez, M. J.; Gago, F., Role of histidine-85 in the catalytic mechanism of thymidine phosphorylase as assessed by targeted molecular dynamics simulations and quantum mechanical calculations. *Biochemistry* **2004,** 43 (2), 405-414; (b) Degano, M.; Gopaul, D. N.; Scapin, G.; Schramm, V. L.; Sacchettini, J. C., Three-dimensional structure of the inosine-uridine nucleoside N-ribohydrolase from *Crithidia fasciculata*. *Biochemistry* **1996,** 35 (19), 5971-5981.

56. Lee, C. E. Structural and biochemical studies on potential drug targets from *Mycobacterium tuberculosis*. University of Auckland, **2007**.

57. Sterner, R.; Kleemann, G. R.; Szadkowski, H.; Lustig, A.; Hennig, M.; Kirschner, K., Phosphoribosyl anthranilate isomerase from *Thermotoga maritima* is an extremely stable and active homodimer. *Protein Sci.* **1996,** 5 (10), 2000-2008.

58. Ivens, A.; Mayans, O.; Szadkowski, H.; Wilmanns, M.; Kirschner, R., Purification, characterization and crystallization of thermostable anthranilate phosphoribosyltransferase from *Sulfolobus solfataricus. Eur. J. Biochem*. **2001,** 268 (8), 2246-2252.

59. Louis-Jeune, C.; Andrade-Navarro, M. A.; Perez-Iratxeta, C., Prediction of protein secondary structure from circular dichroism using theoretically derived spectra. *Proteins* **2012,** 80 (2), 374-381.

60. Greenfield, N. J., Using circular dichroism spectra to estimate protein secondary structure. *Nat. Protoc.* **2006,** 1 (6), 2876-2890.

61. Wilmanns, M.; Priestle, J. P.; Niermann, T.; Jansonius, J. N., 3-dimensional structure of the bifunctional enzyme phosphoribosylanthranilate isomerase - indoleglycerolphosphate synthase from *Escherichia coli* refined at 2.0 A resolution. *J. Mol. Biol.* **1992,** 223 (2), 477-507.

62. Gasteiger E., H. C., Gattiker A., Duvaud S., Wilkins M.R., Appel R.D., Bairoch A, Protein identification and analysis tools on the ExPASy server. John M. Walker (ed): The Proteomics Protocols Handbook **2005**, 571-607

63. (a) Sherman, F.; Stewart, J. W.; Tsunasawa, S., Methionine or not methionine at the beginning of a protein. *Bioessays* **1985,** 3 (1), 27-31; (b) Benbassat, A.; Bauer, K.; Chang, S. Y.; Myambo, K.; Boosman, A.; Chang, S., Processing of the initiation methionine from proteins - properties of the *Escherichia coli* methionine aminopeptidase and its gene structure. *J. Bacteriol.* **1987,** 169 (2), 751-757; (c) Chang, S. Y. P.; McGary, E. C.; Chang, S., Methionine aminopeptidase gene of *Escherichia coli* is essential for cell-growth. *J. Bacteriol.* **1989,** 171 (7), 4071-4072.

64. Ericsson, U. B.; Hallberg, B. M.; DeTitta, G. T.; Dekker, N.; Nordlund, P., Thermofluor-based high-throughput stability optimization of proteins for structural studies. *Anal. Biochem.* **2006,** 357 (2), 289-298.

65. Creighton, T. E.; Yanofsky, C., Chorismate to tryptophan (*Escherichia coli*)—anthranilate synthetase, PR transferase, PRA isomerase, InGP synthetase, tryptophan synthetase. *Method. Enzymol.* Herbert Tabor, C. W. T., Ed. Academic Press: 1970; Vol. Volume 17, Part A, pp 365-380.

66. (a) Hommel, U.; Lustig, A.; Kirschner, K., Purification and characterization of yeast anthranilate phosphoribosyltransferase. *Eur. J. Biochem.* **1989,** 180 (1), 33-40; (b) Gonzalez, J. E.; Somerville, R. L., The anthranilate aggregate of *Escherichia coli* - kinetics of inhibition by tryptophan of phosphoribosyltransferase. *Biochem. Cell Biol.* **1986,** 64 (7), 681-691.

67. Leatherbarrow, R. J. GraFit Version 5, 5.0; Erithacus Software Limited: Horley, UK, **2001**.

68. Zalkin, H.; Henderso.Ej, Tryptophan-mediated substrate inhibition of anthranilate-5-phosphoribosylpyrophosphate phosphoribosyltransferase. *Biochem. Biophys. Res. Commun.* **1969,** 35 (1), 52-&.

69. Brandl, M.; Weiss, M. S.; Jabs, A.; Suhnel, J.; Hilgenfeld, R., C-H···π interactions in proteins. *J. Mol. Biol.* **2001,** 307 (1), 357-377.

70. (a) Zhang, Y.; Luo, M. K.; Schramm, V. L., Transition states of *Plasmodium falciparum* and human orotate phosphoribosyltransferases. *J. Am. Chem. Soc.* **2009,** 131 (13), 4685-4694; (b) Goitein, R. K.; Chelsky, D.; Parsons, S. M., Primary C^{14} and α-secondary H^3 substrate kinetic isotope effects for some phosphoribosyltransferases. *J. Biol. Chem.* **1978,** 253 (9), 2963-2971.

71. Fedorov, A.; Shi, W.; Kicska, G.; Fedorov, E.; Tyler, P. C.; Furneaux, R. H.; Hanson, J. C.; Gainsford, G. J.; Larese, J. Z.; Schramm, V. L.; Almo, S. C., Transition state structure of purine nucleoside phosphorylase and principles of atomic motion in enzymatic catalysis. *Biochemistry* **2001,** 40 (4), 853-860.

72. Takahashi, R.; Nakamura, S.; Nakazawa, T.; Minoura, K.; Yoshida, T.; Nishi, Y.; Kobayashi, Y.; Ohkubo, T., Structure and reaction mechanism of human nicotinamide phosphoribosyltransferase. *J. Biochem.* **2010,** 147 (1), 95-107.

73. González-Segura, L.; Witte, J. F.; McClard, R. W.; Hurley, T. D., Ternary complex formation and induced asymmetry in orotate phosphoribosyltransferase. *Biochemistry* **2007,** 46 (49), 14075-14086.

74. Kim, C.; Xuong, N. H.; Edwards, S.; Yee, M. C.; Spraggon, G.; E Mills, S., The crystal structure of anthranilate phosphoribosyltransferase from the enterobacterium *Pectobacterium carotovorum. FEBS letters* **2002,** 523 (1), 239-246.

75. (a) Schendel, F. J.; Cheng, Y. S.; Otvos, J. D.; Wehrli, S.; Stubbe, J., Characterization and chemical properties of phosphoribosylamine, an unstable intermediate in the *de novo* purine biosynthetic pathway. *Biochemistry* **1988,** 27 (7), 2614-2623; (b) Cheng, Y. S.; Murray, M.; Schendel, F.; Otvos, J.; Wehrli, S.; Stubbe, J., Chemical characterization of phosphoribosylamine, a substrate for newly discovered trifunctional protein containing glycineamide ribonucleotide synthetase activity. *Adv. Enzyme Regul.* **1987,** 26, 319-333.

76. Atkins, P. W., The Elements of Physical Chemistry 3ed.; Oxford University Press: **1993**.

77. (a) Kline, P. C.; Schramm, V. L., Purine nucleoside phosphorylase - catalytic mechanism and transition-state analysis of the arsenolysis reaction. *Biochemistry* **1993,** 32 (48), 13212-13219; (b) Schramm, V. L., Enzymatic transition states and transition state analog design. *Annu. Rev. Biochem.* **1998,** 67, 693-720.

78. (a) Shi, W. X.; Li, C. M.; Tyler, P. C.; Furneaux, R. H.; Cahill, S. M.; Girvin, M. E.; Grubmeyer, C.; Schramm, V. L.; Almo, S. C., The 2.0 angstrom structure of malarial purine phosphoribosyltransferase in complex with a transition-state analogue inhibitor. *Biochemistry* **1999,** 38 (31), 9872-9880; (b) Shi, W. X.; Li, C. M.; Tyler, P. C.; Furneaux, R. H.; Grubmeyer, C.; Schramm, V. L.; Almo, S. C., The 2.0 angstrom structure of human hypoxanthineguanine phosphoribosyltransferase in complex with a transition-state analog inhibitor. *Nat. Struct. Biol.* **1999,** 6 (6), 588-593; (c) Heroux, A.; White, E. L.; Ross, L. J.; Davis, R. L.; Borhani, D. W., Crystal structure of *Toxoplasma gondii* hypoxanthine-guanine phosphoribosyltransferase with XMP, pyrophosphate, and two Mg^{2+} ions bound: insights into the catalytic mechanism. *Biochemistry* **1999,** 38 (44), 14495-14506.

79. Slater, J. C., Atomic radii in crystals. *J. Chem. Phys.* **1964,** 41 (10), 3199-&.

80. Balderas-Hernandez, V. E.; Sabido-Ramos, A.; Silva, P.; Cabrera-Valladares, N.; Hernandez-Chavez, G.; Baez-Viveros, J. L.; Martinez, A.; Bolivar, F.; Gosset, G., Metabolic engineering for improving anthranilate synthesis from glucose in *Escherichia coli. Microb. Cell. Fact.* **2009,** 8.

81. (a) Reyrat, J. M.; Kahn, D., *Mycobacterium smegmatis*: an absurd model for tuberculosis? *Trends Microbiol.* **2001,** 9 (10), 472-473; (b) Gordon, R. E.; Smith, M. M., Rapidly growing, acid fast bacteria: species descriptions of *Mycobacterium phlei* lehmann and neumann and *Mycobacterium smegmatis* (trevisan) lehmann and neumann. *J. Bacteriol.* **1953,** 66 (1), 41-48.

82. Reichau, S.; Jiao, W. T.; Walker, S. R.; Hutton, R. D.; Baker, E. N.; Parker, E. J., Potent inhibitors of a shikimate pathway enzyme from *Mycobacterium tuberculosis* combining mechanism- and modeling-based design. *J. Biol. Chem*. **2011,** 286 (18).

83. (a) Henderso.Ej; Zalkin, H.; Hwang, L. H., Anthranilate synthetase-anthranilate 5-phosphoribosylpyrophosphate phosphoribosyltransferase aggregate - catalytic and regulatory properties of aggregated and unaggregated forms of anthranilate 5-phosphoribosylpyrophosphate phosphoribosyltransferase. *J. Biol. Chem.* **1970,** 245 (6), 1424-&; (b) Ogara, J. P.; Dunican, L. K., Mutations in the trpd gene of *Corynebacterium glutamicum* confer 5-methyltryptophan resistance by encoding a feedback-resistant anthranilate phosphoribosyltransferase. *Appl. Environ. Microbiol*. **1995,** 61 (12), 4477-4479; (c) Sugimoto, S.; Shiio, I., Regulation of tryptophan biosynthesis by feedback inhibition of the 2nd-step enzyme, anthranilate phosphoribosyl-transferase, in *Brevibacterium flavum. Agr. Biol. Chem. Tokyo* **1983,** 47 (10), 2295-2305.

84. Hanahan, D., Studies on transformation of *Escherichia coli* with plasmids. J. Mol. Biol. **1983,** 166 (4), 557-580.

85. Studier, F. W., Protein production by auto-induction in high-density shaking cultures. *Protein Expr. Purif.* **2005,** 41 (1), 207-234.

86. McPhillips, T. M.; McPhillips, S. E.; Chiu, H. J.; Cohen, A. E.; Deacon, A. M.; Ellis, P. J.; Garman, E.; Gonzalez, A.; Sauter, N. K.; Phizackerley, R. P.; Soltis, S. M.; Kuhn, P., Blu-Ice and the distributed control system: software for data acquisition and instrument control at macromolecular crystallography beamlines. *J. Synchrot. Radiat.* **2002,** 9, 401-406.

87. Kabsch, W., XDS. *Acta Crystallogr. Sect. D-Biol. Crystallogr.* **2010,** 66, 125-132

88. Battye, T. G. G.; Kontogiannis, L.; Johnson, O.; Powell, H. R.; Leslie, A. G. W., iMOSFLM: a new graphical interface for diffraction-image processing with MOSFLM. *Acta Crystallogr. Sect. D-Bio. Crystallogr.* **2011,** 67, 271-281

89. Bailey, S., The CCP4 suite - programs for protein crystallography. *Acta Crystallogr. Sect. D-Biol. Crystallogr*. **1994,** 50, 760-763.

90. Karplus, P. A.; Diederichs, K., Linking crystallographic model and data quality. *Science*. **2012,** 336 (6084), 1030-1033

91. Murshudov, G. N.; Vagin, A. A.; Dodson, E. J., Refinement of macromolecular structures by the maximum-likelihood method. *Acta Crystallogr. Sect. D-Biol. Crystallogr*. **1997,** 53, 240-255.

92. Emsley, P.; Cowtan, K., Coot: model-building tools for molecular graphics. *Acta Crystallogr. Sect. D-Biol. Crystallogr.* **2004,** 60, 2126-2132.

93. Chen, V. B.; Arendall, W. B.; Headd, J. J.; Keedy, D. A.; Immormino, R. M.; Kapral, G. J.; Murray, L. W.; Richardson, J. S.; Richardson, D. C., MolProbity: all-atom structure validation for macromolecular crystallography. *Acta Crystallogr. Sect. D-Biol. Crystallogr*. **2010,** 66, 12-21.

94. Schuttelkopf, A. W.; van Aalten, D. M. F., PRODRG: a tool for high-throughput crystallography of protein-ligand complexes. *Acta Crystallogr. Sect. D-Biol. Crystallogr.* **2004,** 60, 1355-1363

95. Technologies, A. Quikchange Primer Design. http://www.genomics.agilent.com/primerDesignProgram.jsp.

96. Engh, R. A.; Huber, R., Accurate bond and angle parameters for x-ray protein-structure refinement. *Acta Crystallogr. Sect. A* **1991,** 47, 392-400.